**THE DISSERTATION COMMITTEE FOR MATTHEW ROBERT BEAUDRY CERTIFIES THAT THIS IS THE APPROVED VERSION OF THE FOLLOWING DISSERTATION:**

# AEROSOL MEASUREMENT AND MITIGATION IN $CO_2$ CAPTURE BY AMINE SCRUBBING

**Committee:**

Gary T. Rochelle, Supervisor

Eric Chen

Lea Hildebrandt Ruiz

Roger T. Bonnecaze

Hanna Knuutila

# AEROSOL MEASUREMENT AND MITIGATION IN $CO_2$ CAPTURE BY AMINE SCRUBBING

BY

**MATTHEW ROBERT BEAUDRY**

**DISSERTATION**

Presented to the Faculty of the Graduate School of

The University of Texas at Austin

in Partial Fulfillment

of the Requirements

for the Degree of

**DOCTOR OF PHILOSOPHY**

**THE UNIVERSITY OF TEXAS AT AUSTIN**

**DECEMBER 2017**

# DEDICATION

To Ed and Kathy Beaudry

# ACKNOWLEDGEMENTS

I would first like to thank Dr. Rochelle for his guidance and support as an advisor. From the beginning of my time in his group, Dr. Rochelle has treated me with incredible kindness and respect. He has accomplished this while pushing me to produce results, often with resistance from my end. His curiosity and dedication are impressive and inspirational. Most importantly, he has motivated me to not only be the best scientist and engineer I can be, but to be a better person as well. I am incredibly grateful for the opportunity to work in his lab.

Working with Eric Chen at Pickle Research Center has been an informative and enjoyable experience. Eric has been a valuable mentor, and someone I could always turn to when projects inevitable went haywire. Through him, I've learned valuable lessons on management and project planning. I admire his positive outlook and willingness to always extend help when needed. His crew has been invaluable as well; special thanks to Virbin, Tolu, Chris, Daniel, Janelle, Racheal, and Michael for all their assistance.

Thanks as well to the rest of my committee: Lea Hildebrandt Ruiz, Roger Bonnecaze, and Hanna Knuutila. I am very grateful their willingness to serve on my committee. Their interest in my research and advice on the direction to take this project has been helpful and is appreciated.

It has been a gratifying experience to work alongside the many members of the Rochelle research group. Special thanks to Steven Fulk, my predecessor on this project. The work that Steven accomplished, both in the lab and in modeling, have been instrumental in everything that was accomplished in my research. His sense of humor,

and passion for sports and coffee, helped make our office a great environment. Thanks to Di Song for putting up with us, and for occasionally laughing at my bad jokes. Korede Akinpelumi is the successor to this project and has been invaluable help for this research. I am confident that he will take this research to new heights, and hope that I have been as valuable of an asset to him as he has been to me. I was fortunate to have Vietnam Nguyen work with me as an undergraduate researcher; his contributions in designing and building the FTIR analyzer system are greatly appreciated.

Other members of the Rochelle lab have helped make working in this group an incredible experience. In particular, Paul Nielsen and Kent Fisher have provided solvent analytical data that has been invaluable in this research. Both have helped with pilot plant campaign setup as well, and have always been a pleasure to work with. Yue Zhang's expertise in modeling has contributed greatly to this research, and her knowledge in DeltaV™ has been a tremendous asset for pilot plant campaigns. Maeve Cooney has always provided humor, and helpful input on writing and travel logistics.

I would like to thank the members of the Luminant Carbon Management Program and the Texas Carbon Management Program for their financial support. Thanks as well to the Engineering Foundation Endowed Graduate Fellowship, the Virginia and Ernest Cockrell, Jr. Fellowship, and the Department of Energy under Award Number DE-FE0005654.

Working with the University of Texas Separations Research Program has been a gratifying experience. Henry Bautista, Steve Briggs, and Robert Montgomery have been outstanding to work alongside. I've learned a great deal from these three, and I

appreciate their willingness to cause process upsets for the sake of my experiments. Jarett Spinhirne has been a valued asset for the plant analyzer systems, and someone who I could always turn to for advice in a variety of situations. I've learned much about project management and pilot plant operations from Dr. Frank Seibert, but I've most appreciated the conversations we've had over our shared passion for Houston sports.

A significant portion of this research has focused on developing analytical techniques for the flexibility of use at different pilot plants. Naturally, this has resulted in extensive field work at other processes besides UT-SRP. At the University of Kentucky, Kentucky Utilities, Louisville Gas and Electric Slipstream plant, Jesse Thompson and Kunlei Liu were invaluable for providing logistics and financial support. Their advice and assistance were instrumental in developing field sampling techniques and data interpretation, and their company was always appreciated at conferences. David Link and Michael Manahan were also helpful advisors. The operations and engineering crews at the slipstream plant were vital in the success of the sampling campaigns.

Justin Anthony and John Carroll at the National Carbon Capture Center were helpful in coordinating the sampling campaign logistics and providing equipment and construction as needed. The operations and maintenance crews at the NCCC SSTU were always friendly and helpful, and a pleasure to work with. Their banter and sports debates provided appreciated entertainment during unit downtimes.

Special thanks to Shallaco McDonald and the CPE machine shop for their contributions in producing equipment for this research. Thanks as well to Dr. John Pearce at CEER, for his invaluable advice and willingness to help me with

troubleshooting equipment and finding parts. Dr. Bruce Eldridge has been not only willingly shared his lab space with us, but has opened up his home and treated me as a member of his own research group. His friendship and support has been greatly appreciated.

For me, graduate school did not begin in the Rochelle research group. I was an understudy in the Manthiram group for the first two years and ten months of my graduate career. During my time in this lab, I was fortunate to acquire lessons in safety and knowledge in materials characterization techniques. Just as importantly, I spent those years learning the value of supportive management and constructive feedback. The opportunity I was given in this group played a role in my growth as a graduate student, ultimately leading me to become who I am today.

I've been incredibly fortunate to have had the ceaseless support of my family through this endeavor. My parents have always offered encouragement and help in any way they can. Thank you to my dad; he taught me how to use all the tools that were necessary to conduct this research. More importantly, he inspired me to work hard and be curious. My mom inspired me to never stop chasing my goals, and to stand up for what I believe in. My brothers and sister provided encouragement and entertainment throughout it all.

Grad school is a tumultuous time for everyone; luckily, we don't have to do it alone. To the friends I have made along the way, I am grateful to have each and every one of you in my life. Your friendship through this process is appreciated, and I hope I have given back as much support as I have received.

Finally, special thanks to Amanda Paine for her love, advice, and sense of humor as I've worked towards this degree. She has inspired me to always give my best effort, and to try to improve myself every day. Amanda, I'm glad I found you, and I look forward to our future together.

# AEROSOL MEASUREMENT AND MITIGATION IN $CO_2$ CAPTURE BY AMINE SCRUBBING

Matthew Robert Beaudry, Ph. D.

The University of Texas at Austin, 2017

Supervisor: Gary T. Rochelle

Amine solvent losses are a significant issue for $CO_2$ capture by amine scrubbing. Solvent lost through aerosol emission represents an environmental hazard with adverse economic implications. This research focuses on developing analytical systems to quantify amine aerosol emissions. Fourier Transform Infrared Spectrometry quantified amine emissions and Phase Doppler Interferometry determined aerosol size and concentration.

Baghouse pretreatment of the flue gas significantly reduced amine emissions through collection of aerosol nuclei. A baghouse at the National Carbon Capture Center (NCCC) reduced monoethanolamine (MEA) emission by over a factor of 10.

An $SO_3$ generator was built to facilitate bench and pilot scale aerosol experiments by reacting $SO_2$ in air over vanadium pentoxide catalyst at 520 $^{o}$C. Aerosol generation at UT-SRP produced up to 1.7 grams per minute of $SO_3$, with conversion exceeding 81 %. Bench scale experiments achieved conversion greater than 97 % and aerosol concentration up to 7E4 $cm^{-3}$.

$SO_3$ increased piperazine (PZ) emission by up to 7.6 mol PZ/ mol $SO_3$. $SO_2$ increased PZ emission by 1 mol/ mol $SO_2$, and increased MEA emissions by 3.9 mol/ mol $SO_2$. $H_2SO_4$ increased PZ emission by 3 mol/ mol $H_2SO_4$.

PZ resisted aerosol emissions with lower $SO_3$ content; this is because a low inlet aerosol nuclei concentration results in rapid aerosol growth and subsequent collection by impaction. Higher process temperatures correlated with decreasing PZ emission, supporting the growth and capture theory. Increasing the solvent PZ content was shown to strongly correlate with increasing PZ emission.

In bench scale experiments, PZ emission and aerosol size both increased as the PZ content in the solvent increased. Lowering the temperature bulge stage reduced PZ emission and the aerosol size. Increasing the inlet $CO_2$ correlated with larger aerosol. Increasing the solvent $CO_2$ loading and the inlet $SO_3$ resulted in greater aerosol concentration.

Operations with a blower upstream of the absorber increased MEA aerosol emission. The upstream blower resulted in larger aerosol in greater quantities, containing a greater quantity of MEA Reduced MEA emission with an intermediate blower are probably due to collection of aerosol through impaction within the blower.

# TABLE OF CONTENTS

# LIST OF TABLES

# LIST OF FIGURES

# CHAPTER 1: INTRODUCTION

Rising worldwide energy demands have resulted in the increased consumption of fossil fuels for energy, causing a dramatic rise in $CO_2$ greenhouse gas emissions and a subsequent atmospheric temperature increase. Greenhouse gases absorb and emit infrared radiation; their growing atmospheric concentration results in increasing temperatures to the detriment of the environment (IPCC, 2007). Alternative energy sources that are non-polluting and sustainable are the key to meeting long-term energy needs. Combining power sources such as wind and solar energy with modernized electrical distribution systems and increasingly efficient energy users can mitigate environmental damage. The conversion from current fossil fuel based energy sources to modern sustainable technologies will be a time consuming and expensive transition. Therefore, bridging technologies are needed to successfully traverse the gap between the fossil fuel and alternative energy eras.

## 1.1 $CO_2$ CAPTURE BY AMINE ABSORPTION/STRIPPING

Post-combustion $CO_2$ capture and sequestration (CCS) is a viable technology for the collection of $CO_2$ emissions prior to atmospheric release. This process removes $CO_2$ from a combustion process exhaust stream. The captured $CO_2$ can then be used as a feedstock for production of a more valuable commodity, as a median to aid in enhanced oil recovery, or can be sequestered underground for permanent storage. Due to the costs associated with CCS facilities, this is a technology best implemented for treating flue gas from point source $CO_2$ emissions, such as power plants, cement production units, and petrochemical refining facilities. Power generation, especially from coal, accounts for

the vast majority of $CO_2$ emissions; by 2050, $CO_2$ from power plants will account for 50% of global $CO_2$ emissions (IPCC, 2005).

A variety of technologies exist for post combustion CCS, the most well practiced and viable of which is alkanolamine scrubbing for acid gas removal. This was first patented by Bottoms in 1930 (Bottoms, 1930), and pairs an absorber column with a stripping column to absorb and subsequently strip $CO_2$ from a gas stream by the use of an amine solvent. The process, modified for $CO_2$ capture, is presented below in Figure 1.1.

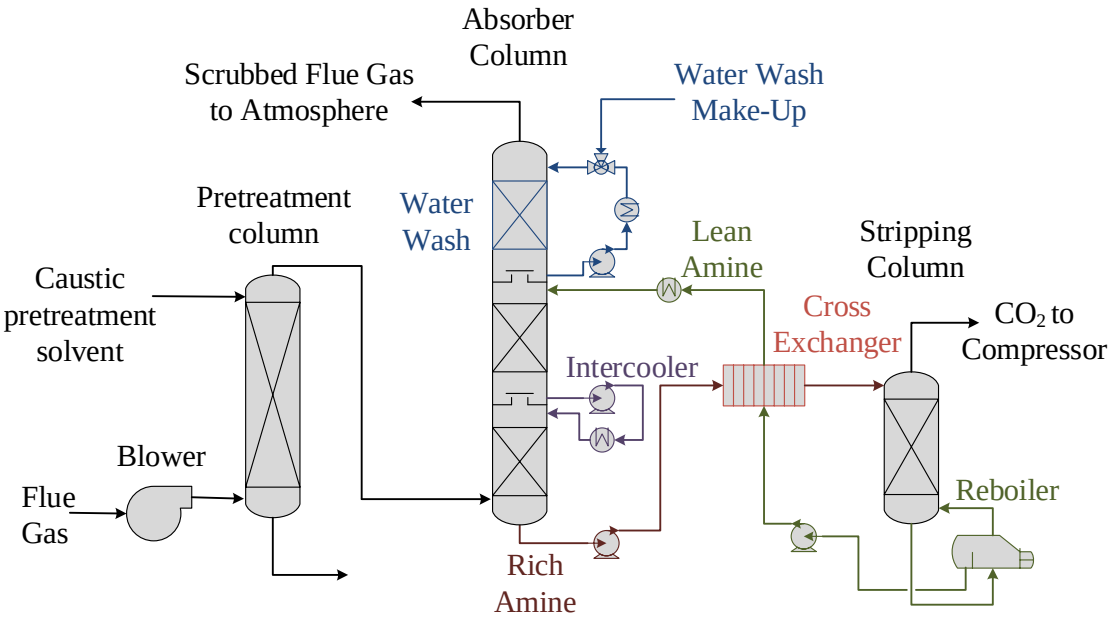


**Figure 1.1: Absorption and Stripping System with Auxiliary Units for $CO_2$ Capture**

A blower is used to provide positive pressure for the flue gas side of the capture process. The flue gas is then passed through a pretreatment column, which uses a caustic solution to remove $SO_2$. The desulfurized flue gas enters the bottom of the absorber column, where it is contacted with an aqueous amine solvent to remove the $CO_2$. Absorber columns will often use multiple packed beds and intercooling systems to

maintain the desired temperature throughout the column and prevent the formation of excessive temperature bulges due to the exothermic heat of the absorption reaction. Absorbers are designed to capture varying percentages of the inlet $CO_2$; 90% is a typical design value. The scrubbed flue gas then enters the water wash, which can be added on top of the absorber column or as a standalone column. The water wash is designed to capture amine and ammonia byproduct volatile vapor emissions. From there, the treated flue gas is released to the atmosphere.

The $CO_2$-laden (Rich) amine that exits the bottom of the absorber column is sent to a cross exchanger, a heat exchanger designed to economically aid the process by conserving the heat from the stripper. The rich amine is heated in the cross exchanger and enters the stripping column, also known as the regenerating column. A reboiler supplies the necessary heat to desorb the $CO_2$ from the amine solvent. The $CO_2$ is released as a vapor at the top of the stripper and is sent to compressors for pipeline shipment. The hot (Lean) amine solvent from the stripper is passed through the cross exchanger to heat the rich amine, then cooled further in a trim cooler and subsequently returned to the top of the absorber column.

Alternative configurations for solvent regeneration have been studied and proven feasible. At the University of Texas Separations Research Program, an advanced flash stripper has been used at the pilot scale (Lin, 2016; Chen, 2014). This process utilizes a a modified cross exchanger configuration to strip $CO_2$ from the amine solvent more efficiently than a simple stripper.

## 1.2 AMINE LOSSES

Alkanolamine scrubbing technology is suitable for $CO_2$ capture; however, significant issues remain to be solved before wide scale implementation can occur. Major concerns include amine losses by degradation and volatile atmospheric releases.

Degradation amine losses can occur through a variety of mechanisms. Prolonged exposure of the solvent to oxygen from the flue gas can lead to oxidative degradation (Sexton, 2008; Closmann, 2011; Freeman, 2011). Contaminants in the flue gas, such as $SO_x$, $NO_x$, $NH_3$, and fly ash particulates, can also contribute to oxidative degradation. The high temperatures used in stripping can result in thermal degradation of the solvent as well (Davis, 2009). The solvent performance suffers as degradation occurs; degradation byproducts, such as heat stable salts, non-volatile organic compounds, and suspended solids, can be toxic and have high disposal costs (Sexton, 2014).

Volatile atmospheric losses are another concern at $CO_2$ capture facilities utilizing amine scrubbing. Amine solvent lost through the overhead of absorber columns not only represents a significant environmental and safety hazard, but also has undesirable economic implications. Amine losses can occur via three different processes: through the gas phase as a function of vapor pressure in the absorber column, through liquid entrainment as a function of the column gas velocity, and as a mist composed of aerosol.

### 1.2.1 Vapor Phase Losses

The amine solvent used in the $CO_2$ scrubbing process can be emitted from the process through the gas phase as a function of vapor pressure. Amines with higher volatility exhibit greater potential for losses through the vapor phase. The amine

volatility is dependent on the amine molecular weight, structure (Hindrance, polarity, functional groups), and $CO_2$ loading (Nguyen, 2013).

Amine losses through the vapor phase can be mostly mitigated by the proper design and use of the water wash. Water washes contact the gas phase with water or a solution with a low amine content, resulting in the transfer of the volatile amine from the gas phase to the liquid. Washing steps are a common unit operation at $CO_2$ capture facilities and are currently used to mitigate the emission of amine degradation products such as ammonia.

### 1.2.2 Entrainment Losses

Amine losses can occur through solvent carryover at the gas outlet of the absorber. This can be caused by foaming or flooding within the column. Foaming can be mitigated by the use of anti-foaming agents. Flooding is a result of excessive gas velocities in the column; high gas flow rates can entrain the amine solvent drops, resulting in amine losses. These losses can be reduced by operating within the designed process parameters and maintaining gas flow rates lower than the rates necessary for entrainment.

### 1.2.3 Aerosol Emissions

Aerosol emissions from absorber columns occur when aerosol nuclei sources are present in the incoming flue gas. Nuclei sources can be fly ash from the coal combustion process or submicron sulfuric acid drops produced from sulfur impurities in the fuel. Nuclei sources can also be homogeneously generated from the vapor phase due to rapid temperature fluctuations. Homogeneous nucleation of aerosol occurs exclusively

between molecules of the condensable components (Mertens, 2013; Wix, 2010). The nuclei sources collect water, amine and $CO_2$ while traveling through the absorber column. The water wash is ineffective at collecting aerosol smaller than 3 microns (Mertens, 2013; Mertens, 2014, Khakhakria, 2015). This is due to the inability of the washing column to collect aerosol with impaction as the small aerosol tends to follow the gas streamlines Brownian diffusion "random walk" pathway.

#### *1.2.3.1 Fly Ash Nuclei Sources*

Coal combustion produces nanoscale fly ash particulates composed primarily of silicon, aluminum, and iron oxides (Du, 2013). Multiple devices are used for fly ash control; baghouses use filters to capture particulates from flowing gas streams, electrostatic precipitators (ESPs) induce an electrostatic charge to remove solid aerosol, and cyclones utilize centrifugal forces to separate the particulates from the gas. These devices are not one hundred percent effective at fly ash removal, as particles of the nanometer size are challenging to capture without incurring substantial pressure losses and increasing operational costs. In addition, wet ESPs generate ozone, and $SO_3$ from $SO_2$ (Mertens, 2014b), thus exasperating the pollutant issue.

#### *1.2.3.2 $SO_3$ Nuclei and $SO_2$*

$SO_2$ and $SO_3$ are precursors to the formation of sulfuric acid and are both produced in the coal combustion process. $SO_3$ can also be present in fly ash (Du, 2013) and can be produced in wet electrostatic precipitator fly ash collection devices (Anderlohr, 2015). $SO_3$ can also be formed in selective catalytic reduction reactors, which mitigate nitrogen oxides, by converting $SO_2$ to $SO_3$ (Brachert, 2014; Cao, 2010).

This gas-phase $SO_3$ hydrolyzes with water vapor to form vapor sulfuric acid, which rapidly condenses to form aerosol nuclei. $SO_3$ can also form sulfuric acid though absorption by condensed water nuclei.

$SO_2$ can also react with ammonia or the solvent amine to form a sulfite salt, which can then hydrolyze to form sulfuric acid. As both ammonia and amine are present in amine-based $CO_2$ scrubbing, this reaction can easily occur. This can result in particle concentrations exceeding 1E8 $cm^{-3}$ (Mertens, 2014a).

## 1.3 AEROSOL EMISSIONS AT AMINE SCRUBBING FACILITIES

Aerosol emissions at amine based $CO_2$ capture pilot plants are a commonly observed issue. Amine aerosol formation can be visually and analytically detected. Physical observation can take place at the flue gas outlet from the pilot plant facility, if the scrubbed flue gas is released to the atmosphere. Photographic evidence of this is presented in Figure 1.2. Analytical techniques, such as Fourier Transform Infrared Spectrometry, Phase Doppler Interferometry, and Electrical Low Pressure Impaction, can also be used to confirm the presence of aerosol if means of visual confirmation are not available, (i.e., the scrubbed flue gas is returned to the power generation unit flue gas header).

**Figure 1.2: Amine Aerosol Release from UT-SRP Pilot Plant**

### 1.3.1 Mitsubishi Heavy Industries

Mitsubishi Heavy Industries (MHI) found an increase of KS-1 (a proprietary solvent) and ethanolamine (MEA) emissions to be proportional to the inlet $SO_3$ to the absorber column (Mitsubishi Heavy Industries, 2011). KS-1 emissions varied from 0.4 to

23.2 ppm after the water wash, and MEA emissions ranged from 0.8 to 67.5 ppm. A white plume was generated at the absorber flue gas outlet as $SO_3$ was introduced to the system. A proprietary multistage washing section, with varying solvent compositions and temperatures, helped partially mitigate the amine emissions (Kamijo, 2013).

### 1.3.2 SINTEF and TNO

SINTEF and the Netherlands Organization for Applied Scientific Research (TNO) collaborated on $CO_2$ capture pilot plant using 30 wt% MEA as the amine solvent (SINTEF, 2012; da Silva, 2013; Khakharia, 2013, Khakharia 2014; Kolderup, 2012). FTIR measurements of amine emissions at the water wash outlet were found to be significantly higher than predicted by the process model, by roughly 88 to 160 ppm. Lithium carbonate and rubidium carbonate tracers were added to the solvent to determine if entrainment was the cause of the excessive emissions; a negligible concentration of the tracers past the water wash determined that entrainment was not the cause of the amine emissions. A Brownian Demister Unit (BDU) was installed downstream of the water wash and reduced emissions to the levels predicted in models. This shows that aerosol were responsible for the majority of amine emissions, as Brownian diffusion is effective at aerosol capture but not vapor removal. The aerosol were found to be dependent on the maximum temperature in the absorber, the number of available nuclei for condensation, and the extent of temperature gradients in the absorber and water wash.

A variety of aerosol sizing technologies were used for aerosol observation. In-situ fog sensors used light extinction coefficients to find the Sauter mean diameters ($d_{Drop}$) of the BDU inlet and outlet. Aerosol entering the BDU ranged in $d_{Drop}$ from 0.76

to 7.88 μm, and from 0.2 to 1.74 μm at the outlet. An Electrical Low-Pressure Impactor (ELPI$^{TM}$) from Dekati with a pre-impactor plate (Anderson $D_{50}$ of 11 μm) was also used in combination with a TSI Aerodynamic Particle Sizer (APS$^{®}$). Isokinetic and isothermal conditions were maintained throughout the sampling system. Various issues plagued these extractive sampling techniques. Significant water condensation occurred in the ELPI™, resulting in shortened sampling run times. The pre-impactor plate was installed to mitigate this issue by removing excessively large drops, but this resulted in an underestimation of the amine content. Dilution was required for the APS$^{®}$, which caused evaporation of volatile components from the drops and significantly affected the particle size measurements. Additionally, the deposition of particles on the APS$^{®}$ inlet nozzle resulted in an underestimation of the particle count.

The BDU was found to be effective at reducing the amine emissions through the aerosol phase, with a removal of MEA at approximately 97% efficiency. However, operating the BDU resulted in an additional 50 mbar of pressure drop across the gas side of the absorption process. This additional pressure drop results in an increase of 2 to 7 % in the total process energy consumption (van der Gjip, 2012; Khakharia, 2015).

### 1.3.3 National Carbon Capture Center

A 2012 pilot plant campaign at the National Carbon Capture Center in Wilsonville, Alabama experienced MEA emissions of over 100 ppm when amine vapor emissions were predicted to be less than 3 ppm (Carter, 2012). The increased amine emissions were found to be due to aerosol with $SO_3$ as the nuclei source. Amine emissions were found to increase with increasing $SO_3$ levels and by deactivating the

upper absorber bed; emissions decreased with reducing the water wash MEA content and increasing the absorber column temperature.

Additional aerosol characterization was performed at this facility by ELPI+$^{TM}$ (Saha, 2017). The aerosol concentration ranged from 1E6 to 1E7 per $cm^3$, with a median aerosol size of 0.12 μm. Aerosol concentration were greater at the inlet than at the water wash outlet, indicating coagulation occurrence in the scrubbing process. Lowering the absorber bed temperatures and using intercooling decreased the total aerosol concentration.

### 1.3.4 ITTK

The Institute for Technical Thermodynamics and Refrigeration (ITTK) at Karlsruhe Institute of Technology (KIT) has performed a variety of tests on the loss of MEA solvent through aerosol emissions at the bench scale.

#### *1.3.4.1 Khakharia*

A condensation particle counter (CPC) was used to measure particulate concentrations, with a soot generator and an $SO_3$ synthesis reactor to produce aerosol nuclei. Figure 1.3 presents the effect of varying the aerosol nuclei concentration and type on the MEA emissions.

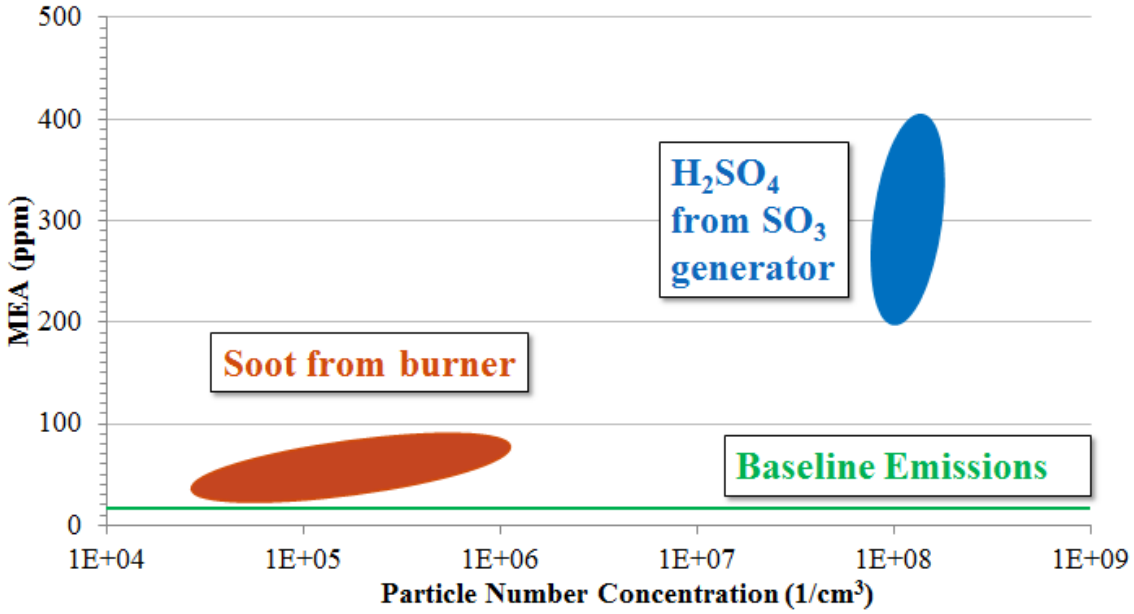


**Figure 1.3: Amine emissions ranges at KIT based on aerosol nuclei**

The soot generator produced aerosol concentrations between 3E4 and 9E5 $cm^{-3}$, which resulted in MEA emissions of 36 to 72 ppm (Khakharia, 2013). The addition of $SO_3$ to the absorber column resulted in aerosol concentrations between 1.0E8 and 1.4E8 $cm^{-3}$, depending on the $SO_3$ synthesis reactor reactant feed rate. This resulted in MEA emissions between 215 and 394 ppm. A baseline MEA emission of 16 ppm was observed without the injection of aerosol nuclei. Summarily, aerosol emissions are strongly correlated with the inlet nuclei concentration; a higher concentration provides a greater surface area for condensation of volatile components.

Khakharia also observed that increasing the supersaturation of volatile components in the gas phase lead to an increase in aerosol sizes (Khakharia, 2015). This can be achieved by increasing the temperature difference between the gas and solvent,

changing the $CO_2$ loading of the solvent, and varying the amine solvent volatility and reaction enthalpy.

Varying the solvent loading resulted in more MEA being free to evaporate from the liquid to the gas phase; once in the gas phase, the volatilized amine can preferentially absorb into aerosol as opposed to the bulk liquid phase. Thus, varying the $CO_2$ within the absorber column can have more of an effect on aerosol formation than simply creating a temperature bulge. As the $CO_2$ content is reduced, the amount of $CO_2$ captured by the solvent lessens, leading to a higher amine activity and higher volatility. This leads to a reduction in the heat released due to the reaction, resulting in lowering the column temperature and the subsequent amine volatility. For the Piperazine-promoted AMP system, the first effect was dominant at above 6% $CO_2$, while the latter effect was dominant at lower $CO_2$.

In varying the amine reactivity, aerosol emissions were determined to be dependent on a promoter. Piperazine promoted AMP and potassium taurate promoted AMP solvents were tested; the Piperazine promoted AMP exhibited significant aerosol emissions, while the potassium taurate promoted solvent did not. Khakharia theorized that this is due to the difference in reaction kinetics between the two systems. Thus, relatively fast kinetics of the presence of a volatile promoter are required for aerosol emissions.

#### *1.3.4.2 Brachert*

Experiments by Brachert et al. confirmed aerosol number concentrations in the range of 1E8 with sulfuric acid nuclei (Brachert, 2013). Reducing the $SO_3$ and increasing

the soot concentration produced the same particle concentration of aerosol, as found with a condensation particle counter. This indicates that homogeneous nucleation produced the vast majority of aerosol over heterogeneous nucleation.

Further work compared measurements between a Condensation Particle Counter (CPC) and ELPI+$^{TM}$ (Brachert, 2014). It was determined that increasing the $H_2SO_4$ in the inlet flue gas resulted in similar aerosol number concentrations, but increased the aerosol sizes. $SO_3$ was produced by oxidizing $SO_2$ with air through a 500 °C microreactor using Pt catalyst on $TiO_2$ microstructured foils. The $SO_3$ hydrolyzes with water to form a sulfuric acid aerosol mist. Aerosol sizes upstream of the amine scrubbing process were found to be well below submicron in size; the $d_{50}$ of produced aerosol was approximately 35 nm.

The CPC and ELPI+™ both required dilution of the sampled gas stream; the CPC required a dilution factor of 1E4, and the ELPI+™ was varied between 1E1 and 1E4. A PALAS GmbH DC10000 cascade dilutor was used. This resulted in significant variations in number concentration measurements, both between analyzers and within the ELPI+™ itself. Figure 1.4 presents the aerosol concentration measurements for both analyzers as a function of the dilution ratios and $SO_2$ flow rate to the microreactor.

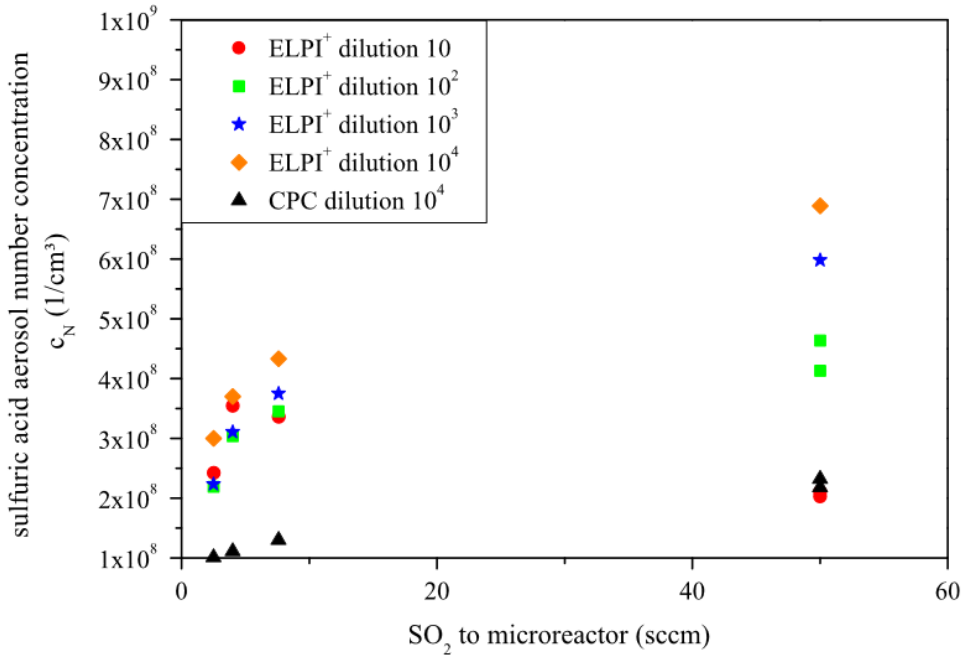


**Figure 1.4: Comparison of measured number concentrations at different sulfuric acid content at the pilot plant with CPC and ELPI+ at different dilutions (Brachert, 2014).**

The CPC was found to return significantly lower concentration values than the ELPI+™ at all $SO_3$ flow rates. In turn, the dilution caused variations of the ELPI+™ measured aerosol number concentrations between 1E8 and 3E8. Dilution error will increase as the concentration of volatile components in the aerosol phase increase. Larger aerosol with higher water content can have significant evaporation, which can result in a shift in the particle size distribution measured by the ELPI+™.

#### *1.3.4.3 Anderlohr*

Work by Anderlohr et al. focused on correlating aerosol emissions with the operating parameters of a lab scale wet electrostatic precipitator (WESP) (Anderlohr,

2015). Wet electrostatic precipitators operate by using induced electrostatic charge to charge particulates, which are then collected by grounded collection plates. This is a continuation of previous research performed at ITTK, with the goal of determining the feasibility of using a WESP as an amine aerosol countermeasure through flue gas pretreatment (Mertens, 2014b). A mix of $SO_2$ and air was fed to a $SO_3$ generating microreactor, and passed through a $H_2O$ quench tower to form $H_2SO_4$ vapor. The WESP was located downstream of the quench tower; it was theorized that it WESP would collect aerosol drops prior to entering the amine scrubbing process, thus mitigating amine aerosol emissions by pretreating the inlet gas stream.

Higher $SO_2$ in the flue gas resulted in reduced aerosol collection efficiencies, due in part to the oxidation of $SO_2$ to $SO_3$ from contacting the corona discharge plasma. As the WESP operating voltage increased, the $SO_3$ production rate increased, resulting in increased supersaturation within the WESP. This supersaturation leads to homogeneous nucleation, and to an increase in the concentration of aerosol drops.

#### *1.3.4.4 Mertens*

Aerosol particle size distributions studies were performed at ITTK by Mertens et al. with the use of an ELPI$^{+™}$ (Mertens, 2014a). The majority of aerosol were found to be smaller than 0.2 μm, but amine emissions were mostly due to aerosol between 0.5 and 2.0 μm. The ELPI+™ results indicated that raising the $H_2SO_4$ through increasing $SO_3$ generation resulted in an increase in the aerosol drop size but caused no significant variation in the particle number concentration. Particulate filtration on the inlet flue gas was found to reduce amine emissions by removal of particulate aerosol nuclei. However,

this was not effective at mitigating aerosol emissions due to $H_2SO_4$ aerosol nuclei; sulfuric acid as low as 0.5 ppm resulted in visible MEA mist formation (Mertens, 2014c). Sampling before and after the absorber column showed that aerosol drops grow significantly in the absorber column while the particle concentration drops by a factor of almost five. It is unclear if this reduction was due to coagulation effects or overestimation by the ELPI+™. Dilution ratio was found the effect the particle size distribution for ELPI+™ measurements at the absorber outlet, due to the increased content of volatile components within the aerosol drops. This uncertainty, combined with the issues of extractive sampling and dilutions, highlights the importance of in-situ or undiluted extractive aerosol measurement techniques.

Additional sampling at the Esbjerg $CO_2$ capture pilot plant found that the extractive sampling geometry had a minimal impact on the measured MEA, due in part to the small aerosol diameters (Mertens, 2013; Mertens, 2014a). A single stage water wash was found to be ineffective at mitigating amine aerosol emissions. FTIR "Hot and wet" sampling was performed alongside two varying manual sampling techniques that utilized chilled impingement trains and thermal desorption systems (Mertens, 2012). Significant discrepancies were found in the amine measurements between the two manual sampling techniques. It was hypothesized that this was due to the presence of amine aerosol. Furthermore, the FTIR measurements revealed amine emissions three times higher than the manual sampling technique. The "Hot and wet" sampling technique maintains a temperature of 180 °C across the entire sampling train, which allows the sampling to occur without removing water, and therefore amine aerosol, from the sampled stream.

Amine emissions were found to be primarily dictated by the flue gas temperature at the top of the absorber, and the flue gas temperature gradient across the washing section. Reducing the temperature of the lean solvent stream was found to have less of an impact on amine emissions than directly reducing flue gas outlet temperature with increasing the water wash flow. Increasing the amine content in the water wash solvent was found to increase amine emissions.

### 1.3.5 Aker Solutions at TCM

Aker Solutions' Mobile Test Unit (MTU) $CO_2$ capture unit experienced amine mist formation resulting from 12 ppm $H_2SO_4$ in the flue gas feed from a residual catalytic cracker at Technology Centre Mongstad (TCM), Norway (Bade, 2014). The resulting amine emissions exceeded 200 ppm during conventional operation. A BDU installed upstream of the absorber column was found to significantly reduce the concentration of catalyst fines and sulfate anions, resulting in a reduction of amine aerosol emissions from the absorber outlet.

The MTU was equipped with the Aker novel emission control system, which uses pH and temperature controlled wash stages to mitigate emissions of volatile alkaline components (Bade, 2014). A direct contact cooler with caustic was used to reduce inlet $SO_2$ content to below 2 ppm, while an upstream BDU reduces inlet particulate quantities to below 1 ppm. Use of the BDU and caustic wash reduced amine emissions to 7.6 ppm without the pH controlling outlet washing stages. With the acid wash at the absorber outlet, amine emissions were further reduced to 2.1 ppm. This indicates that capturing

aerosol downstream of the absorption process can prove to be more effective than upstream pretreatment for aerosol nuclei removal.

### 1.3.6 Rochelle Research Group, University of Texas at Austin

Previous work on amine aerosol emissions has been conducted by Steven Fulk and the Rochelle group at the University of Texas at Austin (Fulk, 2016; Fulk, 2014). Aerosol emissions were studied at both bench and pilot scales. FTIR analysis was used to quantify total amine emissions, while prototype Phase Doppler Interferometers (PDI) were used for aerosol size and number concentration measurements. Bench scale experiments were conducted at the University of Texas through the use of the Aerosol Growth Column, a 1-1/2" ID absorber column with approximately 6' of random packing. Gas and solvent concentrations, temperatures, and flow rates are controllable through a Labview interface. Aerosol were generated with the Liquid Vaporizer and Injector (LVI), which vaporized sulfuric acid and injected it into the process.

Pilot plant aerosol tests were performed at the University of Texas Separations Research Program (UT-SRP) facility. This process is does not use flue gas from a point source; instead, air is mixed with $CO_2$ to create a simulated flue gas. The benefit of this operation is the flexibility for flue gas $CO_2$ composition and the ability to observe increased oxidative degradation. The detriment of this process is the lack of water or aerosol nuclei in the inlet flue gas, which hinders the ability to simulate a real process. For aerosol measurement experiments, Fulk produced aerosol through the injection of $SO_2$ and vaporized $H_2SO_4$ (Fulk, 2016).

Fulk found that $SO_2$ in the inlet flue gas forms aerosol with piperazine solvent; approximately 65% of the $SO_2$ enters the aerosol phase through a variety of reaction mechanisms, some of which are presented in Table 1.1 (Bai, 1994). Aerosol formation was theorized to be similar to the formation of ammonium sulfite/bisulfite in ammonia scrubbers in the absence of photolytic oxidation. This highlights the importance of $SO_2$ polishing scrubbers that are independent of the $CO_2$ absorption process. Water condensation was found to be the primary aerosol growth mechanism in the water wash; reducing the amine content in the water results in increased aerosol growth. Increasing the aerosol residence time in the water wash increases the growth; a doubling of the water wash packing height results in a 13.7% increase in the final aerosol diameter for 8 m piperazine processes. The inlet $CO_2$ content was crucial in creating supersaturation in the absorber; similarly to Khakharia, Fulk determined that the loading difference between the aerosol and the bulk solvent creates a driving force for amine condensation into the aerosol. On a similar note, aerosol grow at a faster rate in non-intercooled absorption processed due to the differences in the solvent $CO_2$ loading and the absorber temperature. Varying the solvent flow rate in the absorber can lead to changes in the absorber temperature profile, which can vary the $CO_2$ removal at different stages and can impact the saturation and supersaturation conditions within the column.

**Table 1.1: Possible $NH_3$-$SO_2$-$H_2O$ vapor-phase reactions and solubility product constants (Bai et al., 1994). Partial pressures used in $K_{sp}$ expressions are atm.**

| | Equilibrium Constant | T [ºC] | |
|---|---|---|---|
| $(NH_4)_2S_2O_2(s) \leftrightarrow 2NH_3(g)+2SO_2(g)+H_2O(g)$ | $K_{sp}=exp[94.6-(39144T/)]$ | 60−110 | (1) |
| | $exp[96.5-(40767T/)]$ | 0−23 | |
| $(NH_4)_2SO_3(s) \leftrightarrow 2NH_3(g)+SO_2(g)+H_2O(g)$ | $K_{sp}=exp[73.8-(30601T/)]$ | 60−110 | (2) |
| | $exp[76.6-(32630T/)]$ | 0−23 | |
| $(NH_4)_2SO_3H_2O(s) \leftrightarrow 2NH_3(g)+SO_2(g)+2H_2O(g)$ | $K_{sp}=exp[93.8-(39144T/)]$ | 60−110 | (3) |
| | $exp[96.7-(40090T/)]$ | 0−23 | |
| $NH_4HSO_3(s) \leftrightarrow NH_3(g)+O_2(g)+H_2O(g)$ | $K_{sp}=exp[53.8-(22116T/)]$ | 60−110 | (4) |
| | $exp[54.7-(22928T/)]$ | 0−23 | |

Pilot plant aerosol emissions measurements were also conducted at the National Carbon Capture Center by the use of FTIR and PDI. Linking these two measurement techniques allowed for the calculation of the concentration of the amine solvent in the aerosol phase. The aerosol amine content was significantly lower than the amine concentration in the bulk solvent. This is due in part to the condensation of water in the

aerosol phase as the aerosol passes through the water wash. Aerosol diameters were found to be significantly greater than submicron, with concentrations ranging from 1E4 to 1E6 per $cm^3$. This differs from the findings of Mertens et al. (2014), who measured submicron aerosol at high concentrations (~1E8). The results by Fulk agree with those of Kolderup (2012), with an average aerosol diameter of 4.3 μm and a concentration of 1E6 per $cm^3$ as measured by ELPI+™. This discrepancy highlights the impact that upstream conditioning and downstream water washed have on the size and concentration of aerosol, and that the physical sampling location can significantly impact the particle size distribution.

### 1.3.7 Key Findings

#### *1.3.7.1 Aerosol formation and growth*

Increasing the aerosol nuclei concentration has resulted in an increase in the amine emission at each facility. Conversely, reducing the aerosol nuclei concentration has reduced the amine emission. Increases in aerosol solvent emissions can result from increases in the aerosol concentration or the aerosol size. For soot and fly ash aerosol nuclei, the amine emission increase is driven by an increase in the aerosol concentration and the aerosol size; in the case of sulfuric acid nuclei, the number concentration remains relatively constant but the aerosol size increases substantially (Khakharia, 2015; Mertens, 2014a).

Homogeneous sulfuric acid aerosol nucleation is a rapidly occurring process, occurring within a second (Wix, 2010). This occurs if the critical degree of saturation is exceeded. The aerosol growth mechanism is dominated by the partial pressure

differences of sulfuric acid and water between the aerosol drops and the gas phase; coagulation of particles is minimal unless approaching the upper bounds of particulate concentrations (Schaber, 1995). Smaller particles (<1 μm) are more likely to be affected by coagulation (Jacobson, 1993). Supersaturation is not reduced by aerosol growth but by new aerosol formation, resulting in a subsequent reduction in the supersaturation of the gas phase (Wix, 2010). Homogeneous nucleation is the dominant mechanism over heterogeneous nucleation, especially as the $SO_3$ increases (Sinanis, 2008). For $SO_3 \leftrightarrow H_2SO_4$ aerosol nuclei, heterogeneous nucleation is induced at roughly one degree of saturation, while homogeneous nucleation requires a higher supersaturation of approximately four degrees.

Aerosol formation and growth within amine-scrubbing processes is comparable to particulate nucleation in the atmosphere. Work by Almeida et al. found that the presence of amines above 3 ppt can enhance sulfuric acid particle formation rates more than 1000-fold as compared to $NH_3$ (Almeida, 2013). This is due to base-stabilization mechanism involving amine-acid pairs, which decreases evaporation from the clusters and reduces dependence on relative humidity and temperature. Sulfuric acid aerosol formation can still occur without the stabilizing presence of amines. Increasing $H_2SO_4$ content and lower temperature encourage nucleation. Nucleation rates are also sensitive to water composition (Yue, 1979a); the growth of drops shortly after formation is relatively slow, as higher water content in the bulk gas causes more water vapor to condense into the drop and reduce the sulfuric acid (Yue, 1979b). Decreasing the relative humidity results in

drop shrinkage due to water evaporation. Thus, changes in particle size depend on the direction of change in relative humidity (Nair, 1975).

#### *1.3.7.2 Aerosol measurement*

The ineffectiveness of water wash columns and the economic implications of impaction based particle collection necessitate additional research into practical and cost effective aerosol emissions control. It is clear that different pilot plants, with different process configurations and amine solvents, experience varying effects from the presence of aerosol nuclei sources in the flue gas feed. Aerosol observation under a variety of conditions is needed. As every $CO_2$ capture pilot plant is different, aerosol measurement techniques need to have the flexibility to adapt to diverse situations and conditions.

For total amine solvent emissions measurements, Fourier Transform Infrared Spectrometry (FTIR) has proven to be more than adequate (Mertens, 2012; Fulk, 2015). FTIR analysis at pilot plants is successful when utilizing a 'Hot and wet' strategy of maintaining a temperature of 180 °C across the sampling system. This prevents the condensation of water and amine within the sample train, which protects the FTIR analyzer from liquids while ensuring no sampled components are lost due to condensation. Mertens' comparison of FTIR sampling to manual low-temperature sampling techniques observed significant differences in measured amine values, due to the removal of water and condensable amine in the manual sampling methods.

The desired size range for an aerosol size measurement device includes the range between 0.5 and 2.0 μm, as Mertens et al. found most amine losses due to drops of this size (Mertens, 2014a). Increased range beyond that size distribution is important, as the

aerosol from ITTK may very well be different from aerosol from other pilot plants. A measurement device needs to be capable of observing drops between 0.1 and 10 μm; demisters are capable of removing larger drops, while smaller ones do not collect enough amine to significantly add to the cumulative emitted mass.

Aerosol measurement at the pilot scale requires extractive sampling techniques. This involves removing a slipstream of process gas for analysis, as opposed to in-situ sampling inside the process itself. Extractive sampling is more feasible due to improvements in practicality over in-situ measurements; maintenance, calibrations, and the frequent failure of process analyzers necessitates removal and repairs of analyzer systems, which cannot be easily performed while the process is running with in-situ measurement techniques.

Sample extraction conditions must be carefully controlled in order to mitigate aerosol losses to the analyzer. The sample port geometry can have an impact on the size distribution of aerosol measured by the analyzer. A sample port positioned perpendicular to the process stream can result in particle losses due to the change in flow direction. Aerosol drops have a higher density than the surrounding gas phase and can impact the walls of the perpendicular sample port due to their increased momentum; aligning the sample extraction port as close to isoaxial as possible to the sampled duct can mitigate these losses to a degree. With this in mind, it is vital that extractive sampling is performed under isokinetic conditions, where the sampled gas extraction velocity matches the duct velocity (Fulk, 2015). Drop losses can also occur due to gravitational settling and diffusional deposition. Thus, extractive sampling geometries should

minimize the distance traveled by the extracted sample, along with reducing the number of bends and contractions in the extraction system.

The temperature and gas phase concentrations in extractive sampling systems should closely mimic the conditions in the sampled duct. As noted previously, changes to the temperature and relative humidity can significantly impact aerosol size distributions. ELPI+™ sampling at NCCC by Saha et al. noted variations in the measured aerosol size distribution and concentration when using a heated dilution gas stream (Saha, 2017). To maintain a truly representative aerosol size sample, the sample extraction technique must maintain a close temperature to that of the sampled duct.

Previous pilot plant aerosol studies have revealed the inadequacies with extractive sampling techniques that require the dilution of the sampled stream. The SINTEF-TNO collaboration experienced a multitude of issues with ELPI+™ measurements, mostly stemming from excessive water condensation in the sampling system. Studies by Mertens et al. at ITTK cast uncertainty on the accuracy of ELPI+™ particle concentration measurements. Dilution of an extracted sample should not have a significant effect on the particle number density if the concentration of sulfuric acid nuclei results in aerosol diameters at or below the dry drop diameter (Brachert, 2014; Mertens, 2014a). However, an increase in the sulfuric acid increases the water content and thus creates the potential for water evaporation from the aerosol, resulting in an inaccurate representation of the true aerosol size distribution.

Dilution of the sampled stream was also required for the use of the APS® and for Condensation Particle Counters (CPC). CPCs expose the aerosol-laden sample stream to

a supersaturated gas, growing the particles to the point of easy detection. Dilution is necessary in these systems to prevent coagulation from occurring and an underestimation of the particle concentration. Coagulation of smaller aerosol can still occur, along with other aerosol losses inherent with extractive sampling techniques. CPCs also require pairing with a separate size selecting device to obtain particle size distribution results.

## 1.4 STRATEGY

Previous work in this group by Fulk has focused on studying the aerosol problem from a fundamental viewpoint by developing heat and mass transfer models for aerosol in $CO_2$ capture processes (Fulk, 2016). Gaining an understanding of aerosol behavior can lead to the development of representative computational simulations, which can be used to determine optimal process operating conditions for aerosol mitigation.

Aerosol particulate dynamic modeling was studied by Fulk using MATLAB® and Aspen Plus®. This focused on simulating the impacts of process variables and unit operating conditions on the aerosol diameter and composition, providing emissions estimations, and generating a theoretical explanation for aerosol growth based on the volatility and $CO_2$ loading of the amine solvent. The aerosol growth rate in the water wash was found to depend on the inlet drop composition and the amine content in the water wash solvent; high amine and $CO_2$ content in the solvent decreased the water driving force and the resulting particle growth rate. Increasing the water wash packing resulted in larger aerosol drops due to the increased residence time.

Other aerosol research has observed effective aerosol removal in packed columns by heterogeneous nucleation mechanisms (Heidenreich, 2000; Johannessen, 1997;

Calvert, 1984). By tuning operating parameters to encourage high degrees of supersaturation, aerosol can be grown to a size that allows for collection of drops by impaction on the column packing. The supersaturation degree is given by the Lewis number, the ratio of the heat and mass transfer rates. Heidenreich found that high concentrations ($10^6$ particles/$cm^3$) of submicron particles can be collected with a two-stage counter-current contactor, operating with high temperature differences between the gas and solvent. A similar column configuration has been explored and tested for amine scrubbing by Aker solutions, with further focus on the pH of the solvent (Bade, 2014).

An alternative strategy for aerosol abatement involves pretreating the flue gas to prevent aerosol nuclei from entering the amine scrubbing process. Caustic polishing scrubbers can be used for $SO_2$ removal; Fulk noted that 65% of $SO_2$ injected at the UT-SRP pilot plant left the process in the aerosol phase, and emphasized that amine scrubbing systems should not be designed for the simultaneous absorption of $CO_2$ and $SO_2$ (Fulk 2016). The use of upstream BDU for aerosol nuclei removal was found to be relatively effective (Bade, 2014), but results in pressure drop and a subsequent increase in operating costs.

While significant progress has been made in understanding aerosol emissions, further research is needed to determine the effectiveness of each strategy for different flue gasses and amine scrubbing processes. Additional studies into the interdependency of the process operating conditions and the dynamics of aerosol particles needs to be conducted in order to condition the aerosol to ease collection. Further analysis of the

impacts of pretreatment of the inlet flue gas, through $SO_2$ polishing or baghouse filtration units, will aid understanding of pretreatment.

## 1.5 RESEARCH SCOPE

The overall scope of this work is focused on experimental research on aerosol measurements and quantification of particle growth rates. This concentrates on the impact of process operating conditions on amine aerosol emission rates. Effective aerosol generation is the first emphasis. The ability to tune aerosol nuclei production rates is vital for aerosol studies. Further experiments are conducted in two different settings; on the bench scale Aerosol Growth Column at the UT Austin Pickle Research Center, and at multiple $CO_2$ capture pilot plants located throughout the United States.

### 1.5.1 Aerosol generation development

Experiments at the bench scale and at the UT-SRP pilot plant require an externally generated aerosol source, as these systems use a synthetic flue gas instead of flue gas form a power generation process. A variety of techniques are available for aerosol generation. This research focuses on $SO_3$ production via synthesis from $SO_2$ over a heated bed with vanadium pentoxide catalyst. The $SO_3$ hydrolyzes with water vapor and condenses to form sulfuric acid nuclei in the supersaturated conditions in the flue gas. The generated aerosol are injected upstream of the absorber on the bench or pilot scale. The generated aerosol should be as similar as possible to the aerosol found in existing amine scrubbing pilot plants. This is necessary for the accurate observation of aerosol concentration and size variations due to process conditions.

A model of the $SO_3$ generator was produced with Polymath computational software and used to size the generator components and determine optimal operating conditions. The reactor was sized to be used at varying scales, from benchtop up to 0.7 MWe pilot scales. The aerosol generator was successfully used during the April 2017 UT-SRP pilot plant campaign and in bench scale tests on the Aerosol Growth Column.

Previous research with the AGC and at the UT-SRP pilot plant utilized the Liquid Vaporizer and Injector (LVI), developed by Fulk (Fulk, 2014). The LVI feeds a liquid solution of sulfuric acid and water through a vaporizer and injects the solution into the process stream. The sulfuric acid rapidly condenses into aerosol nuclei, which are allowed to grow and are observed in the $CO_2$ capture process. The vaporizing of sulfuric acid is a highly corrosive process and results in the plugging and deterioration of the steel components of the LVI. The LVI has typically only been able to operate for a maximum of an hour at a time at the bench scale and 15–20 minutes at the pilot scale. Repairing the LVI after each run is costly in both time and money; therefore, development of an alternative aerosol generation technique has been imperative.

### 1.5.2 Bench scale aerosol quantification

Bench scale experiments are performed to test variables that cannot be easily tested in pilot plant conditions. Changing the amine solvent in a bench scale experiment is a much simpler operation to perform than at the pilot scale. This research proposes bench-scale experiments with varying process conditions to observe the effects on aerosol growth and amine emission quantities.

The gas phase $CO_2$ and $SO_3$ can be easily varied in bench scale experiments, which is not always the case at the pilot scale. The $CO_2$ loading and amine content in the solvent can also be varied at the bench scale without much effort. Experiments varying these process conditions can be performed to quantify their effects on amine aerosol emissions.

The Aerosol Growth Column (AGC) was designed and fabricated by Fulk in the Rochelle lab, and is designed to replicate the absorber side of an amine-based absorber-stripper $CO_2$ capture system on a bench scale. A process flow diagram of the system configuration is presented in Figure 1.5.

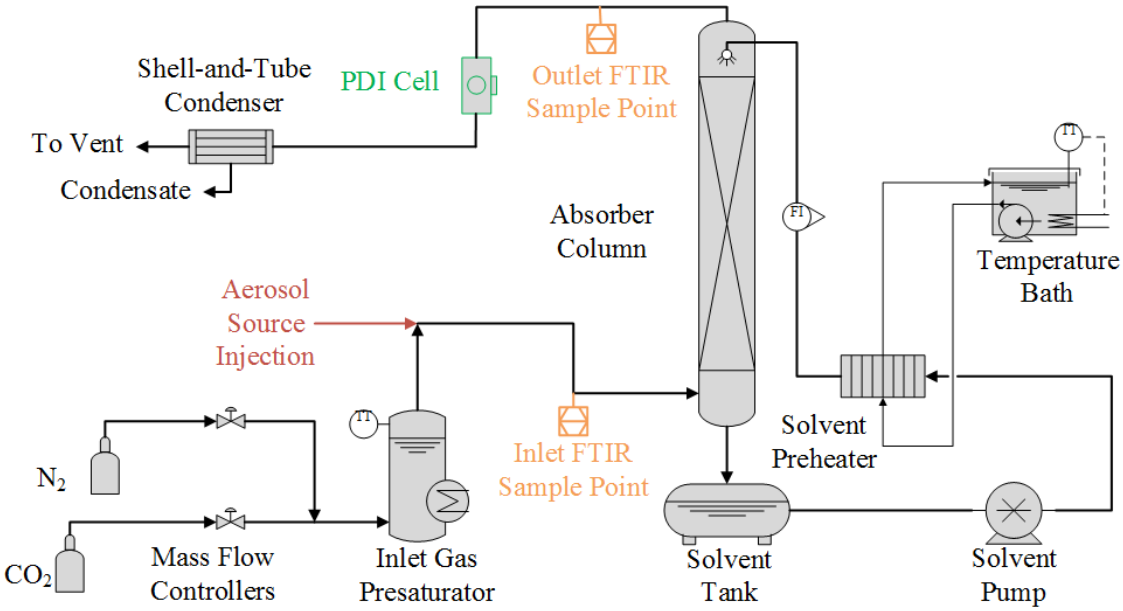


**Figure 1.5: Aerosol Growth Column Configuration**

A synthetic flue gas of nitrogen and carbon dioxide is fed to the presaturator, which bubbles the gas through water to simulate a direct contact cooler and add water to the gas. Gas flow rates are controlled with mass flow controllers with set points

established by Labview process control software. The saturated gas is fed to the absorber column, a 1.5" diameter column containing a single 6 foot bed of random packing. The scrubbed gas passes through a condenser to knock out condensable components and is vented to the fume hood.

The amine solvent used to capture the $CO_2$ is fed to the solvent tank at the bottom of the column. It is returned to the top of the column by a rotary pump, but not before passing through a solvent preheater to maintain the desired solvent temperature for the experiment. Solvent flow rates and temperatures are some of the variable parameters, and the AGC is flexible enough to run a variety of solvent conditions.

The red sections of Figure 3.1 denote the aerosol generation and injection system, and the green portions are locations for the Phase Doppler Interferometer sampling cell. Fourier Transform Infrared Spectrometry (FTIR) sample ports are indicated in orange.

### 1.5.3 Pilot scale aerosol quantification

Pilot-scale experiments can provide valuable opportunities for observing and measuring aerosol in industrially realistic conditions. This research focuses on facilities in three different locations: (1) University of Texas Separations Research Program (UT-SRP), (2) the University of Kentucky, Kentucky Utilities, and Louisville Gas & Electric collaboration (UKy/KU/LG&E), and (3) the National Carbon Capture Center (NCCC).

The pilot scale work expands upon the experiments performed on the bench scale. The effects of the amine solvent and the process operating conditions have been observed under more industrially realistic conditions. When possible, experiments were performed while varying the gas phase $SO_2$ and $CO_2$, along with the amine solvent composition and

$CO_2$ loading. The variation of the water wash temperature and flow rates can impact amine aerosol emissions. Variations of these parameters grant further insight into causes of amine emissions.

#### *1.5.3.1 UT-SRP*

The UT-SRP Pilot Plant is located at the Pickle Research Center in Austin, Texas. This pilot plant is unique in that is not specifically designed for $CO_2$ capture but adapts to a variety of separations processes. The 16.8" diameter column initially contained 2 packed beds with 10 feet of random packing each; upgrades in early 2017 added a third 10 foot bed of packing that can be utilized as a water wash or as a third absorption stage. Prior to the third packed bed installation, this process did not have a proper water wash but utilized a chiller and knockout drum as a simulated one. The facility is sized to capture $CO_2$ from a 0.1 MW power plant. The amine solvent is typically 5m or 8m piperazine, but the facility has the flexibility to use MEA as well. Instead of a typical stripper system for solvent regeneration, the UT-SRP pilot plant uses an advanced flash stripper (Chen, 2014).

The UT SRP is also unique in that it does not have a true flue gas stream from a point $CO_2$ emission source; instead, a synthetic flue gas is produced from air and $CO_2$ kept on site. The synthetic flue gas contains no aerosol nuclei sources, so aerosol generation must be provided. This has been accomplished in the past by the use of the LVI and by direct injection of $SO_2$. Both of these methods have produced aerosol observable through FTIR measurements and visual confirmation. Because of the synthetic nature of the flue gas, a pretreatment column is not needed. A multipoint FTIR

sampling system is used to quantify absorber performance and the emissions of volatile components.

This research focuses primarily on the April 2017 pilot plant campaign at UT-SRP, along with complementary results from aerosol testing during the March 2015 campaign. The April 2017 campaign was the first to utilize the catalytic $SO_3$ generator for aerosol testing.

#### *1.3.3.2 UKy/KU/LG&E Slipstream Plant*

UKy/KU/LG&E collaborate in operating a slipstream pilot plant at the E. W. Brown Generating Station in Harrodsburg, Kentucky. The flue gas from the coal-fired generating station is treated by a FGD and SCR units. The slipstream plant is scaled for capture from a 0.7 MW power plant and utilizes a caustic pretreatment column for $SO_2$ mitigation in the flue gas; this column can be bypassed as desired. The absorber column includes two beds of packing with a simplified water wash. A $CO_2$ recycle system injects $CO_2$ from the stripping section into the flue gas inlet to enrich the flue gas as needed.

This facility does not have an FTIR sampling system and requires the use of a portable system. Sample ports are located at the absorber inlet, the absorber outlet, and the water wash outlet. FTIR sampling at this facility has determined that aerosol are present and account for the majority of amine emissions. Amine emissions were higher than predicted by vapor pressure calculations when the pretreatment column was operated, although allowing $SO_2$ breakthrough by bypassing the pretreatment operation did further increase aerosol emissions. FTIR sampling was performed at the

UKy/KU/LG&E slipstream plant in August 2015 and January 2016, while the unit was operating with MEA solvent.

#### *1.3.3.3 NCCC with Southern Research*

The National Carbon Capture Center (NCCC) is located in Wilsonville, Alabama and utilizes flue gas from the Alabama Power Gaston Station Unit 5, an 880 MW supercritical pulverized coal generation plant. Southern Research runs the facility. Multiple carbon capture slipstream plants enable collaborators to bring their own amines and technologies to the NCCC site for testing. Previous research has confirmed the presence of aerosol at this facility (National Carbon Capture Center, 2012; Fulk, 2016; Saha, 2017).

FTIR and PDI sampling at the NCCC Slipstream Solvent Test Unit (SSTU) were performed December of 2015 and October of 2016. The SSTU was operating with MEA solvent during both campaigns. In early 2016, a baghouse pretreatment unit was brought online for Mercury removal. An added benefit of this pretreatment system was a reduction in $SO_3$, due to adsorption onto the activated carbon injected for the baghouse. FTIR and PDI measurements before and after the baghouse installation quantify the effect this pretreatment has on amine aerosol emissions. Furthermore, an ELPI+™ was used by Southern Research during the December 2015 campaign and allows for a valuable comparison of the PDI to the ELPI.

# CHAPTER 2: ANALYTICAL METHODS AND MATERIALS

This chapter focuses on the analytical techniques used for amine aerosol characterization at the bench and pilot scale. Fourier Transform Infrared Spectroscopy and Phase Doppler Interferometry theory and operation are covered in the first two sections. A third section of this chapter emphasizes the justification behind use of the PDI over comparable aerosol quantification devices. Standard operating procedures for FTIR and PDI analyzers are available in Appendix A and B, respectively. Further description of the multipoint FTIR sampling system used in the April 2017 UT-SRP pilot plant campaign can be found in Appendix C. More in-depth description of PDI theory and operation can be found in the dissertation of Steven Fulk (Fulk, 2016). This chapter is extensively based off and structured similarly to the dissertation chapter by Fulk, 'Analytical Methods and Supporting Equipment', with additional details provided.

## 2.1 FOURIER TRANSFORM INFRARED SPECTROSCOPY (FTIR)

Infrared spectroscopy is an analytical technique used to identify compounds based on the absorption of infrared light. This can be used on solid, liquid, and gas samples to identify composition based on the presence of the component functional groups. Fourier Transform Infrared Spectroscopy is a subset analytical technique of infrared spectroscopy that is used to identify components of a gas stream.

### 2.1.1 FTIR Theory of Operation

Fourier Transform Infrared Spectrometry utilizes a broadband light source cast through a configuration of mirrors to measure how a sample absorbs infrared (600-4,200 $cm^{-1}$) radiation. Only infrared active compounds (polyatomic and hetero-nuclear

diatomic molecules), such as $CO_2$, $H_2O$, $SO_2$, $NH_3$, and amines, will be detected by FTIR. Absorption of infrared light in these compounds leads to the excitation of molecular energy levels, resulting in molecular bond rotation and vibration (Fulk, 2016). Only compounds that are capable of a net dipole moment can absorb infrared light; therefore, monatomic and homo-nuclear diatomic molecules cannot be detected through FTIR.

The energy absorbed by a compound depends on the availability of transition states and the energy contained in the incident photon. This is inversely proportional to the wavelength and proportional to the wavenumber. The quantity and positioning of IR absorption bands is dependent on the types of atoms present in the molecule, the bond angles, and the bond strengths. As the absorption of infrared radiation is unique for each species, this allows for compounds to be identified and isolated in multicomponent samples. Quantification of the amount of each compound can be determined by using a logarithmic absorption law and accurate reference spectra.

FTIR analyzers use an interferometer, a black-body radiation source, and an IR detector to capture absorbance data across the IR frequency spectrum. The process begins by creating a broad spectrum of IR frequencies through the use of the black-body radiator. This radiation is aligned through a collimating lens and sent to an angled beam splitter, as shown in Figure 2.1. The incident light is reflected and refracted to the stationary and moving mirrors, which reflect the light back to the beam splitter for recombination. This generates an interference pattern that is dependent on the mirror position. The moving mirror can be repositioned rapidly, and has its position accurately measured with a reference laser.

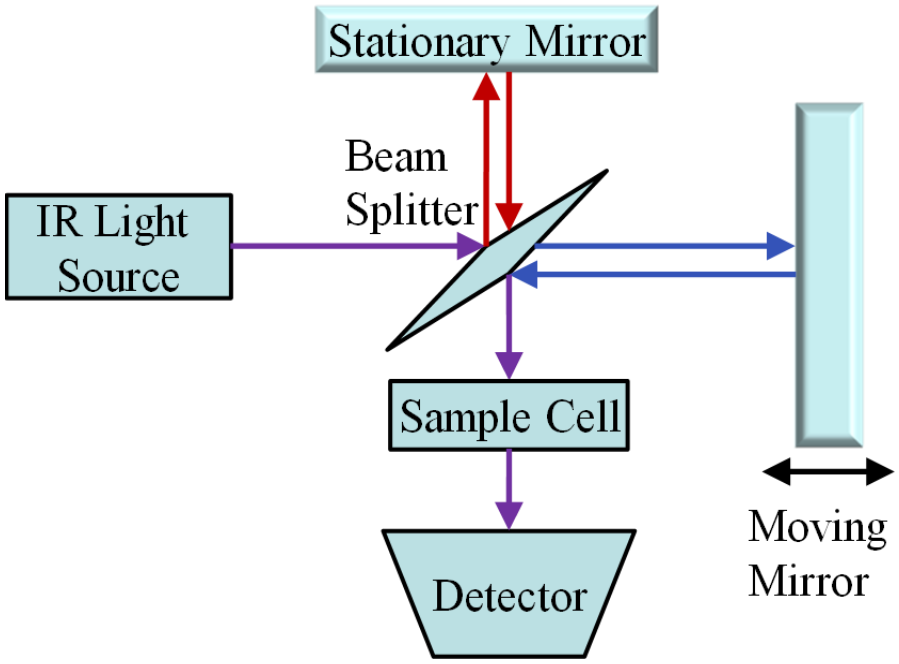


**Figure 2.1: Simplified beam path for an FTIR analyzer**

The recombined light is passed through a sample cell with a fixed optical path length. The sample cell utilizes curved mirrors to reflect the light beam multiple times through the cell, to extend the optical path. It is important to note that any contaminants or imperfections on the mirrors will result in changes to the interference pattern. To mitigate this possibility, the sample cell is heated to a temperature above the vaporization temperature of the sampled components to keep liquids out of the sample cell. A heated filter is used upstream of the FTIR analyzer to prevent solid particulates and non-condensable components from entering the sample cell and damaging the mirrors.

The light beam attenuates as it passes through the gas in the sample cell. A photodetector is used to measure the intensity of the light beam as a function of time upon exiting the sample cell. This generates an interferogram: a plot of the measured

intensity (in voltage) of the light versus the displacement of the moving mirror (the Optical Path Difference). The data in the interferogram is translated into a transmittance plot in the frequency domain by the use of a fast Fourier Transform. The sample absorbance can be determined by comparing the transmittance spectrum plot to a background sample.

Background spectra are generated by passing IR-inactive compounds, such as $N_2$, through the sample cell. As the sample gas is not absorbing IR radiation, transmittance is at its maximum possible value.

The Beer-Lambert law is used to correlate component concentrations to the absorption spectra. This law asserts that changes in the intensity of radiation while passing through an absorbing media are directly proportional to the local intensity, the concentration of the absorbing media, and the molar attenuation coefficient (a measure of how strongly each compound attenuates light at given wavelengths). The Beer-Lambert law is presented in Equation 2.1 in the differential form.

$$-dI = \varepsilon(\lambda) C\, I\, dx \tag{2.1}$$

where:

$I$ = Intensity of radiation

$\varepsilon(\lambda)$ = Molar attenuation coefficient

$C$ = Concentration of absorbing media

$dx$ = Differential thickness of absorbing media

Equation 2.1 can be integrated if the dependence of the molar attenuation coefficient on the concentration is negligible. This is represented in Equation 2.2:

$$A = \log\left(\frac{1}{T}\right) = \log\frac{I_0}{I} = \varepsilon(\lambda) C\, X \tag{2.2}$$

where:

$A$ = Absorbance

$T$ = Transmittance

$I_0$ = Incident radiation intensity

$X$ = Thickness of absorbing media

Equation 2.3 presents the total attenuation of radiation as a sum of the individual compounds in multicomponent mixtures:

$$A_{Tot} = \sum_{i=1}^{N_C} A_i = X \sum_{i=1}^{N_C} \varepsilon_i\,(\lambda) C_i \tag{2.3}$$

where:

$A_{Tot}$ = Total absorbance of mixture

$A_i$ = Absorbance of component *i*

$I$ = Component index

$N_C$ = Number of IR absorbing components in mixture

The total composition of the gas sample can be determined if reference spectra are available for each compound in the mixture. If the molar attenuation coefficient was independent of temperature, pressure, density, and composition, only one reference spectrum would be necessary for each compound, as the absorbance would scale proportionally to the concentration. However, these factors can affect the shape and position of the spectra lines, and subsequently, the molar attenuation across the IR

bandwidth. Temperature influences absorbance via Thermal Doppler Broadening. As temperature changes the velocity of molecules, red and blue Doppler shifts of the radiation frequency occur, which results in a broadening of the observed absorption spectral lines. Increases in pressure increase the frequency of collisions between molecules, until the time between collisions is faster than the absorption energy state transition. This is called Collisional Broadening, and it produces wider spectral features due to increased uncertainty in the energy difference between transitions. Increased pressure also decreases the distance between molecules, resulting in increased van der Waals forces and subsequent disturbances in the available transition states; this is called Quasistatic Broadening (Redziemski, 1987). Temperature, pressure, and concentration errors can be mitigated by analyzing samples at the same conditions as the reference spectra. For the Gasmet™ DX-4000 and CX-4000 analyzers used in this research, pressure and temperature measurements are made with on-board sensors, and compensations are made with the ideal gas law. Compensations due to the path length are made by using the Beer-Lambert law. Each reference spectrum has recorded temperature, pressure, and path length values to allow for corrections for each component.

The spectral resolution and IR detector sensitivity can induce further instrument error. Absorption lines for gases are approximately 0.2 $cm^{-1}$; most FTIR analyzers have a bandwidth resolution of 0.5-10 $cm^{-1}$. This results in a smoothing of the peak maxima over the wider resolution band. The ratio between the spectral peak and the absorbance baseline is greatly impacted for strong and sharp absorption peaks. Furthermore, the

peak maxima can saturate the transmittance measurement. It is recommended that the analysis regions selected avoid excessively strong absorption bands due to losses of concentration and absorption proportionality.

The Gasmet™ DX-4000 and CX-4000 analyzers used in this research have a reported absorbance noise level of ~2%. If an absorbance of 1 is selected as the maximum absorbance, then a spectrum with an absorbance above 1.2 contains no useful information (Goff, 2005). Ideally, the absorbance should stay around 0.1 to prevent oversaturating the detector and to stay within linear calibration range. It is also important to note that the molar attenuation coefficient becomes non-linear at higher concentrations; this effect can be mitigated by the use of multiple reference spectra covering a large range of concentrations.

### 2.1.2 Reference Spectra

Reference spectra are produced by passing gas of a known composition through the FTIR analyzer sample cell and generating a spectrum. These gases can be purchased in cylinders at a known concentration from a gas supply vendor; this is typically the case for compounds commonly found in the gas phase, including $CO_2$ and $NH_3$. Reference spectra can also be generated by blending the IR active compound with $N_2$ by the use of mass flow controllers. This is more commonly performed with compounds found in the liquid state at standard temperature and pressure, such as water and many amine solvents. Compounds that exist as solids at standard temperatures and pressures must be dissolved in a solvent and can then be used to generate reference spectra. Water is the most commonly used solvent for this application.

The Gasmet™ FTIR analyzers used in this research are shipped to the user with a library of reference spectra onboard. These spectra are generally accurate for the life of the analyzer, and are universal between analyzers of the same model, provided the temperature, path length, and pressure are compensated for each analyzer. New reference spectra may be necessary if liquid or particulates in the sample cell require replacement of the analyzer mirrors, or for adding a new measureable component to the Gasmet™ spectra library.

Water reference spectra should be produced annually, or following any maintenance or repairs to the sample cell. The Gasmet™ DX-4000 and CX-4000 analyzers are designed to use the water reference spectra to account for any minor damage that occurs on the sample cell mirrors. With this feature, reference spectra for each compound do not need to be reproduced following cleaning and repairs to the sample cell with the existing mirrors. Thus, water calibrations are vital for FTIR analyzer performance and should be properly performed on schedule.

Water and liquid amine reference spectra require volatilization and mixing with $N_2$ to produce reference spectra. A Gasmet™ Calibrator was used to for water calibrations and to produce reference spectra for amine solvents. This is presented in Figure 2.2.

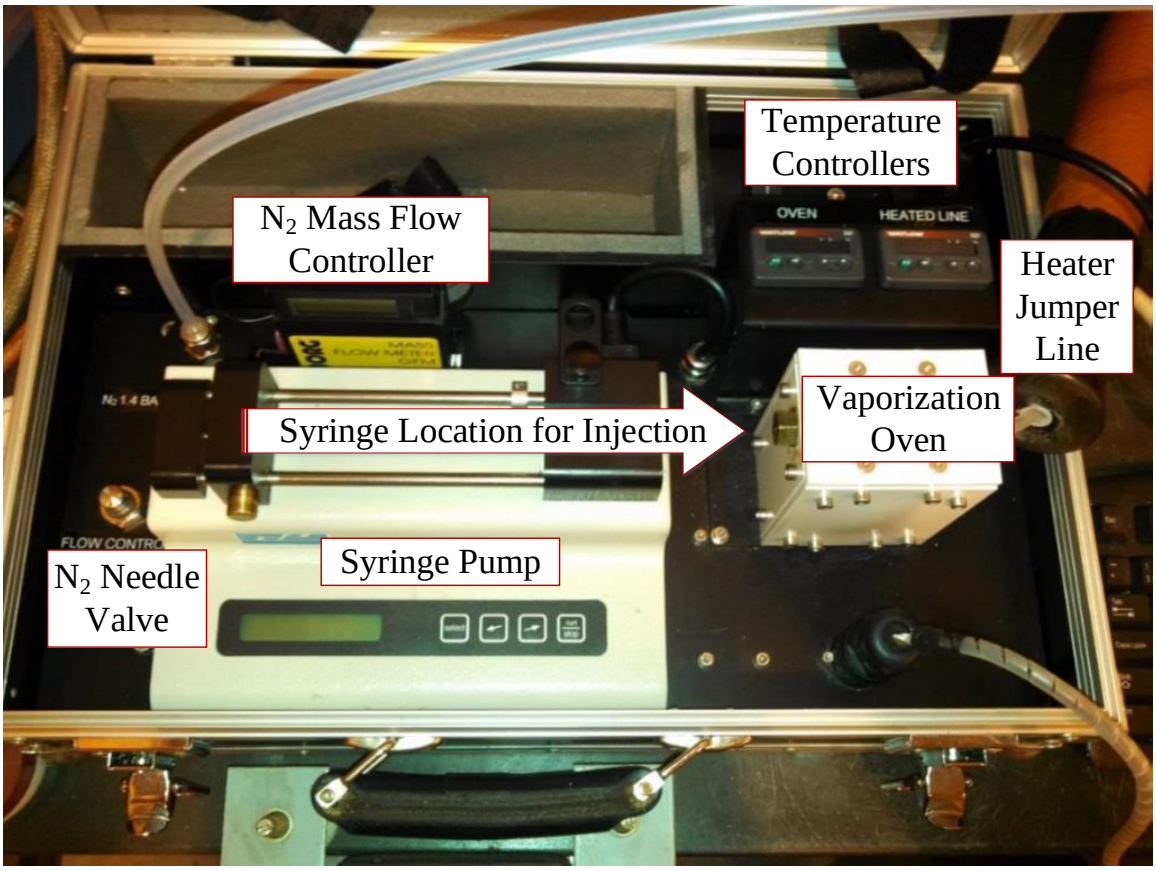


**Figure 2.2: Gasmet™ Calibrator**

This calibrator uses an Aalborg mass flow meter (Model GFM 17) paired with a precision needle valve to control the $N_2$ flow rate. A Cole Parmer (No. 780100C) syringe pump injects the liquid IR active component into the oven, where the sample is vaporized and mixed with the $N_2$. Onboard temperature controllers maintain a temperature of 180 °C in the vaporization oven and in the jumper outlet line from the calibrator to the FTIR analyzer inlet. A high temperature septum mates the syringe with the vaporization oven.

Pure liquids used in the calibrator will produce spectra of only that compound. Solid samples that are dissolvent in solvent will require subtracting out the reference spectra of the solvent.

When using the calibrator, both the $N_2$ carrier gas flow rate and the syringe pump injection rate can be varied. This is critical at higher injection rates of the IR active liquid compound. 500 μL syringes are best used for water calibrations, which require higher volumetric flow rates; smaller syringes can be used for more precision with components that require lower flow rates. Fill the syringe with the solution to be injected, ensuring that no bubbles are formed. Select the syringe type and injection rate on the calibrator onboard computer. Insert the syringe through the septum and into the vaporization oven, and lock the syringe in place. Commence injection via the syringe pump controller, and wait for the FTIR readout to stabilize. Once stable, a three minute scan can be taken to serve as the reference spectrum. Table 2.1 gives the water calibration set flow rates for $N_2$ and injection rates for $H_2O$, for each reference concentration.

**Table 2.1: FTIR $H_2O$ calibration $N_2$ flow rates and $H_2O$ injection rates, for each reference concentration**

| **$N_2$ Flow** ***SLPM*** | **$H_2O$ Flow** ***μL/hr*** | **$H_2O$ Conc.** ***vol %*** |
|---|---|---|
| **1.00** | 990 | 2 |
| **1.00** | 2540 | 5 |
| **0.66** | 2730 | 8 |
| **0.50** | 2990 | 11 |
| **0.38** | 3150 | 14 |
| **0.36** | 3460 | 17 |
| **0.32** | 3630 | 20 |

Residual spectrum files are produced by subtracting the reference spectra from the solvent spectra. These files are saved in Calcmet™ by selecting Options→Autosaving, and in the "Residuals" section, select "All" next to "Autosave Residual Spectra." It is

important to note the time that the residual spectrum was recorded, since the residual spectrum index is independent of the total spectrum index, and timestamps can be used to identify the correct file. Residual spectrum files are saved with a reference file extension (.REF), while spectrum files are saved as (.SPE).

### 2.1.3 Multicomponent Spectra Analysis

Proper FTIR analyzer adjustments for baseline signals, species analysis regions, pressure compensations, and voice coil pressure must be made to ensure accurate quantification of analyzed species.

#### *2.1.3.1 Baseline Corrections*

The sample spectra baseline should show zero absorbance across the IR band when subtracting the $N_2$ background. The baseline slope and curvature can be affected by the interferometer operating conditions, especially the temperature. Baseline corrections can be made with slope correction and curve correction functions. Slope correction is used on a region of the spectrum where no component is absorbing, and applies a linear adjustment to the baseline. For amine-scrubbing sampling purposes, 2,500-2700 $cm^{-1}$ typically contains no absorbing compounds and can be used for slope correction.

In cases where the sample spectrum has absorbance at all wavenumbers, curve correction can be applied. This uses a second order polynomial to perform a background correction, and should only be applied when slope correction is not possible due to absorbance at all wave numbers (Gasmet Technologies Oy, 2009).

#### *2.1.3.2 Analysis Regions*

The analysis regions selected for each component must include characteristic spectra features of the molecule without saturating the detector with an absorbance over 1, while still maintaining a sufficient signal to noise ratio. Spectra characteristics can overlap in multicomponent FTIR analysis; Calcmet™ software can resolve these conflicts if the overlap isn't too severe and if the interference table under 'Analysis Settings' is correctly filled out.

Selected analysis regions must be 3 times the wavenumber resolution of the analyzer in order to provide information on the curvature; as Gasmet™ DX-4000 and CX-4000 analyzers have an 8 $cm^{-1}$ resolution, 24 $cm^{-1}$ is the minimum required bandwidth for analysis regions. Each component should have at least two analysis regions; one to include a unique spectral feature, and another to provide a baseline for baseline curvature adjustments. Table 2.2 presents the analysis regions for each component sampled in this work; these regions were developed by Goff (2005), Sexton (2008), and Voice (2013).

**Table 2.2: Analysis regions used for FTIR analysis**

| Component | Concentration | Range 1 [$cm^{-1}$] | Range 2 [$cm^{-1}$] | Range 3 [$cm^{-1}$] | # of References |
|---|---|---|---|---|---|
| **$H_2O$** | vol % | 2475–2600 | 3000–3375 | -- | 8 |
| **$CO_2$** | vol % | 926–1150 | 2065–2245 | 2550–2700 | 10 |
| **MEA** | ppmv | 895–1380 | 1810–2223 | 2550–3450 | 13 |
| **PZ** | ppmv | 2500–2600 | 2550–3100 | -- | 11 |
| **$NH_3$** | ppmv | 895–1300 | 2475–2600 | -- | 7 |
| **$SO_2$** | ppmv | 1050–1450 | 2500–2600 | -- | 7 |

#### *2.1.3.3 Pressure Compensation*

Gas phase compositions are calculated in relation to the reference spectra concentrations. The reference spectra conditions can be at different pressures than the measured sample; any variations in the density of the gas are compensated for. Sample cell pressure is measured by an on-board cell pressure sensor in some CX-4000 models. Other models use a fixed value or ambient pressure measurements.

#### *2.1.3.4 Voice Coil Pressure*

The interferometer in the FTIR analyzer is not airtight, which can result in the IR beam passing through ambient gas unless an $N_2$ purge is supplied to provide back pressure. This purge is also needed to prevent the possibility of ambient water condensing on the interferometer mirrors, caused by the Peltier-cooled IR detector. $N_2$ flow to the purge is controlled with a pressure regulator and a 0.0004" orifice. Flow rate is kept low enough to prevent excessive back pressure from building up in the cell

because the interferometer mirrors are affixed to a carousel assembly, which is translated by the use of a voice coil. The voice coil can be dampened by excessive pressure; a set pressure of 7-8 psig is typically used for the $N_2$ purge regulator.

### 2.1.4 FTIR Hardware

FTIR sampling has been performed at multiple pilot plant installations. At the UT-SRP facility, a multipoint FTIR sampling system is fully integrated into the DeltaV™ process control scheme. For sampling at UKy/KU/LG&E and NCCC, portable FTIR sampling systems were developed. These portable systems were designed to be assembled and broken down easily, and to transport compactly.

Although these sampling systems vary in scope, there are common pieces of equipment shared by both systems. These include the sample probes, sample pads, and sample lines.

#### *2.1.4.1 Heated Sample Probes*

FTIR gas samples are extracted by the use of Universal Analyzer, Inc. Model 277S heated probes. Each probe contains a heated ceramic filter to remove noncondensable liquids and particulates. Table 2.3 presents the technical specifications of the probes.

**Table 2.3: Universal Analyzers, Inc. Model 277S Heated Probe Technical Specifics**

| Parameter | Value/Description |
|---|---|
| *Operating Specifications* | |
| Sample flow rate | 0–20 L/min. (0.7 CFM) |
| Calibration gas requirement | Sample flow rate plus 10% |
| Operating pressure drop at 10 L/min. | 12" water column (3.0 kPa) |
| Maximum stack gas temperature | 700 ºF (371 ºC) |
| Oven and vaporizer temperature | 350 ºF (176 ºC) |
| Dimensions | 9" x 9" x 10" (230 mm x 230 mm x 250 mm) |
| Weight | 20 lb. (9.1 kg) |
| Input power requirement | 350 W (Custom) |
| Input voltage requirement | 115 VAC, 50/60 Hz |
| | |
| *Material Specifications* | |
| Filter chamber heater type | Rod heaters in aluminum tube, PID controlled |
| Filter chamber material | 316SS |
| Filter element type | Ceramic 2μm (Standard Option) |
| Chamber material | 316SS |

Figure 2.3 presents the mechanical and electrical technical drawing for the sample probes. The thermomechanical switch has since been converted to PID control. Figure 2.4 presents the physical installation arrangement of the probes at the absorber inlet, outlet, and knockout outlet sampling locations. Asioaxial sampling orientation is maintained to mitigate aerosol sampling losses.

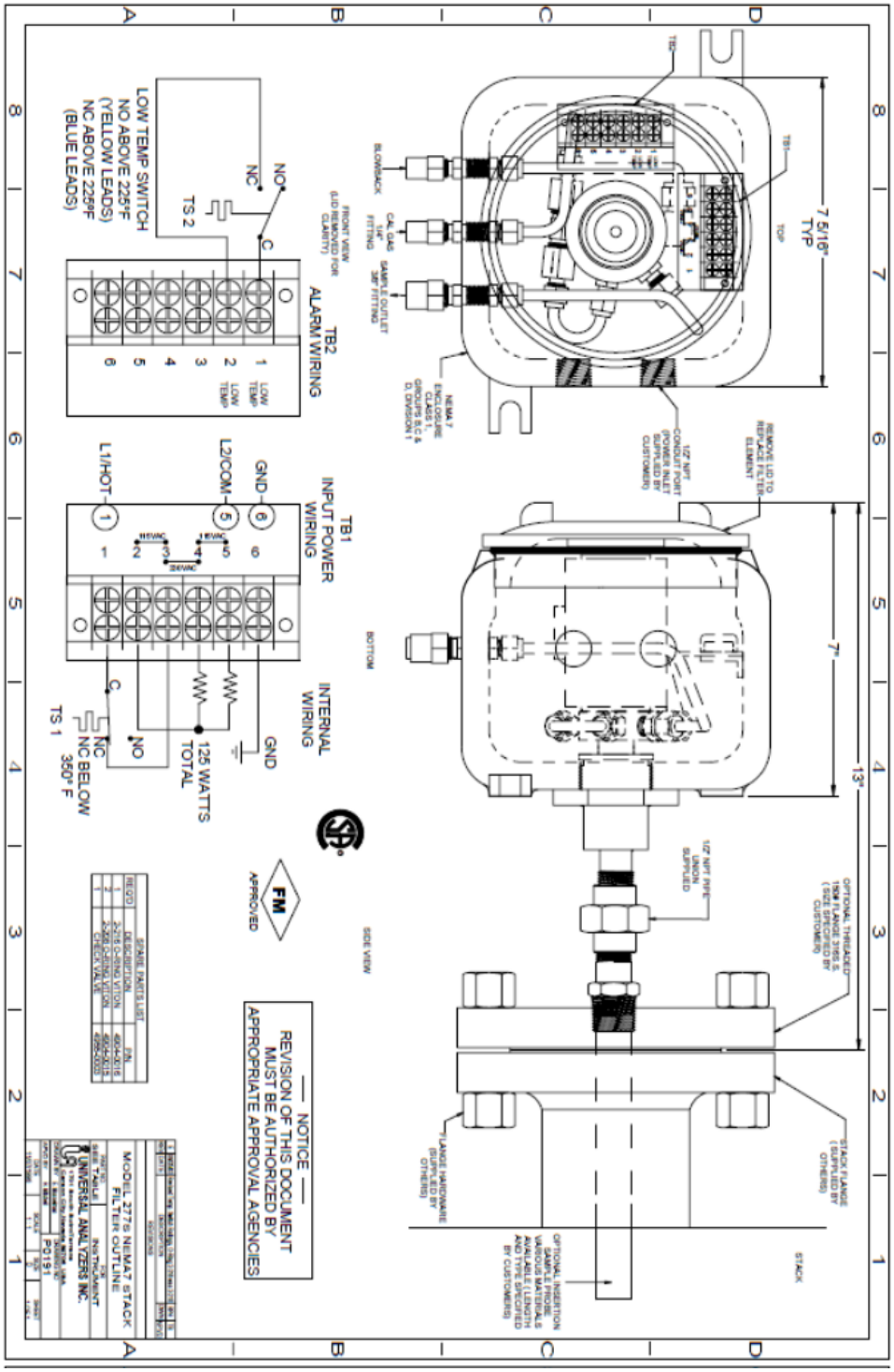


**Figure 2.3: Mechanical and Electrical drawing of Universal Analyzers, Inc. Model 277S heated sample probe**

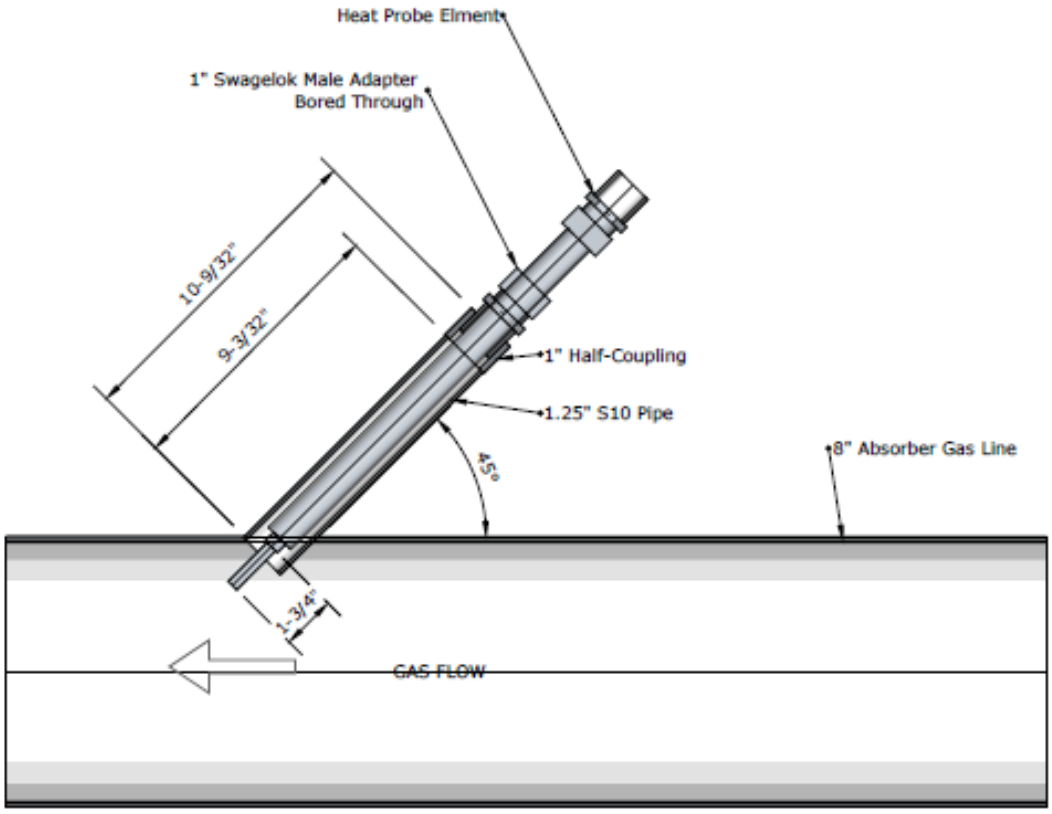


**Figure 2.4: Heated sample probe installation at UT-SRP pilot plant.**

### *2.1.4.2 Heated Sample Pads*

Heated pads are used to maintain the 180 °C temperature across the connection between the FTIR probe and the sample line. This helps to reduce the risk of condensation in the sampling system, which can occur with high water content sampled streams in colder ambient conditions. Cleanair ® SKU 1233 heated pads are used for this purpose. Table 2.4 presents the specifications for the heated pads.

**Table 2.4: CleanAir® SKU heated blanket technical specifications**

| **Parameter** | **Value/Description** |
|---|---|
| *Specification* | |
| Max. Operating Temperature | 400 ºF |
| Ambient Temperature | 0 ºF |
| Heat Output | 42.7 W |
| Operating Voltage | 120 VAC |
| Measured Resistance | 337.1 Ω |
| Latch Mechanism | Velcro® Release |
| Dimensions (Open) | 4" x 3" x 1" (L x W x H) |
| Dimensions (Closed) | 4" x 6" x 1/2" (L x W x H) |

#### *2.1.4.3 Heated Sample Lines*

Heated sample lines are used to transfer the sampled gas stream to the FTIR analyzer. These lines have been procured from Clayborn Labs, and consist of replaceable 1/2" PTFE tubes inside of PFA tubing, wrapped with resistance heaters and insulated. The outside of the lines are protected with corrugated plastic, with fire sleeve socks for the ends closest to the probes. Unheated calibration lines are passed through the sample line structure as well, to enable FTIR calibrations with gases ($CO_2$). Heated sample line specifications are given in Table 2.5.

**Table 2.5: Clayborn Labs heated sample tubes technical specifications**

| **Parameter** | **Value/Description** |
|---|---|
| *Specification* | |
| Carrier Tube Material | PFA |
| Carrier Tube Diameter | 0.5” |
| Carrier Tube Wall Thickness | 0.062” |
| Insert Tube Material | PTFE |
| Insert Tube Diameter | 3/8” |
| Insert Tube Wall Thickness | 0.047” |
| Max Temperature | 200 °C |
| Min Environmental Temperature | -10 °C |
| Thermocouple Type | K-Type |
| Thermocouple Positioning | Midpoint |
| Operating Voltage | 208 AC |

Electrical connections for the resistance heaters include power, neutral, and grounding wires. 3-pin cup-soldered Amphenol® connectors were used for power; K-type thermocouples provided temperature measurements.

#### *2.1.4.4 UT-SRP FTIR Sampling*

FTIR sampling at UT-SRP is performed at 5 total locations with two identically configured CX-4000 analyzers. A single analyzer is devoted to the inlet FTIR sample point; the readout from this analyzer can be used for controlling the $CO_2$ feed rate to the process through DeltaV™. The second analyzer rotates between four different sampling locations; between the 1st and 2nd stages of packing, between the 2nd and 3rd stages of packing (The absorber outlet when using the water wash), the absorber/water wash outlet, and the knockout drum outlet. The sampling positions are shown in relation to the process in Figure 2.5.

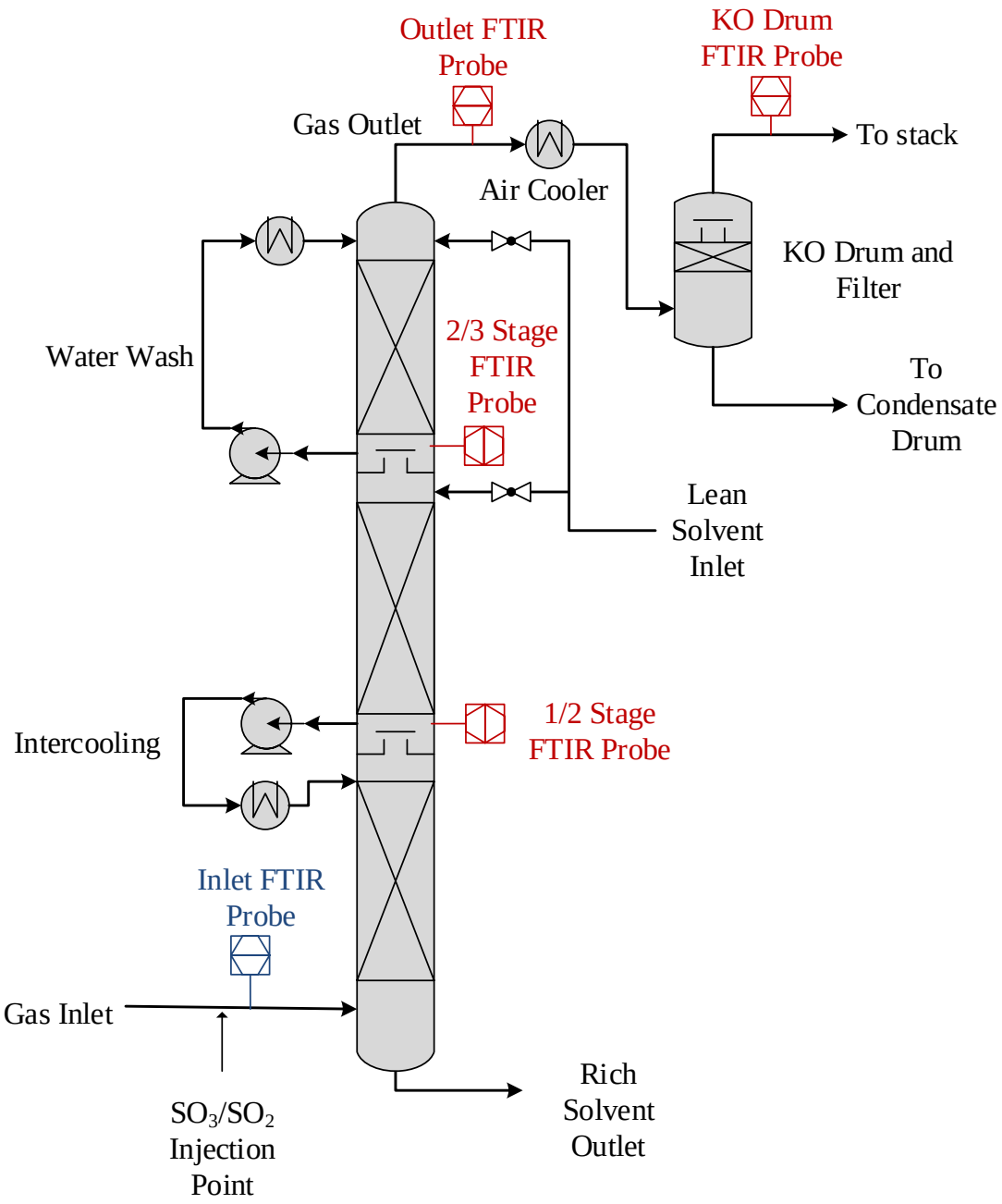


**Figure 2.5: Process flow diagram of UT-SRP absorber column and knockout drum, with FTIR sampling locations.**

*2.1.4.4.1 Multipoint Heated Stream Switcher (MSSH)*

Switching between the four sample points requires the use of a stream switching unit called the Multipoint Heated Stream Switcher (MSSH). This was built by Air Quality Analytical, Inc., D/B/A GASMET-USA™. This unit is capable of switching between up to seven different sample points through the use of a cascade solenoid/pneumatic control system (GASMET-USA, 2014). A process flow diagram of the MSSH sampling system is presented in Figure 2.6.

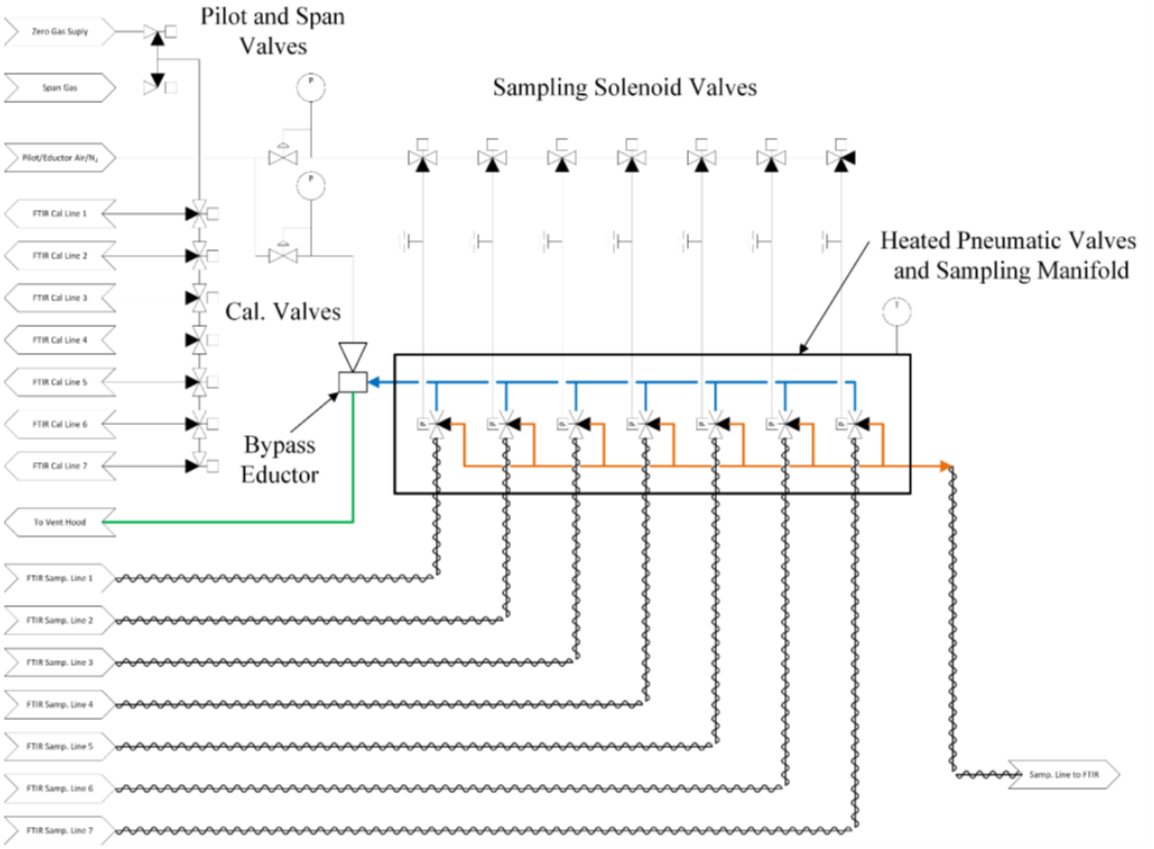


**Figure 2.6: Multipoint Heated Stream Switcher PFD. The waste vent (green) collects the gas from the common bypass manifold (blue). The common sample manifold (orange) is sent to the FTIR analyzer.**

The heated sample lines from the process feed to the heated pneumatic valves and sampling manifold, where they are mated with 3-way valves. The sampling manifold is maintained at 180 °C to prevent condensation. The 3-way valves are normally open to the waste vent; suction provided by an air-powered eductor flushes this gas to a fume hood. This is to continuously draw from all sample lines, in order to prevent condensation from occurring and to reduce the FTIR analyzer response time. If a sampling location is selected, its corresponding 3-way valve is selected to flow to the common sample manifold. This line is sent to the FTIR for analysis; suction is maintained by the FTIR analyzer pump. Upon selection of a different sampling location, an orifice bleeds off the pneumatic valve pressure and flow through the 3-way valve resumes to the waste vent.

*2.1.4.4.2 Sample Filter*

The sampled stream from the MSSH is passed through a heated sample line to the FTIR analyzer cabinet. Prior to entering the FTIR pump, the stream is filtered to remove particulates. An Atmoseal® FPD-4-7/1-B02 filter was selected for this application. This filter uses a bayonet-type T-handle filter with a 1" ID by 7" length element for removal of 0.1 μm or larger particles. Table 2.6 provides technical specifications for the filter unit.

**Table 2.6: Atmoseal ® Filter Technical Specifications**

| Parameter | Value/Description |
|---|---|
| Part number | FPD-4-7/1-B02 |
| Voltage | 120 VAC (60 Hz) |
| Full load amps | 2.0 A |
| Enclosure | 316 SS |
| Thermocouple Type | K |
| Filter Type | Bayonet |
| Maximum Temperature | 400 °F |
| Port Size and Type | ¼" NPT |
| Element Length and ID | 7" x 1" |

*2.1.4.4.3 Sample Pump and Motor*

Suction through the FTIR system is maintained by an Air Dimensions, Inc.® Dia-Vac-R201 heated sample pump, model number R201-FP-IE3-M. A Baldor® Super-E motor powers the pump. Technical specifications on this motor are presented in Table 2.7, and on the pump head in Table 2.8. The pump and head for this sampling system are designed to draw 5 Lpm of gas through 5/16" ID tubing over a length of 200'. This allows for use of the FTIR cabinet at pilot plants with longer sample line lengths. The pump is heated to 180 °C to prevent condensation.

**Table 2.7: Baldor® Super-E® FTIR Sample Pump Motor Technical Specifications**

| Parameter | Value/Description |
|---|---|
| Catalog number | 1202035119-000010 |
| Specification number | M35J302P862 |
| Serial number | X1702M23881 |
| Horsepower | 0.5 |
| Voltage | 230/460 VAC (60 Hz) |
| Phase(s) | 3 |
| Full load amps | 1.54/0.77 A |
| RPM | 1735 |
| NEMA nominal efficiency | 82.5% |
| Power factor | 74% |
| Service factor | 1.25 |
| Frame | 56C |
| Enclosure | TEFC |
| Insulation class | F |
| KVA code | K |
| Design code | B |

**Table 2.8: Baldor® Super-E® FTIR Sample Pump Technical Specifications**

| Parameter | Value/Description |
|---|---|
| Model number | R201-FP-IE3-M |
| Heater power | 150 W (2 x 75 W) |
| Voltage | 115 VAC (60 Hz) |
| Current Draw | 1.3 A |
| Head material | 316SS |
| Diaphragm material | Teflon® |
| Temperature range | 30–400 ºF |
| Max. ambient temperature | 140 ºF |
| Enclosure | Explosion proof |
| Port connectors | 1/4” NPT |

The heated pump flow rate is controlled with a variable frequency drive (VFD). The VFD is used to control the pump motor speed by adjusting the input frequency. The VFD used in this application is a Baldor® Electric ABB Microdrive, model # ACS-250-

01U-02A3-1. The VFD is visible in Figure 2.6 as the white box on the bottom half of the cabinet.

*2.1.4.4.4 CX-4000 Analyzer*

A Gasmet™ CX-4000 FTIR analyzer was used for UT-SRP pilot plant campaigns. The analyzer is housed in a server rack cabinet, along with the CPU and user interface keyboard-monitor unit; this is shown in Figure 2.7. This same analyzer system was utilized for bench scale experiments with the Aerosol Growth Column, covered in Chapter 4. The CX-4000 specifications are shown in Table 2.9.

**Figure 2.7: Gasmet™ CX-4000 FTIR analyzer in server rack**

**Table 2.9: Gasmet™ CX-4000 Technical Specifications**

| **Parameter** | **Value/Description** |
|---|---|
| *Model* | |
| Model # | CX-4000 |
| Mounting Position | Horizontal |
| Line Voltage | 120 VAC |
| Fittings | ¼" Imperial, Compression |
| Gaskets | Kalrez© |
| Software | Calcmet™ V11.118, Windows 7 (64-bit) |
| *Interferometer* | |
| Interferometer Type | Temet Carousel Interferometer (GICCOR) |
| Beamsplitter/Window Material | ZnSe |
| Wavenumber Range | 900-4200 $cm^{-1}$ |
| *Sample Cell* | |
| Temperature | 180 °C |
| Path Length | 5.0 m |
| Sample Cell Volume | 0.4 L |
| Gasket Material | Kalrez® |
| Coating | Ni + Rh + CVD Au |
| Mirrors | Fixed, protected Au coating |
| Protective Coating | $MgF_2$ |
| Window Material | $BaF_2$ |
| Sample Cell Pressure Measurement | Yes |
| Detector Type | Mercury, Cadmium, Tellurium, Pelletier Cooled (MCPT) |
| IR Source | SiC, 1550K |
| *DSP/Power Board Settings* | |
| Speed Setting | 5 Hz |
| Resolution | 8 $cm^{-1}$ |
| Scan Frequency | 10 spectra/s |
| Comport Speed | 57600 bps |
| EPROM Type | Standard |
| Digital Interface | 9-pole D-connector RS232 protocol serial |
| *Measuring Parameters* | |
| Zero point calibration | Every 24 hours with $N_2$ |
| Zero point drift | <2% of measuring range per zero point calibration interval |
| Accuracy | 2% of measuring range |
| Temperature drift | <2% of measuring range per 10K change |

| | |
|---|---|
| Pressure influence | 1% of measuring range per 1% sample pressure change |

*2.1.4.4.5 Communications with DeltaV™ Process Control System*

Communications between the FTIR instrumentation and DeltaV™ control system are necessary for multiple reasons. First, it is vital for data consolidation to integrate the FTIR readings into the DeltaV™ data log. This ensures that all the collected process data is processed in a single spreadsheet and reduces potential transcription errors.

The Delta V™ – FTIR communications link is also vital due to the use of the FTIR analyzer for controlling the inlet $CO_2$ composition. The UT-SRP pilot plant also uses Vaisala CARBOCAP® Carbon Dioxide Transmitter Series GMT220 silicon-based NDIR sensors to measure $CO_2$ at the absorber inlet and knockout drum outlet. These have an upper detection limit of 20 vol % $CO_2$; during the April 2017 campaign, the inlet $CO_2$ content was varied to up to 20 vol %. Thus, proper FTIR integration with the DeltaV™ control system is necessary for pilot plant operations.

The CX-4000 analyzer CPU is physically connected to the DeltaV™ terminal by the use of an RS-232 cable. Upon physical connection, communications must be enabled and configured at both the FTIR analyzer CPU and within the DeltaV™ control system. This is elaborated upon in Appendix C.

*2.1.4.4.6 Temperature control for heated probes and pads*

At the UT-SRP pilot plant, the electrical wires from the heated probes and heated pads are wired to breakout terminal boxes by the use of Liquidtight weatherproof conduit. Shielded thermocouple wiring is also distributed through these boxes. The breakout

boxes connect to the existing conduit system at the plant. This existing conduit was used to run power and thermocouple lines to the Level 2 CHARMS box, which connects to the pilot plant DeltaV™ control system for PID control of the pad and probe temperatures. DeltaV™ is used to control and record the temperatures in the heated pads and probes.

#### *2.1.4.5 Field Sampling System*

A portable FTIR sampling system was developed for use at UKy/KU/LG&E and NCCC. This system was designed to fit in the back of a pickup truck, and to be quickly and easily assembled and disassembled. This system utilizes the same heated sample probes and pads as the UT-SRP FTIR analysis system. The heated sample lines are provided from Clayborn Labs as well, but utilize 120 VAC operating voltage instead of 208 VAC due to power limitations at the UKy/KU/LG&E and NCCC sites.

##### *2.1.4.5.1 Power distribution and temperature control for heated elements*

Electrical power and temperature control to heated sample probes, heated pads, and heated sampling lines is provided by an electrical power distribution box. This was built in-house by the Rochelle group, and is designed to maintain all heated sampling equipment at 180 °C. The temperature controllers used are SOLO® single-loop temperature controllers, 100-240 VAC operating voltage (Model number SL4824-VR). Figure 2.8 presents a photo of this system. Electrical and thermocouple connections are made through the bottom of the unit. The system requires a 120 VAC electrical supply.


**Figure 2.8: Electrical temperature control box for heated sampling equipment.**

*2.1.4.5.2 Sample Pump and Filter*

The Gasmet® DX-4000 FTIR analyzer used for field sampling requires the use of a portable sample pump and filter unit. A diaphragm pump is used to control sample flow to the FTIR analyzer, and is maintained at 180 °C by an onboard temperature controller. A second controller is used to maintain the same temperature across a heated jumper line from the pump to the FTIR analyzer sample cell inlet. The pump filter is used to capture any particulates prior to entering the sample cell. Table 2.10 presents the specifications for the portable sampling pump and filter unit.

**Table 2.10: Gasmet® portable sample pump and filter technical specifications**

| Parameter | Value/Description |
|---|---|
| *General Parameters* | |
| Operating Temperature | 20 ± 20 ºC |
| Voltage | 115 VAC (50-60 Hz) |
| Power Draw | 400-3600 W |
| | |
| *Heated Sample Pump* | |
| Material | 316SS |
| Diaphragm material | Teflon® |
| Temperature | 180 ºC, Max. |
| Flow rate | 4 LPM, constant |
| Enclosure | Explosion proof |
| | |
| *Heated Filter* | |
| Material | Bonded Microfiber (2 μm) or sintered steel (0.1 μm) |
| Temperature | 180 ºC |
| | |
| *Gas Connections* | |
| Sample In/Out | 6 mm Swagelok® |
| Zero Gas In | 6 mm Swagelok® |
| | |
| *Enclosure* | |
| Material | 316SS |
| Dimensions | 400 x 300 x 210 mm |
| Weight | 12.3 kg |

*2.1.4.5.3 DX-4000 Analyzer*

The Gasmet® DX-4000 is identical to the CX-4000 model, but is housed in a ruggedized casing for moderate shock and weather protection. The DX-4000 is labeled in Figure 2.9, along with other components of the portable sampling system.

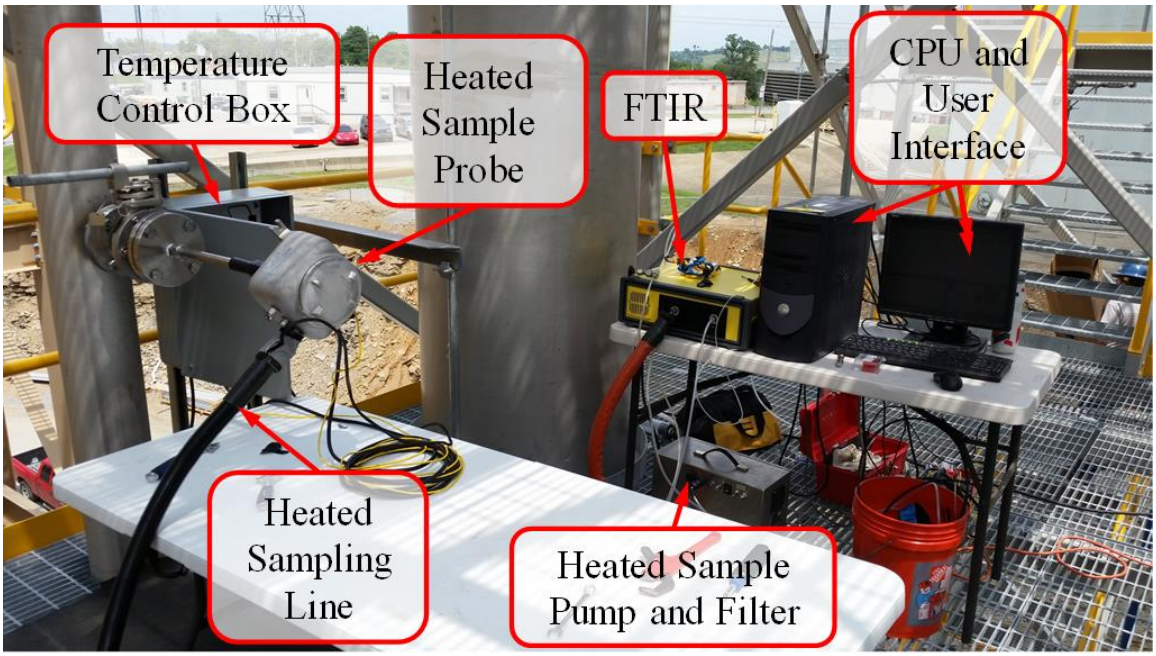


**Figure 2.9: Portable FTIR sampling system at the UKy/KU/LG&E Slipstream Plant**

*2.1.4.5.4 Pilot Plant Sample Blower*

An Ametek® Rotron® EN303AG58L Regenerative Blower is used for combined FTIR and PDI extractive sampling techniques. The blower flow rate is controlled via a variable speed drive; velocity through the extractive sampling look is determined by the PDI. The blower specifications are presented in Table 2.11.

**Table 2.11: Ametek® Rotron® EN303AG58L Regenerative Blower Technical Specifications**

| Parameter | Value/Description |
|---|---|
| Motor enclosure - Shaft Mtl. | Explosion-proof - CS |
| Horsepower | 0.5 |
| Phase - Frequency | Single - 60 Hz |
| Voltage | 115/230 VAC |
| Maximum flow rate | 55 SCFM |
| Maximum pressure | 55" $H_2O$ |
| Maximum vacuum | 45" $H_2O$ |
| Motor nameplate amps | 9.0/4.5 A |
| Max. blower amps | 7.2/3.6 A |
| Inrush amps | 38/19 A |
| Starter size | 00/00 |
| Service factor | 1.0 |
| Thermal protection | Not required |
| XP motor class - group | 1-D |
| Shipping weight | 52 lbs. (23.6 kg) |
| Connections | 1-1/4" NP |

## 2.2 PHASE DOPPLER INTERFEROMETRY (PDI)

Phase Doppler Interferometry is a laser based nondestructive aerosol measurement technique. The PDI instrument measures the particle size distribution, total particulate concentration, and velocity of an aerosol cloud. The analyzer used in this research is designed to measure aerosol drops between 0.1 and 12.0 μm in diameter, at aerosol concentrations greater than $10^6$ $cm^{-3}$. PDI measurement technique uses the phase shift of light for particle sizing, as opposed to the intensity of light. The use of the phase of light as opposed to intensity reduces the attenuation errors caused by optical window fouling and multiple scattering from the same particle. Proper sizing requires for the measured signal amplitude to be greater than the background scattering noise, and that particles pass in the correct flow path (no back flow). Optical window attenuation can

reduce the signal amplitude to a point below detection limits, but this is an issue prevalent in all photodetector-based analysis systems. The reader is referred to publications by Bachalo (1980), Albrecht (2003), and von Benzon (1994).

This section focuses on the theoretical principles of PDI particle sizing and velocity determination, and follows the outline provided by Fulk (2016) and the PDI-100 MD User Manual.

### 2.2.1 Theory of Operation

PDI sampling is based on the principle of the ideal light scattering from a single uniformly illuminated spherical particle passing through the plane of an optical heterodyne created by the intersection of a pair of laser beams. The intensity of the refracted and reflected beams is given by the Fresnel equations. The temporal and spatial frequency of the scattered light interference pattern at any far-right point, relative to the position of the particulate, can be determined by the use of the Lorenz-Mie equations and the particle diameter. The Doppler (temporal) frequency is used to calculate the particle velocity and the spatial frequency measured simultaneously at two locations. This gives a single measurement of the spatial wavelength, or phase shift, of the Doppler signal, which is linearly related to the particle diameter. Working equation development from vectoral two-point ray tracing is covered by Albrecht (2003). The fringe approximation is used in this description for simplification.

A forward scattering PDI schematic is presented in Figure 2.10. A laser of wavelength $\lambda$ is split into two equal beams by a beam splitter. One beam is shifted in frequency by a Bragg cell, an acousto-optic modulator. The frequency shift in the beams

is applied to distinguish particles with 'negative' velocities, as positive and negative frequency shifts are indistinguishable. The Bragg cell translates all Doppler shifts across the measurable velocity range into the positive frequency domain.

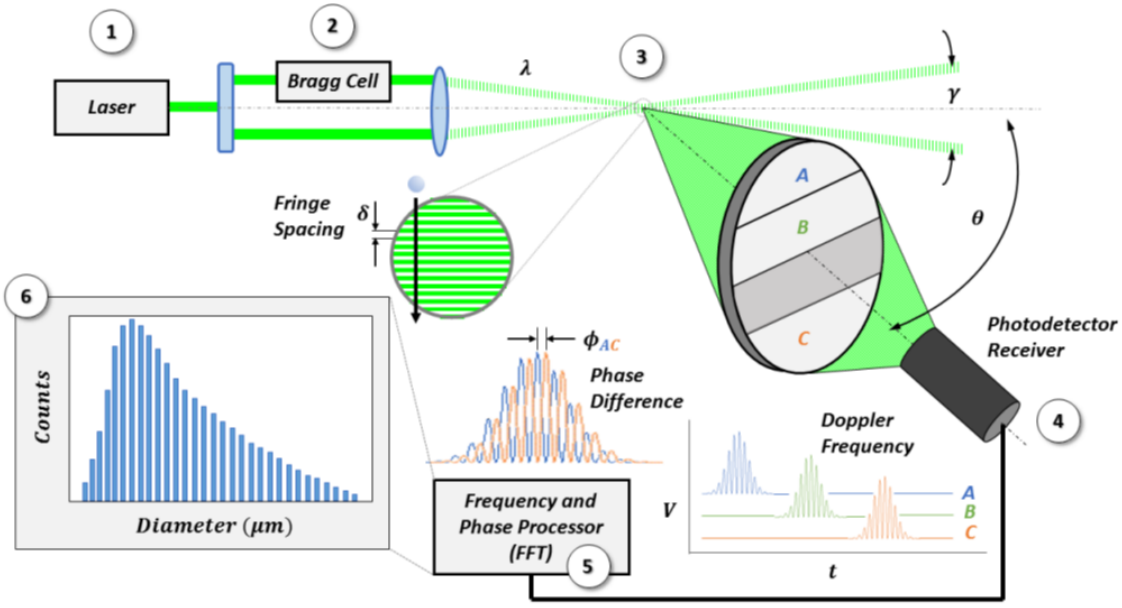


**Figure 2.10: Operational schematic of forward scattering PDI (Fulk, 2016).**

The sample volume is created by the intersection of the two beams, at an angle γ. The beam intersection creates a region of both constructive and destructive interference bands called fringes. The fringe spacing, δ, is a function of the laser properties and the crossing geometry; this can be calculated by using Equation 2.4.

$$\delta = \frac{\lambda}{2\,sin(\frac{\gamma}{2})} \tag{2.4}$$

where:

$\delta$ = Fringe spacing (m)

$\lambda$ = Laser wavelength (m)

$\gamma$ = Laser crossing angle (radians)

Particles passing through the fringe pattern in the sample volume scatter light in an alternating pattern of high and low intensity. This scattered intensity can be observed by placing photodetectors in an optical housing at an elevation angle of $\theta$ orthogonal to the laser crossing plane. This scattered light pattern is referred to as a Doppler burst, and can be quantified as a photomultiplier voltage oscillating in time. The time-spacing between signal peaks is the wavelength of the Doppler signal, and is directly proportional to the velocity of the particle as it traverses the sample volume. Higher particle velocity corresponds with faster scattering pattern movement.

Multiple photodetectors are spaced with a fixed geometry; thus, the Doppler burst arrives at each photodetector at a different time. This difference in arrival time is observed as a phase shift between signals, and is directly related to both the photodetector spacing and the particle diameter. If the Doppler wavelength is smaller than the detector spacing, the phase shift will appear to be greater than 360°.

The curvature of spherical particles acts as a magnifying lens for the interference pattern. Small particles have a large curvature, and larger particles will have a smaller

curvature. Thus, smaller particles will have a larger magnification and a consequent small phase shift, and vice-versa for large particles. This is demonstrated in Figure 2.11.

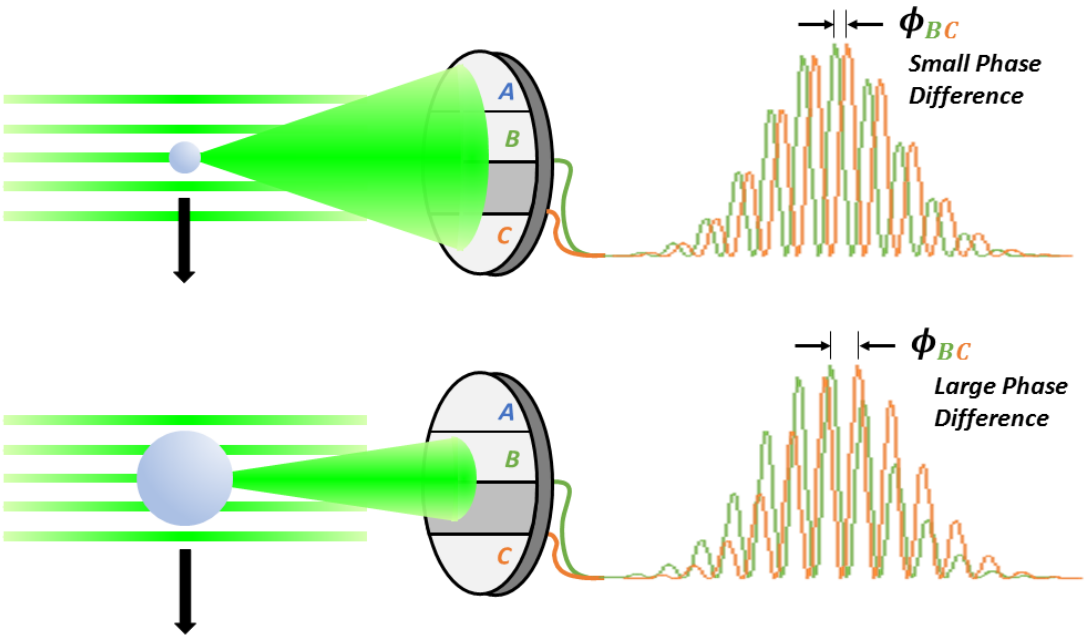


**Figure 2.11: Phase shift difference between particle sizes due to interference signal magnification effects (Fulk, 2016).**

Doppler signals from each photodetector are passed to a signal analyzer, where fast Fourier Transforms are used to quantify the Doppler frequency and the phase shift between each pair of photodetectors. Upon commencing, sampling is performed for each scattering event until a sample set of sufficient statistical size is collected, and a particle size distribution is produced. The total measurement time, dimensions of the measurement volume, and velocity values can be used to calculate the particle flux. The particle flux is used to determine the total particle concentration.

### 2.2.2 Safety

The lasers used in the PDI are Class 3B lasers. While these lasers are not powerful enough to cause a burn risk, they are hazardous for eye exposure. The PDI receiver and transmitter unit is designed to safely encapsulate the laser path and prevent potential beam exposure; the PDI lasers must not be activated without the sample cell mated to the receiver/transmitter unit. For instrument repairs, it is recommended the PDI analyzer be returned to Artium Technologies for repairs. When performing laser alignment or viewing the laser crossing, polarized protective glasses must be worn. Artium Technologies follows the laser class definition defined by the Federal Register 21 CFRF 1040.10, and the laser safety standards of the American National Standards Institute (ANSI Z136.1).

### 2.2.3 Hardware Setup and Connections

Five main hardware components comprise the PDI analysis system: the power supply, signal processer, transmitter optics, receiver optics, and CPU/user interface. An oscilloscope (Tektronix® TDS2014C, 100 MHz, 4-channel, 2G.s), is also utilized for calibration and troubleshooting.

#### *2.2.3.1 Power Supply*

The power supply supplies electrical power and instructions to the transmitter and receiver unit. The PDI used in this work uses a single multi-pin cable that mates with a keyed connection at the transmitter/receiver end. The cable breaks out to power leads for the receiver and transmitter, photomultiplier BNC-type signal connectors, an Ethernet communications connection, and a USB type B cable. The USB cable is used to transmit

information on the photomultiplier tube (PMT) gain, aperture settings, laser settings, and the phase calibration source information.

#### *2.2.3.2 Advanced Signal Analyzer (ASA)*

The ASA performs amplification, filtering, analog to digital conversion, and burst signal detection on the raw signals from the receiving optics. The three BNC cables (Labeled Raw A, Raw B, and Raw C), from the transmitter/receiver cable are connected to the 'input signals' connections at the back of the ASA box- not the 'raw signals' BNC connectors. An Ethernet cable from the computer connects to the ASA box as well; this is used to send digitalized information to the computer for software processing.

The oscilloscope is connected to the ASA box as well, through the use of BNC connectors provided with the oscilloscope. The four channels used are Raw A, Raw B, Raw C, and Gate Out; these display the unfiltered Doppler bursts from each photodetector. The Gate signal indicates the presence of a burst signal, and rises to 5V when a Doppler burst is detected. This is a key signal to look for on the oscilloscope, as the presence of a Gate signal indicates the passage of a measureable aerosol drop through the sample volume. The signals from Raw A, Raw B, and Raw C on the oscilloscope correspond with the three photodetectors; peaks with these signals are used for laser alignment, phase calibration, and real-time assessment of signal quality.

#### *2.2.3.3 Transmitter*

The transmitter in the combined receiver/transmitter unit contains the laser source, Bragg cell, and reflectors to generate beam spacing and the crossing angle for the sample volume. The laser is activated by the use of a keyed switch at the back side of the

receiver/transmitter unit, next to the keyed power cable connection. The laser should not be activated unless the transmitter/receiver unit is properly affixed to the sample cell, to prevent hazardous optical conditions. Figure 2.12 gives a photo of the PDI transmitter/receiver unit.

**Figure 2.12: PDI transmitter/receiver unit**

A laser alignment port is installed on this prototype PDI, as shown at the bottom of the unit in Figure 2.12. This is used to adjust the position of one of the laser beams; moving this beam path up or down impacts the size of the sample volume generated from the beam crossing. This port is capped by a small chained knurled fitting on the side of the receiver/transmitter unit. Opening the knurled knob and inserting a long #2 hex driver allows access to the alignment port. Only minor adjustments are necessary for PDI laser alignment; typically, less than half a turn in either direction is necessary to properly realign the lasers. This is an operation that may need to be performed upon relocation and reinstallation of the PDI system at field sampling sites. Proper laser alignment will

result in an increase in the magnitude and frequency of peaks for signals 1-3 on the oscilloscope, and an increase in the frequency of the Gate signal as well. A visual representation of proper laser alignment is presented in Figure 2.13. The produced Doppler signal should have a well-defined high and low frequency, with a Gaussian pedestal component and a high frequency and amplitude burst signal. Multimodal peaks indicate a misaligned laser, or the presence of multiple aerosol drops in the sample volume. An aerosol source must be present when aligning the laser. A Pari Trek S Compact Nebulizer (Catalog number J-P47F45LCS-CN) provides a steady aerosol stream with water, and is stored with the PDI analyzer system.

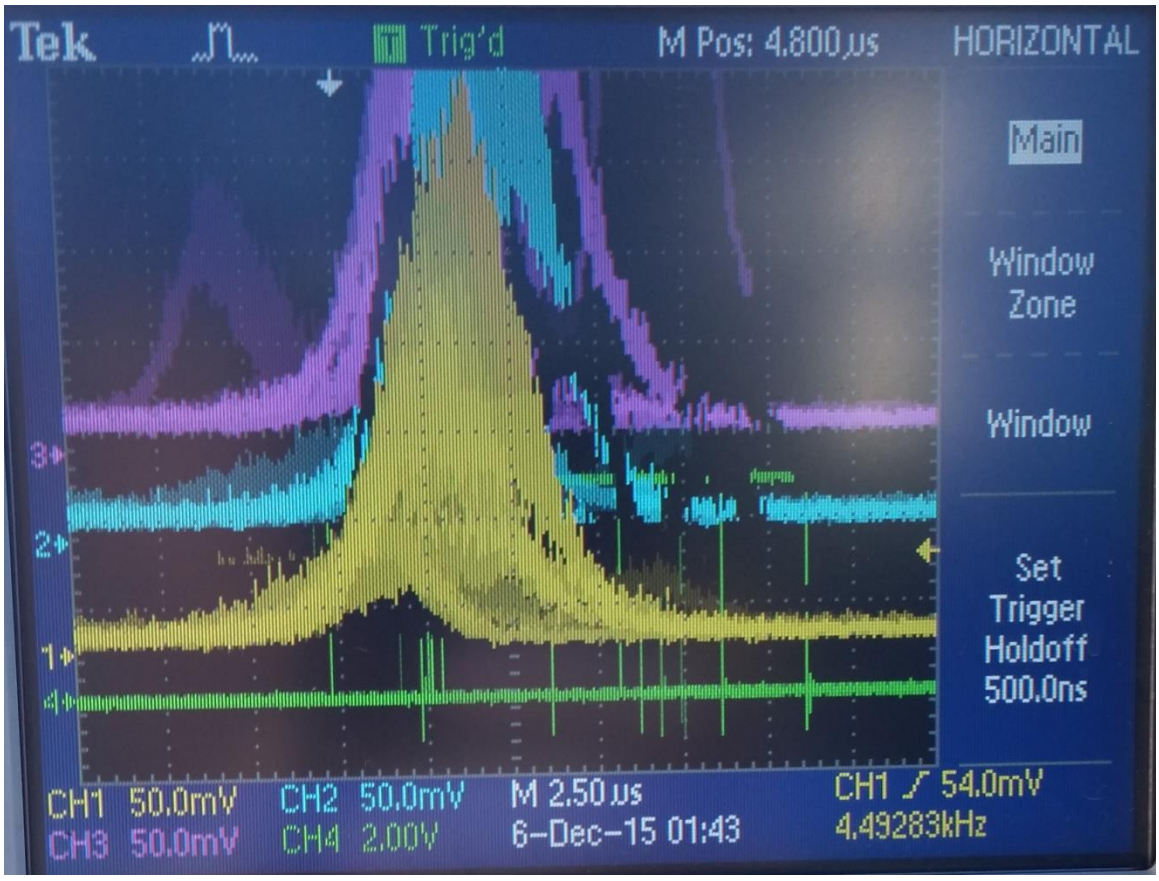

**Figure 2.13: Oscilloscope readout of proper PDI laser alignment. Photodetector signals (Channels 1, 2, and 3) show Doppler bursts, Gate signal (Channel 4) shown with high frequency.**

#### *2.2.3.4 Receiver*

The receiver contained within the combined transmitter/receiver unit includes the photodetectors, aperture, and focusing lenses. The prototype PDI used in this research uses a fixed optical configuration. This eliminates the possibility of using different lenses or apertures, but requires significantly less alignment than previous prototypes. Table 2.12 presents the transmitter and receiver optical parameters.

**Table 2.12: PDI transmitter and receiver optical parameters**

| **Parameter** | **Value** |
|---|---|
| *Transmitter Optics* | |
| Laser wavelength (nm) | 532 |
| Laser beam diameter (mm) | 0.95 |
| Laser beam waist (μm) | 17.8 |
| Focal length (mm) | 25 |
| Beam separation (mm) | 17.46 |
| Beam crossing angle (º) | 38.5 |
| Fringe spacing (μm) | 0.8 |
| | |
| *Receiver Optics* | |
| Collection angle (º) | 65 |
| Focal length (mm) | 35 |
| Slit aperture (μm) | 10 |
| | |
| *Transmitter/Receiver Angle* | |
| Forward scattering angle (º) | 40 |

#### *2.2.3.5 Temperature and Humidity Control*

The PDI transmitter/receiver unit requires temperature and humidity control due to the sensitivity of the laser alignment. The multi-pin power and communications cable to the transmitter/receiver unit provides power to a temperature controller, which uses a heater, Peltier cooler, and convection fan to maintain a suitable temperature in the transmitter/receiver unit. Humidity in the instrument is mitigated by the use of disposable desiccant bags (McMaster-Carr 3492T15). This is accessible through a knurled and chained plastic cap at the optical end of the transmitter/receiver unit.

### 2.2.4 Test Cell

The custom prototype PDI used in this research uses a sample cell for process gas and laser containment. This sample cell is a modified 150# flanged Schedule 10 304SS pipe spool piece. Three crown glass windows are provided for the transmitter, receiver, and for user visual confirmation. Aluminum guides and dowel pins are used to properly align the test cell with the transmitter/receiver unit. The test cell is locked in place by the use of swivel arms with wing nuts. A photo of the test cell is presented in Figure 2.14, and of the optical end of the transmitter/receiver unit in Figure 2.15.

**Figure 2.14: PDI test cell, in bench scale configuration**

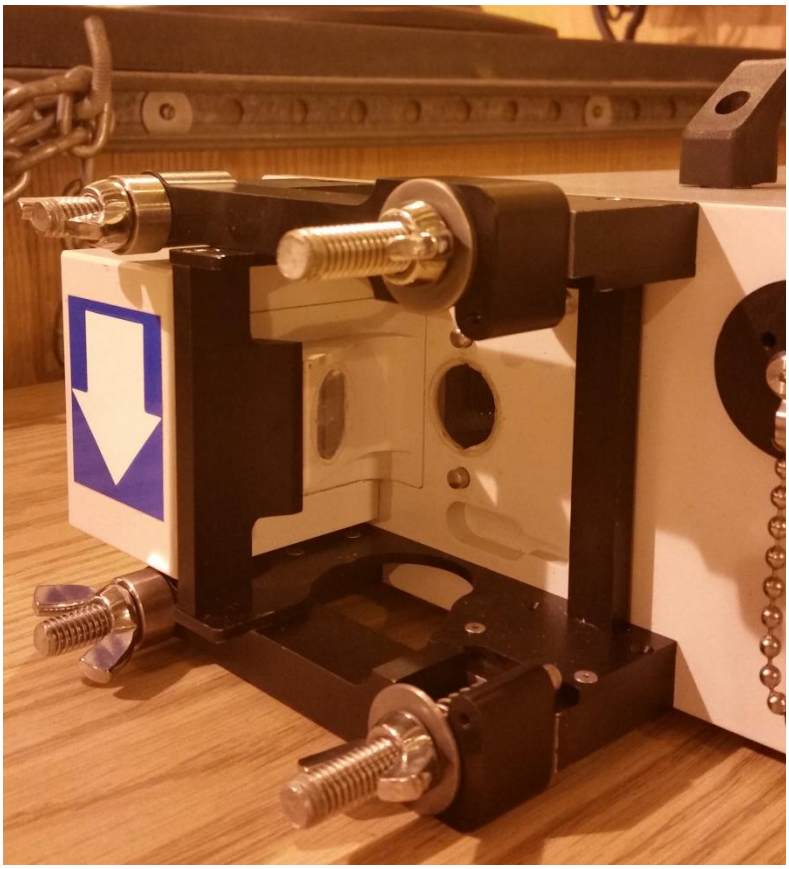

**Figure 2.15: PDI transmitter/receiver optical end, which aligns and secures the test cell.**

Flow direction arrows are indicated on both the transmitter/receiver and the test cell to ensure correct orientation. Within the test cell, protective cones are in place to keep aerosol from contacting the transmitter and receiver optical windows, in order to reduce fogging and attenuation issues. These are machined in a manner to reduce obstructions to the flow path. The windows are also fitted with microchannels for purge and vacuum flow. The purge is designed to sweep the windows to prevent liquid sheeting or fogging on the optical windows. Connections for the purge are made with 1/8" push-to-connect fittings embedded in o-rings in the test cell body. The push-to-

connect fitting seals are supplemented with silicone sealant to further improve the seal. These push-to-connect fittings are visible as the black fittings above and below the test cell windows in Figure 2.14.

### 2.2.5 Software

Artium Integrated Management Software (AIMS) is used to control the PDI and process data. Important parameters and criteria are specified in the following sections.

#### *2.2.5.1 Acquisition Control*

Data collection can be automatically stopped through three different means: a set sampling time, a set number of samples, or free run that stops at the user input. These are selected in AIMS under the Acquisition tab in the Device Controls left-hand tab. Typical sampling criteria invoked a counts threshold of 10,000, or a sampling time of 5 minutes.

#### *2.2.5.2 Auto-Setup*

The PDI processor settings can be automatically configured using the Auto-Setup tab. The algorithms in Auto-Setup collect signals made with the aerosol flowing in the sample volume to determine the optimum processor settings and PMT gain. This is recommended to be used prior to each new physical sampling configuration, such as upon the switch from sampling with bench scale experiments to field use at pilot plant sites.

#### *2.2.5.3 Phase Calibration*

As previously mentioned, phase calibration and laser alignment are to be performed upon moving the PDI to a new sampling location. Phase delays must be accounted for due to the sensitivity of particle sizes to the phase and due to the high frequencies occurring within the analyzer processors, signal cabling, and photodetectors.

Phase delay is calibrated by using a calibration diode that produces synthetic Doppler signals at the expected frequency of the process to be measured. The Doppler frequency is proportional to the "real" particle velocity, requiring a guess of the flow conditions to be made. The signal frequency can be determined by the use of Equation 2.5; the calculated expected signal frequency is inputted into the "Frequency" selection under the Phase Calibration tab in AIMS.

$$f_r = f_D + f_S = \frac{v}{\delta} + f_S \tag{2.5}$$

where:

$f_r$ = Expected signal frequency (MHz)

$f_D$ = Doppler frequency (MHz)

$f_S$ = Bragg cell shift frequency, 40 MHz

$v$ = Expected mean velocity of the process sample (meters/s)

$\delta$ = Fringe spacing, 0.8 μm (m)

Phase calibration is performed with the lasers off. Selecting "Quick Phase Calibration" determines the phase offset of each photodetector pair, and automatically adjusts this value in the software. The phase offset should only vary by a few degrees; this procedure should be repeated until there is little to no change in each offset value. The photodetector signals on the oscilloscope should reach approximately 200 mV; if not, the "Amplitude" value can be adjusted. A typical amplitude value is 0.9, and is a function of the PMT gain. It is sometimes useful to sample the aerosol stream with the uncalibrated PDI to determine approximate PMT gain settings prior to phase calibration.

#### *2.2.5.4 Validation Criteria*

AIMS uses several criteria to validate accurate particulate measurements. These criteria discard samples that might lead to size ambiguity or miscounting.

#### *2.2.5.5 Velocity Filter*

The velocity filter rejects samples that have a low signal to noise ratio. This can be used as a coarse tool to reject outlier velocities that are not used for field averaging post processing. Practically all sampled particulates pass the velocity filter criteria.

#### *2.2.5.6 Maximum Diameter Difference*

The three photodetectors size drops using the phase difference between any two photodetectors. This provides two independent phase pair differences and one absolute phase difference, resulting in redundant droplet sizes for each sampled particle (Sipperly, 2014). Adding a third photodetector substantially increases the detectable size range, as a pair of photodetectors can only detect phase shifts up to 360°. The maximum diameter difference function uses the redundant phase measurements to exclude diameter measurements that are substantially outside the weighted average of the three measurements. A sample is rejected if it does not meet the criteria for any of the three diameter determinations.

#### *2.2.5.7 Maximum Phase Pair Difference*

The droplet size is a linear function of the phase difference for any two photodetectors, to a first approximation. Certain particle trajectories can lead to a combination of refractive and reflective scattering. Configuring the acceptance bandwidth over the pure refractive phase difference line will reject particles presenting

mixed or purely reflective scattering. Phase difference lines for reflection and refraction are spaced to leave no ambiguity between modes. Reflective signals move in the opposite direction from refractive signals and can be relatively easily discerned. Particles passing along the edge of the sample volume will produced mixed reflection and refractive scattering; the phase difference measured by the photodetectors will lie in the region between the reflective and the refractive lines. The maximum phase pair difference function rejects particles that scatter light reflection or mixed scattering.

#### *2.2.5.8 Fast Fourier Transform (FFT) Bins*

The number of fast Fourier Transform (FFT) bins can be adjusted under the "Processors" tab in the "Device Controls" left hand side bar. The measured frequency and phase is calculated by an FFT algorithm. The number of FFT bins is the maximum number of samples that can be collected during the duration of a signal. 1,024 bins is most commonly used, but the resolution can be increased with more bins if desired.

#### *2.2.5.9 Analog Filter*

The analog filter reduces high frequency noise and removes the sum frequency produced by the frequency mixer. A typical value for the analog filter is 20.0 MHz.

#### *2.2.5.10 Mixer*

The frequency that passes through the analog filter is the raw signal (Doppler + Bragg shift) minus the mixer frequency. This can be used to reduce the processed signal frequency into a more manageable range. The mixer frequency should not be set so the velocities of the measured particles produce a mixed signal of zero frequency. A "Variable" selection is typical under the Mixer drop down menu.

#### *2.2.5.11 Variable Mixer*

Fine adjustment of the mixer frequency to values between 5 and 45 MHz is allowed in the variable mixer field. These values are usually set by the auto-setup algorithm; a typical value is 42.0 MHz.

#### *2.2.5.12 Sampling Rate*

The sampling rate is the frequency of the analog to digital converter. The sampling rate is actually double the amount specified in AIMS, as both the real and imaginary components of the signal are analyzed. Auto-setup can also set the sampling rate; a typical value is 80 MHz.

#### *2.2.5.13 Burst Detection (BD) Decimation*

False particle detection can occur with signals with low frequency. BD decimation eliminates a set factor of collected samples used by the burst detection system when high sampling rates are used. A typical BD decimation value is 2.

### 2.2.6 Optics

The next sections specify optical settings under the "Optics" tab in the "Device Controls' left hand menu in AIMS.

#### *2.2.6.1 PMT Gain*

The photodetector signals are amplified several orders of magnitude by the photomultiplier tubes, in order to produce electrical signals. The "Gain" value adjusts the PMT voltage to a point where the scattered light refracted from the aerosol is detectable. The intensity of light scattered from refraction is proportional to the square of the aerosol diameter, so smaller particles need higher gain to be detected. However, increasing the

gain increases the signal noise. A tradeoff exists between minimum detectable size and acceptable signal to noise ratio. The PMT gain is configured in Auto-setup, but can be manually adjusted by viewing the signal intensity versus diameter plots; the gain is set so the largest particles reach the detector saturation.

The PDI collection angle ensures that refraction is the dominant scattering mechanism observed by the receiver; therefore, particles below the minimum refraction have scattering as a result of mixed scattering or reflection. Intensities measured above the maximum line occur when two particles pass through the sample volume simultaneously.

#### *2.2.6.2 Index of Refraction*

Particle sizing for the sampling angle and scattering mode is insensitive to the index of refraction of aerosol in this research. The index of refraction can be set in AIMS if desired; the value 1.33 is the default value.

#### *2.2.6.3 Scattering Mode*

The scattering mode can be changed from refraction to reflection with this pulldown menu, if desired by the user.

#### *2.2.6.4 Data Exporting*

Each post processed data file is exported to a specific directory, either as individual .CSV files or as a single collated .CSV file. Export templates were made for all important data during the initial PDI setup; all data is exported to the specified directory following a successful PDI run. The export templates can be created by right

clicking any graph in the "Results" menu, loading the data set, and selecting "Add to Export Template" → "New Export Template".

### 2.2.7 PDI Calculations

This section provides a summary of the equations used to calculate aerosol size, velocity, and particle concentration.

#### *2.2.7.1 Velocity*

Phase Doppler Interferometry is based on Laser Doppler Velocimetry/Laser Doppler Anemometry (LDV); this technique is used to measure the velocity of particles in a polydisperse cloud. LVD principles are used in determining the velocity of aerosol in the PDI. The beam intersection forming the sample volume generates a fringe pattern of alternating light and dark parallel bands. Drops passing through the sample volume cause incident light reflection and refraction, producing an observable far-field interference pattern. The intensity of the scattered light is observed with a photodetector; the resulting signal is a superposition of the high frequency Doppler signal and the low frequency Gaussian pedestal. The Doppler frequency is directly related to the particle velocity through Equation 2.6. The Gaussian pedestal is a result of the Gaussian intensity profile of the lasers.

$$v = f_D \delta \tag{2.6}$$

where:

$v$ = Particle velocity (m/s)

$f_D$ = Doppler frequency (Hz)

#### *2.2.7.2 Size Determination*

As particles pass through the sample volume, refracted light is scattered in an interference pattern with a spatial frequency that correlates to the particle diameter. The use of multiple photodetectors with a known geometry allows measurement of the Doppler burst signal; the Doppler burst signal arrival at each photodetector is offset according to the far-field scattering pattern. This results in the phase shift between photodetectors. Equation 2.7 (Van Den Moortel, 1997) gives the linear correlation between the phase shift and the droplet diameter.

$$d^P = \frac{F\,\delta\,\Phi}{360\,\Delta\,l} H \tag{2.7}$$

where:

$d^P$ = Particle diameter (m)

$F$ = Receiver focal length (m)

$\Phi$ = Phase shift between any two detectors (deg)

$\Delta\, l$ = Distance between any two detectors (m)

$H$ = Optical constant (--)

Artium determines the particle diameter using the average phase difference relationship, as presented in Equations 2.8 and 2.9.

$$d^P = \frac{F\,\delta}{s\,\Lambda} \tag{2.8}$$

$$\Lambda = 360\left[\frac{k_{12}S_{12}}{\Phi_{12}} + \frac{k_{13}S_{13}}{\Phi_{13}} + \frac{k_{23}S_{23}}{\Phi_{23}}\right]/[k_{12} + k_{13} + k_{23}] \tag{2.9}$$

where:

$s$ = Sizing slope factor (--)

$\Lambda$ = Weighted Doppler spatial wavelength (m)

$S_{ij}$ = Distance between detectors i and j (m)

$k_{ij}$ = Geometric constant for detectors i and j (m)

$\Phi_{ij}$ = Phase shift between detectors i and j (deg)

#### *2.2.7.3 Probe Volume Correction*

There are many challenges associated with calculating the probe volume. A minimum scattering intensity is required for each particle, in order to distinguish it from the background noise. Since particles scatter light in proportion to their surface area and lasers have a Gaussian intensity profile, smaller particles must be closer to the center of the beam to scatter an equivalent amount of light. Therefore, the probe area is a function of the particle diameter. The probe volume correction (PVC) compensates for the variation of the probe sampling volume with the changing particle diameter, as the probe volume, and probe width, decrease with decreasing particle diameter. A diagram of this dependence is presented in Figure 2.16.

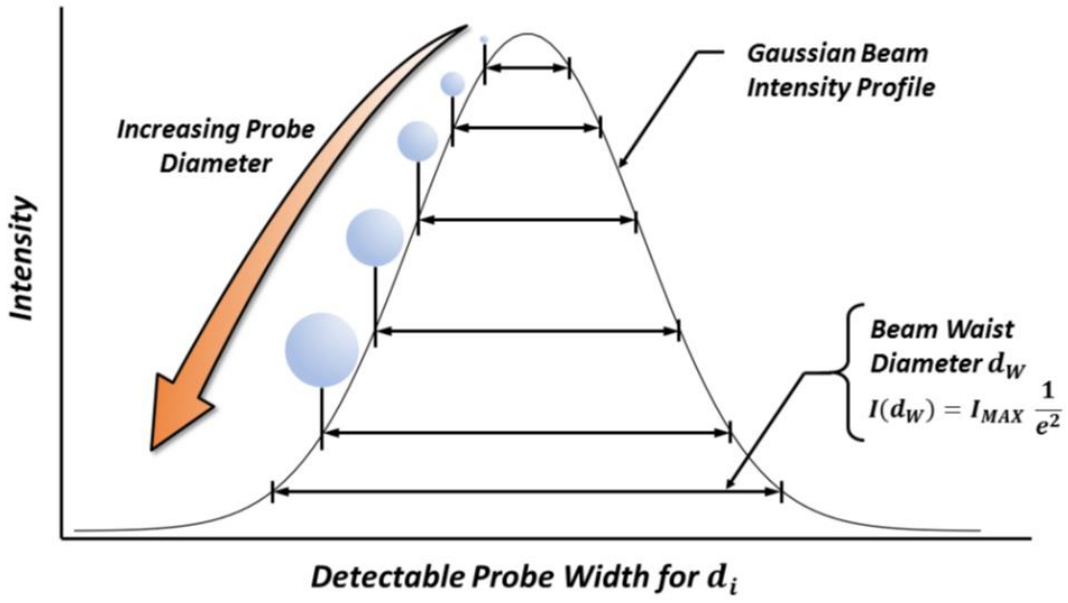


**Figure 2.16: Probe volume as a function of particle diameter, due to Gaussian beam intensity profile and the scattering dependency on the square of the particle diameter (Fulk, 2016).**

The transit method is used to correct the particle flux for variable probe area. A total Doppler burst time and velocity are recorded for each particle detected. The traversed distance is calculated by multiplying velocity by the measured crossing time. AIMS then uses a proprietary method for determining the maximum probe diameter from the collected transit times. Thus, the number of particles in a size class is calculated by using Equation 2.9.

$$n_C(d^P) = n(d^P)PVC(d^P) \tag{2.10}$$

where:

$n_c(d^P)$ = Corrected number of particles of diameter $d^P$ (part/cm$^3$)

$n(d^P)$ = Measured number or particles of diameter $d^P$ (part/cm$^3$)

$PVC(d^P)$ = Probe volume correction for particles of diameter $d^P$ (part/cm$^3$)

The probe volume correction is calculated by the use of Equation 2.11.

$$PVC(d^P) = \frac{D_{max}}{\sqrt{D_{max}^2 - 4\, r_w^2 \ln(\frac{d^P_{max}}{d^P})}} \tag{2.11}$$

where:

$D_{max}$ = Probe diameter of the largest detectable particle (m)

$r_w$ = Laser beam radius (waist); $1/e^2$ (m)

$d^P{}_{max}$ = Largest detectable particle diameter (m)

#### *2.2.7.4 Number Density*

The perpendicular area of the probe volume, the velocity distribution of the aerosol cloud, and the flux of particles are used to calculate the particle concentration. The total aerosol concentration is given by the summation of the flux and the PVC area, as presented in Equation 2.13.

$$PC = \frac{1}{(PA)t_{tot}} \sum_i \frac{n_c(d_i^P)}{|v_i|} \quad (2.12)$$

where:

$PC$ = Total particle concentration (part./cm$^3$)

$PA$ = Probe area for the maximum detectable particle diameter (m$^2$)

$t_{tot}$ = total sampling time (s)

$n_C(d^P_{i)}$ = Probe corrected particle count of diameter class $i$ (part./cm$^3$)

$|v_i|$ = Arithmetic absolute average velocity of diameter class $i$ (m/s)

## 2.3 COMPARISON OF AEROSOL SIZING ANALYZERS

This section briefly describes the capabilities and concerns with three aerosol measurement techniques: condensation particle counters (CPC), electronic low-pressure impactors (ELPI+™), and phase Doppler interferometers (PDI).

### 2.3.1 Condensation Particle Counters

Optical measurement techniques break down when the aerosol drops to be measured are very small (<0.05 μm). Condensation particle counters address this issue by enlarging particulates through inducing a supersaturated environment. The sampled aerosol stream is exposed heated and then cooled to encourage the condensation of working fluid (either water or n-butanol) into the aerosol phase. This growth is sufficient to enable optical measurement techniques. Saturation must be maintained at a level to encourage heterogeneous nucleation but not allow homogeneous nucleation, as this will lead to an inaccurate count of the aerosol density.

A benefit of CPC analysis is the ability to detect very small aerosol drops, down to 2 nm in diameter. CPC analysis is a very well established technique, with higher-end analyzer models providing accurate particle concentrations while still remaining cost effective.

CPC analyzers have several issues that inhibit their potential use in amine-scrubbing applications. Due to the nature of the heating and cooling of the sampled stream, all aerosol sampled grow to roughly the same size. This eliminates the ability to determine a particle size distribution for the sampled stream, unless a preselection impactor device is used upstream of the analyzer. CPC analyzers require an extractive sampling technique; the concerns with ex-situ sampling have been outlined in the previous chapter. Varying the aerosol size with dilution and temperature variations prior to performing optical measurement can give a misrepresentation of the actual aerosol sizes in the sampled process.

### 2.3.2 Electronic Low Pressure Impactors

Electronic Low Pressure Impactor analyzers operate by first electrically charging aerosol particles to a set charge level through the use of a corona charger (Marjamaki, 2003). The particles are then passed into a cascade impaction system, which uses a series of electrically insulated collection stages. Each cascaded stage removes a select cut size of aerosol, based on the geometric configuration of the stage. As the charged particles impact the stage, their electric charge is measured in real time. This measured charge is proportional to the particle number concentration and size. By measuring the signal from

each stage, the particle size distribution and aerosol concentration can be determined in real time.

ELPI+™ analyzers can quantify aerosol drops at sizes down to 6 nm, similar to CPCs. An advantage over CPC analyzers is the ability to determine the particle size distribution in addition to the particle concentration. This makes ELPI+™ analyzers significantly more useful for amine-scrubbing aerosol measurements.

Aerosol measurement with ELPI+™ analyzers requires the use of extractive sampling techniques with dilution of the sample stream; this can result in measured aerosol sizes that are not equivalent to the aerosol in the process. Changing the dilution properties has been shown to significantly impact the measured aerosol values (Saha, 2017; Brachert, 2014). ELPI+™ analyzers are also less cost effective than CPCs. Due to the sensitive nature of the impaction stages, both in geometric configuration and in electronic charge, ELPI+™ analyzers are sensitive to condensation in the system. This has been observed to cause false measurements and instrument failure.

### 2.3.3 Phase Doppler Interferometers

PDI theory and operating requirements have been outlined previously in this chapter. The benefits of PDI analysis include the capability to perform measurements in-situ if necessary. While this may pose maintenance and calibration issues on the larger pilot scale, this is a desirable asset at the bench scale. PDI analyzers do not require dilution of the sampled aerosol stream, which can allow for a more accurate representation of the aerosol sizes in the process. Aerosol concentrations and particle

size distributions are produced from PDI analysis, making this technique adequate for amine-scrubbing processes.

Due to the prototype nature of the PDI used in this research, a number of issues were discovered with the PDI technique. Significant effort must be taken in calibrating the PDI prior to operation. Laser alignment is not a trivial factor in data collection rates; misaligned lasers can inhibit the sizes and concentrations of aerosol. The optical lenses used in the transmitter/receiver unit are fragile, and cracks can interfere with the laser path. The lenses must also be kept clean to allow uninhibited laser passage, which can be difficult to achieve in pilot plant settings. The transmitter/receiver unit is sensitive to impacts and environmental conditions, which can result in equipment malfunction or measurement errors. These analyzers can be the most expensive out of all the analyzers discussed in this section.

The PDI analyzer was chosen for this research for multiple reasons. CPC analysis was eliminated due to the inability to measure particle size distributions. There are concerns with sample dilution and heating/cooling the sampled stream required for operating an ELPI+™. Furthermore, operating ELPI+™ analyzers requires a significant manpower investment, due to a number of operating parameters that must be constantly watched and adjusted. The prototype PDI analyzer in this work could be installed and operated by a single person, while an ELPI+™ requires a small team. While the PDI poses durability issues in pilot plant sampling, it encountered fewer operational issues than an ELPI+™ analyzer in a comparable timespan. Thus, the PDI analysis technique was chosen as the optimal aerosol measurement technique for this research.

# CHAPTER 3: AEROSOL GENERATOR DEVELOPMENT

This chapter outlines the design, construction, and operational capabilities of an $SO_3$ generation reactor for aerosol nuclei production. A background covers the necessity of aerosol generation techniques and the choice of $SO_3$ aerosol nuclei. The design basis, modeling equations, and generator construction parts lists are presented. The model results and optimal predicted operating conditions shown, followed by experimental results at the pilot and bench scale. Updates to the model accuracy are then presented.

## 3.1 BACKGROUND

### 3.1.1 Justification

The emission of volatile compounds is a major concern at $CO_2$ capture facilities utilizing amine scrubbing. Amine solvent lost through the overhead of absorber columns not only represents an environmental and safety hazard, but also has undesirable economic implications. The most significant solvent losses from amine-based $CO_2$ scrubbing processes occur due to aerosol emissions.

Aerosol emissions in amine scrubbing facilities occur due to heterogeneous nucleation onto existing aerosol nuclei. Nuclei sources can be fly ash or sulfur byproducts from the coal combustion process. These aerosol nuclei collect water, amine, and $CO_2$ while traversing the absorber column.

Fly ash nuclei are nanoscale particulates composed primarily of silicon, aluminum, and iron oxides (Du, 2013). $SO_2$ and $SO_3$ are both produced in coal combustion processes, and are precursors to the formation of sulfuric acid in amine scrubbing. $SO_3$ can also be produced in wet electrostatic precipitators (Anderlohr, 2015),

in selective catalytic reduction nitric oxide reduction systems (Brachert, 2014; Cao, 2010), and in flue gas desulfurization units (Cao, 2010). $SO_3$ vapor forms sulfuric acid through hydrolyzing with water. The sulfuric acid rapidly condenses to form nanoscale drops, which collect water and amine in the scrubbing system.

$SO_2$ can react with ammonia or the solvent amine to form a sulfite salt, which can then by oxidized to form a sulfate salt. As both ammonia and amine are present in amine-based $CO_2$ scrubbing, this reaction can easily occur. Sulfate salt hydrolyzes to form sulfate solutions in nanometer-scale drops, with particle concentration exceeding 1E8 $cm^{-3}$ (Mertens, 2014a).

Aerosol formation and growth within amine-scrubbing processes behaves in similar mechanisms to particulate nucleation in the atmosphere. Almeida et al. found atmospheric amine above 3 ppt can enhance sulfuric acid particle formation rates more than 1000-fold as compared to $NH_3$ (Almeida, 2013). This is owing to the base-stabilization mechanism involving amine-acid pairs, which decreases evaporation rates from the clusters.

### 3.1.2 Prior Aerosol Generation at UT Austin

Experiments at the bench scale and at the UT-SRP pilot plant require an externally generated aerosol source, as these systems use a synthetic flue gas instead of flue gas from a power generation process. Synthetic flue gas lacks aerosol nuclei that are necessary for aerosol growth and observation. Previous aerosol generation techniques at UT Austin focused on homogeneously nucleating vaporized sulfuric acid in the presence of water vapor. This was attempted with an apparatus called the Liquid Vaporizer and

Injector (LVI), built by Air Quality Analytical, Inc. The LVI was designed to produce between 350 and 1,750 ppm of $H_2SO_4$ in 1 cfm of carrier gas. The carrier gas with $H_2SO_4$ vapor was then injected into the process flue gas inlet, with a goal of producing 1-5 ppm of $H_2SO_4$ at the UT-SRP pilot plant scale.

At the pilot scale, the LVI operated by pumping a sulfuric acid solution to the suction side of an eductor. $N_2$ at 325 °C is used as the motive fluid. The $H_2SO_4$ is drawn through the eductor with the $N_2$ and is sent to a packed tube furnace to provide additional vaporization heat to the sulfuric acid. For bench scale operation, dilute $H_2SO_4$ is used, which enables a bypassing of the additional furnace step. The $N_2/H_2SO_4$ mixture is then injected into the process stream, where the resulting nuclei are allowed to grow in the $CO_2$ capture process.

Fulk identified the LVI as the biggest issue in UT aerosol studies (Fulk, 2016). This was due to the frequent development of plugs in multiple places within the LVI system. Cold spots within the system resulted in condensation of sulfuric acid, which caused significant corrosion and plugging of the process with accumulated solids. It was recommended that the entire heated LVI system be replaced with glass components, or that a new aerosol generation technique be developed.

### 3.1.3 $SO_3$ Generation

Due to the difficulties associated with injecting vaporized sulfuric acid, an $SO_3$ generator is preferred as a method for creating aerosol nuclei. These operate by oxidizing $SO_2$ over a heated vanadium pentoxide catalyst. This reaction, the oxidation of $SO_2$ to

form $SO_3$, is presented in Equation 3.1. The $SO_3$ produced can then be hydrolyzed to form sulfuric acid aerosol nuclei within the water saturated process.

$$SO_2 + \frac{1}{2}O_2 \rightarrow SO_3 \tag{3.1}$$

Researchers have used a variety of techniques to produce $SO_3$ aerosol nuclei at pilot plants. Khakharia, Brachert, and Mertens used an $SO_3$ generator for aerosol measurements at Institute for Technical Thermodynamics and Refrigeration at Karlsruhe Institute of Technology (Khakharia, 2013; Brachert, 2013; Mertens, 2014a). This $SO_3$ generator used platinum on $TiO_2$ microstructured titanium foils, as outlined by Pfiefer (2011). Work by Anderlohr at this site used a wet electrostatic precipitator to produce $SO_3$, with limited success (Anderlohr, 2015; Mertens, 2014b).

Research by Pfeifer et al. (2011) has focused on the use of a platinum-based catalyst in microreactors for $SO_2$ oxidation. The main issue encountered in this research concerned the eventual deactivation of the catalyst due to the presence of water in the feed to the reactor. This can be mitigated by purging the process with nitrogen during startup and shutdown, and by adequate pressurization and sealing of the process. Another issue encountered involved the heat released from the reactor due to the exothermic nature of the $SO_2$ oxidation. This can be counteracted by diluting the $SO_2$ in the feed gas and by strictly controlling the reactor temperature. Finally, solid sulfur can form on the catalyst in the absence of oxygen in the system. Utilizing a mix of $SO_2$ and air in a single cylinder can prevent catalyst degradation due to sulfur buildup.

$SO_3$ generation by $SO_2$ oxidation was further studied Benzinger et al. (2011). Experiments were performed and models made of the generation process at flow rates

similar to those necessary at the bench scale. Increasing the oxygen and $SO_2$ inlet feed were found to decrease the conversion rates. The reactor apparatus used in the experiments released less heat by the exothermic process than by heat transfer, indicating that excessive heat buildup should not prove to be a debilitating issue at the bench scale.

## 3.2 DESIGN METHODOLOGY

The following sections outline the design parameters and model development methodology for the UT Austin $SO_3$ generator. The generator construction and parts are listed, along with addresses to safety concerns.

### 3.2.1 Design Basis

Operational flexibility is of key importance to the design of the $SO_3$ generator due to the need to use the generator at both bench and pilot scale environments. The ranges of operating conditions are presented in Table 3.1 for both bench and pilot scale operations.

**Table 3.1: Operating conditions for $SO_3$ generation at bench and pilot scales**

| | **Bench Scale** | | **Pilot Scale** | |
|---|---|---|---|---|
| | *Low* | *High* | *Low* | *High* |
| **$SO_3$ (ppm)** | 5 | 50 | 1 | 10 |
| **Process Gas (LPM)** | 50 | 125 | 9900 | 19800 |
| **$CO_2$ (vol %)** | 0 | 15 | 0 | 20 |
| **Temperature (C)** | 70 | 30 | 50 | 30 |
| **Pressure (psia)** | 14.7 | 14.7 | 14.7 | 17.6 |
| **$H_2O$ (vol %)** | 2 | 15 | 2 | 15 |

The low and high columns for each scale represent the minimum and maximum value for each of the parameters in the leftmost column. Table 3.1 shows significant

variation in the process conditions, both between the bench and pilot scale and between the low and high conditions for each scale. Higher process flow conditions require greater quantities of $SO_3$ than lower flow conditions. Thus, operational flexibility is vital to meet all process requirements.

### 3.2.2 $SO_3$ Generator Model

A relevant industrial example of the oxidation of $SO_2$ to form $SO_3$ can be found in *Elements of Chemical Reaction Engineering, Fourth Edition* (Fogler, 2006). A vanadium-based catalyst is used in the process described, and exhibits similar properties to the catalyst obtained for this project. Fogler uses a feed rate of 7900 lbmol/hr with a reactor containing 4,631 tubes of 3" diameter and 20' length; for bench and pilot scale $SO_3$ generation, two 3' lengths of 1" tubing are sufficient. Other relevant properties of the reaction, such as the heat transfer coefficient and $\Delta H_{Rx}$, are identical or were assumed to be a close approximation to reaction properties of the aerosol generator.

Equation 3.2 gives the differential form of the design equation for the reaction.

$$F_{A0}\frac{dX}{dW} = -r'_A \tag{3.2}$$

where:

$F_{A0}$ = Initial molar flow of $SO_2$ (lbmol/hr)

$X$ = Conversion (fraction)

$W$ = Catalyst weight (lb)

$r'_A$ = Rate law

The rate law is given in Equation 3.3 (for $x < 0.05$) and 3.4 (for $x > 0.05$).

$$-r'_{SO2} = k(0.848 - \frac{0.012}{K_P^2}) \tag{3.3}$$

$$-r'_{SO2} = k\sqrt{\frac{1-X}{\Theta_{SO3}+X}}\left[\frac{P}{P_0}P_{A0}\frac{\Theta_{O2}-\frac{X}{2}}{1+\varepsilon X} - \left(\frac{\Theta_{SO3}-X}{1+X}\right)^2\frac{1}{K_p^2}\right] \tag{3.4}$$

where:

$k$ = Defined in Equation 3.5

$K_p$ = Defined in Equation 3.6

$P_i$ = Defined in Equation 3.7

Equation 3.5 defines parameter $k$.

$$k = 3600e^{\left(-\frac{176008}{T}-(110.1ln(T))+912.8\right)} \tag{3.5}$$

where:

$T$ = Temperature (°F)

Equation 3.6 takes the following form:

$$K_p = e^{\left(\frac{42331}{RT}-11.24\right)} \tag{3.6}$$

where:

$R$ = Ideal Gas Constant (1.987 kcal $K^{-1}$ $mol^{-1}$)

Equation 3.7 defines each $P_i$.

$$P_i = P_{A0}\frac{(\Theta_i+v_iX)P}{(1+\varepsilon X)P_0} \tag{3.7}$$

Substituting for partial pressures in the rate law produces Equation 3.8

$$\frac{dX}{dW} = \frac{k}{F_{A0}}\sqrt{\frac{1-X}{\Theta_{SO3}+X}}\left[\frac{P}{P_0}P_{A0}\frac{\Theta_{O2}-\frac{X}{2}}{1+\varepsilon X} - \left(\frac{\Theta_{SO3}-X}{1+X}\right)^2\frac{1}{K_p^2}\right] \tag{3.8}$$

Additional variables presented in Equation 3.8 are defined in Table 3.2. The steady state energy balance is defined next, using Equation 3.9.

$$\frac{dT}{dW} = \frac{\left(\frac{4U}{\rho_b D}\right)(T_a - T) + (-r'_A)[-\Delta H_{Rx}(T)]}{F_{A0}(\Sigma \Theta_i C_{Pi} + X \Delta C_P)} \tag{3.9}$$

where:

$\Delta H_{Rx}$ = Heat of reaction, defined in Equation 3.10.

$$\Delta H_{Rx}(T) = \Delta H^{\circ}_{Rx}(T_R) + \Delta\alpha(T - T_R) + \frac{\Delta\beta}{2}(T^2 - T_R^2) + \frac{\Delta\gamma}{3}(T^3 - T_R^3) \tag{3.10}$$

and:

$$\Sigma \Theta_i C_{Pi} = 57.23 + 0.014T - 1.94E^{-6}T^2 \tag{3.11}$$

Pressure drop is calculated next, as defined in Equation 3.12.

$$\frac{dP}{dz} = -\frac{(1-\varphi)G(1+\varepsilon X)}{\rho_0 (P/P_0)(T_0/T) g_c D_P \varphi^3}\left[\frac{150\mu(1-\varphi)}{D_P} + 1.75G\right] \tag{3.12}$$

Where $G$ is defined in Equation 3.13:

$$G = \frac{\sum F_{i0} M_i}{A_c} \tag{3.13}$$

where:

$M_i$ = Molecular weight of $i$

$A_c$ = Cross sectional area, given in Equation 3.14.

$$A_c = \frac{\pi D^2}{4} \tag{3.14}$$

Equation 3.12 can be redefined as Equation 3.15.

$$\frac{dP}{dW} = -\frac{GTP_0(1-\varphi)(1+\varepsilon X)}{\rho_0 A_c \rho_b P T_0 g_c D_P \varphi^3}\left[\frac{150\mu(1-\varphi)}{D_P} + 1.75G\right] \tag{3.15}$$

Table 3.2 presents the variables used in the aforementioned equations, including units and values if applicable.

**Table 3.2: $SO_3$ generator design equation variables**

| | Value | Unit |
|---|---|---|
| **ε** | -0.55 | |
| **$P_{A0}$** | 0.22 | atm |
| **Δα** | -1.56 | |
| **Δβ** | 0.003 | |
| **Δγ** | -7E-07 | |
| **$T_R$** | 1260 | R |
| **$\Theta_{SO2}$** | 1 | |
| **$\Theta_{O2}$** | 0.91 | |
| **$\Theta_{SO3}$** | 0 | |
| **$\Theta_{N2}$** | 7.17 | |
| **$P_0$** | 2 | atm |
| **$P_b$** | 38.23 | $lb/ft^3$ |
| **R** | 1.99 | kcal $K^{-1}$ $mol^{-1}$ |
| **$Ca_0$** | 0.04 | vol fraction |
| **φ** | 0.45 | |
| **ρ0** | 0.05 | $lb/ft^3$ |
| **$D_p$** | 0.02 | ft |
| **μ** | 0.09 | lb/ft*hr |
| **U** | 10 | BTU/(hr*$ft^2$*R) |
| **$A_c$** | 0.042 | $ft^2$ |
| **$T_0$** | 1400 | R |
| **$g_c$** | 4E+08 | lb(m)*ft/lb(f)*$hr^2$ |
| **D** | 0.08 | ft |
| **L** | 3 | ft |
| **W** | 0.63 | lb |

The $SO_3$ generation reaction was modeled by the use of Polymath 5.1. Design equations were inputted, followed by explicit equations to define variables. This is presented in Figure 3.1.

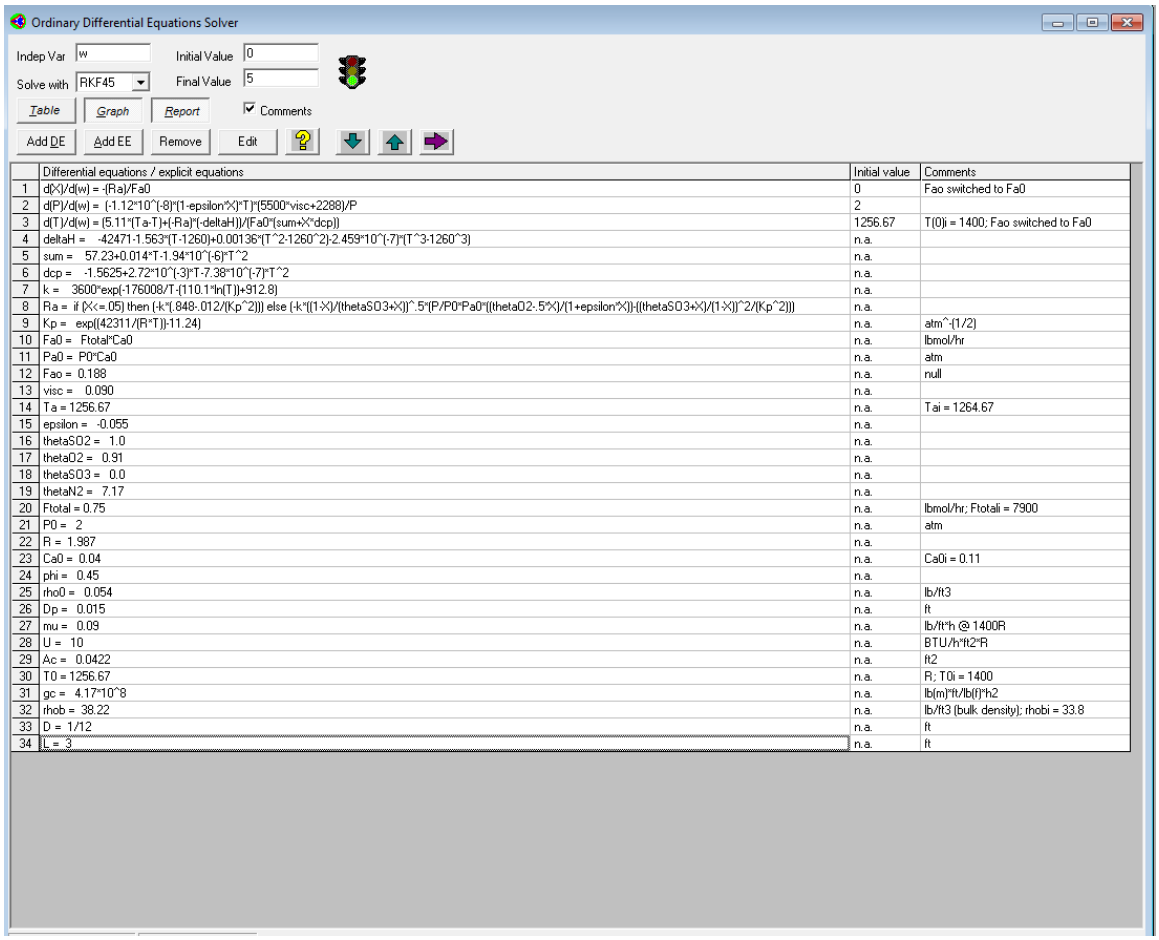


| | Differential equations / explicit equations | Initial value | Comments |
|---|---|---|---|
| 1 | d(X)/d(w) = -(Ra)/Fa0 | 0 | Fao switched to Fa0 |
| 2 | d(P)/d(w) = (-1.12*10^(-8)*(1-epsilon*X)*T)*(5500*visc+2288)/P | 2 | |
| 3 | d(T)/d(w) = (5.11*(Ta-T)+(-Ra)*(-deltaH))/(Fa0*(sum+X*dcp)) | 1256.67 | T(0)i = 1400; Fao switched to Fa0 |
| 4 | deltaH = -42471-1.563*(T-1260)+0.00136*(T^2-1260^2)-2.459*10^(-7)*(T^3-1260^3) | n.a. | |
| 5 | sum = 57.23+0.014*T-1.94*10^(-6)*T^2 | n.a. | |
| 6 | dcp = -1.5625+2.72*10^(-3)*T-7.38*10^(-7)*T^2 | n.a. | |
| 7 | k = 3600*exp(-176008/T-(110.1*ln(T))+912.8) | n.a. | |
| 8 | Ra = if (X<=.05) then (-k*(.848-.012/(Kp^2))) else (-k*((1-X)/(thetaSO3+X))^.5*(P/P0*Pa0*((thetaO2-.5*X)/(1+epsilon*X)))/((thetaSO3+X)/(1-X))^2/(Kp^2))) | n.a. | |
| 9 | Kp = exp((42311/(R*T))-11.24) | n.a. | atm^-(1/2) |
| 10 | Fa0 = Ftotal*Ca0 | n.a. | lbmol/hr |
| 11 | Pa0 = P0*Ca0 | n.a. | atm |
| 12 | Fao = 0.188 | n.a. | null |
| 13 | visc = 0.090 | n.a. | |
| 14 | Ta = 1256.67 | n.a. | Tai = 1264.67 |
| 15 | epsilon = -0.055 | n.a. | |
| 16 | thetaSO2 = 1.0 | n.a. | |
| 17 | thetaO2 = 0.91 | n.a. | |
| 18 | thetaSO3 = 0.0 | n.a. | |
| 19 | thetaN2 = 7.17 | n.a. | |
| 20 | Ftotal = 0.75 | n.a. | lbmol/hr; Ftotali = 7900 |
| 21 | P0 = 2 | n.a. | atm |
| 22 | R = 1.987 | n.a. | |
| 23 | Ca0 = 0.04 | n.a. | Ca0i = 0.11 |
| 24 | phi = 0.45 | n.a. | |
| 25 | rho0 = 0.054 | n.a. | lb/ft3 |
| 26 | Dp = 0.015 | n.a. | ft |
| 27 | mu = 0.09 | n.a. | lb/ft*h @ 1400R |
| 28 | U = 10 | n.a. | BTU/h*ft2*R |
| 29 | Ac = 0.0422 | n.a. | ft2 |
| 30 | T0 = 1256.67 | n.a. | R; T0i = 1400 |
| 31 | gc = 4.17*10^8 | n.a. | lb(m)*ft/lb(f)*h2 |
| 32 | rhob = 38.22 | n.a. | lb/ft3 (bulk density); rhobi = 33.8 |
| 33 | D = 1/12 | n.a. | ft |
| 34 | L = 3 | n.a. | ft |

**Figure 3.1: Polymath model for $SO_3$ generation reaction**

### 3.2.3 $SO_3$ Generator Construction

Figure 3.2 presents a diagram of the $SO_3$ generator design. A mix of $SO_2$ and air is fed through a rotameter to a catalyst bed that makes two passes through a furnace. The vanadium pentoxide catalyst oxidizes the $SO_2$ with oxygen in the air to form $SO_3$. Temperature in the bed is controlled by the use of a tube furnace. The reacted gas is then fed to the process. An $N_2$ purge is used through the catalyst bed during system startup and shutdown. The $SO_2$/Air mix feed pressure is regulated by a single stage gauge diaphragm valve.

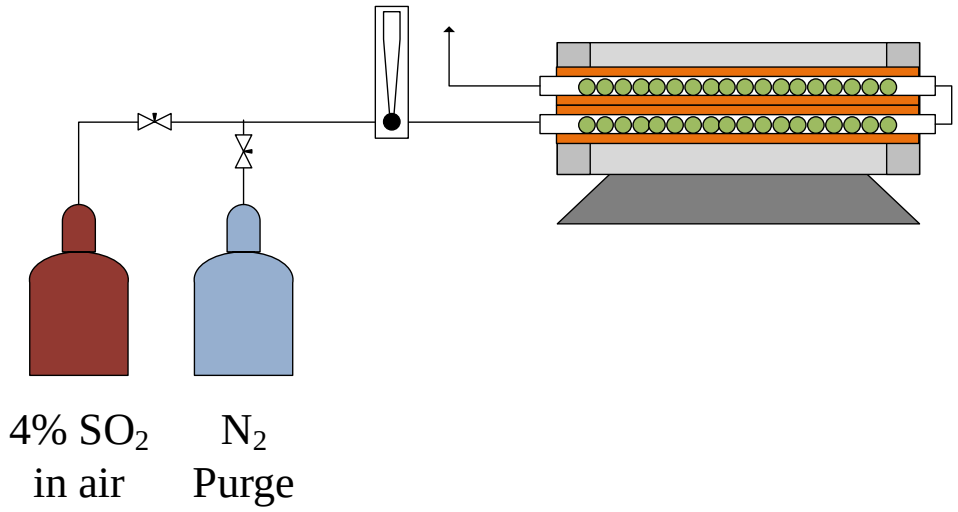


**Figure 3.2: Diagram of $SO_3$ generator**

### *3.2.3.1 Furnace*

The temperature-controlled catalyst bed is one of the most important components of the $SO_3$ generator. The $SO_3$ generator design is centered on this catalyst bed, which is sized to operate at both the bench and pilot scale. A tube furnace was selected for this process; a Carbolite HST 12/900 furnace was chosen due to its operational flexibility. The HST 12/900 has a heated length of 36", which allows enough catalyst mass to have very high $SO_2$ oxidation rates at the bench scale and moderate rates at the pilot scale. The temperature of the catalyst bed is measured by N-type thermocouples within the heated bed. Table 3.3 presents the operating specifications for the furnace.

**Table 3.3: Carbolite HST 12/900 furnace specifications**

| Parameter | Value |
|---|---|
| **Max Temperature (°C)** | 1200 |
| **Number of heated zones** | 1 |
| **Max Tube Diameter (mm)** | 110 |
| **Heated Length (mm)** | 900 |
| **Tube length (mm)** | 1050 |
| **Furnace Length (mm)** | 1050 |
| **Furnace Height (mm)** | 350 |
| **Furnace Depth (mm)** | 410 |
| **Heat-up time (min)** | 45 |
| **Control Module Height (mm)** | 222 |
| **Control Module Width (mm)** | 370 |
| **Control Module Depth (mm)** | 376 |
| **Uniform Length +/- 5 °C (mm)** | 450 |
| **Max Power (W)** | 4500 |
| **Holding Power (W)** | 1450 |
| **Thermocouple Type** | N |
| **Weight (kg)** | 60 |

Figure 3.3 presents the Carbolite HST 12/900 furnace with the control unit, and Figure 3.4 shows the furnace with the two pass catalyst bed.


**Figure 3.3: Carbolite HST 12/900 furnace with control unit (on right)**

**Figure 3.4: Carbolite HST 12/900 furnace with two-pass catalyst bed**

#### *3.2.3.2 Catalyst*

The catalyst for $SO_2$ oxidation was purchased from Research Catalysts, Inc., a division of Catalyst Central. The catalyst is composed of vanadium pentoxide and alkali

sulfates on a porous silica carrier, and was obtained as cylindrical extrudes. Table 3.4 presents the catalyst physical properties.

**Table 3.4: Research Catalysts, Inc., $V_2O_5$ catalyst properties**

| Parameter | Value |
|---|---|
| **Form** | Extrudes |
| **Diameter (mm)** | 8 |
| **Bulk Density (lb/L)** | 1.35 |
| **Knife Edge Hardness (kg)** | 4.5 |
| **Ignition T (°C)** | 380 |
| **Operating T (°C)** | 415-630 |

The catalyst is contained in a pair of 1" steel tubes for each pass through the tube furnace. 1" to ¼" Swagelok® compression fittings are used for the connections between the tubes and at the inlet and outlet. The catalyst extrudes are held in place by fused quartz wool (Wale Apparatus Co., #17-1780).

Steel construction of the catalyst bed and downstream tubing is important due to the effects of thermal expansion. Early $SO_3$ generator designs raised concerns about glass to steel connections; the varying degrees of thermal expansion can lead to the development of leaks when operating. By constructing the catalyst bed and downstream tubing out of matching material, thermal expansion concerns are significantly mitigated.

#### *3.2.3.3 Flow Control*

Flow rates through the $SO_3$ generator for the $SO_2$/Air mix and $N_2$ purge gases are maintained by precision rotameters, obtained through Aalborg Co. Table 3.5 outlines the specifications for the rotameters used at the bench and pilot scale. Significantly lower flow rates are required for bench scale experiments, requiring the procurement of the

separate rotameter with a narrower range of operation. Both rotameters have accuracies of +/- 2.0 %, with a repeatability of 0.25 %.

**Table 3.5: Aalborg precision rotameter specifications for bench and pilot scale $SO_3$ generation**

| Parameter | Pilot | Bench |
|---|---|---|
| **Part No.** | PMR1-017689 | PMR1-017158 |
| **Body Size (mm)** | 150 | 150 |
| **Flow Range (SLPM)** | 0-60 | 0-0.5 |
| **Pressure (psia)** | 14.7 | 14.7 |
| **Float Material** | Carboloy | Sapphire |
| **Seals** | Vinton-A | Vinton-A |
| **Connections** | FNPT | FNPT |
| **Connection Size (in)** | 1/4 | 1/4 |
| **Connection Material** | 316 SS | 316 SS |
| **Needle Valve Size** | #7 | #3 |

#### *3.2.3.4 $SO_2$ Source and Containment*

The $SO_2$/Air (Praxair AI SD8ZC-AQ) mixture is stored in a gas cylinder cabinet (Safety Equipment Corporation Model 7100 Gas Cabinet) in the walk-in fume hood during bench scale experiments. An exhaust fan (Home Depot 202797333 Inductor 6" Crimped In-Line Duct Dan) provides constant suction from the gas cabinet to the fume hood outlet, to safely exhaust the gas in the event of a regulator leak. During pilot scale experiments, the $SO_2$/Air mix is stored outside within the battery limits of the plant. The $SO_2$/Air mix from the tank is regulated by a ProSpec 4022 Series Single Stage Gauge Diaphragm Valve CGA-660 (Praxair PRS40223331-660).

For bench scale experiments, a 3-way valve at the outlet of the gas cylinder cabinet allows the user to switch between nitrogen and $SO_2$/Air flow to the $SO_3$

generator. The selected gas flows to the rotameter (Aalborg PMR1-017158) for flow rate regulation. After exiting the $SO_3$ generator heated catalyst bed, the gas is fed through a check valve (Swagelok® SS-4C-1) with a set pressure of 1 psig. The gas enters the AGC column process at a location immediately after the presaturator. The check valve is in place to ensure that the humid gas from the presaturator is not allowed to enter the $SO_3$ generator catalyst bed. Water in the catalyst bed will hydrolyze the $SO_3$ to form $H_2SO_4$, and can cause corrosion and possible structural failure in the catalyst containment system.

For pilot scale experiments, the $SO_2$/Air mix from the cylinder is fed through the south wall of the CEER building to a gas manifold. The $SO_2$/Air mix or $N_2$ purge can be selected at this point for flow through the rotameter (Aalborg PMR1-017689). The flow from the rotameter is fed to the $SO_3$ generator catalyst bed. 10' of ¼" OD coiled steel tubing is used downstream of the heated catalyst bed to provide ambient cooling of the reaction gas. The gas mix is then fed to a location upstream of the UT-SRP absorber inlet FTIR sample location.

### 3.2.4 Safety

The $SO_3$ generator furnace, exposed catalyst bed, and outlet tubing all pose burn risks while operating. The exposed end of the catalyst bed has been covered with protective insulation to partially mitigate the risk of skin contact. The $SO_3$ generator outlet tubing is left unprotected; this is by design, to allow for partial cooling of the outlet gas.

The $SO_3$ generator catalyst bed is to be only operated in ventilated fume hoods. At the pilot scale, the generator can be placed in the fume hood in CEER 1.704. Wall

ports are available for the $SO_2$/Air mix to be fed in from the unit and for the line to the absorber inlet. All tubing connections at the outlet of the catalyst bed must be contained within the fume hood itself, in the event of a leak developing at this location due to thermal expansion.

At the bench scale, the $SO_3$ generator is physically located within the walk-in fume hood that contains the Aerosol Growth Column. This is shown in Figure 3.5. In the event of a leak, the furnace can be shut down and switched to $N_2$ purge from outside the fume hood. There is always risk of gas leakage from the $SO_3$ generator system. Due to this risk, it is recommended that the supplied face shield and respirator unit (Advantage™ 3000 Respirator, ZORO G3258857) be worn when entering the fume hood. The exhaust vent to the $SO_2$/Air gas cabinet should be on at all times.

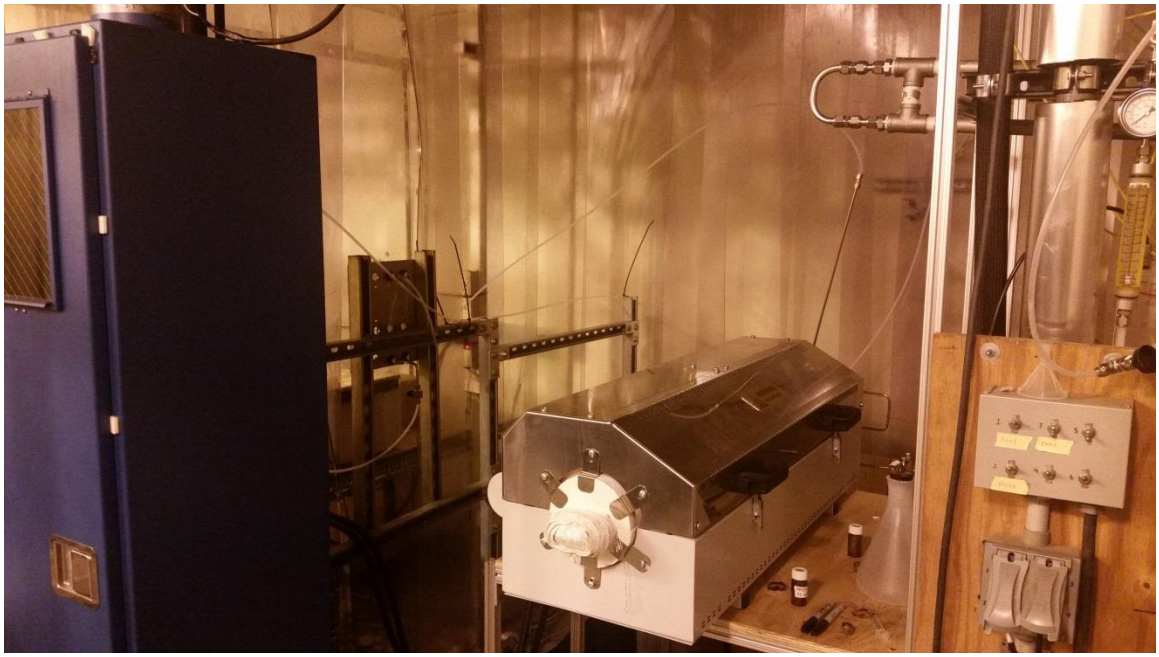

**Figure 3.5: $SO_3$ generator at the bench scale. The Aerosol Growth Column is to the right, with the $SO_2$/Air gas cylinder cabinet to the left.**

## 3.3 MODEL RESULTS

The Polymath model was used to determine optimal operating conditions for bench and pilot scale operations. As presented in Table 3.1, there are significant discrepancies in the process conditions between the bench and pilot scale, and within the high and low process flow conditions at either scale. At both scales, higher flow conditions will require significantly greater $SO_3$ generation rates.

For modeling purposes, it was assumed that the $V_2O_5$ catalyst obtained from Research Catalysts, Inc., would exhibit the same properties as the Fogler model catalyst.

### 3.3.1 Temperature Effects

Figure 3.6 presents the calculated conversionof $SO_2$ to $SO_3$ at each scale and process condition as a function of the catalyst bed temperature.

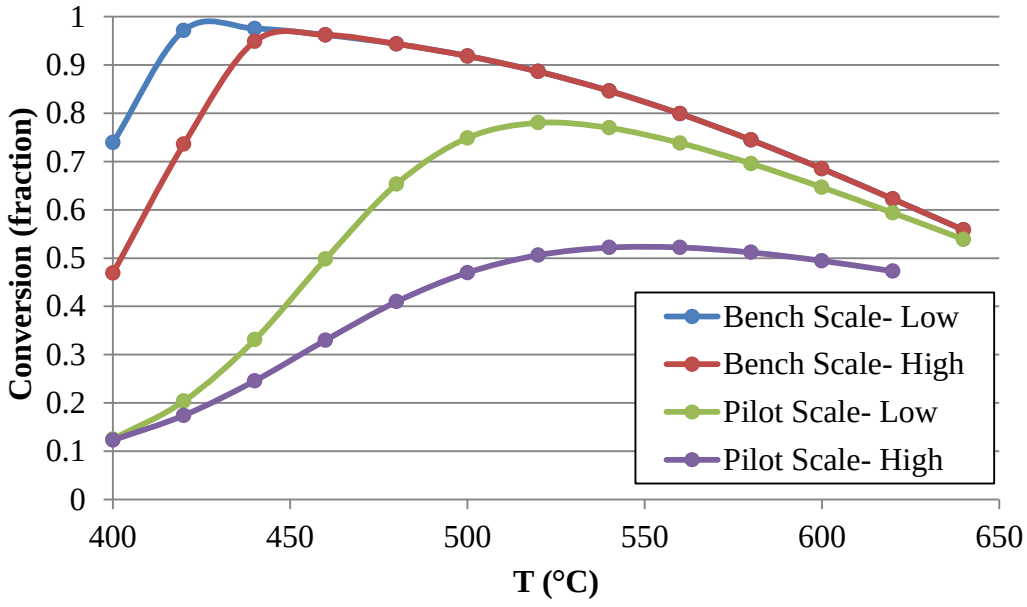


**Figure 3.6: $SO_2$ conversion at bench and pilot scale for each process condition**

Optimal bench-scale temperatures were found to be significantly lower than the optimal temperatures for pilot-scale operations. At low bench-scale flow rates, the optimal catalyst bed temperature is 440 °C, and 460 °C for higher bench-scale process flow conditions. For the pilot scale, the optimal temperature for $SO_2$ conversion is 520 °C at lower flow rates and 580 °C for process conditions that require a higher $SO_3$ generation rate.

Conversion rates were modeled to be significantly lower at the pilot scale than the bench scale. Close to 100% conversion was anticipated at bench scale operations, while conversions at the pilot scale were predicted to be between 78 and 52 %. This is due to the same mass of catalyst for both scales, but significantly higher $SO_2$ inlet flow rates at the pilot scale. This also impacts the energy balance of the system; hence the higher optimal temperature for the pilot scale.

### 3.3.2 Compositional Effects

Figure 3.7 examines the calculated effect of the feed gas $SO_2$ composition. The left y-axis presents the $SO_2$ converted to $SO_3$ (●), and the right y-axis presents the amount of $SO_3$ produced in grams per second on a logarithmic scale (▲).

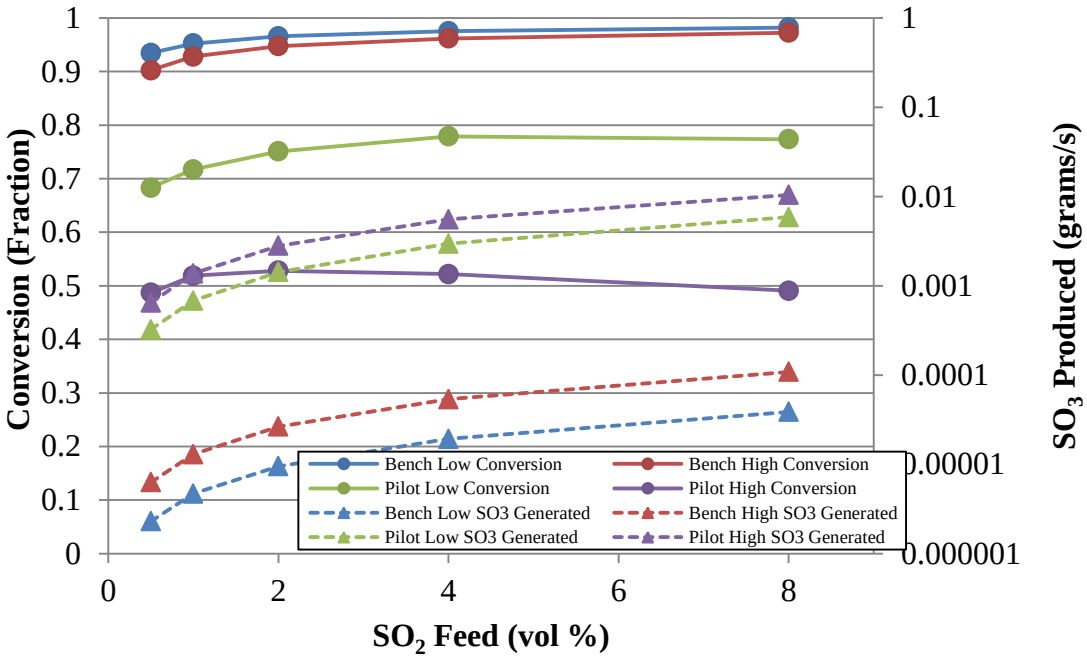


**Figure 3.7: Conversion of $SO_2$ (●) and grams per second of $SO_3$ produced (▲) as a function of the $SO_2$ % composition in the generator feed gas**

At the bench scale, there is a moderate continuous increase in conversion as the $SO_2$ increases in the feed gas. For the pilot scale, a maximum conversionoccurs with 4% $SO_2$ at the low flow conditions and 2% $SO_2$ at the high flow conditions.

At the pilot scale, the amount of $SO_3$ produced is more important than the conversion. As expected, the amount of $SO_3$ produced increases as the $SO_2$ composition in the feed gas increases; the minimal reduction in conversion is not enough to offset the increased $SO_3$ production granted by the higher $SO_2$ in the feed. The drawback of using a higher $SO_2$ feed is the increase in heat generated from the exothermic oxidation reaction, which can cause the catalyst bed to overheat if not monitored, as observed by Pfeifer et al. (2011).

## 3.4 APRIL 2017 UT-SRP CAMPAIGN

Aerosol emissions tests were required during the UT-SRP April 2017 campaign. This was the first opportunity to test the completed $SO_3$ generator. the generator was tested at the pilot scale prior to the bench scale due to theoretical concerns with adsorption of the $SO_2$ onto the catalyst. At the bench scale, reaching $SO_2$ saturation on the catalyst adsorption sites could potentially take a significant amount of time due to the lower flow rates. By doing initial run at the pilot scale, this length of time required for saturation could be reduced.

### 3.4.1 Calibration

The precision rotameter (Aalborg PMR1-017689) for the $SO_2$/Air mix feed was calibrated prior to beginning $SO_3$ generation. This was accomplished by running the $SO_2$/air mix through the reactor without turning on the heating components, and observing the $SO_2$ at the absorber inlet FTIR sample point. Figure 3.8 presents the inlet FTIR data for 4/25/17, when the calibration was performed.

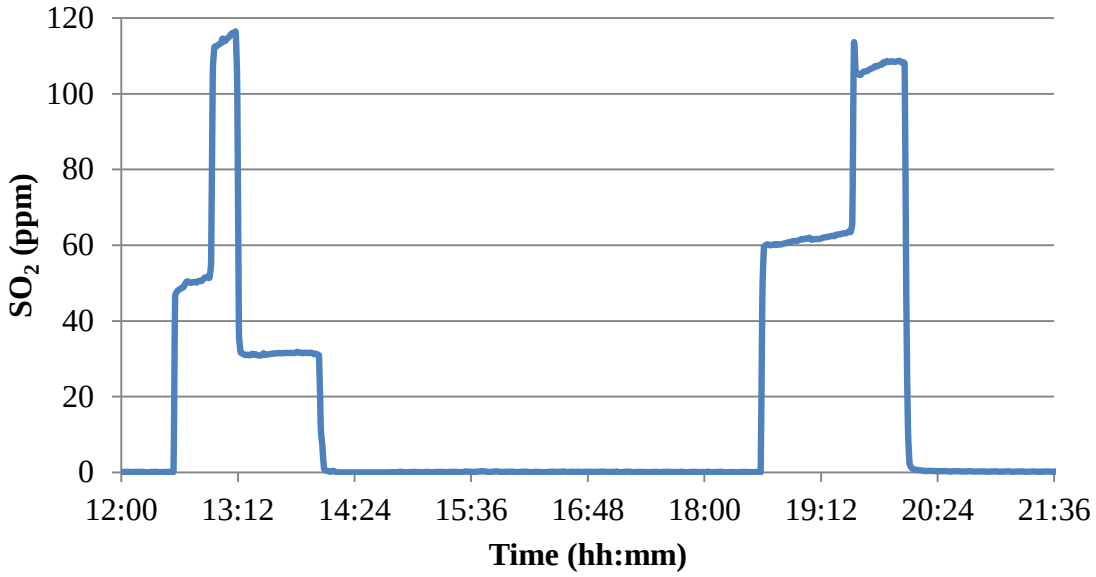


**Figure 3.8: FTIR results of rotameter calibration with $SO_2$**

The results of Figure 3.8 are summed up in Table 3.6. The first three tests starting shortly after noon utilized 4% $SO_2$ in air, and the last two tests at 18:30 used 8% $SO_2$ in air.

**Table 3.6: UT-SRP pilot plant rotameter calibration results**

| **Run** | **Start Time** | **End Time** | **$SO_2$ Tank Conc.** | **Rotameter Flow** | **Regulator Pressure** | **FTIR $SO_2$ Conc.** |
|---|---|---|---|---|---|---|
| *#* | *(hh:mm)* | *(hh:mm)* | *vol %* | *LPM* | *psi* | *ppm* |
| **1** | 12:29 | 12:55 | 4 | 10 | 20 | 50 |
| **2** | 12:55 | 13:11 | 4 | 20 | 30 | 113 |
| **3** | 13:11 | 14:02 | 4 | 5 | 20 | 31 |
| **4** | 18:34 | 19:31 | 8 | 5 | 20 | 62 |
| **5** | 19:31 | 20:04 | 8 | 10 | 20 | 107 |

Figure 3.9 plots $SO_2$ in ppm as a function of the rotameter flow rate in LPM, for $SO_2$ tank compositions of 4% and 8%.

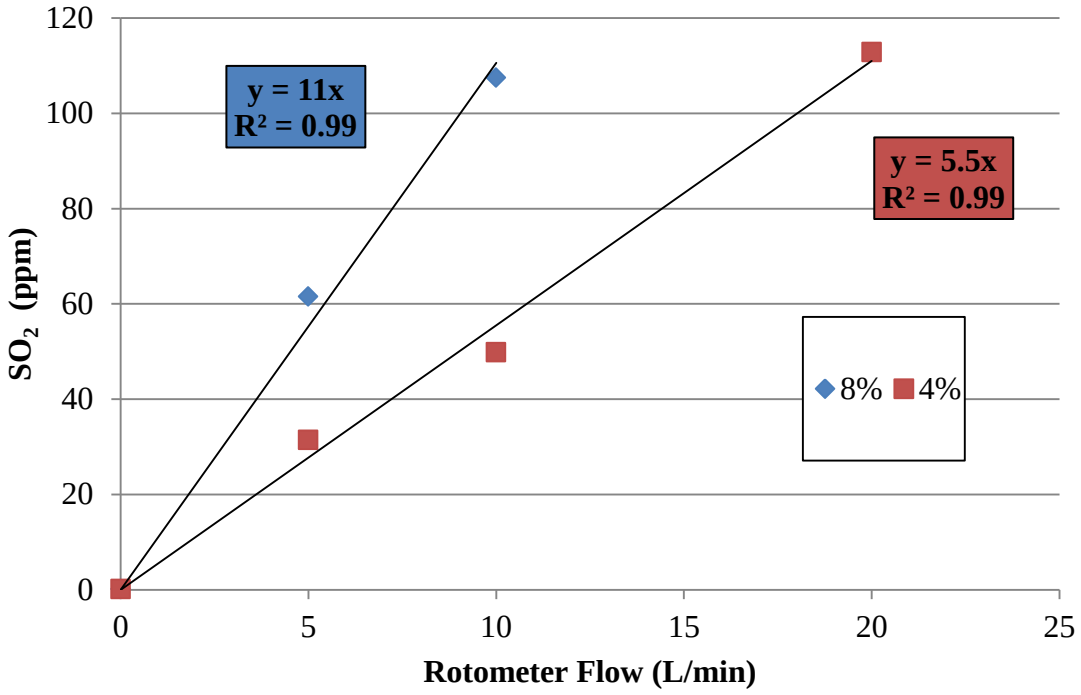


**Figure 3.9: Plot and fitting equations for calibrating $SO_3$ generator rotameter at UT-SRP pilot scale**

FTIR spectra for the GASMET™ CX-4000 analyzer are not available for $SO_3$. This complicates the ability to determine the effectiveness of the aerosol generator. Fortunately, $SO_2$ reference spectra are available in the CALCMET™ library. Calibrations with $SO_2$ can determine the converted $SO_3$ upon repeating the same test conditions with the $SO_3$ generator catalyst bed heated. The $SO_2$ conversion rate is determined as well.

### 3.4.2 Results

Figure 3.10 presents an example of inlet FTIR results during an $SO_3$ injection test. 8% $SO_2$/Air was passed through the heated $SO_3$ generator at a flow rate of 5 LPM and 20

psi. This was expected to produce 62 ppm of $SO_2$ if no conversion occurs, and no $SO_2$ would be visible if 100% conversion occurs. The $SO_3$ generator bed was heated to 520 °C; this was predicted by the model to produce the highest conversion rate at the UT-SRP process conditions.

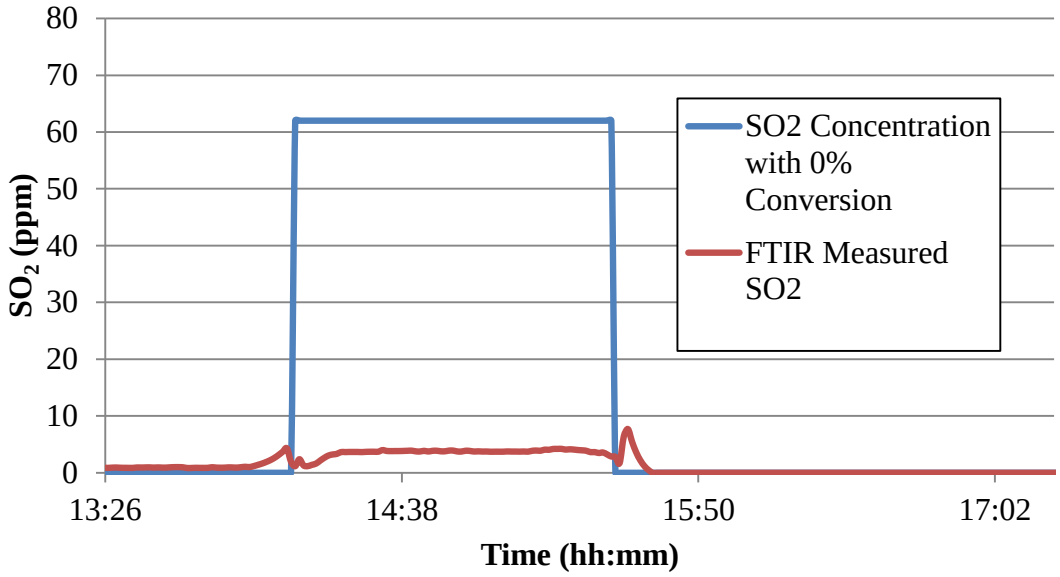


**Figure 3.10: Inlet FTIR result of $SO_3$ generator test on 4/26/2017. The blue line is the expected $SO_2$ composition with no conversion, and the red line is the measured FTIR $SO_2$ content at the absorber inlet.**

Approximately 4 ppm of $SO_2$ was measured at the absorber inlet during this test. This indicates that 52 ppm of $SO_3$ was generated, at a conversion rate of 94%. A production rate of 1.34 grams per minute of $SO_3$ was achieved during this run.

Aerosol production can be confirmed through both analytical and visual methods. FTIR measurements at the absorber outlet will indicate an increased presence of amine solvent as it is collected and emitted through the aerosol phase. In addition, the UT-SRP

flue gas is released to the atmosphere after exiting the scrubbing process; visual confirmation of aerosol can be determined by the presence of a mist.

A second FTIR analyzer is used to monitor emissions at multiple sampling locations in the UT-SRP pilot plant, as outlined in Chapter 2. Figure 3.11 presents the outlet FTIR results for the 4/26/2017 $SO_3$ generation experiments. This produced $SO_3$ at 1.34 grams per minute, giving an $SO_3$ composition of 53 ppm at the absorber inlet. $SO_3$ injection began at 14:12 and concluded at 15:30. Gray vertical lines indicate the switching of FTIR sampling locations from the absorber outlet to other sampling locations, as outlined in Chapter 2.

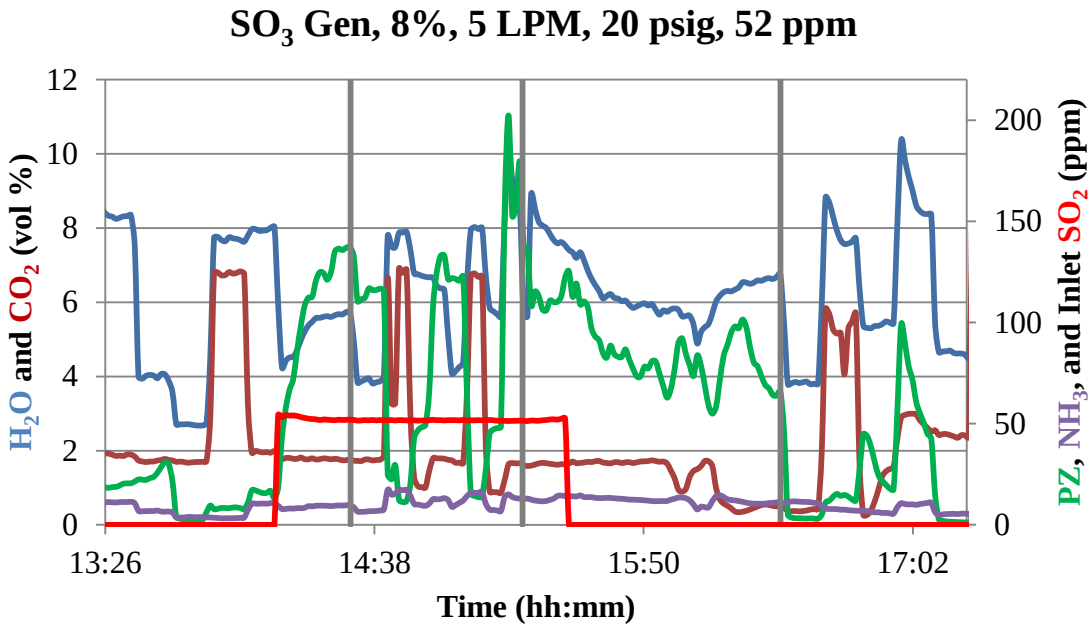


**Figure 3.11: Outlet FTIR results of $SO_3$ generator test on 4/26/2017. The bright red line is the calculated $SO_3$ content in the absorber inlet.**

Piperazine emissions increase from 17 ppm to over 120 ppm at the absorber outlet, with spikes in emissions over 200 ppm. This is more than can be accounted for by volatility emissions, indicating the presence of aerosol emissions. Visual confirmation of the presence of aerosol in the flue gas outlet is presented in Figure 3.12.

**Figure 3.12: Aerosol cloud at flue gas outlet, 4/26/17**

A total of 16 $SO_3$ generation aerosol tests were performed over a span of 8 days. Table 3.7 summarizes the $SO_3$ generation results, with the inlet flow conditions, $SO_3$ production rates and content, and $SO_3$ conversion rates. The reactor temperature was maintained at 520 °C for each test.

**Table 3.7: UT-SRP April 2017 Campaign $SO_3$ injection tests summary**

| **Date** | **Start Time** | **End Time** | **$SO_2$ Tank Conc.** | **Inlet Flow Rate** | **Pressure** | **$SO_3$** | **$SO_3$ Conversion** | **$SO_3$ Generated** |
|---|---|---|---|---|---|---|---|---|
| | *hh:mm* | *hh:mm* | *vol %* | *LPM* | *psi* | *ppm* | *%* | *g/min* |
| 4/26/17 | 14:12 | 15:30 | 8 | 5 | 20 | 52 | 93.9 | 1.34 |
| 4/27/17 | 18:05 | 20:00 | 8 | 1 | 20 | 9 | 81.3 | 0.23 |
| 4/27/17 | 20:00 | 20:33 | 8 | 5 | 20 | 51 | 92 | 1.32 |
| 5/1/17 | 13:20 | 15:19 | 8 | 2 | 20 | 20 | 90.6 | 0.52 |
| 5/2/17 | 12:43 | 13:00 | 8 | 6 | 20 | 112 | 98.1 | 1.68 |
| 5/2/17 | 13:00 | 13:27 | 8 | 1.7 | 20 | 31 | 94.8 | 0.46 |
| 5/2/17 | 13:27 | 14:34 | 8 | 5 | 20 | 92 | 97.5 | 1.39 |
| 5/3/17 | 12:45 | 15:17 | 8 | 5 | 20 | 53 | 96.5 | 1.38 |
| 5/4/17 | 12:15 | 13:35 | 8 | 5 | 20 | 93 | 97.8 | 1.4 |
| 5/4/17 | 18:16 | 19:38 | 8 | 3 | 20 | 31 | 93.4 | 0.8 |
| 5/9/17 | 14:56 | 15:13 | 8 | 3 | 20 | 32 | 95.1 | 0.82 |
| 5/9/17 | 15:13 | 15:29 | 8 | 1 | 20 | 10 | 90.3 | 0.26 |
| 5/9/17 | 15:29 | 16:11 | 8 | 2 | 20 | 21 | 94.7 | 0.54 |
| 5/9/17 | 16:11 | 17:09 | 8 | 1 | 20 | 10 | 89.7 | 0.26 |
| 5/10/17 | 9:12 | 9:42 | 8 | 3 | 20 | 32 | 96.9 | 0.83 |
| 5/10/17 | 9:42 | 10:54 | 8 | 1 | 20 | 10 | 93.4 | 0.27 |

On average, $SO_3$ was produced at a rate of 0.84 grams per minute. The lowest generation rate was 0.23 grams per minute, and the generator successfully produced up to 1.68 grams per minute. The reaction was much more successful than initially predicted by the Polymath model; conversion rates were between 81 and 98%. $SO_3$ at the absorber inlet ranged from 9 to 112 ppm. $SO_3$ conversion appears to be more favorable at higher

flow rates, which counters the predicted conversion rates presented in Figure 3.6. This may be a result of uncertainty in the FTIR analyzer; at lower $SO_2$ feed rates, any error in measurement will lead to higher error in the conversion calculation. Given the success of the reactor at higher generation rates, it is possible to produce $SO_3$ at rates that are adequate for pilot plants that are larger than the 0.1 MW-equivalent unit at UT-SRP. Further analysis on the results from the April 2017 UT-SRP campaign can be found in Chapter 5.

## 3.5 BENCH SCALE EXPERIMENTAL

The $SO_3$ generator was reconfigured to operate at the bench scale for Aerosol growth Column (AGC) experiments. A goal of the bench scale tests was to quantify the aerosol produced by the $SO_3$ generator by the use of the Phase Doppler Interferometer (PDI). The PDI was unavailable during the April 2017 UT-SRP pilot plant testing. Parameters tested during AGC experiments included inlet $CO_2$ content, solvent flow rates, solvent compositions, and inlet $SO_3$ content.

### 3.5.1 Calibration

Calibration for bench scale experiments was performed in a similar manner to pilot scale calibration. Flow through the AGC was maintained at 100 LPM of $N_2$. The precision rotameter (Aalborg PMR1-017158) for the feed was used to regulate the 8% $SO_2$/Air flow rate through the unheated $SO_3$ generator, and FTIR sampling was performed at the AGC inlet sample location downstream of the aerosol injection point. Figure 3.13 presents the calibration results.

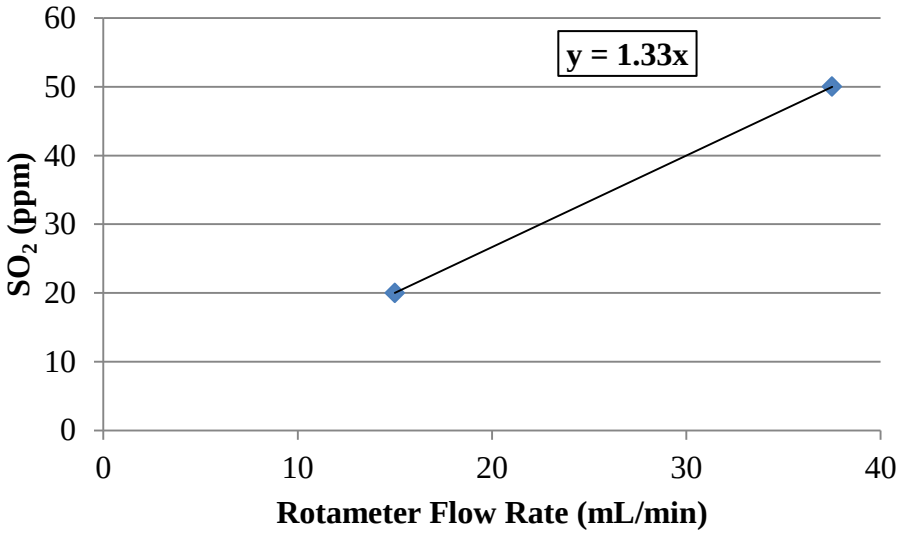


**Figure 3.13: $SO_3$ generator rotameter calibration for AGC experiments**

A flow rate of 15 mL/min through the rotameter corresponded with an $SO_2$ content of 20 ppm, and a flow rate of 37.5 mL/min resulted in an $SO_2$ content of 50 ppm.

### 3.5.2 Results

A total of 24 different test conditions were performed on the ACG. $SO_3$ at 20 and 50 ppm were used for these experiments. FTIR measurements at the AGC inlet quantified the performance of the $SO_3$ generator at the bench scale. Table 3.8 presents the FTIR results from $SO_3$ generation.

**Table 3.8: FTIR results from AGC $SO_3$ generation**

| Test | $SO_2$/Air Feed Rate | $SO_2$ In Conc. (FTIR) | $SO_3$ In | $SO_2$ Conversion |
|---|---|---|---|---|
| *#* | *mL/min* | *ppm* | *ppm* | *%* |
| **1** | 15 | 0 | 20 | 100 |
| **2** | 15 | 0 | 20 | 100 |
| **3** | 15 | 0 | 20 | 100 |
| **4** | 15 | 0 | 20 | 100 |
| **5** | 15 | 0 | 20 | 100 |
| **6** | 15 | 0 | 20 | 100 |
| **7** | 37.5 | 0 | 50 | 100 |
| **8** | 37.5 | 0 | 50 | 100 |
| **9** | 37.5 | 0 | 50 | 100 |
| **10** | 37.5 | 0 | 50 | 100 |
| **11** | 37.5 | 0 | 50 | 100 |
| **12** | 37.5 | 0 | 50 | 100 |
| **13** | 15 | 0 | 20 | 100 |
| **14** | 15 | 0 | 20 | 100 |
| **15** | 15 | 0 | 20 | 100 |
| **16** | 15 | 0 | 20 | 100 |
| **17** | 15 | 0.1 | 19.9 | 99.7 |
| **18** | 15 | 0.1 | 19.9 | 99.7 |
| **19** | 37.5 | 0.3 | 49.7 | 99.3 |
| **20** | 37.5 | 0.3 | 49.7 | 99.3 |
| **21** | 37.5 | 0.9 | 49.1 | 98.1 |
| **22** | 37.5 | 0.9 | 49.1 | 98.1 |
| **23** | 37.5 | 1.1 | 48.9 | 97.8 |
| **24** | 37.5 | 1.1 | 48.9 | 97.8 |

The $SO_3$ generator succeeded in converting almost all inlet $SO_2$ to $SO_3$, with conversion rates greater than 97.8% for all experiments.

The PDI was used to quantify the aerosol emissions at the AGC outlet. As $SO_3$ aerosol nuclei pass through the AGC absorber, the nuclei collect water, $CO_2$, and amine.

These aerosol are quantified by the PDI through optical techniques discussed in Chapter 2. Table 3.9 presents the PDI results from the AGC outlet, along with the FTIR measured amine emissions.

**Table 3.9: PDI results summary from AGC $SO_3$ generation, with FTIR amine emissions**

| Test | $SO_3$ In | Count | Aerosol Concentration | Mean | Standard Deviation | PZ Out (FTIR) |
|---|---|---|---|---|---|---|
| *#* | *ppm* | *#* | *#/cm$^{-3}$* | *μm* | *μm* | *ppm* |
| **1** | 20 | 2955 | 23631 | 1.64 | 0.489 | 0 |
| **2** | 20 | 4155 | 32069 | 1.8 | 0.768 | 0 |
| **3** | 20 | 1153 | 9040 | 1.72 | 0.65 | 0 |
| **4** | 20 | 3432 | 27342 | 1.72 | 0.865 | 0.1 |
| **5** | 20 | 564 | 4344 | 1.86 | 0.784 | 0 |
| **6** | 20 | 1955 | 16129 | 1.93 | 1.122 | 0.1 |
| **7** | 50 | 1617 | 13129 | 1.5 | 0.577 | 0 |
| **8** | 50 | 3544 | 27107 | 1.69 | 0.898 | 0.1 |
| **9** | 50 | 6856 | 51234 | 1.79 | 0.585 | 0.1 |
| **10** | 50 | 8757 | 65165 | 1.74 | 0.704 | 0.2 |
| **11** | 50 | 10002 | 70507 | 2.24 | 0.724 | 0.3 |
| **12** | 50 | 7124 | 47164 | 1.97 | 0.74 | 0.4 |
| **13** | 20 | 1650 | 13578 | 2.06 | 0.624 | 0.8 |
| **14** | 20 | 1246 | 12656 | 1.77 | 0.797 | 1.2 |
| **15** | 20 | 3412 | 28760 | 2.04 | 0.598 | 0.5 |
| **16** | 20 | 4506 | 51869 | 1.78 | 0.567 | 7.4 |
| **17** | 19.9 | 2845 | 23408 | 1.98 | 0.619 | 1.4 |
| **18** | 19.9 | 4111 | 51821 | 1.73 | 0.578 | 7 |
| **19** | 49.7 | 6604 | 53961 | 2.24 | 0.6 | 3.9 |
| **20** | 49.7 | 5556 | 53176 | 2.07 | 0.561 | 9.3 |
| **21** | 49.1 | 5110 | 47122 | 2.18 | 0.684 | 1.2 |
| **22** | 49.1 | 5399 | 50040 | 1.9 | 0.57 | 4.2 |
| **23** | 48.9 | 5508 | 49214 | 2.27 | 0.719 | 1.3 |
| **24** | 48.9 | 4914 | 47369 | 1.88 | 0.627 | 2.2 |

Aerosol concentrations ranged from 4,344 to 70,507 per $cm^{-3}$. These aerosol had average diameters between 1.5 and 2.3 μm, and resulted in piperazine emissions between 0 and 9.3 ppm. The aerosol measurements and analysis from these experiments are presented in Chapter 4.

## 3.6 $SO_3$ Generator Operating Procedure

The $SO_3$ generator furnace, exposed catalyst bed, and outlet tubing all pose burn risks while operating. Caution must be exercised around the furnace and tubing while operating.

The $SO_3$ generator catalyst bed is only to be operated in ventilated fume hoods. During UT-SRP aerosol tests, the generator can be placed in the fume hood in CEER 1.704. All tubing connections at the outlet of the catalyst bed must be contained within the fume hood itself, in the event of a leak developing at these locations due to thermal expansion. The fume hood sash must remain closed during operation. The supplied face shield and respirator unit (Advantage™ 3000 Respirator, ZORO G3258857) must be kept nearby when the $SO_3$ generator is operating.

### 3.6.1 $SO_3$ Generator Startup

Ensure that the Carbolite HST 12/900 furnace is plugged in. Establish $N_2$ flow through the catalyst bed. At the bench scale, 100-200 mL/min is sufficient; for pilot scale experiments, 1-2 LPM is adequate. Flow through the bed and into the amine scrubbing process should be unimpeded. Plant $N_2$ is available at multiple ports in the lab. Ensure that $N_2$ is used, as the compressed air for the CEER building contains water that can severely damage the catalyst bed.

Turn on the furnace. This is accomplished by switching the top switch on the control unit to turn on the controller, and then the second switch to turn on power to the heated elements. The furnace will now heat the catalyst bed to 520 °C. This set temperature can be changed by following the instructions in the Carbolite HST 12/900 manual.

The generator will take approximately 100 minutes to reach temperature. Periodically check on the flow through the rotameter to ensure no flow disruptions are occurring.

### 3.6.2 Steady State Operation

Upon reaching 520 °C, the $SO_2$/Air mix can be passed through the system. Open the cylinder and regulator at for the $SO_2$/Air mix. Ensure outlet pressure is regulated to 10 psig for bench-scale experiments and 20 psig for pilot scale. Turn the 3-way valve from $N_2$ to $SO_2$/Air flow, and adjust the flow through the rotameter to the desired rate.

Ensure that no leaks are present in the $SO_3$ generation process. $SO_3$ will rapidly hydrolyze with water vapor to form a sulfuric acid mist; this will be easily spotted at higher flow rates. If a leak forms, follow shutdown procedures and take corrective actions.

If work is to be performed at this time near the flue gas outlet on the UT-SRP plant, the provided face shield and respirator unit is to be worn.

### 3.6.3 System Shutdown

Turn off the Carbolite HST 12/900 furnace by flipping both switches off. Turn off the $SO_2$/Air mix at the cylinder and bleed the line. Switch flow to the catalyst bed back to $N_2$ purging, at the same rates as startup.

Allow the furnace to cool. Upon reaching approximately 200 °C, the $N_2$ purge can be stopped.

## 3.7 MODEL UPDATE

The $SO_3$ generator performance during the April 2017 UT-SRP campaign proved to be superior to the performance predicted by the Polymath model. On average, 0.04 lbmol/hr of 8% $SO_2$/Air mix was fed to the reactor, corresponding to an $SO_2$ feed of 0.76 grams per minute. An average conversion rate of 93.5 % produced 0.84 grams per minute of $SO_3$.

Using the initial Polymath model with the experimental inlet conditions, $SO_2$ is converted to $SO_3$ at a rate of 91.5 %. This results in a production rate of 0.82 grams per minute of $SO_3$.

A number of experimental parameters were not identical to the values used in the model. Most notably, corrections were necessary for the catalyst density and mass used, and the reactor operating pressure. Additional corrections were made to the activation energy used in the model design equations.

### 3.7.1 Catalyst Mass and Density

The actual catalyst bulk density was found to be greater than the specified bulk density. The specified bulk density was listed at 38.22 lb/ft$^3$; weighing the remaining

catalyst that was not added to the bed determined that the bulk density of the catalyst used in the $SO_3$ generator was actually 42.13 lb/ft$^3$. This resulted in an increase in the catalyst mass to 1.19 lb.

### 3.7.2 Pressure Correction

Polymath models were initially run with a set pressure of 2 atm. However, the pressure was set at 20 psig (2.36 atm) at the regulator during actual aerosol generation tests. This increase in pressure increased the amount of $SO_2$ fed to the reactor.

### 3.7.3 Activation Energy Correction

With the updates to the operating pressure and the catalyst bulk density, the Polymath model predicted a conversion rate of 92.1 %. Slight adjustments were made to the Polymath model explicit equations. The activation energy in the Arrhenius equation, Equation 3.6, was adjusted to fit the experimental results. Increasing the activation energy from 42,331 to 42,900 allowed the Polymath model to fit the experimental results. Thus, Equation 3.6 is corrected to Equation 3.16:

$$K_p = e^{\left(\frac{42900}{RT} - 11.24\right)} \tag{3.16}$$

## 3.8 CONCLUSIONS

$SO_3$ was reliably and safely provided at 10 to 100 ppm for the bench-scale (100 LPM) and pilot scale (10,000 LPM) test systems with a vanadium pentoxide catalytic reactor using $SO_2$ in air. The design and construction of the $SO_3$ aerosol generator is a significant achievement from this research. Experiments at the UT-SRP pilot plant and on the bench-scale Aerosol Growth Column require an aerosol source for the synthetic flue gas.

### 3.8.1 $SO_3$ Generator Model

A Polymath model was developed to size the reactor and predict optimal $SO_3$ generation rates. These optimal operating conditions were used to establish operational guidelines for the generator.

Upon completing $SO_3$ generator tests at the pilot scale, the Polymath model was updated with more accurate parameters. This included an increase in the activation energy from 42,331 to 42,900 kJ/mol in the Arrhenius equation (Equation 3.16). This allowed the reactor model to more accurately predict the $SO_3$ conversion, increasing the model conversion from 92.1 % to the experimentally determined 93.5 %.

### 3.8.2 Pilot Scale $SO_3$ Generator Experiments

The generator produced $SO_3$ at rates between 0.23 and 1.68 grams per minute, at $SO_2$ conversions between 81 and 98 %. This resulted in $SO_3$ between 9 and 112 ppm, which was sufficient for amine aerosol generation. The $SO_3$ generator was tested during the April 2017 UT-SRP pilot plant campaign. $SO_3$ generation was performed in 16 test runs with varying process conditions and reactor flow rates. Due to the success of the reactor at higher generation rates, it is possible to produce $SO_3$ at rates that are sufficient for pilot plants larger than the 0.1 MWe UT-SRP unit, including the 0.7 MWe PSTU unit at the National Carbon Capture Center.

### 3.8.3 Bench Scale $SO_3$ Generator Experiments

$SO_3$ generation experiments on the bench scale Aerosol Growth Column produced 20 to 50 ppm of $SO_3$ in the synthetic flue gas, at conversions in excess of 97 %. Mean aerosol diameters from this process measured between 1.5 and 2.3 μm, with aerosol

concentrations in the gas stream between 4E3 and 7E4 per $cm^3$. The $SO_3$ generator is shown to be as equally effective at the bench scale as the pilot scale.

## 3.9 ACKNOWLEDGEMENTS

Thank you to David Artrip of Research Catalyst, Inc., for help in finding and procuring the $V_2O_5$ catalyst used in the $SO_3$ generator. Thanks as well to Kevin Fisher of Trimeric Corporation, and Andrew Wang of AECOM, for providing valuable insight and advice in the design and construction of the $SO_3$ generator. Andrew in particular gave appreciated insight into eliminating leaks in the system.

Korede Akinpelumi was of great help during both bench and pilot scale setup and experiments with the $SO_3$ generator. Vietnam Nguyen provided much needed assistance with aerosol generation during the UT-SRP April 2017 campaign.

Dr. John Gossage of Lamar University provided valuable lessons and examples in the use of the Polymath modeling software. Thanks as well to Dr. Rochelle for financial and scientific support.

# CHAPTER 4: BENCH SCALE AEROSOL GENERATION AND MEASUREMENT

This chapter first outlines the purpose and prior results from bench-scale amine absorption aerosol testing. The Aerosol Growth Column at UT Austin is briefly presented, along with an overview of aerosol generation and observation techniques. The experimental parameters and run matrix are presented, followed by the methodology for interpreting the experimental results. Finally, the results from 24 different run conditions are compared to gather insight into the causes and mechanisms of amine aerosol emissions.

## 4.1 BACKGROUND

### 4.1.1 Justification

Amine aerosol emissions are a relatively recently discovered phenomenon that has significant environmental and economic implications for amine absorption technology. Amine exposure is damaging to aquatic life, and can cause burns to the eyes, skin, and respiratory and gastrointestinal tracts of mammalian fauna. The amine make-up to compensate for aerosol losses at full-scale $CO_2$ capture facilities can prove to be expensive; for a 500 MWe process emitting 100 ppm of MEA solvent, this can result in solvent replacement cost of approximately $1,000/hour.

Excessive solvent losses at early amine-scrubbing $CO_2$ capture pilot plants prompted research into aerosol emissions. $SO_3$ was found to increase amine solvent emissions at Mitsubishi Heavy Industries (Kamijo, 2013). A joint study by the

Netherlands Organization for Applied Scientific Research (TNO) and The Foundation for Scientific and Industrial Research (SINTEF) produced aerosol measurements at the Maasvlakte pilot plant (van der Gjip, 2012; Kolderup, 2012). These measurements included aerosol size distributions and concentrations. Emissions studies at the National Carbon Capture Center in Wilsonville, AL, US, discovered MEA solvent emissions exceeding the amounts justified by vapor pressure; $SO_3$ aerosol were found to be the nuclei source (Carter, 2012). Aker Solutions at Technology Centre Mongstad in Norway found amine emissions exceeding 200 ppm due to the presence of 12 ppm $H_2SO_4$ aerosol nuclei in the flue gas (Bade, 2014).

Work at The Karlsruhe Institute of Technology Institute for Technical Thermodynamics and Refrigeration (ITTK) centered on bench-scale aerosol emissions tests. Khakharia used a condensation particle counter with a soot generator and $SO_3$ synthesis reactor to quantify MEA emissions by aerosol nucleus type and concentration (Khakharia, 2013). Varying the supersaturation of volatile components by changing the amine type and $CO_2$ loading was found to impact the amine emissions. Brachert confirmed aerosol concentrations in the range of 1E8 $cm^{-3}$ with $SO_3$ nuclei; although the aerosol concentration was found to vary minimally when increasing the $SO_3$ injection rate, the amine emissions were found to increase (Brachert, 2013; Brachert, 2014). Mertens used an ELPI+™ to observe aerosol size distributions (Mertens, 2014a). The majority of aerosol were found to be smaller than 0.2 μm in diameter, but the majority of amine emissions were due to aerosol in the range of 0.5 to 2.0 μm. Upstream filtration was found to effectively remove particulate aerosol nuclei, but had no effect on $H_2SO_4$

aerosol. A sulfuric acid concentration as low as 0.5 ppm resulted in the formation of a visible MEA mist (Mertens, 2014c).

### 4.1.2 Prior UT Aerosol Research

Previous research at UT Austin has focused on developing simplified heat and mass transfer models of aerosol in $CO_2$ capture processes. This is to confirm the hypothesis that altering the process operating conditions or physical design of the plant can cause aerosol to grow to a point where collection by impaction occurs within the process itself. This has been justified by research on the removal of high density aerosol in packed columns by Heidenreich (2000), Johannessen (1997), and Calvert (1984). Heidenreich found that the use of a two-stage counter-current packed column can remove high aerosol concentrations ($1E^6$ $cm^{-3}$) by increasing the temperature difference between the inlet gas and solvent.

Aerosol modeling and emission studies were conducted by Fulk in the Rochelle group at UT Austin. Emissions experiments were performed at both the bench and pilot scale. FTIR analysis was used to quantify the total amine emissions, while several generations of PDI analyzers were used for aerosol size distribution and concentration measurements. Bench-scale experiments were performed with the Aerosol Growth Column (AGC), a 1-1/2" ID absorber column with 6' of random packing. $H_2SO_4$ aerosol nuclei were generated with a Liquid Vaporizer and Injector (LVI).

The AGC was found to be capable of 90% $CO_2$ removal from a synthetic flue gas. A control and data logging system was configured in LabVIEW™ to collect temperature and inlet gas compositional data, and to control the inlet gas flow rates. Operation of the

LVI was problematic and achieved limited success; this issue has been addressed by the $SO_3$ generator outlined in Chapter 3 of this work. $CO_2$ content was found to significantly impact the aerosol size distribution, with a maximum average particle diameter and aerosol concentration existing between 0 and 10 vol %. This is due to the inlet $CO_2$ creating a supersaturated environment, resulting in heterogeneous aerosol growth. Increasing the solvent flow rate resulted in increased aerosol sizes and concentrations.

This work continues the research of Fulk through improvements to the AGC and the aerosol generation techniques. The ability to regulate the aerosol nuclei concentration enables greater control in experimental parameters, and an increase in the time allowed for experiments. This enables full testing of a greater quantity of bench-scale operating conditions.

## 4.2 EXPERIMENTAL APPARATUS

A brief overview of the Aerosol Growth Column (AGC) is presented in this section; further details and operating procedures are provided in Appendix D. The $SO_3$ generator from Chapter 3 is used to produce aerosol nuclei. The sampling configurations for the FTIR and PDI analyzers are presented as well.

### 4.2.1 Aerosol Growth Column

The AGC is designed as a batch process in order to simplify operations and the control scheme. A stripping section is not involved in the process; while this allows for ease of operation, the solvent in the system cannot be regenerated and eventually becomes saturated with $CO_2$. This requires the changing of the amine solvent for each experiment.

Figure 4.1 presents a process flow diagram of the AGC. Synthetic flue gas is fed to a presaturator, which humidifies and heats the gas to a set temperature. Aerosol nuclei are introduced to the process immediately downstream of the presaturator. The humid gas is fed to the bottom of the absorber column, where the amine solvent countercurrently contacts the gas and absorbs the $CO_2$. Outlet flue gas passes through a shell and tube condenser to knock out condensable components, and is then vented to the fume hood.

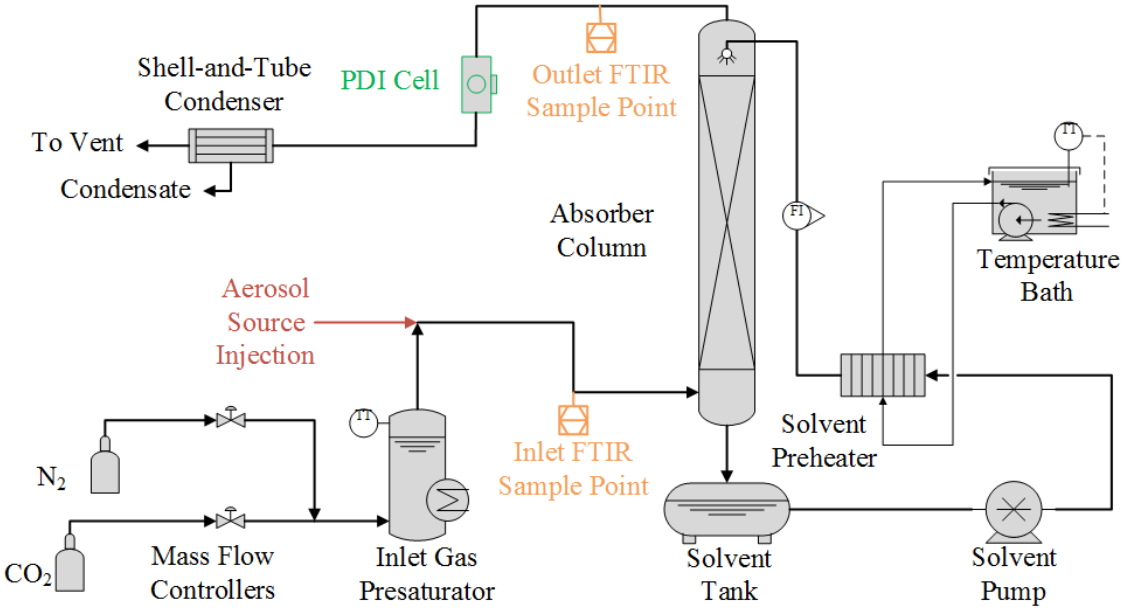


**Figure 4.1: Aerosol Growth Column process flow diagram**

The 1-1/2" ID absorber column contains 6' of random packing (RSR 0.3). The temperature profile in the absorber is measured by 6 K-type thermocouples. Additional temperature measurements are made at the presaturator, gas inlet and outlet, and solvent inlet. All temperatures are recorded in LabVIEW™.

$N_2$ flow for the process is provided from a large dewar; a manifold at the wall supplies $N_2$ for the AGC and accessory components. $CO_2$ can be obtained from the UT-

SRP storage tank or from gas cylinders. Gas flow rates are controlled through the LabVIEW™ application on the provided laptop.

Solvent for the AGC process is stored in a 16 gallon tank located underneath the $SO_3$ generator. A pump and console drive control the flow rate through the solvent loop. Solvent is heated to the desired temperature by a plate and frame exchanger that uses recirculated water on the hot side. The solvent flow rate is measured by the use of a rotameter. Solvent samples can be obtained from septa ports at two locations; upstream of the pump, or downstream of the rotameter.

Greater details on the AGC equipment and operating procedures can be found in Appendix D. A description of the design methodology and control system is provided in the dissertation by Fulk (2016).

### 4.2.2 $SO_3$ Aerosol Generation

Design and operation of the $SO_3$ aerosol generator has been outlined in Chapter 3. The 8% $SO_2$/Air mixture is stored in a gas cylinder cabinet in the walk-in fume hood. A 3-way valve at the outlet of the gas cylinder cabinet allows the user to switch between nitrogen and $SO_2$/Air flow to the $SO_3$ generator. The selected gas flows to a rotameter for flow rate regulation. After exiting the $SO_3$ generator heated catalyst bed, the gas is fed through a check valve with a set pressure of 1 psig. The gas enters the AGC column process at a location immediately after the presaturator. The check valve is in place to ensure that the humid gas from the presaturator is not allowed to enter the $SO_3$ generator catalyst bed. Water in the catalyst bed will hydrolyze the $SO_3$ to form $H_2SO_4$, and can cause corrosion and possible structural failure in the catalyst containment system.

The $SO_3$ generator furnace, exposed catalyst bed, and outlet tubing all pose burn risks while operating. The exposed end of the catalyst bed has been covered with protective insulation to partially mitigate the risk of skin contact. The $SO_3$ generator outlet tubing is left unprotected; this is by design, to allow for partial cooling of the outlet gas prior to entering the AGC system, for the purpose of reducing the risk of thermal shock on the AGC plastic components.

### 4.2.3 FTIR Sampling

FTIR sample extraction on the AGC occurs at the inlet and outlet of the absorber column. $H_2O$, $CO_2$, PZ, $NH_3$, and $SO_2$ are measured at both locations. Sample point selection is made by a heated, manual stream switching box maintained at 180 °C. Figure 4.2 presents an inside picture of the stream switching box. A pair of 3-way valves are used to select flow from each sample location. One line should be selected at a time for sampling. A needle valve inside the heated stream switching box regulates the flow to the FTIR pump. This valve is to be left open at all times.

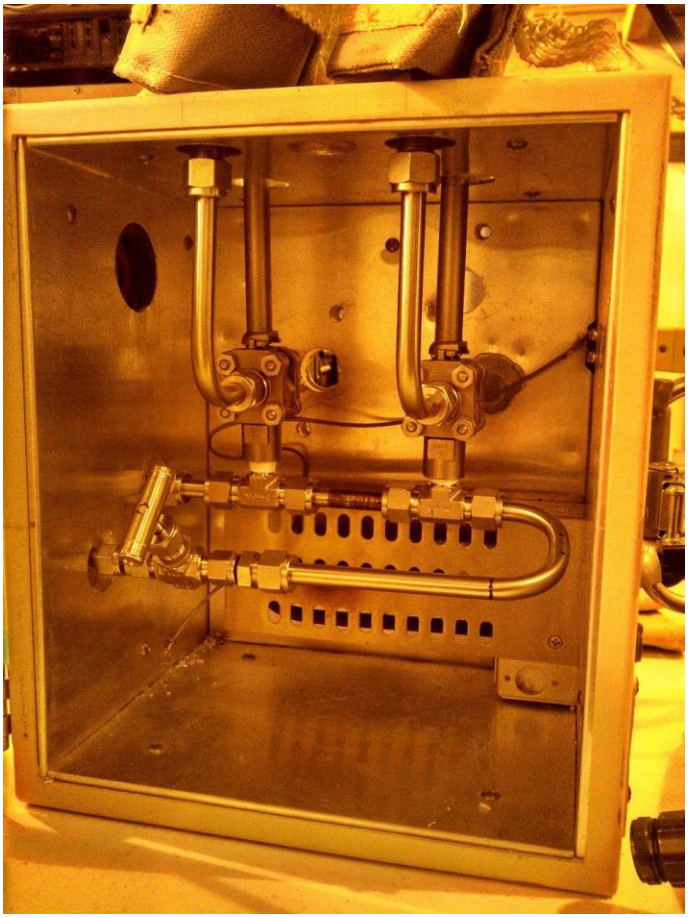

**Figure 4.2: Heated sample switching box. Heated sample lines connect at the top of the box. Flow is selected through the 3-way valves and fed to the FTIR pump.**

An $N_2$ purge is located outside the box. $N_2$ purge gas is selected for the FTIR analyzer by closing both of the sample valves and opening the needle valve for the purge gas. This is performed during background scans and when the AGC is not in use.

Samples are extracted by heated sample lines maintained at 180 °C. No sample probes are installed on the AGC; the heated sample lines connect directly to the process.

A heated jumper line connects the stream switching box with the heated filter unit in the FTIR analyzer cabinet. The FTIR cabinet is presented in Figure 4.3, and has been detailed in Chapter 2.

**Figure 4.3: FTIR analyzer cabinet**

### 4.2.4 PDI Sampling

PDI sampling can be performed at the absorber inlet or at the absorber outlet. The inlet measurement location is between the presaturator and the absorber inlet, while the outlet location is between the absorber outlet and the condenser. Typical configuration

places the PDI analyzer at the absorber outlet, as aerosol at the inlet are likely to be below the minimum size detection limit (0.1 μm) for the analyzer. A replaceable spool piece is installed at the inlet sampling location, and can be swapped with the PDI sample cell located at the absorber outlet if inlet PDI measurements are required.

The full flow rate of the AGC system is designed to pass through the PDI sample cell. This makes the system an in-site measurement technique on the bench scale, rendering the sample extraction pump unnecessary. The windows in the PDI test cell are cleared by a $N_2$ purge system, as outlined in Chapter 2. Figure 4.4 presents the PDI installed at on the AGC.

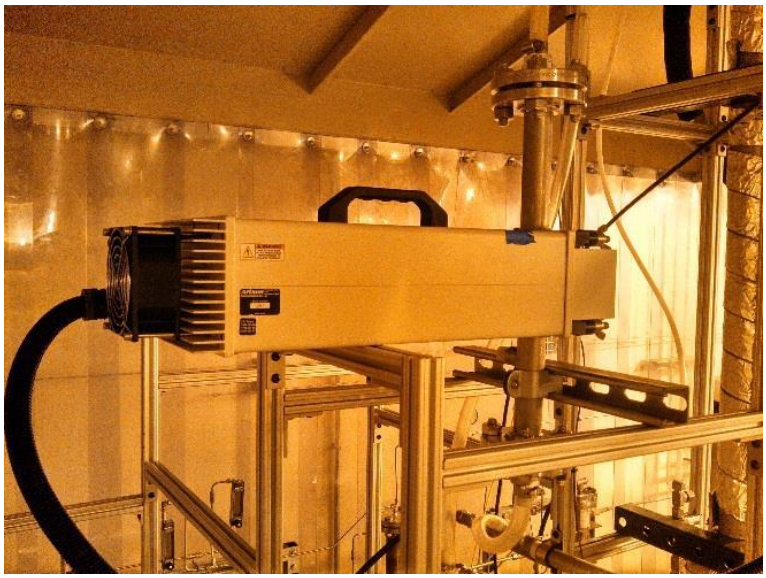

**Figure 4.4: PDI analyzer and test cell in place on AGC.**

## 4.3 EXPERIMENTAL PARAMETERS

The Aerosol Growth Column has the flexibility to run a wide range of absorber conditions. Gas and solvent temperatures, compositions, and flow rates can all be changed. The AGC can be used with a multitude of different aerosol generation sources,

which can produce differing concentrations of aerosol nuclei. The operating condition variations are discussed in this section. The justifications for each variation are presented.

### 4.3.1 Solvent Flow Rate

The solvent flow rate on the AGC can be varied between 0 and 4 liters/min. Fulk observed that the solvent flow rate has a significant impact on aerosol properties; a 2.5x increase in the solvent flow rate resulted in a 10% increase in the average particle diameter and a 69% increase in the aerosol concentration (Fulk, 2016).

The solvent flow rates were varied between set points of 0.8 to 2.4 liters/minute in the experiments conducted. Based on Fulk, the threefold increase in the solvent flow rates should be substantial enough to produce significant aerosol size and concentration variations.

### 4.3.2 Inlet $CO_2$

Research by Fulk has noted the influence of the inlet $CO_2$ on the size distribution and concentration of aerosol (Fulk, 2016). The AGC experiments conducted in this research varied the absorber inlet $CO_2$ at 3.5, 9.0, and 12.0 vol %. These conditions were chosen as the most relevant to industrial applications of amine scrubbing. Flue gas from gas-fired combined cycle power plants (e.g., NGCC) contains roughly 3.5 vol % $CO_2$. Gas-fired boilers such as those at the oil sands produce 9%. Flue gas from coal-fired power plants contains about 12.0 vol % $CO_2$.

Due to limitations on the measurement capabilities of the PDI, a total gas flow rate of 100 LPM was maintained throughout all AGC experiments in this research. As

noted in Chapter 2, laser alignment and calibration issues inhibited the measurement capabilities of the prototype PDI analyzer. In the AGC experiments presented here, the PDI was successfully tuned to operate at a gas flow rate of 100 LPM, and deviations from this flow rate could result in a misrepresentation of the measured particle size distribution and aerosol concentration.

### 4.3.3 Inlet $SO_3$

The injected aerosol nuclei concentration can play a significant role in the amine emissions. Khakharia noted that increasing the soot concentration in the inlet flue gas from 3E4 to 9E5 doubled the MEA emissions from 36 to 72 ppm, and increasing the $SO_3$ aerosol concentration at the inlet from 1.0E8 to 1.4E8 increased amine emissions from 215 to 394 ppm (Khakharia, 2013). Due to the unstable nature of the LVI used by Fulk, an accurate and repeatable measurement of the aerosol nuclei concentration in his work was not possible.

The development and construction of the catalytic $SO_3$ generator allows for precise and replicable aerosol injection rates. $SO_3$ aerosol nuclei can be generated at a wide range of rates. For the purpose of this research, aerosol concentrations of 20 and 50 ppm were desired. This is due to two factors: the limited lower range on the rotameter selected, and the resistance of the piperazine solvent to forming aerosol required an overproduction of aerosol nuclei. The calibration of the rotameter is covered in detail in Chapter 3.

### 4.3.4 Solvent $CO_2$ and Amine Content

The properties of aerosol as a function of the amine solvent composition have not been fully understood. Increasing the gas phase supersaturation for the amine is hypothesized to increase the amine aerosol emissions, through an increase in the uptake of the amine by the aerosol phase. However, this effect has mostly been achieved by changing the $CO_2$ loading in the solvent, rather than varying the amine solvent while maintaining a relatively constant $CO_2$ loading.

Solvents of 21.8 and 28.1 mass % piperazine are used in this research. These compositions provide enough variation (~22%) to impact aerosol size and concentration. In addition, the solvent amine content varied throughout experiments, due to temperature changes. The initial $CO_2$ in the solvent was close to 5.0 mass % for each amine composition, and increased with AGC run times. Khakharia observed that decreasing the solvent loading allowed more solvent to volatilize, thus increasing the amine emissions through the aerosol phase (Khakharia, 2015). Changes in the aerosol properties due to the amine content alone have yet to be quantified.

### 4.3.5 Solvent and Gas Temperatures

Variations in the solvent and gas temperatures can have a significant impact on the aerosol size and concentration. Differences in the temperatures in the gas and solvent can result in supersaturated conditions, leading to aerosol growth. Taking advantage of this growth mechanism is a method advocated by Heidenreich for aerosol removal in packed-bed columns (Heidenreich, 2000).

No experiments were performed in this work during which the inlet gas or solvent temperatures changed. Changing the gas temperature is a process that takes at least 45 minutes to reach steady state; in that time, the solvent loading has significantly changed within the AGC process. Changes in solvent temperature take a substantial amount of time as well. Variations in the solvent flow rate and inlet gas $CO_2$ composition are shown to have an effect on the temperature profile within the absorber column, and the gas outlet temperature. This allows the amine emissions and aerosol properties to be quantified in regards to changes to the absorber temperature profile and gas outlet temperature for each run.

All experiments in this research are conducted with an inlet gas temperature of 40 °C and a solvent temperature of 40 °C. Future experiments should be conducted with solvent and gas set temperatures up to 50 °C or above to further quantify the impact of temperature variations on aerosol properties.

### 4.3.6 Parametric Testing Matrix

The previous sections provide a multitude of process variations that can be tested on the AGC. The inlet $CO_2$, inlet $SO_3$, solvent flow rate, solvent composition, and solvent $CO_2$ loading are all varied in this work. As the loading is a function of $CO_2$ capture rate and time, this gives four variables that can be directly controlled and a fifth that varies with the run time. Thus, 24 different run conditions exist, as outlined in Table 4.1.

**Table 4.1: Run matrix for AGC piperazine experiments, 9/27/17 and 10/04/17**

| Run | Gas T | Solvent T | Solvent | $SO_3$ | Inlet $CO_2$ | Solvent Flow |
|---|---|---|---|---|---|---|
| *#* | *°C* | *°C* | *mass %* | *ppm* | *vol %* | *Liters/min* |
| **1** | 40 | 40 | 21.8 | 20 | 3.5 | 0.8 |
| **2** | 40 | 40 | 21.8 | 20 | 3.5 | 2.4 |
| **3** | 40 | 40 | 21.8 | 20 | 9 | 0.8 |
| **4** | 40 | 40 | 21.8 | 20 | 9 | 2.4 |
| **5** | 40 | 40 | 21.8 | 20 | 12 | 0.8 |
| **6** | 40 | 40 | 21.8 | 20 | 12 | 2.4 |
| **7** | 40 | 40 | 21.8 | 50 | 3.5 | 0.8 |
| **8** | 40 | 40 | 21.8 | 50 | 3.5 | 2.4 |
| **9** | 40 | 40 | 21.8 | 50 | 9 | 0.8 |
| **10** | 40 | 40 | 21.8 | 50 | 9 | 2.4 |
| **11** | 40 | 40 | 21.8 | 50 | 12 | 0.8 |
| **12** | 40 | 40 | 21.8 | 50 | 12 | 2.4 |
| **13** | 40 | 40 | 28.1 | 20 | 3.5 | 0.8 |
| **14** | 40 | 40 | 28.1 | 20 | 3.5 | 2.4 |
| **15** | 40 | 40 | 28.1 | 20 | 9 | 0.8 |
| **16** | 40 | 40 | 28.1 | 20 | 9 | 2.4 |
| **17** | 40 | 40 | 28.1 | 20 | 12 | 0.8 |
| **18** | 40 | 40 | 28.1 | 20 | 12 | 2.4 |
| **19** | 40 | 40 | 28.1 | 50 | 3.5 | 0.8 |
| **20** | 40 | 40 | 28.1 | 50 | 3.5 | 2.4 |
| **21** | 40 | 40 | 28.1 | 50 | 9 | 0.8 |
| **22** | 40 | 40 | 28.1 | 50 | 9 | 2.4 |
| **23** | 40 | 40 | 28.1 | 50 | 12 | 0.8 |
| **24** | 40 | 40 | 28.1 | 50 | 12 | 2.4 |

Experiments were split into two days, with a change in the solvent in between. Lower $SO_3$ (20 ppm) experiments were performed first, followed by runs at 50 ppm $SO_3$. The $CO_2$ inlet was 3.5, 9.0, and 12.0 vol %, and the solvent flow rate was varied from 0.8 to 2.4 liters per minute.

## 4.4 DATA INTERPRETATION

The following section outlines the data collection and interpretation methodologies for aerosol growth column experiments. Data from LabVIEW™, amine solvent titration, FTIR analysis, and PDI sampling are compiled to provide further insight into aerosol growth properties.

### 4.4.1 Aerosol Growth Column Temperatures and Flows

The gas and solvent temperatures and gas flow rates in the AGC are recorded through the LabVIEW™ application and can be retrieved upon ending the experiment. Upon closing LabVIEW™, follow the directory to the file save location and open the .CSV file for the run. The data log will open in Excel; this can be saved and exported as a delimited text file for processing on another computer.

The start and end times for each experiment set point are recorded in the FTIR log. These timestamps are used to identify the experiment set point start and end times in LabVIEW™ as well. The average flow rates and temperatures can be determined for each experiment. Table 4.2 presents the gas side flow rates, absorber solvent inlet temperatures, and absorber gas inlet and outlet temperatures for each experiment.

**Table 4.2: Gas flow rates, solvent inlet temperatures, and gas inlet and outlet temperatures for AGC experiments**

| Run | $N_2$ Flow | $CO_2$ Flow | Solvent In T | Gas In T | Gas Out T |
|---|---|---|---|---|---|
| *#* | *SLPM* | *SLPM* | *°C* | *°C* | *°C* |
| **1** | 96.89 | 3.50 | 38.1 | 39.1 | 37.5 |
| **2** | 96.87 | 3.50 | 36.2 | 39.3 | 35.7 |
| **3** | 91.35 | 9.01 | 39.1 | 39.5 | 39.2 |
| **4** | 91.30 | 9.07 | 38.5 | 39.8 | 38.2 |
| **5** | 88.34 | 12.02 | 39.5 | 40.0 | 40.0 |
| **6** | 88.35 | 12.02 | 39.7 | 40.2 | 39.5 |
| **7** | 96.88 | 3.50 | 39.7 | 40.5 | 39.4 |
| **8** | 96.69 | 3.66 | 39.9 | 40.6 | 39.3 |
| **9** | 91.35 | 9.01 | 39.7 | 40.8 | 39.8 |
| **10** | 91.36 | 8.91 | 40.1 | 41.0 | 39.8 |
| **11** | 88.34 | 12.01 | 39.8 | 41.4 | 40.0 |
| **12** | 88.36 | 12.02 | 40.5 | 41.7 | 40.2 |
| **13** | 96.88 | 3.50 | 37.5 | 40.5 | 36.5 |
| **14** | 96.87 | 3.50 | 34.4 | 41.0 | 34.0 |
| **15** | 91.35 | 9.00 | 38.6 | 39.4 | 39.0 |
| **16** | 91.35 | 7.73 | 37.7 | 38.6 | 37.4 |
| **17** | 88.34 | 11.71 | 39.1 | 37.5 | 39.6 |
| **18** | 88.34 | 11.39 | 39.3 | 36.7 | 39.2 |
| **19** | 96.87 | 3.50 | 39.4 | 35.7 | 39.0 |
| **20** | 96.72 | 3.62 | 39.2 | 35.3 | 38.7 |
| **21** | 91.35 | 9.01 | 39.3 | 34.9 | 39.5 |
| **22** | 91.27 | 9.04 | 39.4 | 34.4 | 39.2 |
| **23** | 88.35 | 12.00 | 39.4 | 34.2 | 39.7 |
| **24** | 88.34 | 11.79 | 39.7 | 34.2 | 39.6 |

The AGC absorber temperature profile is determined by six K-type thermocouples located equidistantly within the column. These are useful for determining the highest temperature location in the column, which can indicate the presence of a temperature bulge. Table 4.3 presents the average temperatures at each thermocouple in the AGC absorber for each run condition. The $T_{max}$ column in Table 4.3 indicates the stage with the highest temperature, or the location of the absorber temperature bulge.

**Table 4.3: Average column temperature by location for AGC experiments. $T_{max}$ indicates the stage with the highest temperature. T6 is the bottom of the column, and T1 is the top.**

| Run | T6 | T5 | T4 | T3 | T2 | T1 | $T_{max}$ Stage |
|---|---|---|---|---|---|---|---|
| # | °C | °C | °C | °C | °C | °C | Stage |
| **1** | 40.2 | 39.6 | 40.3 | 40.2 | 39.6 | 38.9 | 4 |
| **2** | 37.7 | 36.8 | 37.0 | 36.6 | 36.3 | 36.0 | 6 |
| **3** | 42.3 | 42.6 | 43.1 | 43.2 | 42.9 | 41.7 | 3 |
| **4** | 40.8 | 40.3 | 40.7 | 40.0 | 39.5 | 39.0 | 6 |
| **5** | 42.7 | 42.6 | 43.4 | 43.5 | 43.1 | 42.1 | 3 |
| **6** | 42.0 | 41.6 | 42.0 | 41.4 | 40.9 | 40.4 | 4 |
| **7** | 41.4 | 40.7 | 41.1 | 41.0 | 40.7 | 40.2 | 6 |
| **8** | 40.7 | 40.2 | 40.4 | 40.1 | 39.9 | 39.7 | 6 |
| **9** | 42.5 | 42.0 | 42.5 | 42.5 | 42.0 | 41.3 | 4 |
| **10** | 41.8 | 41.4 | 41.6 | 41.2 | 40.8 | 40.5 | 6 |
| **11** | 42.5 | 42.2 | 42.6 | 42.6 | 42.2 | 41.5 | 4 |
| **12** | 42.2 | 41.7 | 42.0 | 41.6 | 41.3 | 40.9 | 6 |
| **13** | 40.0 | 39.1 | 40.5 | 40.1 | 39.5 | 38.6 | 4 |
| **14** | 36.8 | 35.5 | 36.0 | 35.5 | 35.0 | 34.7 | 6 |
| **15** | 41.6 | 42.9 | 44.2 | 43.8 | 44.0 | 41.8 | 4 |
| **16** | 39.4 | 39.1 | 39.7 | 39.1 | 38.6 | 38.2 | 3 |
| **17** | 41.0 | 42.2 | 43.1 | 43.5 | 42.6 | 42.0 | 3 |
| **18** | 40.9 | 41.2 | 41.8 | 41.4 | 40.7 | 40.3 | 4 |
| **19** | 38.0 | 40.1 | 40.5 | 40.6 | 40.4 | 40.0 | 3 |
| **20** | 38.8 | 39.5 | 39.8 | 39.6 | 39.3 | 39.1 | 4 |
| **21** | 36.8 | 41.4 | 41.7 | 42.1 | 41.8 | 41.2 | 3 |

| | | | | | | | |
|---|---|---|---|---|---|---|---|
| **22** | 39.8 | 40.7 | 41.1 | 40.9 | 40.4 | 40.1 | 4 |
| **23** | 36.8 | 41.6 | 41.6 | 42.2 | 41.9 | 41.4 | 3 |
| **24** | 40.3 | 41.1 | 41.6 | 41.3 | 40.8 | 40.4 | 4 |

The even-numbered (shaded) runs use a solvent flow rate of 2.4 lpm, while the odd-numbered (unshaded) runs use 0.8 lpm. Run conditions are paired off in consecutive numbers. Runs 1 and 2 have identical conditions, except for an increase in the solvent flow rate from 0.8 to 2.4 lpm. The inlet $CO_2$ composition is changed every other run (From Run 1 to Run 3). $SO_3$ flow is changed on the 7$^{th}$, 12$^{th}$, and 18$^{th}$ runs. In Table 4.3, the runs with high solvent flow rates show the presence of the temperature bulge at lower column locations than the lower solvent flow runs. The maximum temperature is also greater with the low solvent flow. An increased solvent flow rate lowers the column temperature and pushes the temperature bulge lower down the column. The temperature bulge location can significantly impact aerosol properties due to gas phase supersaturation.

### 4.4.2 Determination of Solvent Amine and $CO_2$ Content

The solvent amine and $CO_2$ content are determined prior to beginning each day through titration methods outlined in Appendix D. Solvent samples are also taken at the middle and end of each day. For these experiments, solvent samples were obtained prior to run 1, during runs 6 and 12, prior to run 13, and during runs 18 and 24.

The solvent amine content and $CO_2$ loading are interpolated for each run condition where solvent samples were not obtained. The solvent amine dilutes slightly as a function of experiment run time. The $CO_2$ loading in the solvent is dependent on the

run length and the $CO_2$ absorption rate; the loading will increase at a faster rate when the time spent at higher capture rate increases. Table 4.4 presents the solvent amine and $CO_2$ content for each run. The line between runs 12 and 13 indicates switching to a higher concentration of amine solvent.

**Table 4.4: Solvent amine and $CO_2$ content for each AGC run condition. The values in shaded rows were determined through titrations, while unshaded row values were interpolated with respect to time and $CO_2$ absorption.**

| Run | PZ | $CO_2$ |
|---|---|---|
| *#* | *Mass %* | *Mass %* |
| **1** | 21.79 | 5.08 |
| **2** | 21.77 | 5.33 |
| **3** | 21.75 | 5.62 |
| **4** | 21.74 | 6.01 |
| **5** | 21.73 | 6.25 |
| **6** | 21.72 | 6.62 |
| **7** | 21.65 | 6.88 |
| **8** | 21.63 | 6.94 |
| **9** | 21.60 | 7.07 |
| **10** | 21.56 | 7.31 |
| **11** | 21.53 | 7.42 |
| **12** | 21.52 | 7.43 |
| **13** | 28.12 | 4.96 |
| **14** | 27.65 | 5.10 |
| **15** | 27.50 | 5.19 |
| **16** | 27.20 | 5.44 |
| **17** | 26.99 | 5.57 |
| **18** | 26.78 | 5.78 |
| **19** | 26.65 | 6.10 |
| **20** | 26.60 | 6.19 |
| **21** | 26.53 | 6.33 |
| **22** | 26.48 | 6.53 |
| **23** | 26.40 | 6.64 |
| **24** | 26.37 | 6.74 |

The solvent steadily increases in $CO_2$ content throughout operation, due to the absence of a regeneration section in the AGC system. As the solvent $CO_2$ increases, the amount of free piperazine available for condensation into the aerosol phase decreases. In theory, the amine aerosol emissions should decrease as the experiment run time increases. However, this is counteracted by other experimental factors, such as increasing the $SO_3$ aerosol nuclei concentration, varying the $CO_2$ in the inlet gas, and changes to the amine solvent flow rate.

The amine concentration can be represented by either weight percent or molality. 21.8 wt % piperazine gives a molality of roughly 3 m, and 28.1 % piperazine corresponds with a molality of approximately 5 m. Both methods of reporting piperazine content are used interchangeably in this work.

### 4.4.3 FTIR Measurements

FTIR data was retrieved at the end of each experimental day. Follow the directory path to the save location; the file to retrieve is a delimited text file named "RESULTS". The directory path can be found in Calcmet™ by selecting "Options" in the menu bar and clicking "Autosaving"; the popup window presents the save directory path. A log of the experiment should be recorded on the FTIR analyzer computer. A simple notepad file with time stamps of process set point changes is invaluable during data processing.

The delimited results file contains time-stamped values from the FTIR analyzer and was processed in Excel. The values of most significance are the concentrations of the analyzed components. Figure 4.5 presents an example of processed data from the

FTIR results. This snippet is from runs 19 and 20. The absorber inlet was sampled first, to confirm the $CO_2$ content in the inlet. The absorber outlet was sampled next for Run 19; once steady state was achieved and a PDI sample run completed, the run conditions were changed for Run 20. As only the solvent flow rate was changed, the inlet was not sampled again. Steady state was achieved and PDI sampling was performed.

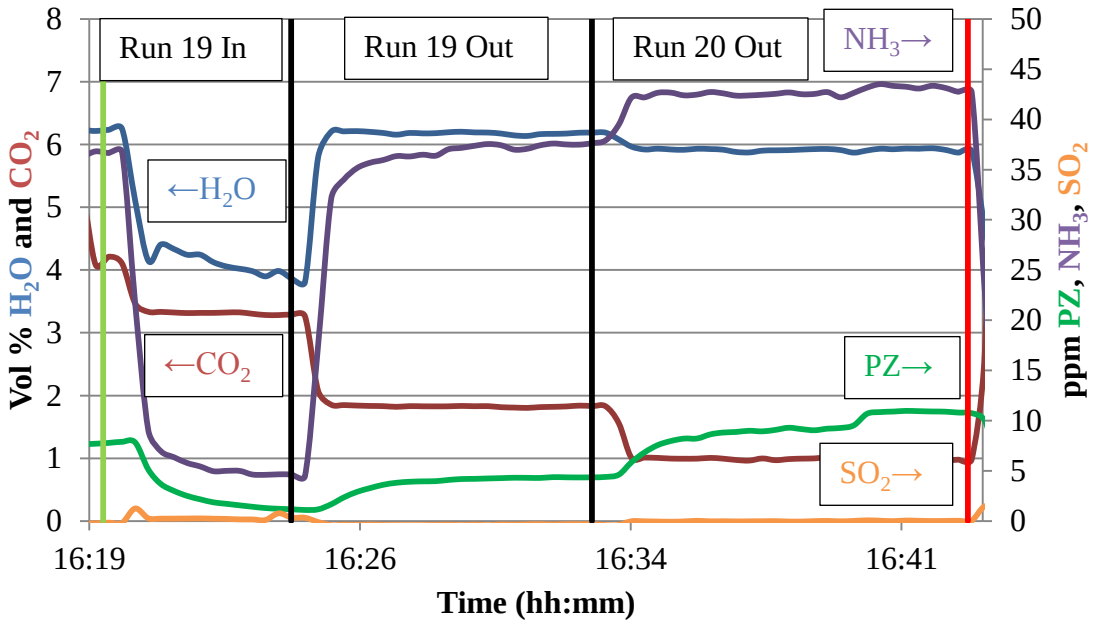


**Figure 4.5: FTIR results for Runs 19 and 20. The green vertical line indicates sampling at the absorber inlet. The first black vertical line indicates sampling for Run 19 at the outlet, and the second black vertical line indicates Run 20 outlet. The red vertical line indicates changing conditions from Run 20.**

The inlet flue gas contains approximately 3.3 % $CO_2$. In Run 19, the absorber column reduces the $CO_2$ to 1.8%. Amine solvent is emitted through the aerosol phase at

4.4 ppm. The solvent flow rate is increased to 2.4 lpm for Run 20. This reduces the outlet $CO_2$ to 1.0 %, while causing the piperazine emissions to increase to 10.9 ppm.

FTIR analysis was also used to determine the conversion rate of the $SO_3$ generator. Flow rates through the $SO_3$ generator were calibrated with the rotameter and FTIR while the furnace is off; 15 mL/min through the generator produced 20 ppm of $SO_2$, and 37.5 mL/min produced 50 ppm. When the $SO_3$ generator catalyst bed was heated, the same flow rates were repeated. The amount of $SO_2$ detected by FTIR analysis is the unconverted amount of $SO_2$, and the $SO_3$ generator conversion rate can be determined. Runs 1–6 and 13–18 used 20 ppm of $SO_3$ in the inlet flue gas, and Runs 7–12 and 18–24 used 50 ppm.

Table 4.5 presents the tabulated FTIR results for each run condition. The $CO_2$ inlet and outlet compositions are given, and the resulting $CO_2$ capture rate is calculated. The $SO_2$ is used to provide the $SO_3$ conversion rate and $SO_3$ inlet. The piperazine and ammonia content at the AGC absorber outlet are also given.

**Table 4.5: FTIR results for each AGC run**

| Run | $CO_2$ In | $CO_2$ Out | $CO_2$ Capture | $SO_2$ In | $SO_3$ In | $SO_2$ Conversion | PZ Out | $NH_3$ Out |
|---|---|---|---|---|---|---|---|---|
| *#* | *vol %* | *vol %* | *%* | *ppm* | *ppm* | *%* | *ppm* | *ppm* |
| **1** | 3.24 | 1.50 | 53.7 | 0.0 | 20.0 | 100.0 | 0.0 | 32.5 |
| **2** | 3.24 | 0.72 | 77.8 | 0.0 | 20.0 | 100.0 | 0.0 | 58.6 |
| **3** | 9.20 | 5.35 | 41.8 | 0.0 | 20.0 | 100.0 | 0.0 | 31.4 |
| **4** | 9.20 | 2.78 | 69.8 | 0.0 | 20.0 | 100.0 | 0.1 | 49.0 |
| **5** | 12.42 | 8.98 | 27.7 | 0.0 | 20.0 | 100.0 | 0.0 | 22.3 |
| **6** | 12.42 | 5.44 | 56.2 | 0.0 | 20.0 | 100.0 | 0.1 | 39.1 |
| **7** | 3.27 | 2.13 | 34.8 | 0.0 | 50.0 | 100.0 | 0.0 | 31.3 |
| **8** | 3.27 | 1.50 | 54.1 | 0.0 | 50.0 | 100.0 | 0.1 | 44.4 |
| **9** | 9.26 | 6.28 | 32.2 | 0.0 | 50.0 | 100.0 | 0.1 | 25.9 |
| **10** | 9.26 | 3.85 | 58.4 | 0.0 | 50.0 | 100.0 | 0.2 | 35.7 |
| **11** | 11.91 | 9.56 | 19.7 | 0.0 | 50.0 | 100.0 | 0.3 | 22.7 |
| **12** | 11.91 | 6.56 | 44.9 | 0.0 | 50.0 | 100.0 | 0.4 | 28.5 |
| **13** | 3.01 | 1.12 | 62.8 | 0.0 | 20.0 | 100.0 | 0.8 | 0.7 |
| **14** | 3.01 | 0.95 | 68.5 | 0.0 | 20.0 | 100.0 | 1.2 | 0.5 |
| **15** | 9.23 | 4.08 | 55.8 | 0.0 | 20.0 | 100.0 | 0.5 | 18.7 |
| **16** | 9.23 | 2.53 | 72.6 | 0.0 | 20.0 | 100.0 | 7.4 | 43.7 |
| **17** | 12.52 | 7.29 | 41.8 | 0.1 | 19.9 | 99.7 | 1.4 | 19.2 |
| **18** | 12.52 | 3.90 | 68.8 | 0.1 | 19.9 | 99.7 | 7.0 | 37.7 |
| **19** | 3.32 | 1.83 | 44.9 | 0.3 | 49.7 | 99.3 | 3.9 | 36.5 |
| **20** | 3.32 | 1.00 | 70.0 | 0.3 | 49.7 | 99.3 | 9.3 | 42.7 |
| **21** | 9.37 | 5.84 | 37.7 | 0.9 | 49.1 | 98.1 | 1.2 | 23.1 |
| **22** | 9.37 | 3.36 | 64.2 | 0.9 | 49.1 | 98.1 | 4.2 | 34.8 |
| **23** | 11.49 | 9.27 | 19.3 | 1.1 | 48.9 | 97.8 | 1.3 | 20.4 |
| **24** | 11.49 | 5.92 | 48.5 | 1.1 | 48.9 | 97.8 | 2.2 | 26.5 |

$CO_2$ capture ranged from 19.3% to 77.8%. The $SO_3$ generator provided excellent conversion in excess of 97% for each run. Piperazine emissions were lower than expected; emissions were minimal with the first 12 conditions using the 21.8 wt % solvent and slightly higher with the last 12 runs utilizing the 28.1 wt % piperazine. Both ammonia and piperazine emissions were higher for runs that utilize higher solvent flow rates, in the shaded rows.

### 4.4.4 PDI Measurements

Every PDI sampling run produced 29 different Excel files, each containing a certain category of data. The AGC experiments in this chapter utilize the Excel files labeled "Count_Diameter", "Diameter Counts Total", "Number Density", "SNR_Frequency_Pass", and "Start_Time". The "Count_Diameter" gives the particle size distribution of the measured aerosol. "Diameter Counts Total" provides the total number of aerosol that were quantified. This is useful for normalizing the aerosol count diameter. "Number_Density" gives the measured aerosol concentration per $cm^3$. "SNR_Frequency_Pass" gives the rate at which measured aerosol exceed the signal-to-noise ratio; above 60% is adequate for AGC aerosol measurement. "Start_Time" gives the start time of the PDI sample run, and is used to link the PDI data to other AGC process data. The directory paths to these files can be found by opening AIMS and selecting "Data Library" on the left-hand menu.

Upon completing a sample run in AIMS, the particle size distribution for the sampled aerosol will appear under the "PDI Statistics" tab in the "Results" left-hand menu in AIMS. The "Count_Diameter" file for each sample run can be plotted to

replicate the particle size distribution in Excel. This is presented in Figure 4.6, for AGC run condition 11.

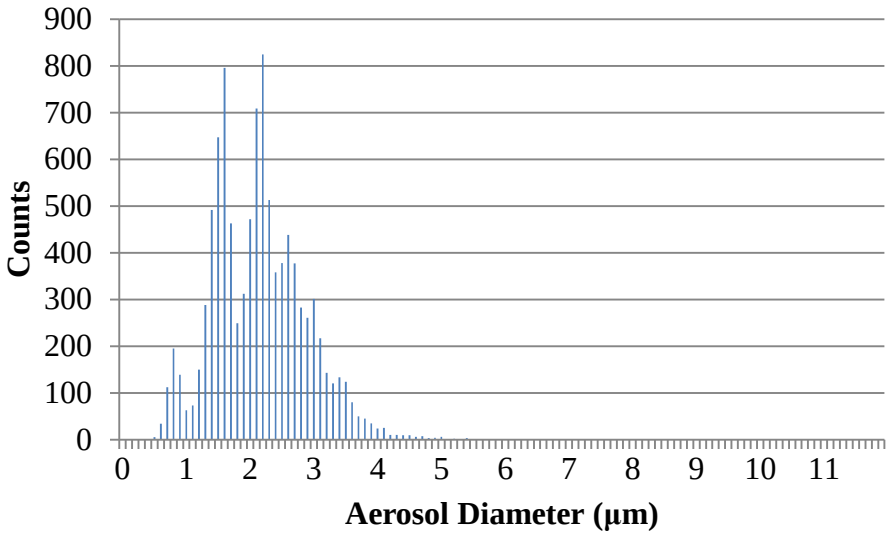


**Figure 4.6: Aerosol size distribution for AGC Run 11**

Each PDI sample run quantifies a varying amount of aerosol, up to 10,000 per run. Since the measured aerosol count will vary from run to run, the particle size distribution for each sample run must be normalized by the "Diameter Counts Total" value in order to compare particle size distributions between sample runs.

Statistical analysis methods were used in Excel to quantify the particle size distributions for each sample run. The mean, median, and mode aerosol diameters were quantified and are tabulated in Table 4.6. The mean is the calculated average aerosol diameter for the sampled aerosol. The median value is the midpoint of the range of the sampled aerosol, and the mode is the peak aerosol diameter, which is the aerosol diameter most observed by the PDI. The standard deviation gives the shape of the particle size

distribution; a higher standard deviation indicates that the aerosol size distribution has a wider shape, and in this case, is more likely to contain larger aerosol.

**Table 4.6: Statistical analyses for AGC aerosol size distributions**

| Run | Count | Mean | Median | Mode | Standard Deviation | Standard Error |
|---|---|---|---|---|---|---|
| # | # | $\mu m$ | $\mu m$ | $\mu m$ | $\mu m$ | $\mu m$ |
| **1** | 2955 | 1.64 | 1.7 | 1.7 | 0.489 | 0.009 |
| **2** | 4155 | 1.80 | 1.7 | 1.7 | 0.768 | 0.012 |
| **3** | 1153 | 1.72 | 1.7 | 1.7 | 0.650 | 0.019 |
| **4** | 3432 | 1.72 | 1.6 | 1.7 | 0.865 | 0.015 |
| **5** | 564 | 1.86 | 1.7 | 1.6 | 0.784 | 0.033 |
| **6** | 1955 | 1.93 | 1.7 | 0.9 | 1.122 | 0.025 |
| **7** | 1617 | 1.50 | 1.5 | 1.7 | 0.577 | 0.014 |
| **8** | 3544 | 1.69 | 1.6 | 0.9 | 0.898 | 0.015 |
| **9** | 6856 | 1.79 | 1.7 | 1.7 | 0.585 | 0.007 |
| **10** | 8757 | 1.74 | 1.7 | 1.7 | 0.704 | 0.008 |
| **11** | 10002 | 2.24 | 2.2 | 2.3 | 0.724 | 0.007 |
| **12** | 7124 | 1.97 | 1.8 | 1.7 | 0.740 | 0.009 |
| **13** | 1650 | 2.06 | 2.0 | 1.7 | 0.624 | 0.015 |
| **14** | 1246 | 1.77 | 1.6 | 1.6 | 0.797 | 0.023 |
| **15** | 3412 | 2.04 | 2.0 | 2.3 | 0.598 | 0.010 |
| **16** | 4506 | 1.78 | 1.7 | 1.7 | 0.567 | 0.008 |
| **17** | 2845 | 1.98 | 1.8 | 1.7 | 0.619 | 0.012 |
| **18** | 4111 | 1.73 | 1.7 | 1.7 | 0.578 | 0.009 |
| **19** | 6604 | 2.24 | 2.2 | 2.2 | 0.600 | 0.007 |
| **20** | 5556 | 2.07 | 2.1 | 2.2 | 0.561 | 0.008 |
| **21** | 5110 | 2.18 | 2.2 | 1.7 | 0.684 | 0.010 |
| **22** | 5399 | 1.90 | 1.8 | 1.7 | 0.570 | 0.008 |
| **23** | 5508 | 2.27 | 2.2 | 2.2 | 0.719 | 0.010 |
| **24** | 4914 | 1.88 | 1.7 | 1.7 | 0.627 | 0.009 |

Amine emission rates are heavily dependent on the volumes of the aerosol emitted. Doubling the diameter of an aerosol drop increases the contained volume by a

factor of eight. Aerosol diameter distributions are translated into volume distributions through Excel. Once normalized, the particle volume distributions are presented in cumulative volume distribution plots. Cumulative volume distributions give the fraction of aerosol at or below a certain volume as a function of the measured aerosol diameter. For example, for Run 11, 50% of the total emitted aerosol volume comes from aerosol drops that were smaller than 2.8 μm in diameter. Figure 4.7 gives a cumulative volume distribution plot comparing Runs 11 and 12.

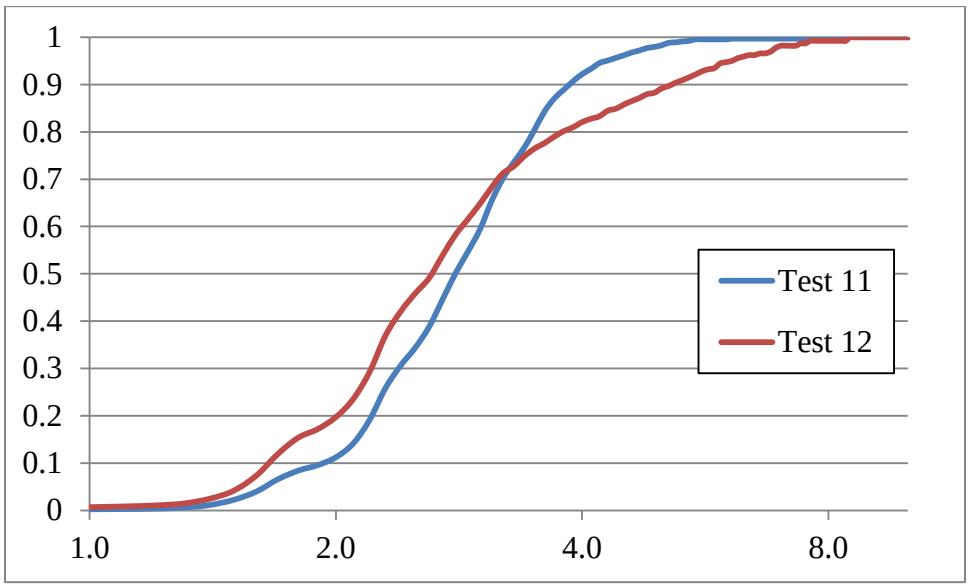


**Figure 4.7: Cumulative volume distribution comparison of AGC Runs 11 and 12**

Table 4.7 summarizes the PDI measurements and processed data for each of the 24 AGC runs. The aerosol concentration (in #/cm$^3$) is provided by the "Number_Density" file from AIMS, while the SNR column is from the "SNR_Frequency_Pass" AIMS file. The median aerosol diameter, 50% diameter cutoff, and 50% volume cutoff were calculated values. The 50% diameter cutoff represents

where 50% of the emitted aerosol have diameters below the given diameter, and the 50% volume cutoff represents where 50% of the emitted aerosol have volumes below the corresponding diameter. The 50% volume cutoff number is important due to the aforementioned impact of aerosol volumes on the amine emissions.

**Table 4.7: Summary of PDI measurements for AGC experiments**

| Run | Aerosol Concentration | SNR Pass Rate | Median Aerosol Diameter | 50% Diameter Cutoff | 50% Volume Cutoff |
|---|---|---|---|---|---|
| *#* | *# $cm^{-3}$* | *%* | *µm* | *µm* | *µm* |
| **1** | 23631 | 65.74 | 1.7 | 1.6 | 1.9 |
| **2** | 32069 | 68.07 | 1.7 | 1.6 | 2.8 |
| **3** | 9040 | 67.62 | 1.7 | 1.6 | 2.3 |
| **4** | 27342 | 68.41 | 1.7 | 1.6 | 3.2 |
| **5** | 4344 | 67.40 | 1.6 | 1.7 | 2.7 |
| **6** | 16129 | 70.52 | 0.9 | 1.6 | 3.8 |
| **7** | 13129 | 67.03 | 1.7 | 1.5 | 2.0 |
| **8** | 27107 | 67.73 | 0.9 | 1.5 | 3.3 |
| **9** | 51234 | 69.08 | 1.7 | 1.7 | 2.2 |
| **10** | 65165 | 68.86 | 1.7 | 1.6 | 2.4 |
| **11** | 70507 | 72.02 | 2.3 | 2.2 | 2.8 |
| **12** | 47164 | 70.34 | 1.7 | 1.8 | 2.6 |
| **13** | 13578 | 64.17 | 1.7 | 1.9 | 2.5 |
| **14** | 12656 | 60.44 | 1.6 | 1.6 | 3.1 |
| **15** | 28760 | 67.00 | 2.3 | 2.0 | 2.4 |
| **16** | 51869 | 62.88 | 1.7 | 1.6 | 2.2 |
| **17** | 23408 | 65.39 | 1.7 | 1.8 | 2.4 |
| **18** | 51821 | 64.32 | 1.7 | 1.6 | 2.2 |
| **19** | 53961 | 68.25 | 2.2 | 2.2 | 2.6 |
| **20** | 53176 | 66.37 | 2.2 | 2.0 | 2.4 |
| **21** | 47122 | 66.53 | 1.7 | 2.1 | 2.7 |
| **22** | 50040 | 64.55 | 1.7 | 1.7 | 2.2 |
| **23** | 49214 | 69.06 | 2.2 | 2.2 | 2.8 |
| **24** | 47369 | 64.13 | 1.7 | 1.7 | 2.3 |

Aerosol concentration ranged from 4,344 to 70,507 $cm^{-3}$. These values are much lower than expected, as aerosol measurements at pilot plants have found concentrations typically in the range of 10E6 $cm^{-3}$. Signal-to-noise ratios were maintained at values greater than 60% for all PDI sample runs. Median aerosol diameters ranged from 0.9 to 2.3 µm. The 50% diameter cutoff varied between 1.5 and 2.2 µm, while the 50% volume cutoff ranged from 1.9 to 3.8 µm.

## 4.5 RESULTS

The following sections outline the impacts of process conditions on the aerosol properties. The amine emissions, mean aerosol diameter, aerosol 50% volume cutoff diameter, and aerosol concentration are examined.

Scatter plots were generated for each aerosol property with respect to variable process conditions. The variable process conditions include the solvent $CO_2$ and piperazine compositions, gas outlet temperatures, and the temperature bulge stage.

The data points on the scatter plots are colored, shaped, and filled to represent different set conditions. The data point fill represents the solvent flow rate: high flow rates (2.4 liters/min) have no fill (○), while low solvent flow rates (0.8 liters/min) are filled (●). Color corresponds with the inlet $CO_2$: **Red** for 3.5 vol % $CO_2$, **blue** for 9 vol %, and **green** for 12 vol %. The data point shape indicates the inlet $SO_3$: a diamond (◊) represents the high $SO_3$ at 50 ppm, while a square (□) data point is for runs with inlet $SO_3$ at 20 ppm. For example, a data point that appears as a filled blue square (■) represents a run with low solvent flow rate, 9 vol % inlet $CO_2$, and low (20 ppm) inlet $SO_3$.

### 4.5.1 FTIR Measured Amine Emissions

FTIR sampling determines the amine in the flue gas leaving the AGC outlet. These averaged values for each run are listed in Table 4.5 under the 'PZ Out' column. Figure 4.8 presents the piperazine emissions for each run as a function of the solvent $CO_2$ composition.

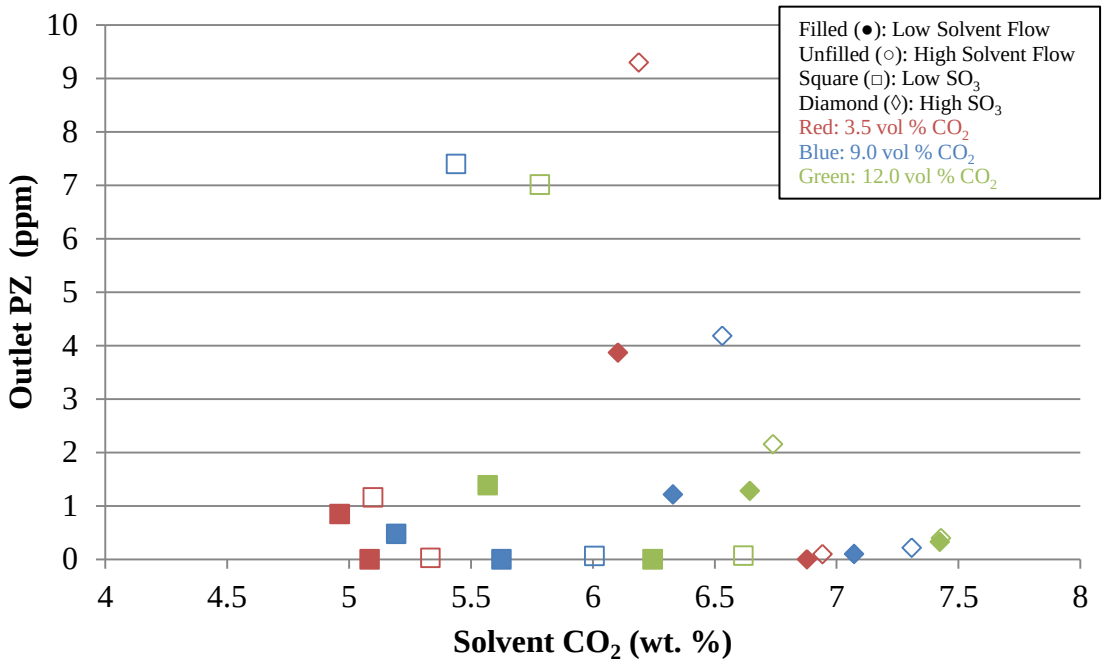


**Figure 4.8: Piperazine emissions as a function of solvent $CO_2$ content**

Most piperazine emissions were below 2 ppm, due in part to the very low aerosol concentrations. Out of the 6 runs with piperazine emissions greater than 2 ppm, 5 utilized a high solvent flow rate (2.4 liters/min), as indicated by the unfilled data markers (□). However, there is no discernible trend relating the solvent $CO_2$ content with the outlet piperazine emissions.

Figure 4.9 is similar to Figure 4.8, but presents the outlet amine emissions as a function of the solvent piperazine content for each run.

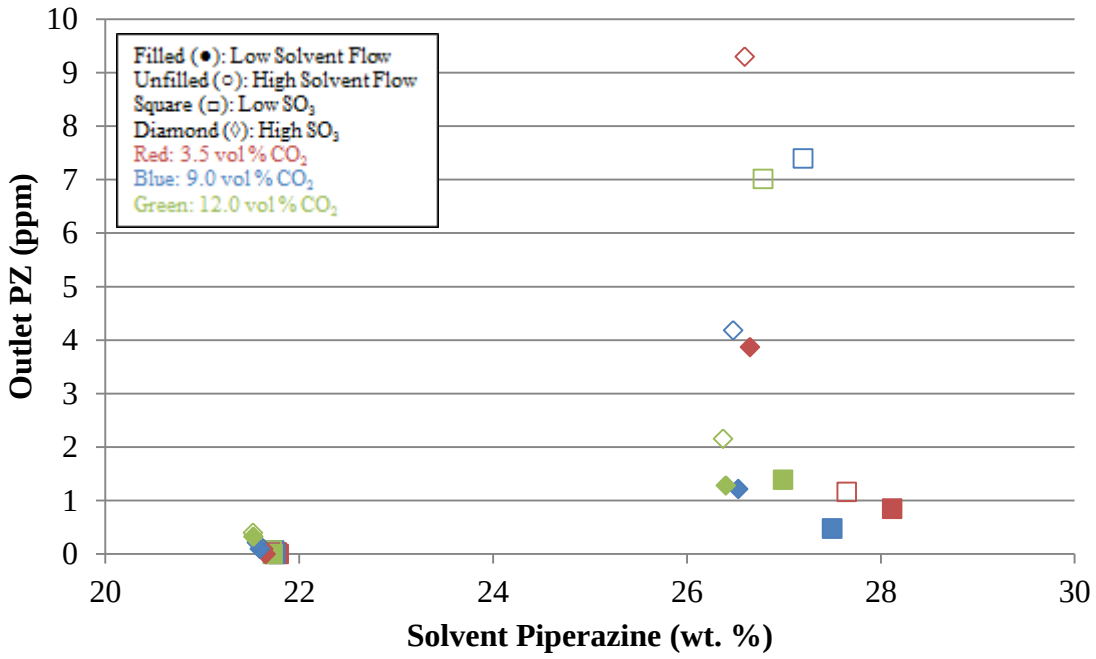


**Figure 4.9: Piperazine emissions as a function of solvent piperazine content**

The runs conducted with less amine in the solvent (3 m) never emitted more than 1 ppm of piperazine. Amine emissions increased substantially for runs using the 5 m piperazine solvent; this indicates that the solvent amine content is a critical factor in the amine emissions. Further evidence to support this is given in Chapter 5 of this work.

Figure 4.10 presents the piperazine emissions as a function of the AGC absorber gas outlet temperature.

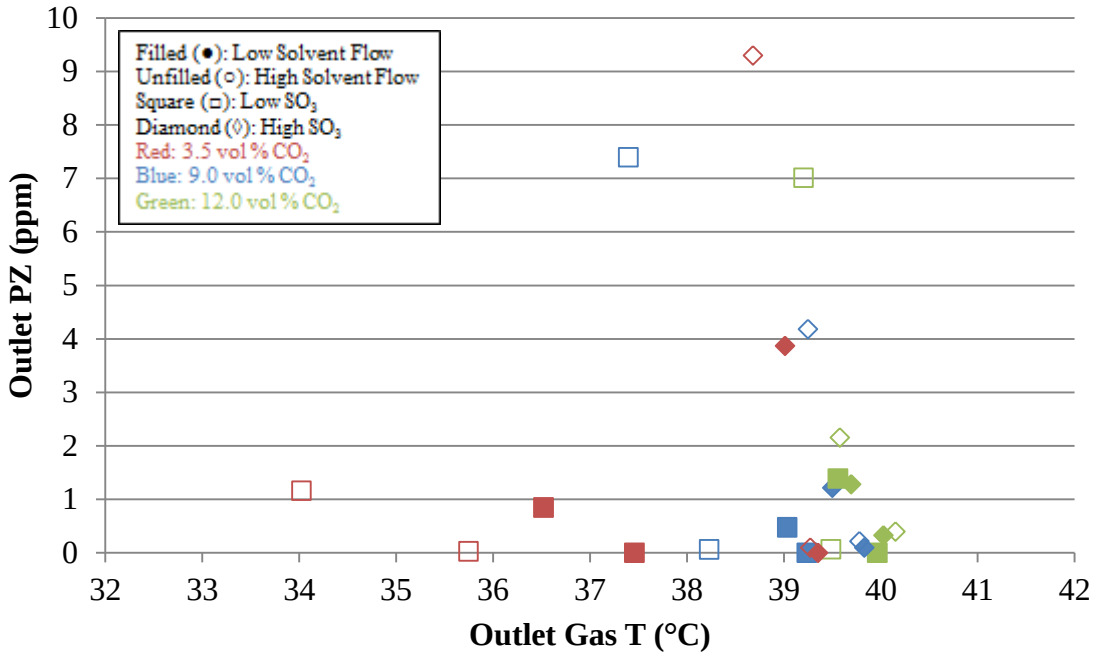


**Figure 4.10: Piperazine emissions as a function of AGC gas outlet temperature**

Higher inlet $CO_2$ (color) tend to correlate with a higher outlet gas temperature. 12 vol % inlet $CO_2$ results in gas outlet temperatures between 39 and 40 °C, while 3.5 vol % $CO_2$ gives anywhere from 34 to 39 °C. This is partly due to the location of the temperature bulge within the column, which is represented in Figure 4.11 in relation to the amine emissions for each run.

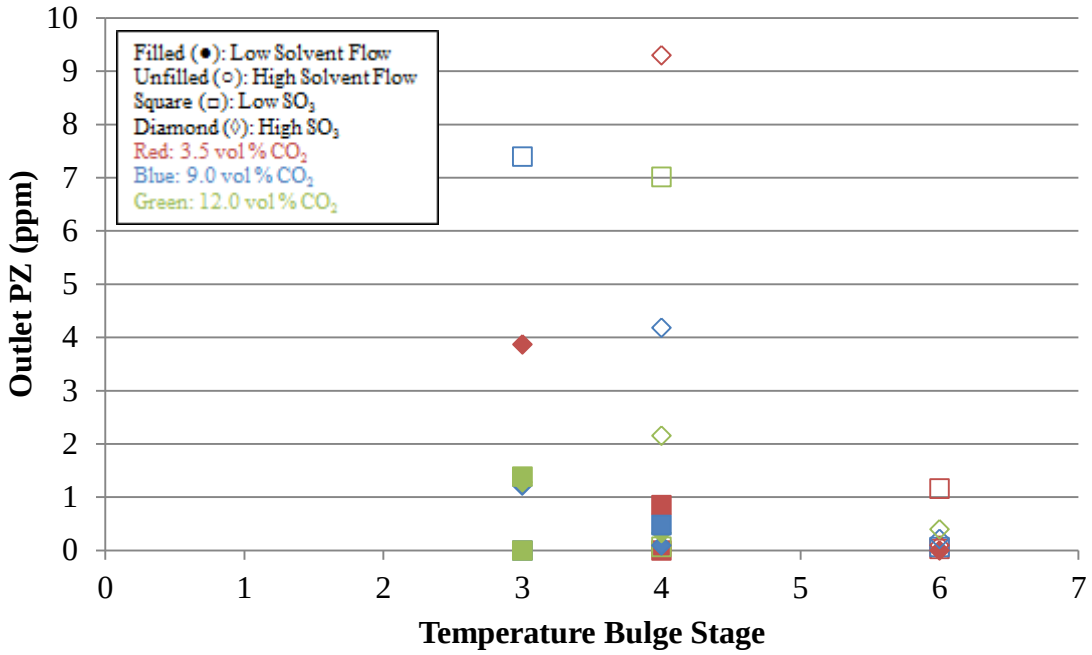


**Figure 4.11: Piperazine emissions as a function of AGC temperature bulge stage location. Higher stages correspond to a location lower in the column.**

Temperature bulges at lower column stages correspond with reductions in amine emissions. Temperature bulges typically occurred at the 4$^{th}$ stage of the AGC, and resulted in amine emissions between 0 and 9.3 ppm. Lowering the location of the temperature bulge to the 6$^{th}$ stage resulted in amine emissions between 0 and 1.2 ppm.

Overall, the AGC gas outlet amine was found to be impacted by the solvent flow rate, solvent piperazine content, and temperature bulge location. Increasing the solvent flow rate and the solvent piperazine composition increased the amine emissions. Lowering the stage of the temperature bulge decreased the amine in the absorber gas outlet.

### 4.5.2 Mean Aerosol Diameter

The mean aerosol diameter is the average size of the aerosol that exit the AGC absorber. These values for each run are given in Table 4.6, under the 'Mean' column. Figure 4.12 presents the mean aerosol diameter for each run as a function of the solvent $CO_2$ composition.

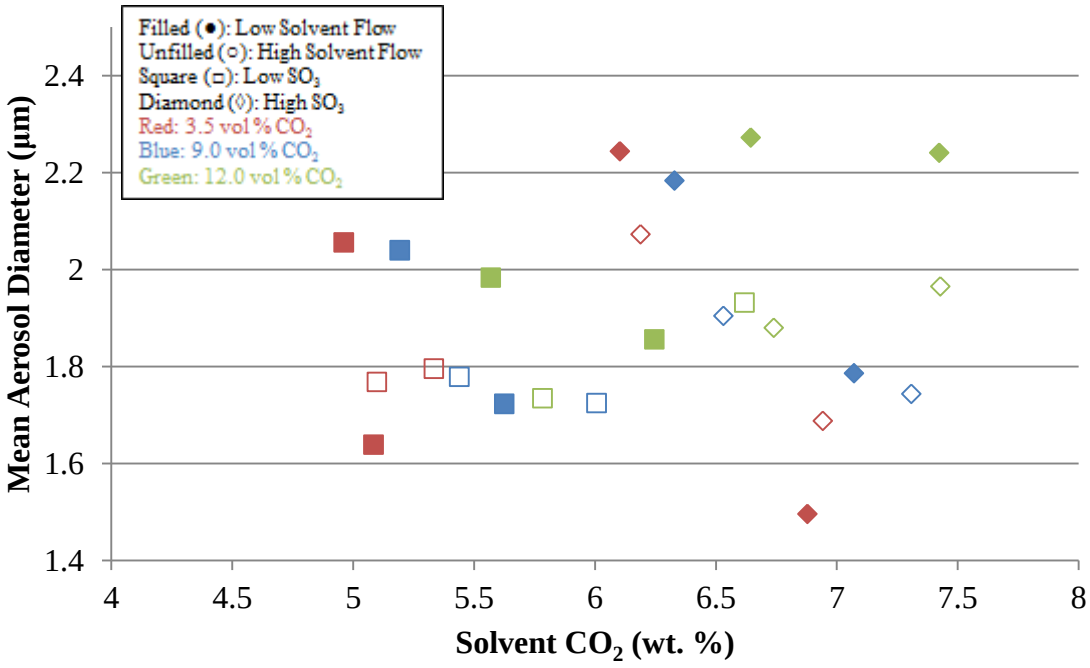


**Figure 4.12: Mean aerosol diameter as a function of solvent $CO_2$ content**

Most mean aerosol diameters were below 2.0 µm; of the 7 runs that had larger mean diameters, 6 utilized a low solvent flow rate (●; 0.8 liters/min). Higher inlet $SO_3$ compositions (◊; 50 ppm) were maintained in 5 of the 7 runs with mean aerosol diameters greater than 2.0 µm. There is no notable trend between the solvent $CO_2$ content and the mean aerosol diameter. Figure 4.13 presents the mean aerosol diameter as a function of the solvent amine content.

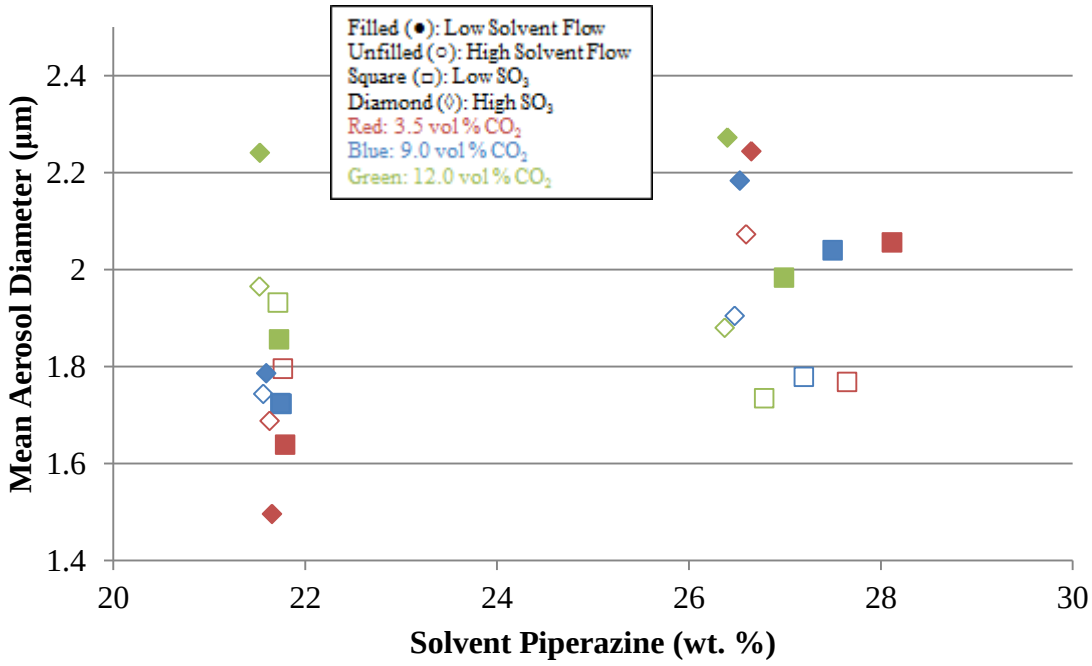


**Figure 4.13: Mean aerosol diameter as a function of solvent piperazine content**

With the 3 m piperazine solvent, there is a very noticeable stratification in the mean aerosol diameter as the inlet $CO_2$ changes (color). Mean aerosol diameters range between 1.5 and 1.8 µm for inlet $CO_2$ at 3.5 vol. %, and increase to 1.86 to 2.24 µm as the inlet $CO_2$ increases to 12 vol %. This trend of increasing aerosol diameters with increasing inlet $CO_2$ is not followed as the piperazine in the solvent increases.

As the solvent piperazine content increases, the mean aerosol diameter also increases. Mean aerosol diameters ranged from 1.5 to 2.25 µm for 3 m piperazine solvent, and between 1.73 and 2.27 µm for 5 m piperazine.

Figure 4.14 presents the mean aerosol diameter as a function of the AGC absorber gas outlet temperature.

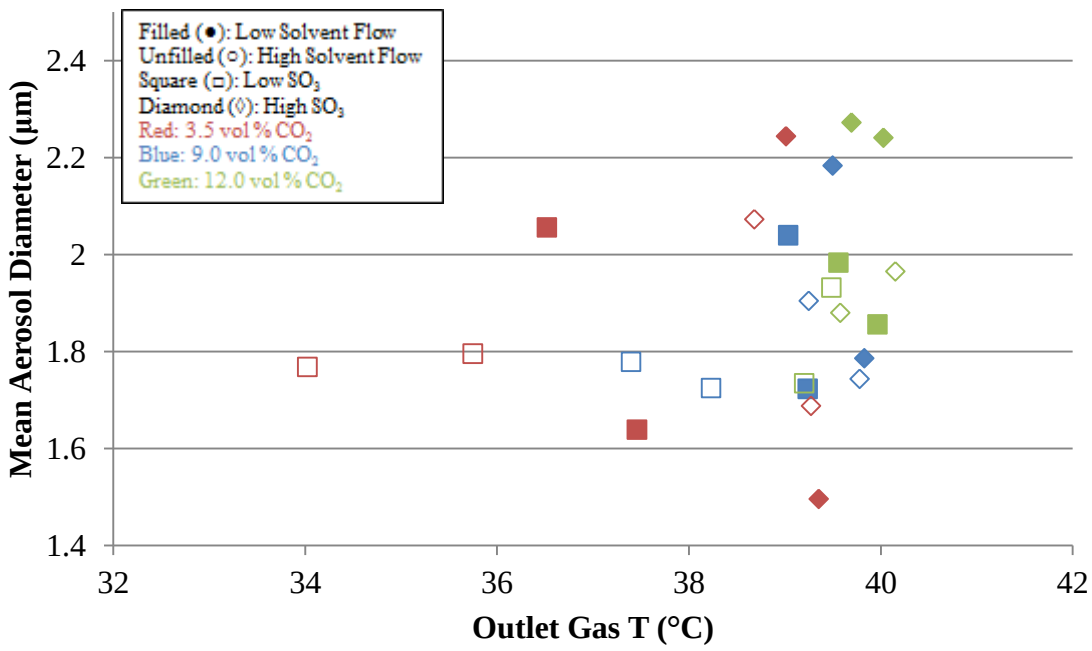


**Figure 4.14: Mean aerosol diameter as a function of AGC gas outlet temperature**

In general, increasing the outlet gas temperature resulted in increases in the mean aerosol diameters. The trend of higher inlet $CO_2$ compositions (color) corresponding with higher outlet gas temperatures is again visible. Figure 4.15 presents the mean aerosol diameter as a function of the column temperature bulge location.

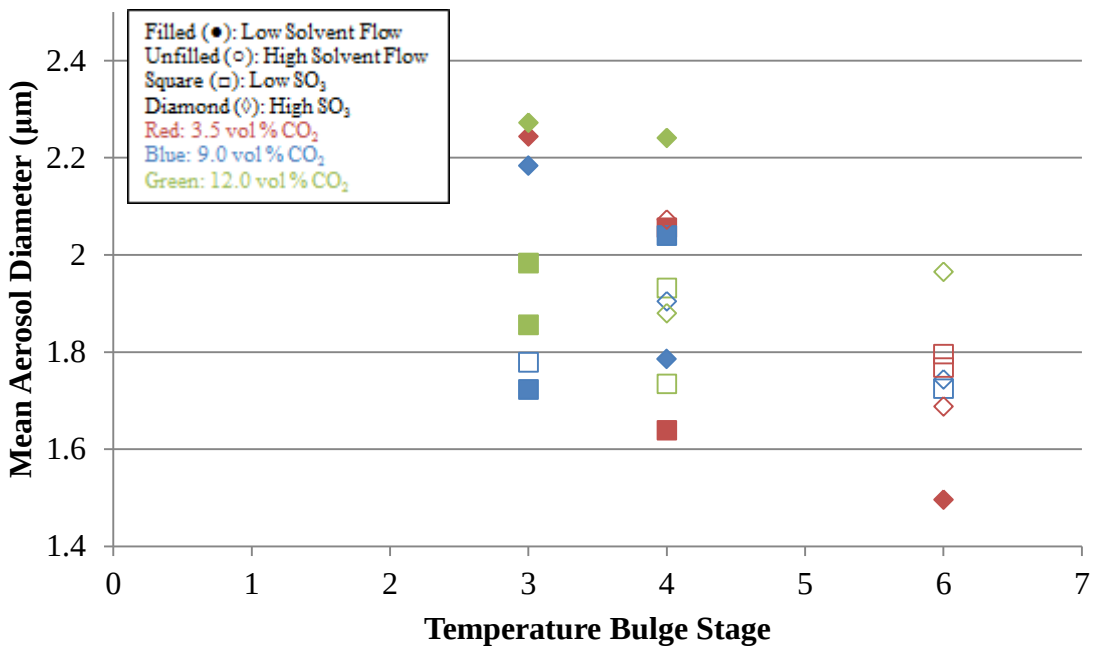


**Figure 4.15: Mean aerosol diameter as a function of AGC temperature bulge stage**

Lowering the stage of the temperature bulge results in smaller mean aerosol diameters. With the temperature bulge at the bottom of the column, mean aerosol diameters range from 1.5 to 1.96 µm; as the temperature bulge moves up the column, the mean aerosol diameter increases to a range between 1.72 and 2.27 µm. Higher solvent flow rates (○) result in lower stages for the temperature bulge, and subsequently smaller mean aerosol diameters.

Summarily, lower solvent flow rates (●) and higher inlet $SO_3$ (◊) corresponded with increased mean aerosol diameters. With less amine in the solvent, increasing the inlet $CO_2$ increased the mean aerosol diameter. As the amine in the solvent increases, the mean aerosol diameter increases. Increasing the absorber gas outlet temperature and raising the temperature bulge stage also result in increases to the mean aerosol size.

### 4.5.3 Aerosol 50% Volume Cutoff Size

The aerosol 50% volume cutoff size refers to the aerosol diameter at which 50% of the emitted aerosol volume is below the corresponding diameter. This is a volume-weighted averaging term for aerosol sizes; as amine emissions are heavily dependent on the volume of each aerosol, this is an important parameter to evaluate for emissions. The 50% volume cutoff size for each run is presented in Table 4.7 under the '50% Volume Cutoff' column. Figure 4.16 presents the 50% volume cutoff size for each run as a function of the solvent $CO_2$ content.

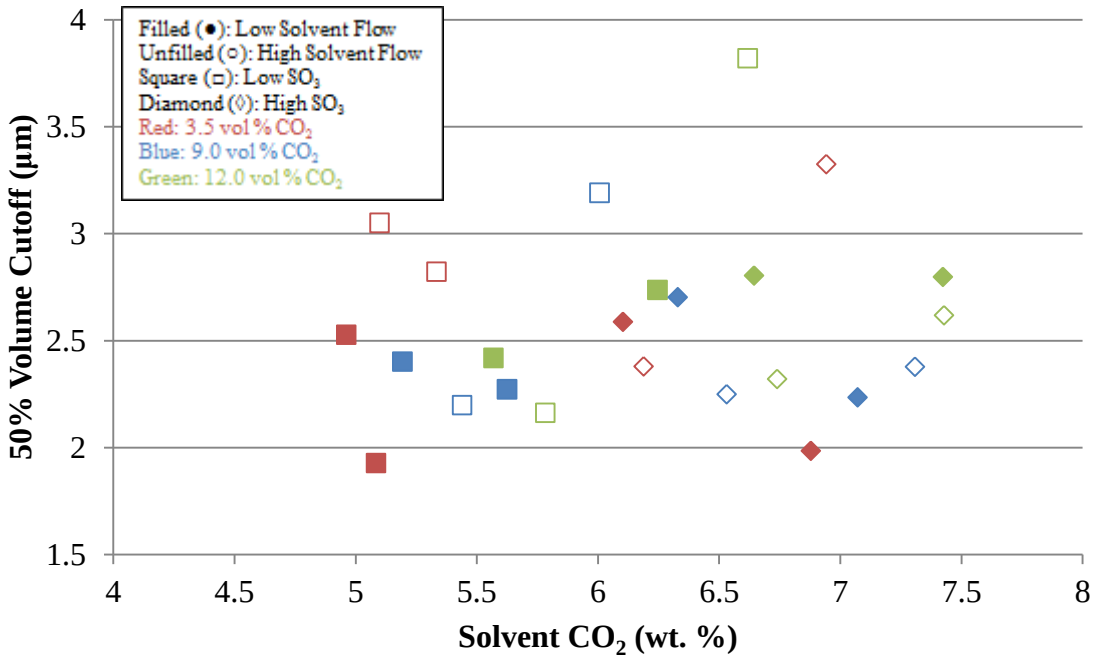


**Figure 4.16: Aerosol 50% volume cutoff size as a function of solvent $CO_2$ content**

The 4 runs with aerosol 50% cutoff volumes greater than 3.0 µm all used a high (○; 2.4 liters/min) solvent flow rate. Similarly to the mean aerosol diameter, there does not appear to be a trend between the solvent $CO_2$ content and the 50% volume cutoff size.

Figure 4.17 presents the 50% volume cutoff size as a function of the solvent amine content.

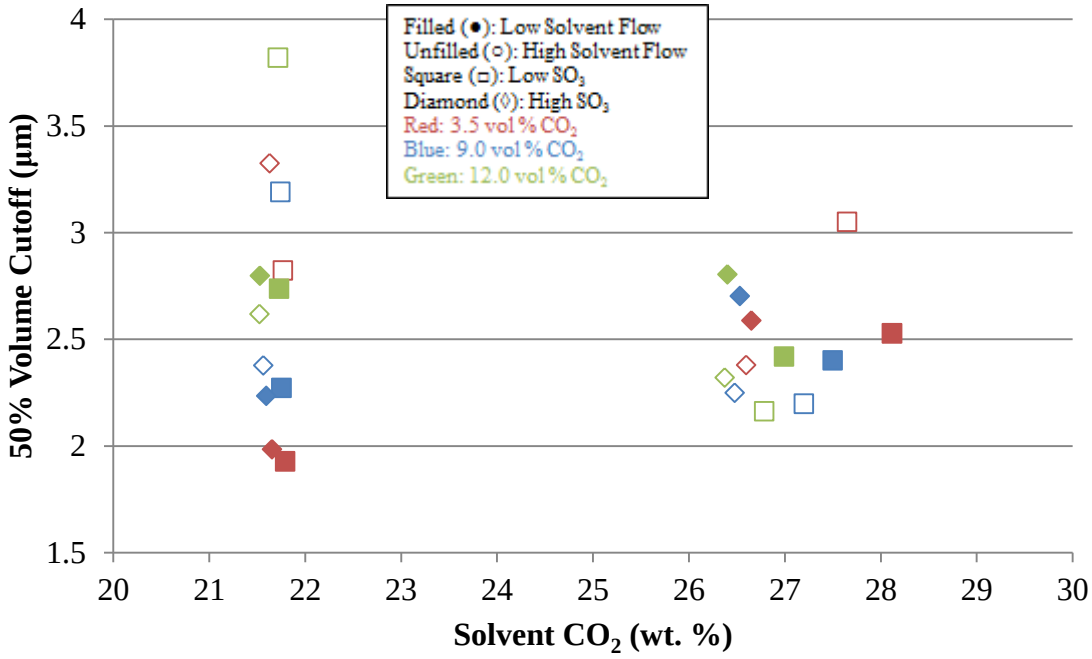


**Figure 4.17: Aerosol 50% cutoff volume size as a function of solvent piperazine content**

With the 3 m piperazine solvent, there is again stratification in the 50% volume cutoff size as the inlet $CO_2$ changes. Aerosol 50% volume cutoff sizes range between 1.93 and 3.32 µm for inlet $CO_2$ at 3.5 vol. %, and increase to 2.62 to 3.82 µm as the inlet $CO_2$ increases to 12 vol %. This trend of increasing aerosol diameters with increasing inlet $CO_2$ is not followed as the piperazine in the solvent increases. Overall, there does not appear to be any correlation between the 50% volume cutoff size and the solvent amine content.

Figure 4.18 presents the 50% volume cutoff size as a function of the AGC absorber gas outlet temperature.

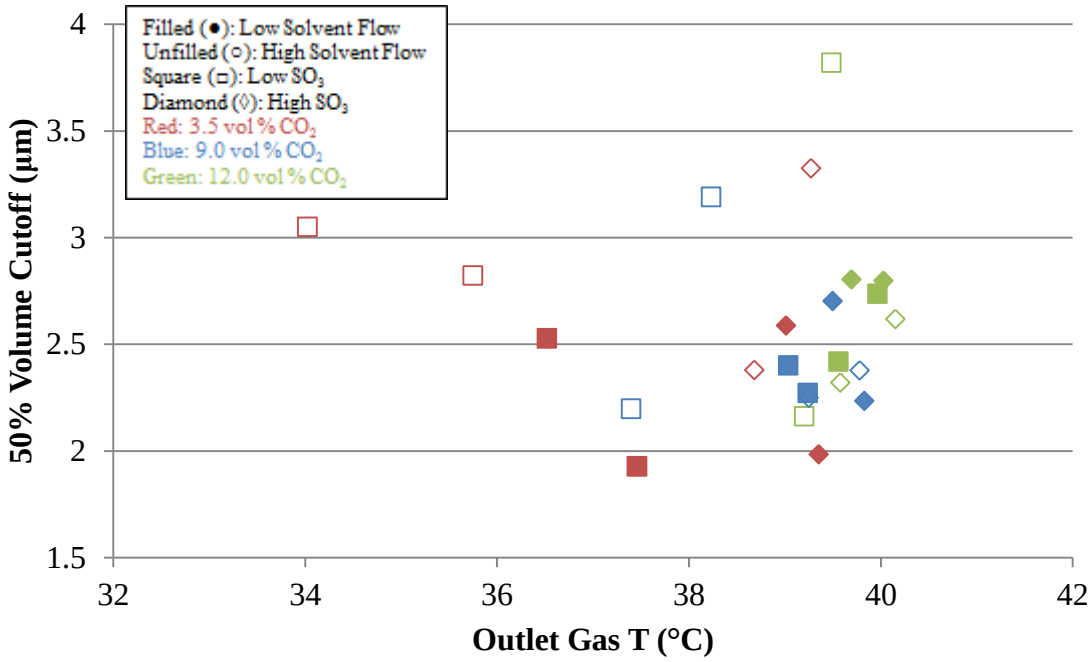


**Figure 4.18: Aerosol 50% volume cutoff size as a function of AGC gas outlet temperature**

There does not appear to be any general correlation between the absorber gas outlet temperature and the 50% volume cutoff size. Figure 4.19 gives the 50% volume cutoff size as a function of the column temperature bulge stage.

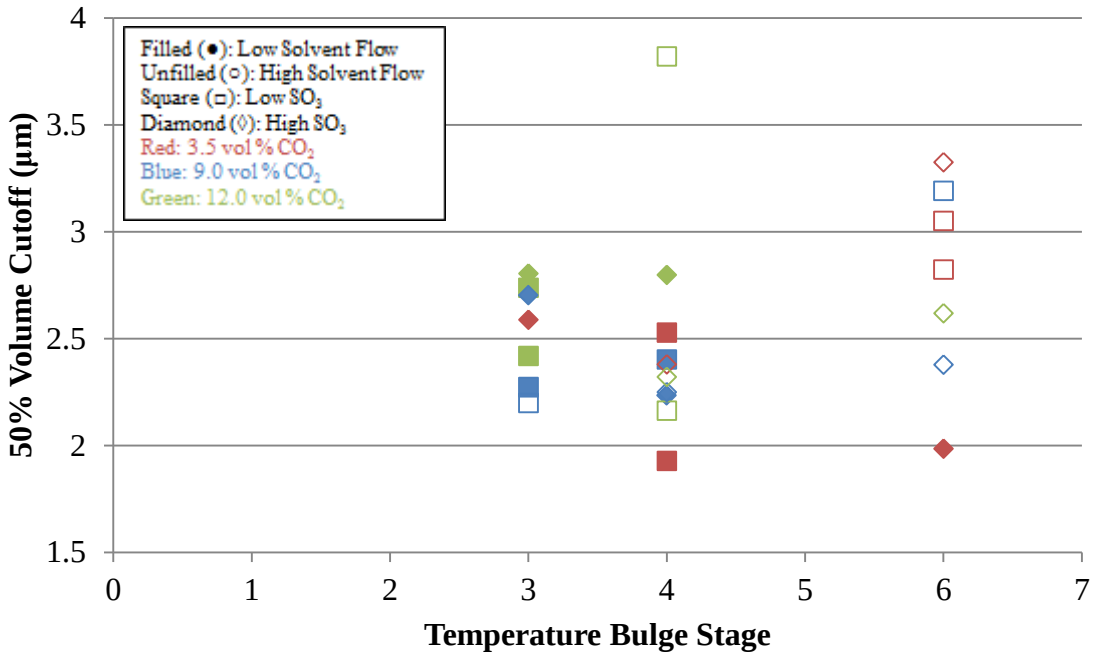


**Figure 4.19: Aerosol 50% volume cutoff size as a function of temperature bulge stage**

There do not appear to be any significant discernable correlations of the 50% volume cutoff size with the temperature bulge stage location.

Overall, higher solvent flow rates increase the 50% volume cutoff size for aerosol. At reduced amine in the solvent, increasing the inlet $CO_2$ increases the 50% volume cutoff size, but this effect is lessened with increased amine in the solvent.

### 4.5.4 Aerosol Concentration

The aerosol concentration is measured directly by the PDI, and is the amount of aerosol drops present in a single $cm^{-3}$. Increases in the aerosol concentration result in an increase in the amine emissions with all other factors held constant. Table 4.7 provides the aerosol concentration for each run under the 'Aerosol Concentration' column. Figure

4.20 gives the aerosol concentration for each run as a function of the $CO_2$ content in the solvent.

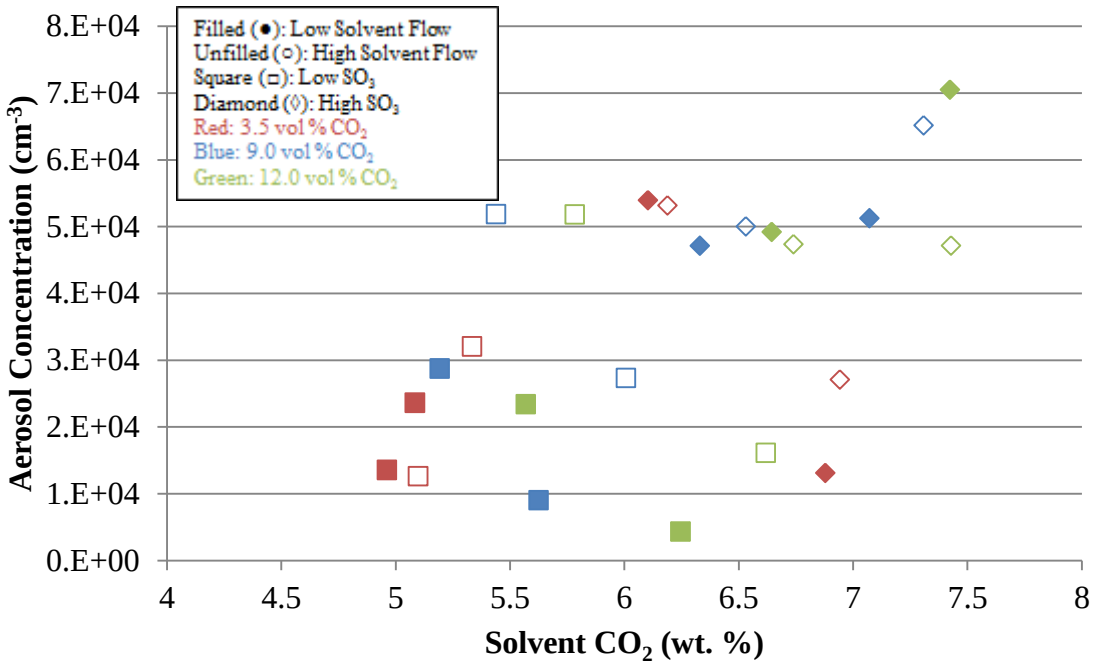


**Figure 4.20: Aerosol concentration as a function of solvent $CO_2$ content**

The aerosol concentration increases as the $CO_2$ in the solvent increases. Out of the 12 runs with the highest aerosol concentration, 10 had a high inlet $SO_3$ (◊) of 50 ppm.

Figure 4.21 presents the aerosol concentration for each run as a function of the solvent amine content.

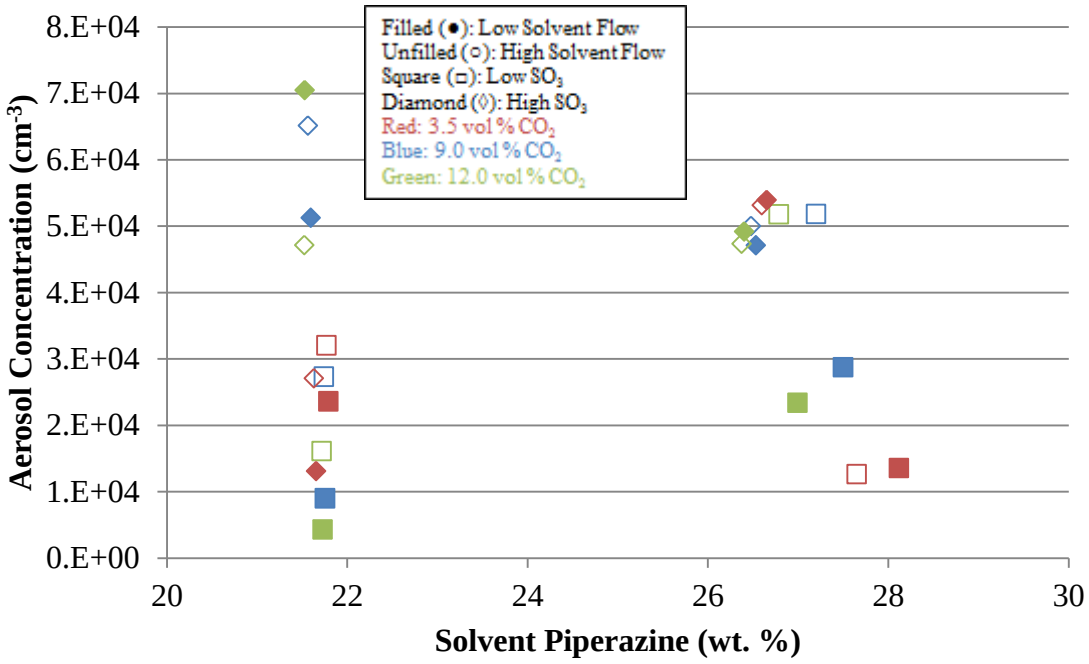


**Figure 4.21: Aerosol concentration as a function of solvent piperazine content**

The solvent piperazine content does not appear to express any discernable relationship with the aerosol concentration. Figure 4.22 presents the aerosol concentration as a function of the AGC absorber gas outlet temperature.

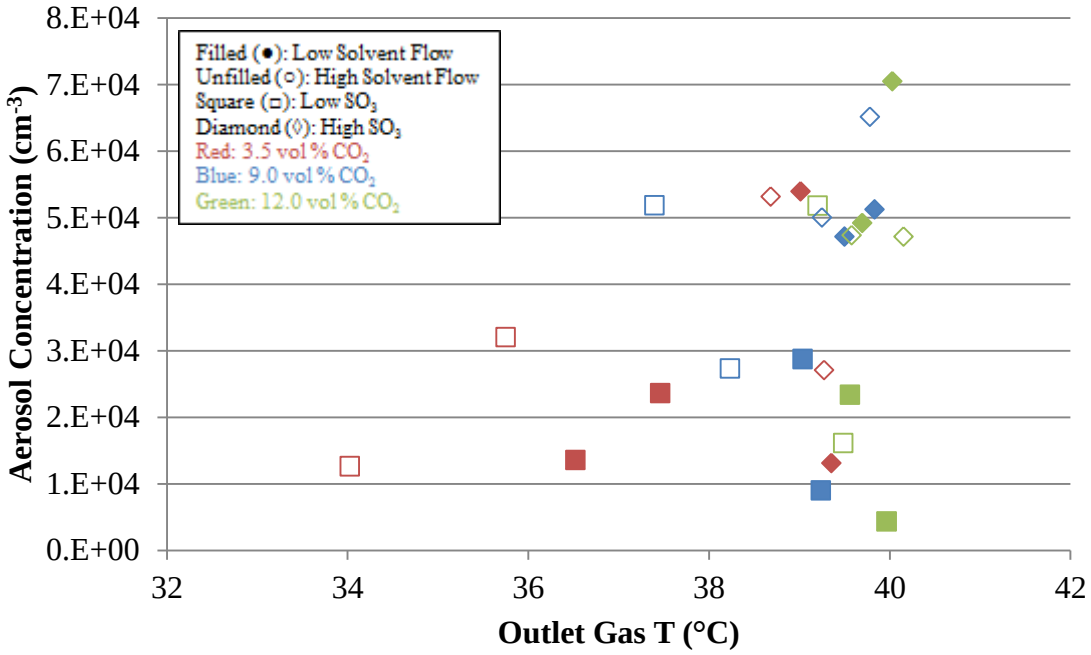


**Figure 4.22: Aerosol concentration as a function of AGC gas outlet temperature**

The aerosol number concentration generally increases as the absorber outlet temperature increases. As the mean aerosol diameter also increases, this indicates that higher temperatures result in a higher concentration of larger aerosol leaving the absorber column when the outlet temperature is increased. However, this does not necessarily increase the amine emissions as detected by FTIR, as evidenced in Figure 4.10. Instead, the amount of amine lost through the aerosol phase appears to be more dependent on the solvent amine composition, as shown in Figure 4.9.

Figure 4.23 presents the aerosol concentration at the absorber outlet as a function of the AGC column temperature bulge stage.

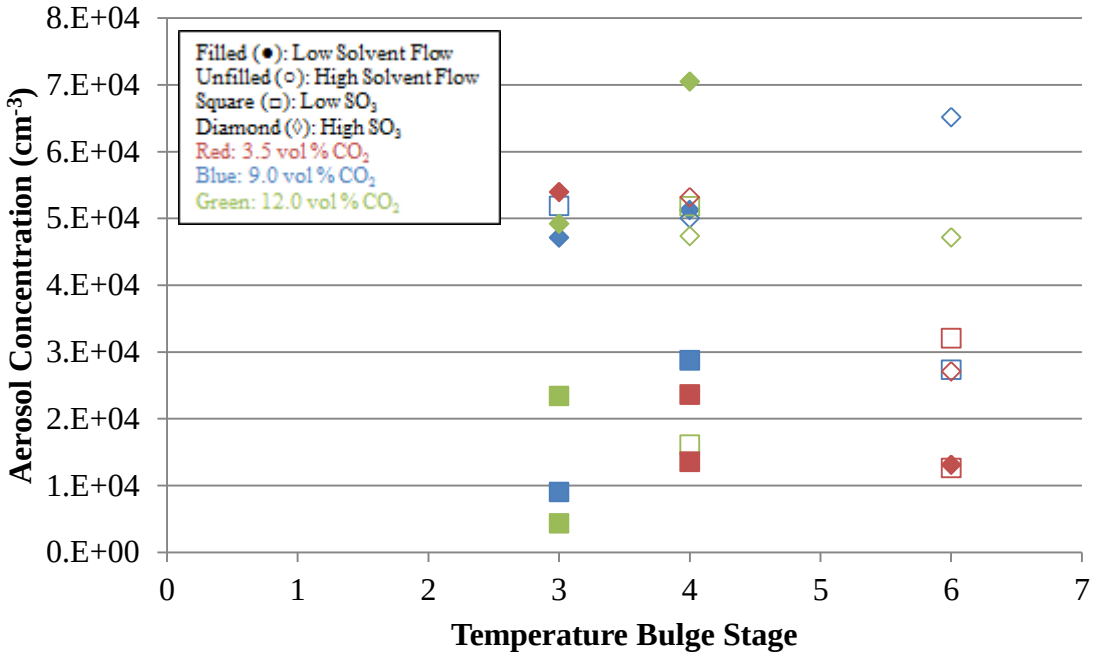


**Figure 4.23: Aerosol concentration as a function of AGC temperature bulge stage**

No correlation appears to exist between the temperature bulge stage and the aerosol concentration at the absorber outlet.

Summarily, the aerosol concentration increases as the $CO_2$ in the solvent increases. Increasing the inlet $SO_3$ also correlates with an increasing aerosol concentration. A higher gas outlet temperature displays a positive relationship with the aerosol concentration, similarly to the relationship with the mean aerosol diameter. Higher aerosol concentrations and larger aerosol diameters do not necessarily increase amine emissions; that is more dependent on the solvent amine content.

### 4.5.5 Aerosol and Amine Emission Regression Analysis

Regression analysis was performed to gain insight into how the AGC operating conditions affected the aerosol concentration, mean diameter, 50% volume cutoff size,

and amine emissions. The data analysis tool pack regression function in Excel was used for this analysis. Table 4.8 presents the regression analysis results for the aerosol concentration, mean diameter, 50% volume cutoff size, and amine emissions.

**Table 4.8: Regression analysis results with standard errors for aerosol concentration, mean diameter, 50% volume cutoff size, and amine emissions.**

| | Aerosol Conc. | 50% Volume Cutoff | Mean Diameter | Outlet PZ Conc. |
|---|---|---|---|---|
| | *#/cm$^3$* | *μm* | *μm* | *ppm* |
| **$R^2$** | 0.7117 | 0.51 | 0.61 | 0.65 |
| **Significance F** | 0.0262 | 0.31 | 0.12 | 0.07 |
| **Standard Error** | 1.36E+04 | 0.41 | 0.18 | 2.11 |
| ***Coefficients*** | | | | |
| **Intercept** | 7.22E+04 | -3.56 | -0.94 | -63.77 |
| **Solvent Flow (lpm)** | -1.50E+04 | 0.85 | 0.04 | 4.66 |
| **$CO_2$ In (vol %)** | 9.63E+03 | -0.2 | -0.02 | 0.01 |
| **$CO_2$ Out (vol %)** | -4.06E+03 | 0.17 | 0.09 | -0.01 |
| **$SO_3$ In (ppm)** | 2.84E+03 | -0.07 | 0.01 | 0.03 |
| **Solvent In (°C)** | 5.42E+03 | -0.18 | 0.16 | -0.01 |
| **Gas Out (°C)** | 9.47E+03 | 0.28 | -0.02 | 3.53 |
| **Gas In (°C)** | 5.05E+03 | -0.03 | 0.02 | 0.32 |
| **Avg Column T (°C)** | -1.48E+04 | -0.09 | -0.09 | -1.94 |
| **SolventPZ(wt %)** | -1.66E+03 | 0.1 | 0.04 | 0.56 |
| **Solvent $CO_2$ (wt %)** | -5.21E+04 | 1.28 | -0.21 | -3.37 |
| ***Standard Errors*** | *#/cm$^3$* | *μm* | *μm* | *ppm* |
| **Solvent Flow (lpm)** | 38,420 | 1.17 | 0.49 | 5.95 |
| **$CO_2$ In (vol %)** | 3,556 | 0.11 | 0.05 | 0.55 |
| **$CO_2$ Out (vol %)** | 4,300 | 0.13 | 0.05 | 0.67 |
| **$SO_3$ In (ppm)** | 971 | 0.03 | 0.01 | 0.15 |
| **Solvent In(°C)** | 14,976 | 0.46 | 0.19 | 2.32 |
| **Gas Out (°C)** | 20,298 | 0.62 | 0.26 | 3.14 |
| **Gas In (°C)** | 3,346 | 0.1 | 0.04 | 0.52 |
| **Avg T (°C)** | 9,695 | 0.3 | 0.12 | 1.5 |
| **Solvent PZ (wt%)** | 2,197 | 0.07 | 0.03 | 0.34 |
| **Solvent $CO_2$ (wt%)** | 27,660 | 0.84 | 0.35 | 4.28 |

For the aerosol concentration, the solvent $CO_2$ content had the most significant impact, relative to the other parameters, followed by the solvent flow rate. The 50% volume cutoff size was most heavily influenced by solvent $CO_2$ content and the solvent flow rate. The solvent $CO_2$ content and solvent inlet temperature had the most significant impacts on the mean aerosol diameter. Finally, the outlet amine emissions was most closely correlated with the solvent flow rate and gas outlet temperature.

The standard errors for each coefficient for each regression are presented in Table 4.8. Standard error values dictate which coefficients have the most variation and uncertainty within the regression models. Dividing the standard errors by the coefficient values in Table 4.8 gives the magnitude of the error; a larger error to coefficient ratio indicates higher uncertainty in regards to that parameter. These normalized standard errors are given in Table 4.9.

**Table 4.9: Regression analysis standard error magnitude for aerosol concentration, mean diameter, 50% volume cutoff size, and amine emissions**

| | **Aerosol Conc.** | **50% Volume Cutoff** | **Mean Diameter** | **Outlet PZ Conc.** |
|---|---|---|---|---|
| ***Coefficients*** | *#/cm$^3$* | *μm* | *μm* | *ppm* |
| **Solvent Flow (lpm)** | -2.56 | 1.38 | 11.69 | 1.28 |
| **$CO_2$ In (vol %)** | 0.37 | -0.53 | -2.14 | 44.40 |
| **$CO_2$ Out (vol %)** | -1.06 | 0.78 | 0.58 | -111.64 |
| **$SO_3$ In (ppm)** | 0.34 | -0.45 | 2.22 | 4.72 |
| **Solvent In(°C)** | 2.76 | -2.57 | 1.19 | -234.36 |
| **Gas Out (°C)** | 2.14 | 2.24 | -10.78 | 0.89 |
| **Gas In (°C)** | 0.66 | -3.08 | 1.99 | 1.64 |
| **Avg T (°C)** | -0.65 | -3.17 | -1.42 | -0.77 |
| **Solvent PZ (wt%)** | -1.32 | 0.67 | 0.63 | 0.61 |
| **Solvent $CO_2$ (wt%)** | -0.53 | 0.66 | -1.69 | -1.27 |

In Table 4.9, the larger values correspond to greater magnitude of the standard error. For the aerosol concentration regression, the solvent flow rate and inlet temperature have the highest error. The gas inlet temperature and average bed temperature generate the largest magnitude of error for the 50% volume cutoff size regression. The solvent flow rate and gas outlet temperature have the largest normalized standard error for the mean diameter, and the solvent inlet temperature and $CO_2$ outlet composition produce the largest standard error for the outlet piperazine emission regression model.

Smaller values in Table 4.10 relate to a greater fit of the regression model with the parameter; in other words, these lower value parameters have a greater effect on the aerosol property and amine emissions. The inlet $CO_2$ and $SO_3$ produced the smallest normalized error for the aerosol concentration regression, along with the inlet gas temperature, average bed temperature, and solvent $CO_2$ composition. For the 50% volume cutoff size, the inlet $CO_2$ and $SO_3$ compositions, $CO_2$ outlet composition, and solvent piperazine and $CO_2$ compositions had the lowest normalized errors. The mean aerosol diameter is most impacted by the $CO_2$ outlet content and the solvent piperazine composition. The outlet piperazine emissions is most affected by the gas outlet temperature and the solvent piperazine composition.

A second set of regression models were produced for the aerosol concentration, 50% volume cutoff, mean aerosol diameter, and outlet piperazine emissions. The updated models only took into account variables that had normalized standard errors less than 1.0 from Table 4.9. This was performed to eliminate variables that are not relevant

to aerosol properties or amine emissions. Table 4.10 presents the results from these updated models.

**Table 4.10: Updated regression analysis results and standard errors for aerosol concentration, mean diameter, 50% volume cutoff size, and amine emissions**

| | Aerosol Conc. | 50% Volume Cutoff | Mean Diameter | Outlet PZ Conc. |
|---|---|---|---|---|
| | *#/cm$^3$* | *μm* | *μm* | *ppm* |
| **$R^2$** | 0.6 | 0.37 | 0.45 | 0.35 |
| **Significance F** | 0.0035 | 0.11 | 0.0019 | 0.0104 |
| **Standard Error** | 13689 | 0.4 | 0.16 | 2.24 |
| ***Coefficients*** | | | | |
| **Intercept** | 182563 | -5.62 | 0.76 | -21.3 |
| **Solvent Flow (lpm)** | - | - | - | - |
| **$CO_2$ In (vol %)** | 4388 | -0.13 | - | - |
| **$CO_2$ Out (vol %)** | - | 0.07 | 0.04 | - |
| **$SO_3$ In (ppm)** | 1756 | -0.06 | - | - |
| **Solvent In (°C)** | - | - | - | - |
| **Gas Out (°C)** | - | - | - | 0.22 |
| **Gas In (°C)** | 1465 | - | - | - |
| **Avg Column T (°C)** | -4475 | - | - | - |
| **Solvent PZ(wt %)** | - | 0.18 | 0.04 | 0.6 |
| **Solvent $CO_2$ (wt %)** | -19088 | 1.33 | - | - |
| ***Standard Erros*** | | | | |
| **Intercept** | 88821 | 3.23 | 0.32 | 14.5 |
| **Solvent Flow (lpm)** | - | - | - | - |
| **$CO_2$ In (vol %)** | 1667 | 0.06 | - | - |
| **$CO_2$ Out (vol %)** | - | 0.06 | 0.01 | - |
| **$SO_3$ In (ppm)** | 648 | 0.02 | - | - |
| **Solvent In (°C)** | - | - | - | - |
| **Gas Out (°C)** | - | - | - | 0.32 |
| **Gas In (°C)** | 1923 | - | - | - |
| **Avg Column T (°C)** | 2309 | - | - | - |
| **Solvent PZ(wt %)** | - | 0.06 | 0.01 | 0.18 |
| **Solvent $CO_2$ (wt %)** | 12861 | 0.45 | - | - |

Parity plots for each updated regression model are presented in Figures 4.24 through 4.27. The values predicted by the regression models are plotted with respect to the experimental values. Points further from the line indicate failure of the updated model to predict the experimentally determined aerosol properties and amine emissions.

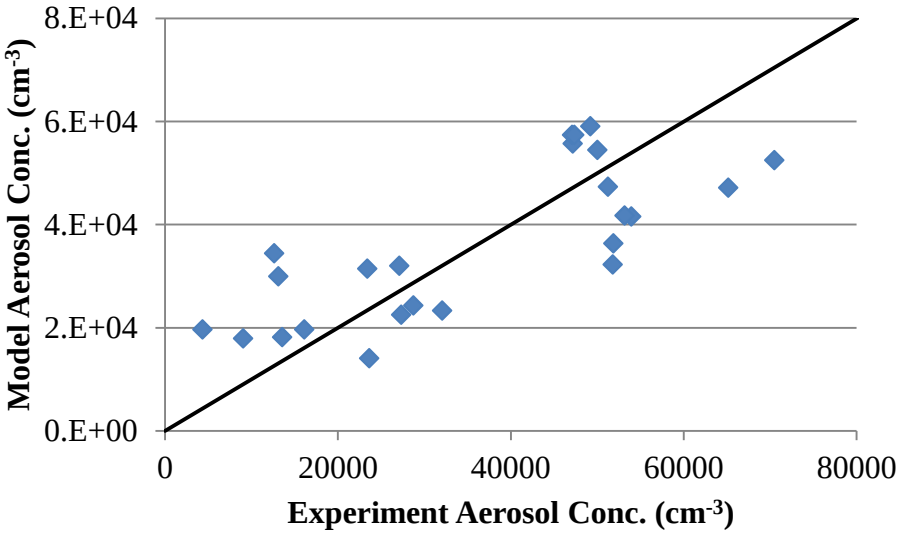


**Figure 4.24: Parity plot of experimentally determined aerosol concentrations versus regression model predicted aerosol concentrations**

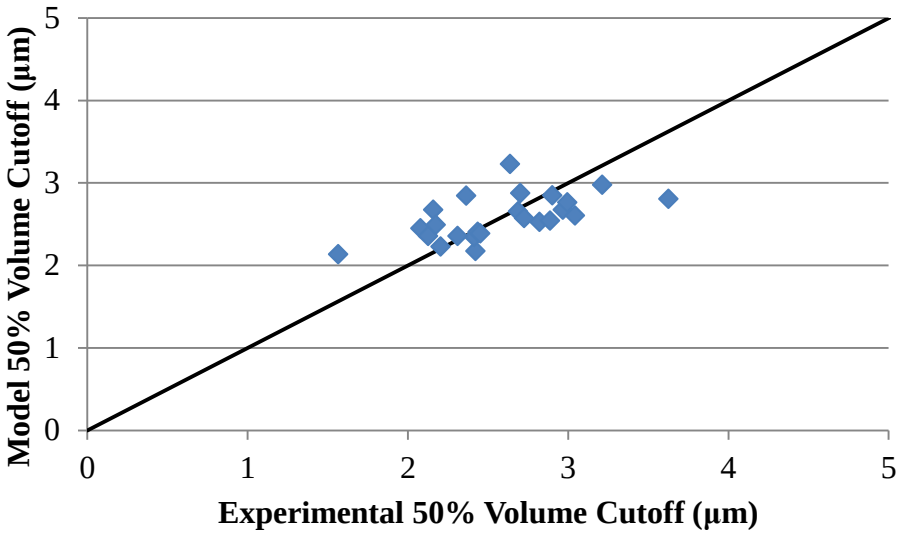


**Figure 4.25: Parity plot of experimentally determined aerosol 50% volume cutoff size versus regression model predicted 50% volume cutoff size**

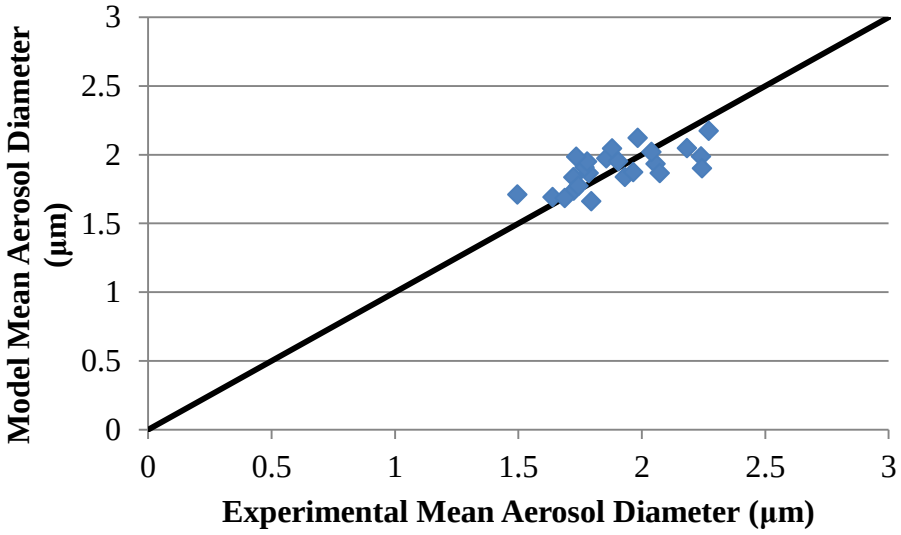


**Figure 4.26: Parity plot of experimentally determined mean aerosol diameter versus regression model predicted mean aerosol diameter**

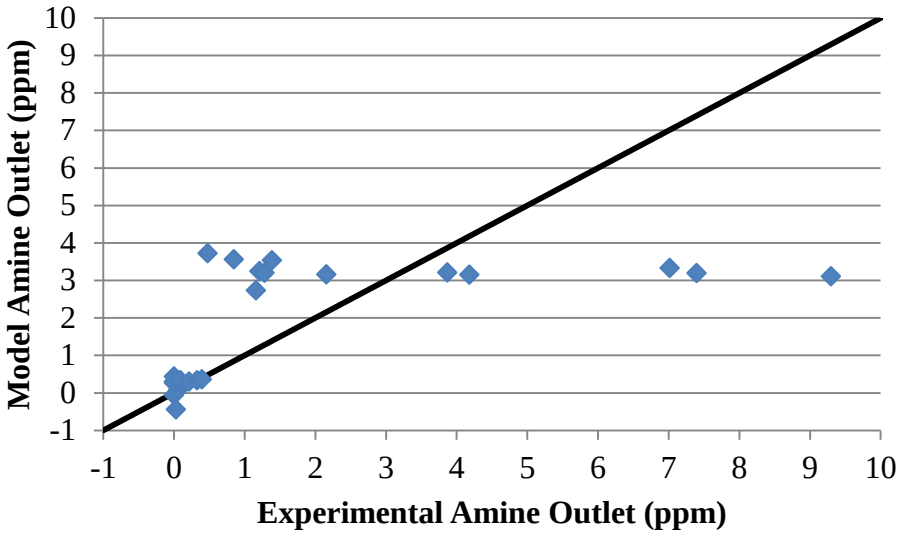


**Figure 4.27: Parity plot of experimentally determined amine emissions versus regression model predicted amine emissions**

The updated regression model for the mean aerosol diameter performs the best at predicting the aerosol properties. The 50% volume cutoff size model also does an adequate job of predicting the experimentally determined 50% volume cutoff size. The aerosol concentration regression model is not as effective as the two aerosol size models. Finally, the amine emissions model does not predict any piperazine emissions greater than 4 ppm; it is relatively effective at lower amine emissions but deficient at higher experimentally determined emissions values.

## 4.6 AGC Experimental Results Conclusions

### 4.6.1 Amine Emissions

Piperazine emissions were below 0.5 ppm with 3 m piperazine; increasing the amine solvent concentration to 5 m resulted in piperazine emissions to range from 0.5 to

9.3 ppm. Increasing the solvent flow rate from 0.8 to 2.4 LPM resulted in increased piperazine emissions by up to 6.9 ppm. Lowering the temperature bulge from the middle of the column to the bottom decreased piperazine emissions by a factor of eight; this is due in part to a reduction in the absorber outlet temperature by up to 5 °C.

### 4.6.2 Mean Aerosol Diameter

Reducing solvent flow increased mean aerosol diameters by up to 0.4 μm. Increased inlet $SO_3$ increased mean aerosol diameters by up to 0.4 μm. With 3 m piperazine, the mean aerosol diameter ranged between 1.5 and 2.24 μm. As the solvent piperazine increased, the mean aerosol diameter increased to a range between 1.73 and 2.27 μm.

At reduced solvent piperazine, increasing the inlet $CO_2$ increased the mean aerosol diameter by up to 0.09 μm per 1 vol % $CO_2$. This effect was lessened as the solvent amine content increased. Raising the temperature bulge stage from the bottom to the middle of the absorber increased the mean aerosol size by up to 0.3 μm.

### 4.6.3 Aerosol 50% Volume Cutoff Size

Higher solvent flow increased the aerosol 50% volume cutoff size by up to 1.3 μm. At reduced amine in the solvent, increasing the inlet $CO_2$ increased the 50% volume cutoff size by up to 0.12 μm per 1 vol % $CO_2$, This effect was lessened with increased amine in the solvent. The temperature bulge stage location and gas outlet temperature did not present significant correlations with the aerosol 50% volume cutoff size.

### 4.6.4 Aerosol Concentration

The aerosol concentration was found to increase as the $CO_2$ in the solvent increased; increasing the solvent $CO_2$ by 1 % increased the aerosol concentration by up to 2.5E4 per $cm^3$. Increasing the inlet $SO_3$ also correlated with an increasing aerosol concentration, with an $SO_3$ increase of 30 ppm resulting in aerosol concentration increases up to 6.6E4 per $cm^3$.

### 4.6.5 Process Condition Correlations with Aerosol Properties

For the aerosol concentration regression model, the solvent $CO_2$ content had the most significant impact, followed by the solvent flow rate. The 50% volume cutoff size model was most heavily influenced by solvent $CO_2$ content the solvent flow rate. The solvent $CO_2$ content and solvent inlet temperature had the most significant impacts in the mean aerosol diameter regression. Finally, the outlet amine emissionsmodel was most closely correlated with the solvent flow and gas outlet temperature.

Updated regression models were produced for the aerosol concentration, 50% volume cutoff, mean aerosol diameter, and piperazine emissions properties. The updated regression model for the mean aerosol diameter performed the best at predicting the aerosol properties. The 50% volume cutoff size model was adequate in predicting the experimentally determined 50% volume cutoff size. The aerosol concentration regression model was not as effective as the two aerosol size models. Finally, the amine emissions model did not predict any piperazine emissions greater than 4 ppm; it is relatively effective at lower amine emissions but deficient at higher experimentally

determined emissions values. These results show that process parameters can be used to adequately predict the sizes of aerosol, but not the concentrations or amine emissions.

## 4.7 RECOMMENDATIONS

There are three main recommendations for future experiments: variations in the amine solvent, temperature variations, and reductions in the inlet $SO_3$.

The amount of piperazine in the solvent was found to significantly impact the aerosol properties and amine emissions. Future experiments should observe how the amine structure and the presence of functional groups on the amine compound effect the aerosol concentration and size distribution.

As noted previously, inlet temperature conditions were not varied in this work. Due to the effects of the temperature bulge location and outlet gas temperatures on the aerosol properties and amine emissions, it is recommended that future experiments be conducted with variations of inlet solvent and gas temperature.

The inlet $SO_3$ composition was varied between 20 and 50 ppm for the experiments in this research. Future experiments on the AGC should attempt to use lower $SO_3$, in the range of 1 to 10 ppm. This presents a more realistic scenario to compare to full scale amine scrubbing processes. An additional base case test of the AGC without aerosol injection would be helpful in providing baseline data on operations.

The AGC provides an interesting test bed for qualifying the effectiveness of aerosol removal devices. Swirl tubes or other cyclonic separators could easily be tested on the apparatus without significant modifications.

The design and construction of a water wash column for the AGC would provide additional data on aerosol growth within amine scrubbing processes. Due to the extensive work required for this expansion, this is a lower priority recommendation.

The random packing used in the AGC does not provide a large amount of surface area for gas-liquid contact. Replacing the random packing with a structured packing that is designed to allow aerosol passage would improve the solvent flow distribution within the column. Designing and 3D printing structured packing components would be a useful project for an undergraduate researcher.

## 4.8 ACKNOWLEDGEMENTS

Special thanks to Dr. Steven Fulk for designing and building the Aerosol Growth Column. The LabVIEW™ control scheme and operating instructions for the system were invaluable. Korede Akinpelumi helped considerably in configuring and conducting the experiments described in this chapter. Aramide Eseyin and Chris Hardy contributed in the second half of experiments by lending their reclaimer apparatus and knowledge to concentrate amine solvent. Henry Bautista was of considerable help in obtaining and inventorying the solvent used in these experiments. Thanks as well to Dr. Charles Zaiontz for the creation and free release of the Real Statistics Microsoft Excel add-on; this feature significantly simplified analysis of PDI data. As always, thank you to Dr. Rochelle for financial and scientific support.

# CHAPTER 5: PILOT PLANT $SO_3$ GENERATION AND FTIR ANALYSIS

This chapter focuses on amine aerosol generation and testing at the UT-SRP pilot plant during the April 2017 campaign. The UT-SRP pilot plant process is presented, along with the FTIR sampling system and $SO_3$ generation technique. Notable results on aerosol tests and amine emissions are then shown, followed by an analysis of the effects of process conditions on the overall amine emissions. Conclusions on the campaign results and recommendations for further tests are provided.

## 5.1 BACKGROUND

The atmospheric emission of volatile solvent is a significant concern for amine-scrubbing $CO_2$ capture processes. Amine solvent lost through the gas outlet of the absorber column represents an environmental and safety hazard, and presents undesirable economic implications as well. Aerosol emissions have been identified as the primary cause of amine losses.

Aerosol emissions occur when aerosol nuclei sources are present in the incoming flue gas. Nuclei sources can be fly ash from the coal combustion process or submicron sulfuric acid drops produced from sulfur impurities in the fuel. The nuclei sources collect water, amine and $CO_2$ while traveling through the absorber column. Water washes are ineffective at collecting aerosol at diameters less than 3 microns (Mertens, 2013; Mertens, 2014, Khakhakria, 2015). This is due to the inability of the washing column to

collect aerosol via impaction as the aerosol travel along a Brownian diffusion "random walk" pathway.

### 5.1.1 Amine Aerosol Emissions at Pilot Plants

Mitsubishi Heavy Industries (MHI) observed an increase of KS-1 solvent and ethanolamine (MEA) emissions proportional to the inlet $SO_3$ to the absorber column (Mitsubishi Heavy Industries, 2011). A white fog was produced at the absorber flue gas outlet as $SO_3$ was introduced to the system. A multistage washing section, with varying solvent composition and temperature, helped partially mitigate the amine emissions (Kamijo, 2013).

SINTEF and the Netherlands Organization for Applied Scientific Research (TNO) collaborated on a $CO_2$ capture amine scrubbing pilot plant (SINTEF, 2012; da Silva, 2013; Khakharia, 2013, Khakharia 2014; Kolderup, 2012). FTIR measurements of amine emissions, and the installation of a Brownian Diffusion Unit downstream of the water wash, provided evidence of the presence of aerosol. Aerosol emissions were found to be dependent on the maximum temperature in the absorber, the number of available nuclei for condensation, and the extent of temperature gradients in the absorber and water wash.

The National Carbon Capture Center (NCCC) in Wilsonville, Alabama experienced MEA emissions in excess of 100 ppm due to aerosol, with $SO_3$ from the coal combustion process as the nuclei source (Carter, 2012). Amine emissions increased with increasing $SO_3$ and by deactivating the upper absorber bed; emissions decreased with reducing the water wash MEA content and increasing the absorber temperature. An ELPI+™ was used for aerosol characterization at this facility, and found aerosol

concentrations between 1E6 and 1E7 per $cm^3$, with a median aerosol diameter of 0.12 μm (Saha, 2017).

Mertens observed amine aerosol emissions during sampling at the Esbjerg $CO_2$ capture pilot plant in Denmark (Mertens, 2013; Mertens, 2014a). FTIR "Hot and wet" sampling was performed; this maintains a temperature of 180 °C across the sampling system to prevent condensation (Mertens, 2012). FTIR measurements revealed amine emissions three times higher than measurements by manual amine sampling techniques. The manual techniques condensed water prior to analysis, removing aerosol from the sampling system and failed to provide a representative sample of the process conditions.

Aker Solutions Mobile Test Unit (MTU) $CO_2$ capture unit experienced amine mist formation due to 12 ppm $H_2SO_4$ in the flue gas feed at Technology Centre Mongstad (TCM), Norway (Bade, 2014). Amine emissions exceeded 200 ppm during conventional operation. A BDU installed upstream of the absorber column was found to significantly reduce the concentration of aerosol nuclei, and lowered amine aerosol emissions from the absorber outlet.

### 5.1.2 Prior UT-SRP Pilot Plant Aerosol Campaigns

Pilot scale amine scrubbing experiments with piperazine have been conducted at the University of Texas Separations Research Program since 2008. This process uses air mixed with $CO_2$ to create a simulated flue gas. A benefit of this configuration is the ability to vary the inlet $CO_2$, to simulate $CO_2$ capture processes ranging from natural gas combustion to enriched $CO_2$ sources.

The absorber side of the process uses a pair of 10' packed beds to countercurrently contact amine solution with the synthetic flue gas. RSP-250 has been used as the structured packing.

Early tests began with a simple absorber and simple stripper, and have been performed with increasingly complex process configurations in recent years. Absorber intercooling was added in 2010, and a two-stage flash regeneration system in 2010/2011. The two-stage flash regenerator was upgraded with a warm-rich bypass in 2011, and then reconfigured as a single stage flash with a cold-rich bypass in 2013.

#### *5.1.2.1 November 2013 UT-SRP Campaign*

Initial aerosol tests were conducted in November 2013 with a second generation Phase Doppler Interferometer (PDI). As outlined in Chapter 2, the PDI quantifies aerosol size and concentration within the process gas through optical light scattering measurements.

Aerosol tests at the UT-SRP facility were conducted by Fulk (Fulk, 2016; Fulk, 2014). While the UT-SRP pilot plant process configuration allows a range of inlet $CO_2$ for testing, the lack of water vapor and aerosol nuclei hinder how well the pilot plant can simulate a true amine scrubbing process. For aerosol measurements, Fulk produced aerosol through the injection of $SO_2$ and vaporized $H_2SO_4$ (Fulk, 2016).

$SO_2$ injection rates were controlled by the use of a large needle valve and rotameter, with inlet compositions verified by FTIR analysis. These tests experienced relative consistency, with adequate and repeatable control of the $SO_2$ injection rates. Fulk determined that piperazine emissions increased at close to stoichiometric rates of

$SO_2$ injection: the ratio of the increase in piperazine emissions to inlet $SO_2$ was 1.26 on a molar basis.

$H_2SO_4$ addition to the process inlet was performed with the Liquid Vaporizer and Injector (LVI). The LVI proved to be inconsistent in $H_2SO_4$ aerosol nuclei generation, due to frequent plugging in the system from corrosion caused by condensing sulfuric acid. Due to these issues, aerosol measurements from $H_2SO_4$ injection were inconclusive.

Sampling with the second generation PDI proved to be problematic, with very low concentrations of aerosol detected. The aerosol size and concentration did not match the values predicted through material balances. Following the campaign, Artium Technologies began work on a customized PDI capable of measuring aerosol at diameters down to 0.1 μm.

#### *5.1.2.2 March 2015 UT-SRP Campaign*

The 2015 UT-SRP campaign varied piperazine from 5 to 8 m. The one-stage flash regeneration was upgraded to the advanced flash stripper with a cold/warm rich bypass. This campaign also utilized the third generation PDI and an upgraded Liquid Vaporizer and Injector (LVI) for aerosol experiments.

The FTIR sampling system was used to quantify aerosol emissions caused by the injection of $SO_2$ and $H_2SO_4$ into the absorber inlet. $SO_2$ injection yielded piperazine emissions ratios of 0.03 to 3.99 mol piperazine emitted/mole $SO_2$ injected. Amine emissions due to $H_2SO_4$ injection were between 0.93 and 6.73 moles/mole sulfuric acid added. A material balance of $SO_2$ injected and sulfate in the solvent determined that 34.9

% of the injected $SO_2$ was absorbed by the solvent; the remaining $SO_2$ exited the process as aerosol.

Visual confirmation of aerosol is presented in Figure 5.1. The mist from $SO_2$ injection appeared thin and brown in color, and the $H_2SO_4$ plume was heavier and white.

**Figure 5.1: $SO_2$ (left) and $H_2SO_4$ (right) plumes at the UT-SRP absorber outlet (Fulk, 2016).**

Due to a number of unfortunate circumstances, only a single measurement was taken with the PDI. The aerosol concentration was determined to be 9.9E5 per $cm^3$ during $H_2SO_4$ injection testing. 50 % of the observed aerosol had diameters below 0.28 μm; however, 50 % of the emitted aerosol volume was due to aerosol larger than 1.02 μm.

## 5.2 UT-SRP PILOT PLANT

Extensive upgrades were performed on the UT-SRP pilot plant prior to the April 2017 campaign. These included modifications to the pilot plant process itself, and expansions to the FTIR sampling system. Due to issues encountered with the LVI, an $SO_3$ generation system was developed and used for aerosol tests during this campaign. Greater detail on the $SO_3$ generator can be found in Chapter 3.

### 5.2.1 Process Overview

Previous campaigns at the UT-SRP pilot plant utilized an absorber with two packed beds and intercooling, with piperazine as the amine solvent. A designated water wash column was not used; instead, the flue gas from the outlet of the absorber was passed through an air chiller to condense volatile components, and then through a knockout drum and filter to remove entrained drops. This is presented in Figure 5.2.

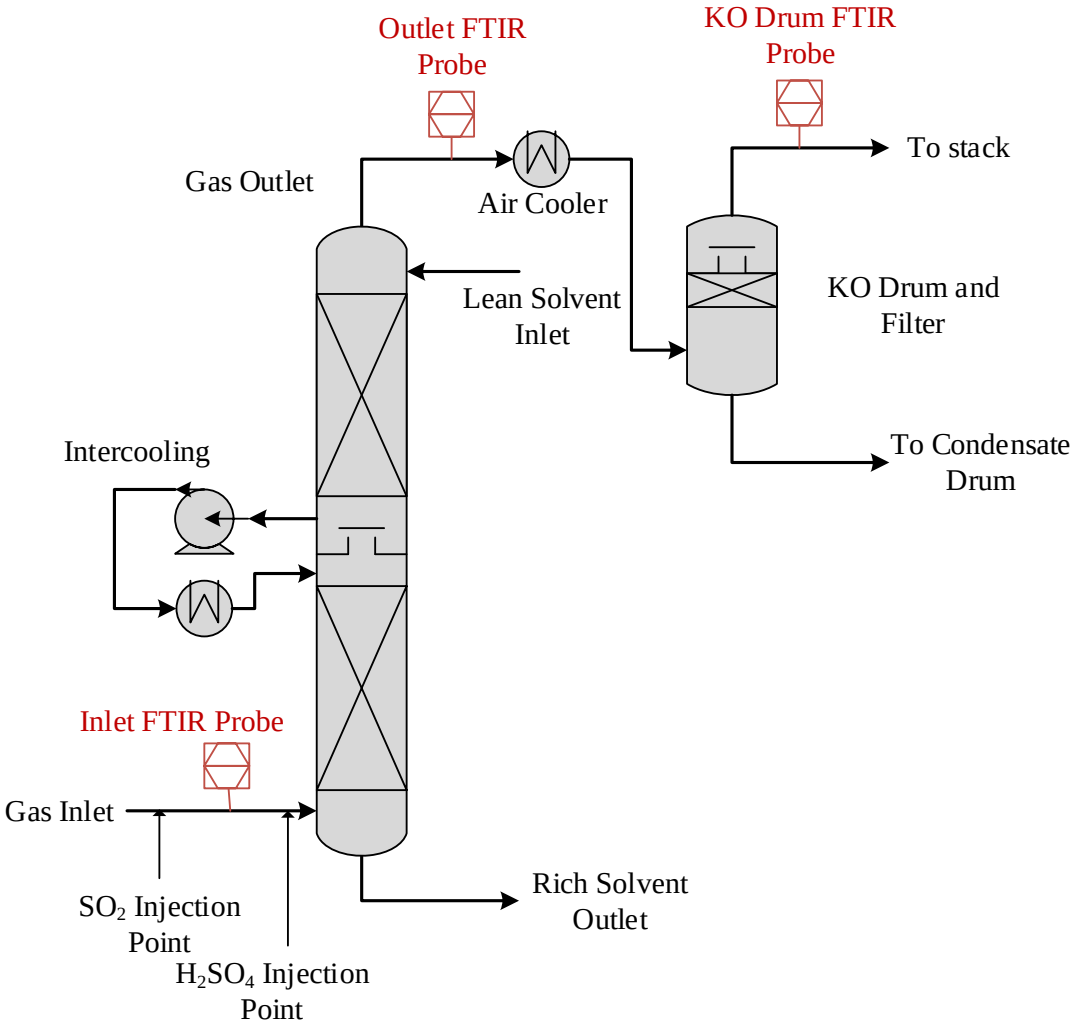


**Figure 5.2: Gas side of previous iteration of the UT-SRP pilot plant. FTIR sampling locations are marked in red.**

The main modification added prior to the April 2017 campaign was a third 10' bed of packing. This was designed to be used either as a third bed for $CO_2$ absorption, or as a water wash. RSR-250 structured packing was used in this bed. Figure 5.3 gives an updated process flow diagram with the additional packing bed.

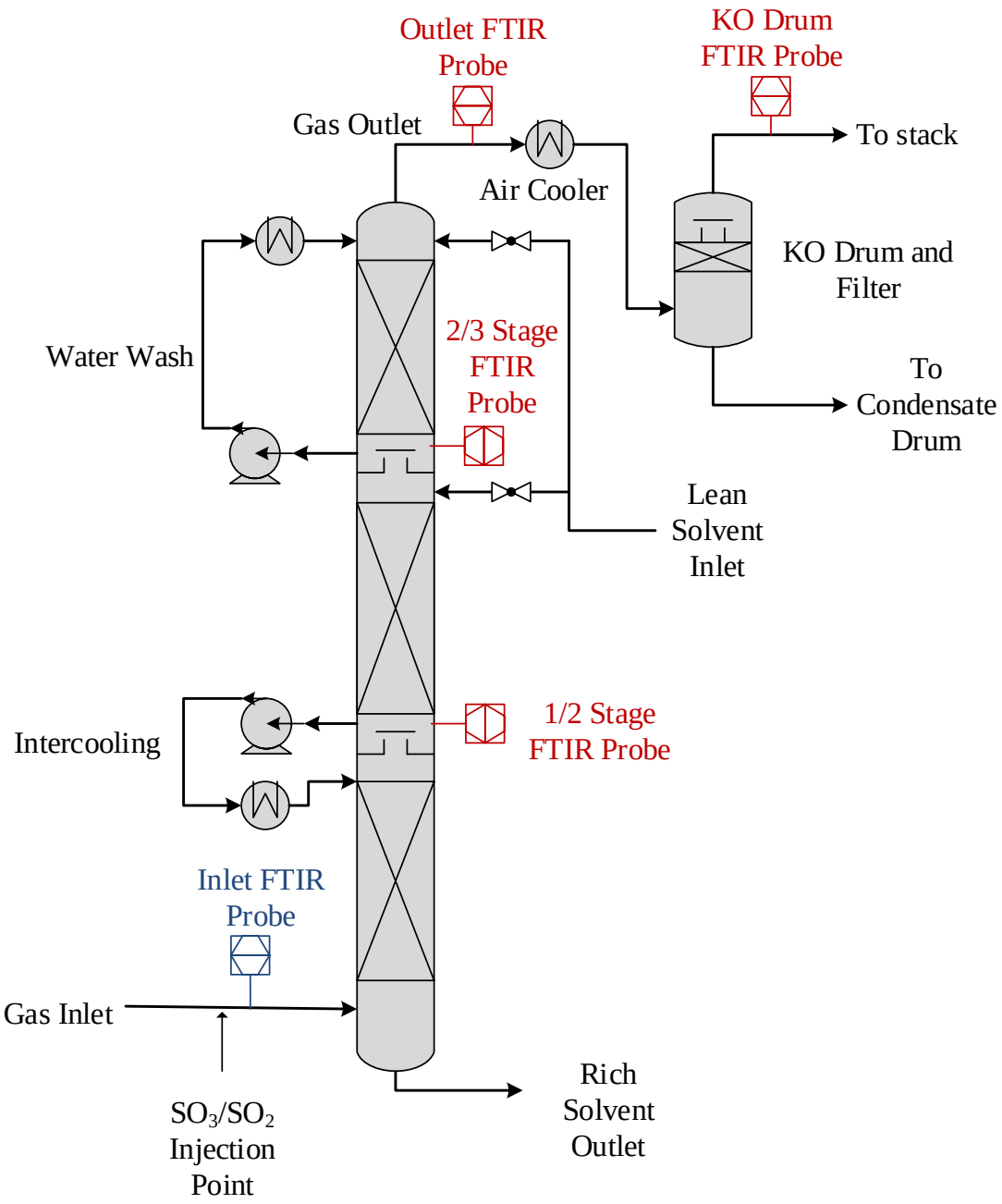


**Figure 5.3: Gas side of UT-SRP pilot plant for April 2017 campaign. Rotating FTIR sampling locations are marked in red. The designated inlet FTIR sample point is marked in blue.**

Further upgrades to the UT-SRP process included an expansion of the advanced flash stripper to allow for increased $CO_2$ flow rates.

### 5.2.2 FTIR Sampling

As evidenced in Figure 5.3, expansions were made to the UT-SRP FTIR sampling system. The first modification involved the addition of a second FTIR analyzer. This unit is a GASMET™ CX-4000 and is identical to the existing analyzer used during previous UT-SRP campaigns. This FTIR is dedicated to performing absorber inlet measurements, and is interfaced with the DeltaV™ control system for use in controlling the process inlet $CO_2$. Further details on this analyzer and supporting systems are presented in Chapter 2 and Appendix C.

The original FTIR analyzer, another GASMET™ CX-4000, samples from four different locations in the process. This is indicated in Figure 5.3 by the red sampling locations. Two additional FTIR sample points were added for the April 2017 campaign: one between the first and second stage of packing, and another between the second and third. Figure 5.4 presents the probe between the first and second stages, and Figure 5.5 shows the probe between the second and third stages.

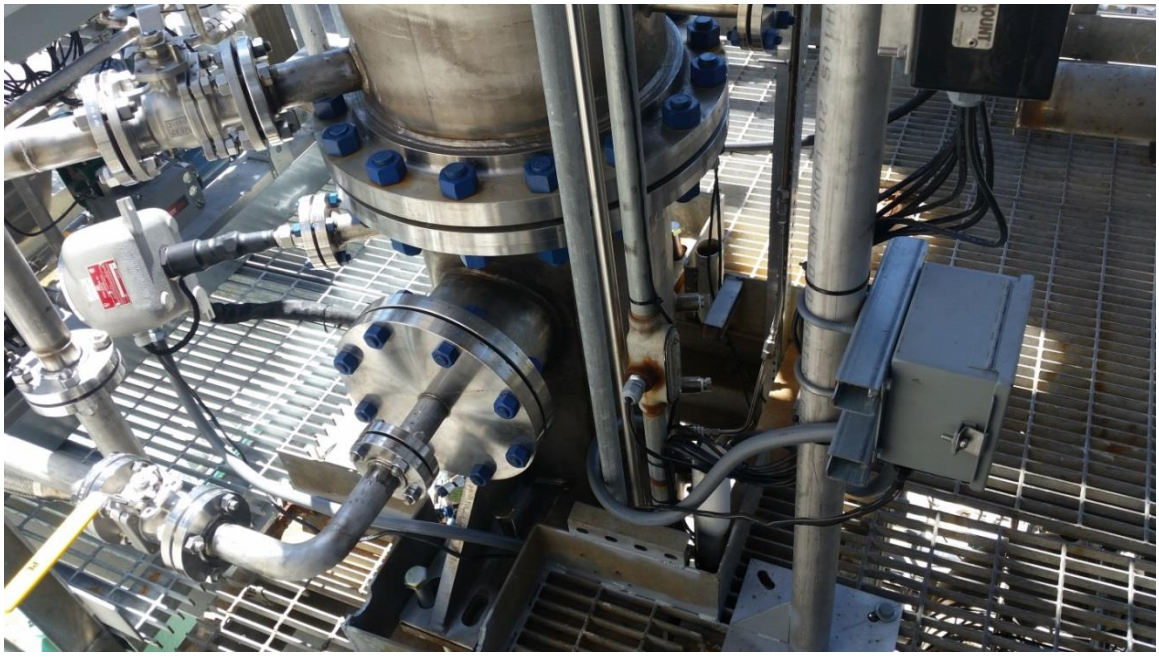

**Figure 5.4: FTIR probe (to the left) for sample extraction between first and second stages of packing at UT-SRP pilot plant.**

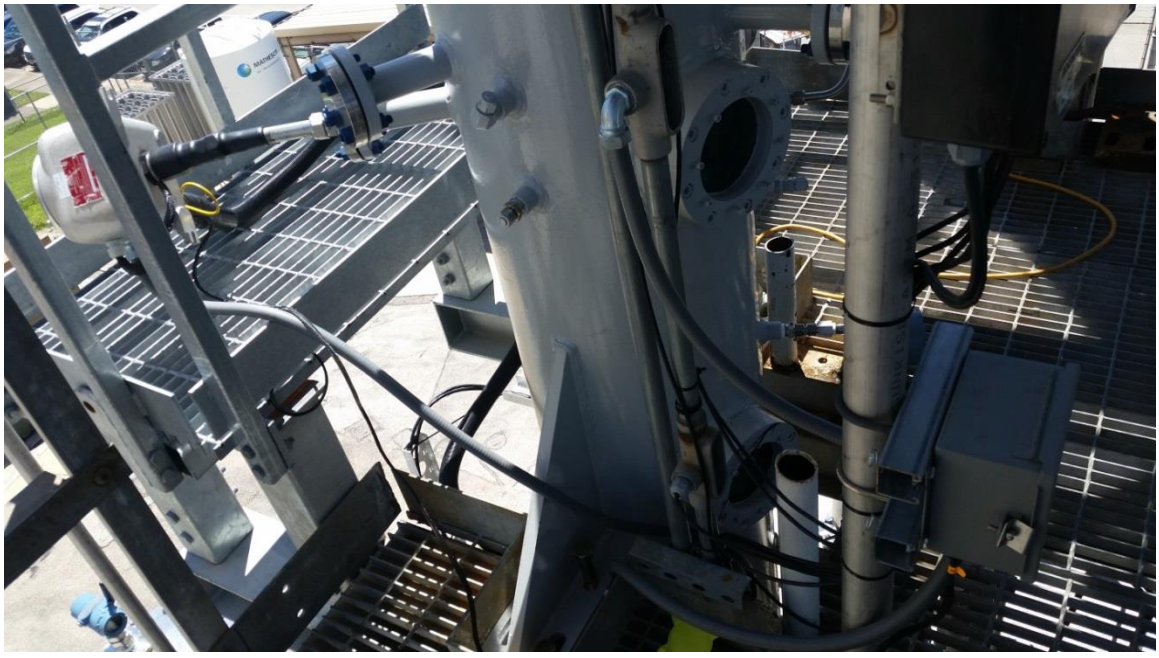

**Figure 5.5: FTIR probe (to the left) for sample extraction between second and third stages of packing at UT-SRP pilot plant.**

Samples extracted for analysis by this FTIR are passed via heated sample lines to the Multi-point Heated Sample Switching System (MSSH). The MSSH is linked to the DeltaV™ control system; this can be used to select the sample location for FTIR analysis. Further details on the setup and operation of this system are available in Chapter 2 and Appendix C. Standard operating procedures for FTIR operations are available in Appendix A.

### 5.2.3 $SO_3$ Generation

The difficulties in $H_2SO_4$ vaporization and injection led to the development of an $SO_3$ generator. The $SO_3$ generator operates by oxidizing $SO_2$ in air over a heated vanadium pentoxide catalyst bed; a schematic of this process is presented in Figure 5.6. Flow is controlled through the catalyst bed by precision rotameters. The 1" OD catalyst bed makes two 36" passes through a tube furnace maintained at 520 °C, as presented in Figure 5.7. Gas from the outlet of the generator is fed to the UT-SRP absorber inlet at a location upstream of the inlet FTIR sample point. A $N_2$ purge is used during startup and shutdown of the generator, while a mix of 8% $SO_2$ in air is used as feedstock for the $SO_3$ generation. Chapter 2 of this work provides additional details on the $SO_3$ generator.

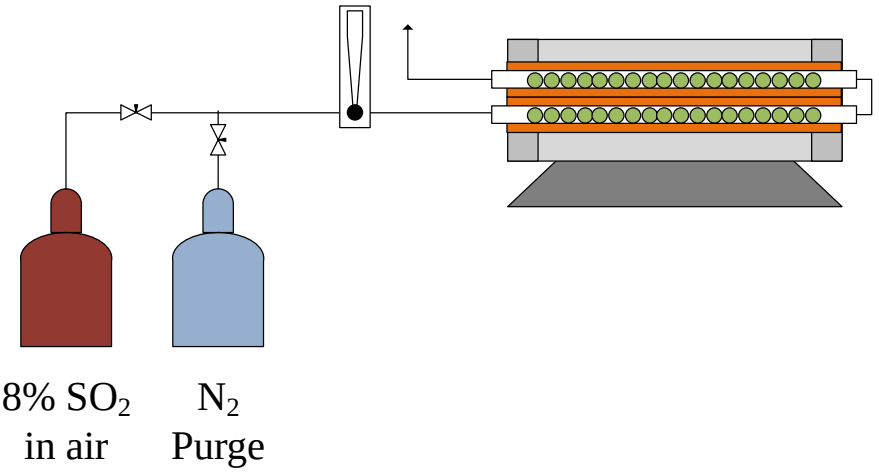


**Figure 5.6: $SO_3$ generator used in UT-SRP April 2017 campaign**

**Figure 5.7: Heated tube furnace with catalyst bed for $SO_3$ generation**

## 5.3 RESULTS

### 5.3.1 $SO_3$ Generation Tests

Over the course of the April 2017 campaign, 16 different aerosol tests were performed. 8% $SO_2$ in air was fed at 20 psig to the $SO_3$ generator. Flow rates were varied for each test. Table 5.1 presents pertinent $SO_3$ generation results for each test.

**Table 5.1: UT-SRP April 2017 $SO_3$ injection summary**

| Run | Campaign Condition | Date | Start Time | End Time | Inlet Flow Rate | $SO_3$ Generated | $SO_3$ Conc. |
|---|---|---|---|---|---|---|---|
| # | # | | *hh:mm* | *hh:mm* | *LPM* | *g/min* | *ppm* |
| **1** | 16 | 4/26/17 | 14:12 | 15:30 | 5.0 | 1.34 | 52 |
| **2** | 21 | 4/27/17 | 18:05 | 20:00 | 1.0 | 0.23 | 9 |
| **3** | 21 | 4/27/17 | 20:00 | 20:33 | 5.0 | 1.32 | 51 |
| **4** | 19 | 5/1/17 | 13:20 | 15:19 | 2.0 | 0.52 | 20 |
| **5** | 22 | 5/2/17 | 12:43 | 13:00 | 6.0 | 1.68 | 112 |
| **6** | 22 | 5/2/17 | 13:00 | 13:27 | 1.7 | 0.46 | 31 |
| **7** | 22 | 5/2/17 | 13:27 | 14:34 | 5.0 | 1.39 | 92 |
| **8** | 29 | 5/3/17 | 12:45 | 15:17 | 5.0 | 1.38 | 53 |
| **9** | 28 | 5/4/17 | 12:15 | 13:35 | 5.0 | 1.4 | 93 |
| **10** | 28 | 5/4/17 | 18:16 | 19:38 | 3.0 | 0.8 | 31 |
| **11** | 31 | 5/9/17 | 14:56 | 15:13 | 3.0 | 0.82 | 32 |
| **12** | 31 | 5/9/17 | 15:13 | 15:29 | 1.0 | 0.26 | 10 |
| **13** | 31 | 5/9/17 | 15:29 | 16:11 | 2.0 | 0.54 | 21 |
| **14** | 31 | 5/9/17 | 16:11 | 17:09 | 1.0 | 0.26 | 10 |
| **15** | 17B | 5/10/17 | 9:12 | 9:42 | 3.0 | 0.83 | 32 |
| **16** | 17B | 5/10/17 | 9:42 | 10:54 | 1.0 | 0.27 | 10 |

The 16 different $SO_3$ injection tests spanned 8 different process run conditions. This resulted in almost 17 total hours of aerosol testing. $SO_2$/Air flow rates varied between 1.0 and 6.0 LPM, producing between 0.23 and 1.68 grams $SO_3$/minute. The resulting inlet $SO_3$ varied from 9 to 112 ppm.

### 5.3.2 Tabulated Amine Emission Results

Amine in the gas was measured by FTIR sampling at four locations within the process, as outlined in Figure 5.3: between the first and second stages of packing, between the second and third stages, at the third stage outlet, and at the knockout drum outlet. Figure 5.8 presents an example FTIR readout for this sampling. The MSSH is

used to rotate through the different sample locations. This aerosol test was performed on 5/1/17, and involved generating 0.52 grams $SO_3$/minute to produce 20 ppm inlet $SO_3$.

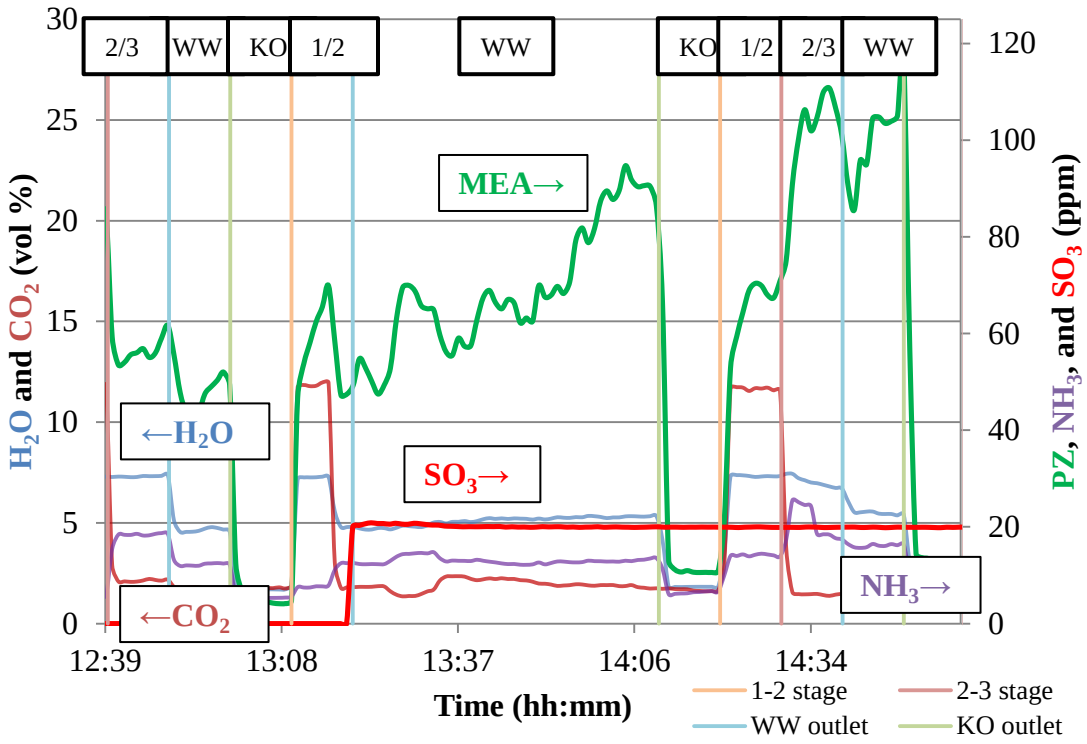


**Figure 5.8: FTIR results for 5/1/17 $SO_3$ generation aerosol tests. FTIR sampling locations are labeled at the top of the plot, with time on the bottom axis. 0.52 grams per minute of $SO_3$ were injected.**

Over the course of this aerosol test, amine emissions at the water wash outlet increased from 50 to 120 ppm. Amine between the first and second stages of packing remained relatively unchanged. However, amine between the second and third stages (the absorber stage outlet) increased from 60 to 110 ppm, and emissions from the knockout drum increased from 4 to 12 ppm. Figure 5.9 gives visual evidence of aerosol formation through emission at the flue gas outlet.

**Figure 5.9: Aerosol emissions from $SO_3$ generation and injection during April 2017 UT-SRP campaign**

Tables 5.2 through 5.5 summarize the FTIR amine analysis for each of the 16 aerosol tests. Table 5.2 presents baseline piperazine at each of the four FTIR sample locations. The piperazine at each FTIR sample location during $SO_3$ injection experiments is presented in Table 5.3. Table 5.4 gives the amine increase at each stage during the aerosol injection tests, or the amine with the baseline values subtracted out (Table 5.3 minus Table 5.2). Finally, the ratios of the increase in piperazine increase to $SO_3$ injected are presented in Table 5.5.

**Table 5.2: Baseline piperazine at each FTIR sample point for $SO_3$ injection experiments.**

| Run | Date | 1/2 Stage | 2/3 Stage | WW Out | KO Out |
|---|---|---|---|---|---|
| # | | *ppm* | *ppm* | *ppm* | *ppm* |
| **1** | 4/26/17 | 6 | 20 | 31 | 3 |
| **2** | 4/27/17 | 13 | 23 | 14 | 1 |
| **3** | 4/27/17 | 13 | 23 | 14 | 1 |
| **4** | 5/1/17 | 65 | 56 | 50 | 4 |
| **5** | 5/2/17 | 16 | 30 | 35 | 2 |
| **6** | 5/2/17 | 16 | 30 | 35 | 2 |
| **7** | 5/2/17 | 16 | 30 | 35 | 2 |
| **8** | 5/3/17 | 19 | 106 | 102 | 2 |
| **9** | 5/4/17 | 16 | 15 | 18 | 1 |
| **10** | 5/4/17 | 9 | 6 | 54 | 6 |
| **11** | 5/9/17 | 3 | 7 | 40 | 7 |
| **12** | 5/9/17 | 3 | 7 | 40 | 7 |
| **13** | 5/9/17 | 3 | 7 | 40 | 7 |
| **14** | 5/9/17 | 3 | 7 | 40 | 7 |
| **15** | 5/10/17 | 5 | 6 | 9 | 4 |
| **16** | 5/10/17 | 5 | 6 | 9 | 4 |

In Tables 5.3, 5.4, and 5.5 '-' represent when no sample was taken at that location.

**Table 5.3: $SO_3$ injection rates and corresponding piperazine at each FTIR sample point for each $SO_3$ injection experiment.**

| Run | Date | $SO_3$ Conc. | 1/2 Stage | 2/3 Stage | WW Out | KO Out |
|---|---|---|---|---|---|---|
| # | | *ppm* | *ppm* | *ppm* | *ppm* | *ppm* |
| **1** | 4/26/17 | 52 | 12 | 48 | 137 | 116 |
| **2** | 4/27/17 | 9 | 60 | 60 | 82 | 9 |
| **3** | 4/27/17 | 51 | 94 | 77 | 170 | 50 |
| **4** | 5/1/17 | 20 | 69 | 105 | 117 | 13 |
| **5** | 5/2/17 | 112 | - | - | 64 | - |
| **6** | 5/2/17 | 31 | - | - | 50 | - |
| **7** | 5/2/17 | 92 | 15 | 44 | 152 | 6 |
| **8** | 5/3/17 | 53 | 27 | 202 | 172 | 9 |
| **9** | 5/4/17 | 93 | 96 | 74 | 189 | 20 |
| **10** | 5/4/17 | 31 | 15 | 33 | 124 | 24 |
| **11** | 5/9/17 | 32 | - | - | 46 | - |
| **12** | 5/9/17 | 10 | - | - | 38 | - |
| **13** | 5/9/17 | 21 | - | - | 36 | - |
| **14** | 5/9/17 | 10 | 3 | 27 | 41 | 6 |
| **15** | 5/10/17 | 32 | - | - | 9 | - |
| **16** | 5/10/17 | 10 | 60 | 6 | 11 | 3 |

**Table 5.4: $SO_3$ injection rates and corresponding piperazine increase at each FTIR sample point for each $SO_3$ injection experiment.**

| Run | Date | $SO_3$ | 1/2 Stage | 2/3 Stage | WW Out | KO Out |
|---|---|---|---|---|---|---|
| # | | *ppm* | *ppm* | *ppm* | *ppm* | *ppm* |
| **1** | 4/26/17 | 52 | 6 | 28 | 106 | 113 |
| **2** | 4/27/17 | 9 | 47 | 37 | 68 | 8 |
| **3** | 4/27/17 | 51 | 81 | 54 | 156 | 49 |
| **4** | 5/1/17 | 20 | 4 | 49 | 67 | 9 |
| **5** | 5/2/17 | 112 | - | - | 29 | - |
| **6** | 5/2/17 | 31 | - | - | 15 | - |
| **7** | 5/2/17 | 92 | 0 | 14 | 117 | 4 |
| **8** | 5/3/17 | 53 | 8 | 96 | 70 | 7 |
| **9** | 5/4/17 | 93 | 80 | 59 | 171 | 19 |
| **10** | 5/4/17 | 31 | 6 | 27 | 70 | 18 |
| **11** | 5/9/17 | 32 | - | - | 6 | - |
| **12** | 5/9/17 | 10 | - | - | 0 | - |
| **13** | 5/9/17 | 21 | - | - | 0 | - |
| **14** | 5/9/17 | 10 | 0 | 20 | 1 | 0 |
| **15** | 5/10/17 | 32 | - | - | 0 | - |
| **16** | 5/10/17 | 10 | 55 | 0 | 2 | 0 |

**Table 5.5: $SO_3$ injection rates, and ratios of piperazine increase per ppm of $SO_3$ injected at each FTIR sample point for $SO_3$ injection experiments.**

| Run | Date | $SO_3$ Conc. | 1/2 Stage | 2/3 Stage | WW Out | KO Out |
|---|---|---|---|---|---|---|
| # | | *ppm* | *ppm* | *ppm* | *ppm* | *ppm* |
| **1** | 4/26/17 | 52 | 0.12 | 0.54 | 2.04 | 2.18 |
| **2** | 4/27/17 | 9 | 5.23 | 4.11 | 7.56 | 0.89 |
| **3** | 4/27/17 | 51 | 1.59 | 1.06 | 3.07 | 0.96 |
| **4** | 5/1/17 | 20 | 0.20 | 2.45 | 3.35 | 0.45 |
| **5** | 5/2/17 | 112 | - | - | 0.26 | - |
| **6** | 5/2/17 | 31 | - | - | 0.49 | - |
| **7** | 5/2/17 | 92 | 0.00 | 0.15 | 1.27 | 0.04 |
| **8** | 5/3/17 | 53 | 0.15 | 1.80 | 1.31 | 0.13 |
| **9** | 5/4/17 | 93 | 0.86 | 0.64 | 1.85 | 0.21 |
| **10** | 5/4/17 | 31 | 0.19 | 0.87 | 2.26 | 0.58 |
| **11** | 5/9/17 | 32 | - | - | 0.19 | - |
| **12** | 5/9/17 | 10 | - | - | 0.00 | - |
| **13** | 5/9/17 | 21 | - | - | 0.00 | - |
| **14** | 5/9/17 | 10 | 0.00 | 2.02 | 0.10 | 0.00 |
| **15** | 5/10/17 | 32 | - | - | 0.00 | - |
| **16** | 5/10/17 | 10 | 5.32 | 0.00 | 0.19 | 0.00 |

$SO_3$ aerosol caused piperazine between the first and second stages of absorber packing to increase at a ratio between 0 and 5.32 moles amine / mole $SO_3$. Between the second and third stages of packing, this ratio ranged from 0 to 4.11; after the third stage, between 0 and 7.56. The knockout drum outlet was the sampling location that showed the lowest effect from aerosol tests, with outlet amine increases ranging from 0 to 2.18 moles / mole of $SO_3$ in the inlet flue gas. This can be attributed to the effectiveness of the air chiller and knockout drum/filter at condensing and removing amine aerosol.

The third bed of packing was used as a water wash for experiments 1-9 and 15-16; during these tests, the amine at the water wash outlet was generally higher than the amine immediately upstream of the water wash (Table 5.3). This is an unexpected finding, as no amine is added to the process in the water wash.

This was theorized to be due to an excessive amine buildup in the water wash solvent; however, this is refuted by a lack of correlation between amine emissions and the water wash amine content, as presented later in this chapter. The current hypothesis is that the actual amount of amine is not varying between the water wash inlet and outlet, but the water wash is condensing water from the vapor phase. This is changing the net flow rates at each sample point, giving a higher amine concentrations at the water wash outlet than the inlet. Due to a lack of sensitivity in FTIR measurements with respect to water, this is difficult to prove. Water is measured on a volume percent basis, which is 10,000 times the ppm basis of amine measurements. Further investigation is recommended to resolve this phenomenon.

### 5.3.3 Inlet $SO_3$

The construction of the $SO_3$ generator has allowed for safe and reliable production of aerosol nuclei. Just as importantly, this generator allows the aerosol concentration to be easily varied by adjusting the feedstock flow rate. Previous research has shown that increasing the amount of aerosol nuclei leads to an increase in amine emissions at amine-scrubbing $CO_2$ capture facilities (Kamijo, 2013; Khakharia, 2015). With the development of the $SO_3$ generator at UT Austin, this observation could be tested with piperazine solvent.

An experiment varying the inlet $SO_3$ was performed on 5/2/2017. The $SO_2$/Air feed to the $SO_3$ generator was increased from 1.7 to 5.0 LPM. This increased the production rate of $SO_3$ from 0.46 to 1.39 grams per minute, and caused an increase in the absorber inlet $SO_3$ from 31 ppm to 92 ppm. Figure 5.10 presents the FTIR measurements from this process change.

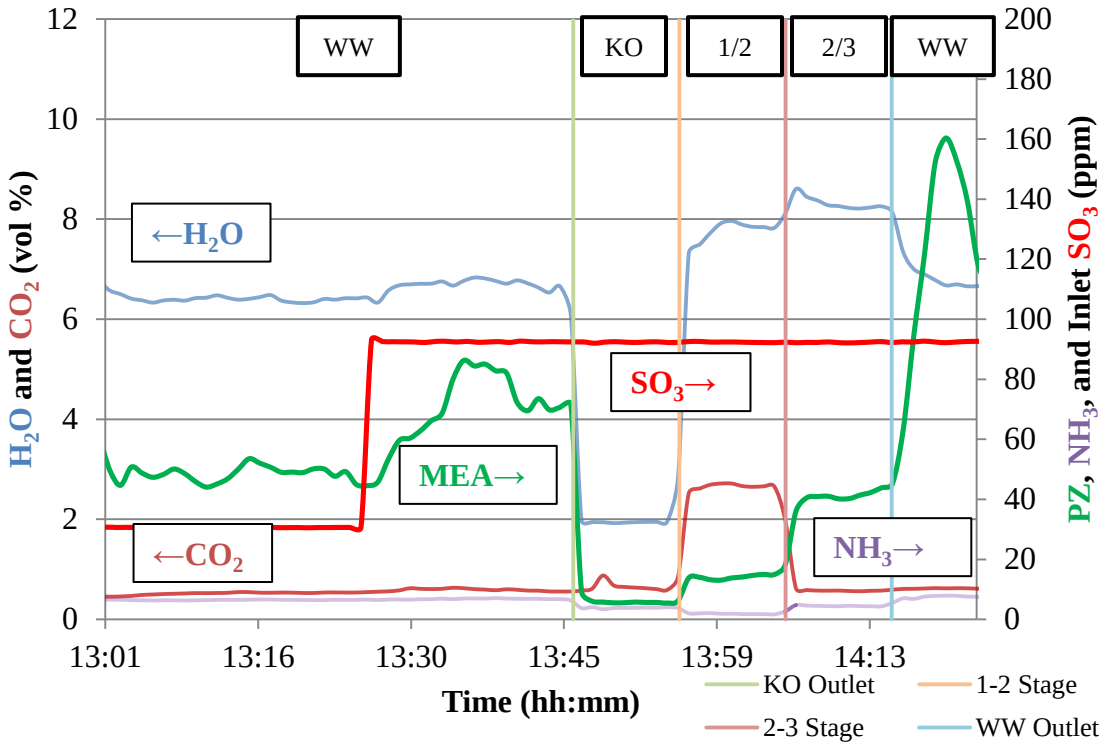


**Figure 5.10: FTIR measurements with increasing inlet $SO_3$**

Piperazine emissions at the water wash outlet increased from 50 ppm to peaks at roughly 160 ppm through an increase in the inlet $SO_3$. Figure 5.11 presents the net piperazine emission increase per ppm of inlet $SO_3$ for each aerosol experiment.

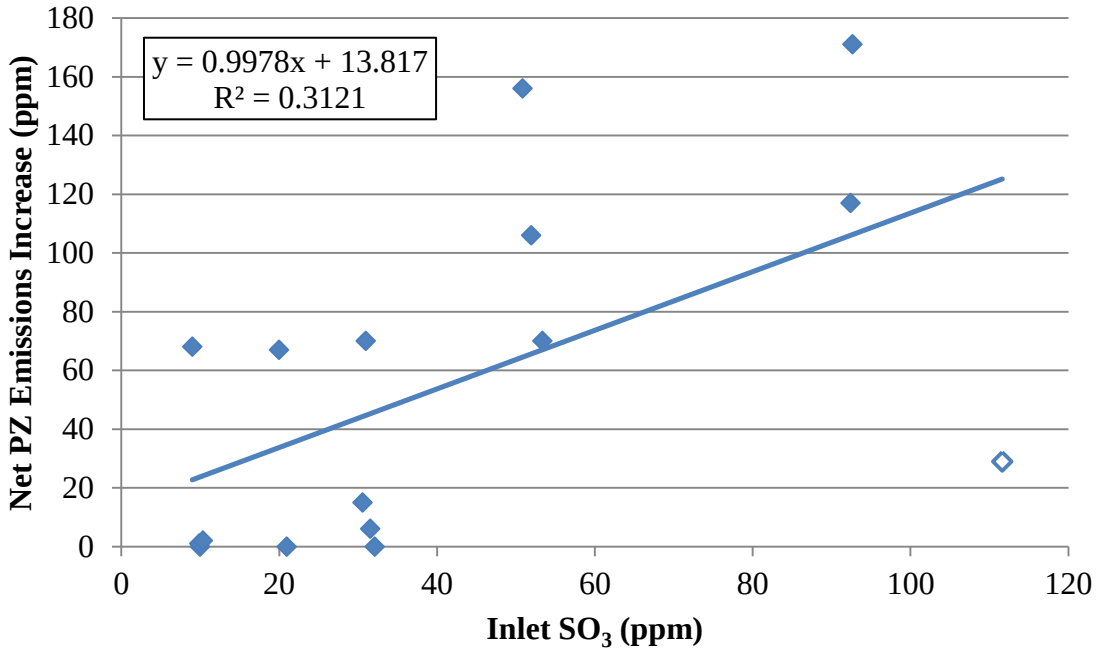


**Figure 5.11: Net piperazine emissions increase as a function of inlet $SO_3$**

As the inlet gas $SO_3$ content increases, the outlet net piperazine emissions increase. Piperazine solvent showed resistance to emissions through aerosol. During aerosol tests, 30 ppm of $SO_3$ was often insufficient to produce a measureable amine emission increase. One test injecting 112 ppm of $SO_3$ only increased piperazine emissions by 29 ppm; this test is indicated by the unfilled marker in Figure 5.11.

Piperazine appears to be significantly more resistant to aerosol emissions than monoethanolamine (MEA). At the National Carbon Capture Center, inlet $SO_3$ to the Slipstream Solvent Test Unit (SSTU) ranged from 7 to 9 ppm (J. Anthony, personal communication, 2/20/2017). This resulted in MEA emissions at the SSTU water wash outlet in excess of 100 ppm, as shown in Chapter 6 of this work and by Carter (2012). MEA aerosol emissions at MHI were observed to increase to 30 ppm with 1 ppm of $SO_3$,

and to almost 70 ppm with 3 ppm of $SO_3$ (Kamijo, 2013). Research at the Institute for Technical Thermodynamics and Refrigeration (ITTK) at Karlsruhe Institute of Technology (KIT) has confirmed a strong increase in MEA aerosol emissions with increasing inlet $SO_3$ content (Khakharia, 2013; Brachert, 2013; Brachert, 2014; Mertens, 2014a).

Work by Zhang has hypothesized on why piperazine is more resistant to aerosol emissions than MEA (Zhang, 2017). Aerosol growth and amine condensation into the aerosol drops are largely functions of the piperazine driving forces between the bulk gas, bulk solvent, and the aerosol. The aerosol condensation driving forces are significantly impacted by the aerosol nuclei concentration. With a lower concentration of aerosol nuclei, aerosol drop growth is limited by the bulk gas to the aerosol phase. This results in a relatively low number of very large aerosol drops; these large drops are collected by impaction within the process.

At a higher aerosol nuclei concentration, aerosol drop growth is limited by the driving force from the bulk solvent to the bulk gas. Amine in the bulk gas rapidly condenses into the aerosol drops. Due to the high availability of aerosol nuclei to condense into, each aerosol drop does not grow to as large of a size as possible in a low nuclei concentration environment. Less aerosol are collected in the process due to impaction forces, which results in a subsequent increase in the amine emitted to the atmosphere.

Summarily, piperazine does readily form aerosol in the presence of $SO_3$. At lower quantities of $SO_3$, the gas phase piperazine rapidly condenses into the aerosol

drops, causing growth to a point that allows for collection within the process. As the inlet $SO_3$ increases, an excess of available aerosol nuclei limits the growth rate for the aerosol drops; this leads to a higher quantity of smaller aerosol drops that are not captured by impaction.

### 5.3.4 Water Wash Operating Conditions

The effects of varying water wash conditions were investigated. Prior research has observed that water washes have been ineffective at mitigating aerosol emissions (Mertens, 2013; Mertens, 2014; Khakharia, 2015). This is due to the inability of the washing column packing to collect aerosol through impaction as the aerosol travel along a Brownian diffusion "random walk" pathway.

A main focus of this research is on using process operation parameters to mitigate aerosol emissions. This can be achieved by shrinking aerosol to a size small enough to not cause significant amine emissions, or to grow aerosol to a size large enough to be collected by impaction in the process. Changing the water wash solvent properties can potentially condition the aerosol to grow or shrink, thus affecting the amine emissions. Tests with varying the water wash flow rate and temperature were performed on 5/3/17. The $SO_3$ generator produced 1.4 grams per minute of $SO_3$, resulting in 53 ppm of $SO_3$ at the absorber inlet. FTIR measurements over the test time frame are presented in Figure 5.12.

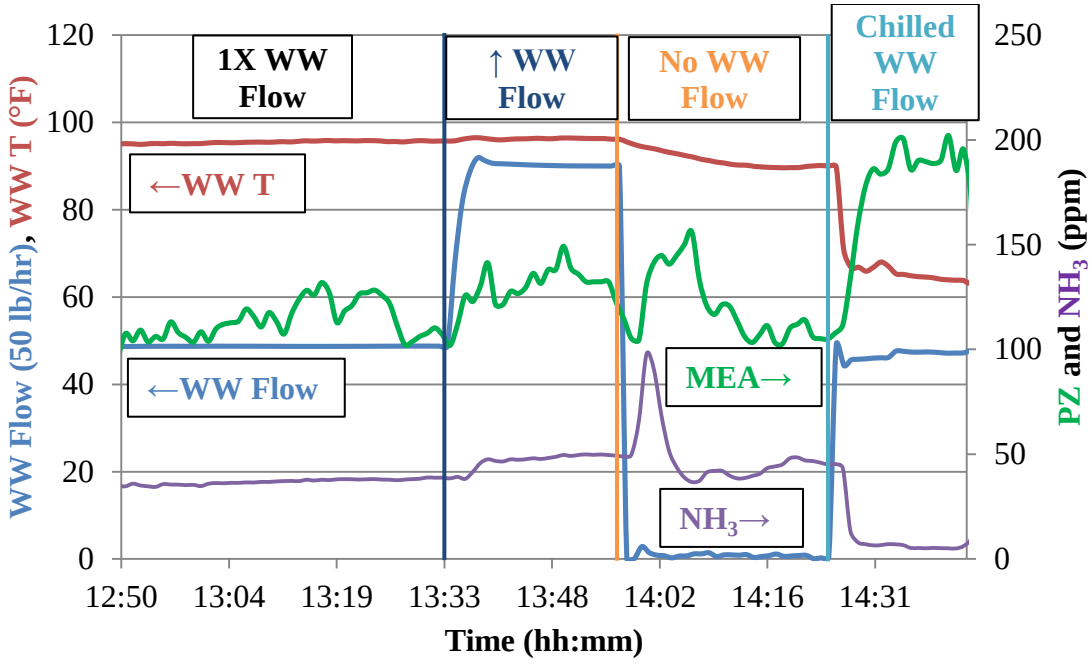


**Figure 5.12: FTIR observed effects on amine emissions from varying water wash flow rate and solvent temperature**

The water wash was initially operating with a flow rate of 2000 lb/hr and an inlet temperature of 96 °F. During this time, amine emissions from the water wash outlet ranged from 110 to 130 ppm. At 13:34, the water wash flow rate was increased to 4500 lb/hr, as indicated by the dark blue vertical line in Figure 5.12. This resulted in an increase in the piperazine emissions to 120-150 ppm.

The water wash flow was stopped completely at 13:58, as represented by the orange vertical line in Figure 5.12. Upon reaching steady state, the amine at the water wash outlet was determined to be roughly 110 ppm. Without temperature changes, increasing the water wash flow rate increases the amine at the water wash outlet.

The impact of the water wash solvent temperature was subsequently investigated. Water wash flow was resumed at 2000 lb/hr, but was returned to the process at a set point temperature of 65 °F instead of 95 °F. The light blue vertical line in Figure 5.12 indicates this process change. This resulted in a dramatic increase in piperazine emissions, from 110 ppm to 190-200 ppm. This concentration increase is not an artifact of reduced total flow due to the condensation of water, as evidenced by significant decrease in the $NH_3$ concentration. The cooler water wash condenses gas-phase volatile components but increases amine aerosol emissions.

Decreases in the water wash solvent temperature lead to a reduction of the temperature in the gas phase at the water wash outlet. This temperature drop increases condensation of water vapor from the gas phase into the bulk liquid, leading to a reduction in the sizes of aerosol drops. It is hypothesized that, at higher temperature, the larger aerosol are impacting on packing and physical features within the process, and are not emitted to the atmosphere. At lower temperature, the aerosol are smaller and are not collected through impaction; these aerosol are subsequently released to the atmosphere, increasing the amine emissions. Summarily, amine emissions at the UT-SRP pilot plant are found to decrease by operating the water wash at a lower flow rate and a higher temperature.

## 5.4 AMINE EMISSIONS CORRELATIONS

Upgrades in aerosol generation and process parameter measurements in the April 2017 UT-SRP pilot plant campaign allowed for significant improvements in amine aerosol data collection. The $SO_3$ generator allows for repeatable production rates for

aerosol nuclei. The upgrades to the UT-SRP plant prior to the campaign included increasing temperature measurements in the absorber column, improved flow meters, and dedicated FTIR measurement of the process inlet gas for $CO_2$ composition control.

During aerosol testing, process parameters were held at a reasonable approximation of steady state, with the exception of the water wash testing. This allows average values for process conditions to be obtained for parameters that could potentially impact amine aerosol emissions. By using the average values for process parameters, statistical regression analysis can be performed to determine the extent of correlation between process parameters and amine emissions. Due to the large number of process parameters, the following sections are divided by the process type: temperature, liquid flow rate, gas phase composition, and solvent composition.

### 5.4.1 Temperature Correlations with Amine Emissions

Eight different average temperatures are observed in relation to the amine emissions. These are presented in Table 5.6. The bottom, middle, and top bed temperature are obtained by averaging the values from six temperature probes in each section over the length of the aerosol test. The inlet and outlet gas temperatures are taken from temperature probes at the absorber gas inlet and outlet, respectively. The top bed inlet temperature gives the average temperature of the solvent or water wash liquid. The middle bed presents the average temperature for solvent returned at this point, and the intercooling return temperature gives the average temperature of the solvent returned to the process downstream of the intercooler.

**Table 5.6: Average temperature values throughout UT-SRP absorber during aerosol tests**

| Run | Date | Bottom Bed | Middle Bed | Top Bed | Inlet Gas | Gas Out | Top Bed Inlet | Mid Bed Inlet | IC Return |
|---|---|---|---|---|---|---|---|---|---|
| # | | °F | °F | °F | °F | °F | °F | °F | °F |
| **1** | 4/26/17 | 104.6 | 112.2 | 93.7 | 92.6 | 90.3 | 75.1 | 106.3 | 103.7 |
| **2** | 4/27/17 | 98.7 | 106.8 | 78.1 | 83.6 | 76.6 | 75.1 | 82.7 | 113.1 |
| **3** | 4/27/17 | 98.5 | 106.1 | 76.7 | 81.5 | 75.2 | 73.7 | 81.0 | 113.3 |
| **4** | 5/1/17 | 107.7 | 106.2 | 86.6 | 88.7 | 88.0 | 87.9 | 104.1 | 103.5 |
| **5** | 5/2/17 | 105.6 | 115.0 | 99.8 | 95.8 | 100.0 | 99.6 | 101.5 | 103.9 |
| **6** | 5/2/17 | 106.0 | 115.8 | 100.0 | 96.9 | 99.1 | 98.2 | 101.7 | 104.3 |
| **7** | 5/2/17 | 105.4 | 116.8 | 102.1 | 98.0 | 98.8 | 95.8 | 101.9 | 102.2 |
| **8** | 5/3/17 | 113.1 | 110.7 | 90.5 | 90.5 | 92.1 | 90.2 | 105.1 | 104.1 |
| **9** | 5/4/17 | 122.1 | 117.2 | 96.6 | 86.4 | 98.1 | 97.8 | 103.6 | 104.5 |
| **10** | 5/4/17 | 99.3 | 107.3 | 100.8 | 81.6 | 102.6 | 104.3 | 76.5 | 86.9 |
| **11** | 5/9/17 | 106.4 | 114.2 | 102.4 | 77.4 | 102.0 | 103.8 | 75.1 | 104.5 |
| **12** | 5/9/17 | 106.3 | 115.6 | 103.0 | 77.5 | 101.9 | 103.6 | 75.5 | 104.4 |
| **13** | 5/9/17 | 105.6 | 115.4 | 102.8 | 76.7 | 101.5 | 103.4 | 74.9 | 103.6 |
| **14** | 5/9/17 | 104.9 | 108.8 | 100.6 | 75.7 | 101.7 | 103.6 | 73.5 | 103.3 |
| **15** | 5/10/17 | 106.7 | 106.1 | 90.0 | 75.3 | 92.2 | 93.2 | 104.1 | 104.0 |
| **16** | 5/10/17 | 106.8 | 106.2 | 90.1 | 75.9 | 92.2 | 93.2 | 104.3 | 104.0 |

The average temperatures for each process location can be plotted with respect to amine emissions per mole of $SO_3$ injected. This is presented in Figures 5.13 through 5.15. These are broken up by bed temperatures, gas temperatures, and solvent/water wash inlet temperatures, respectively.

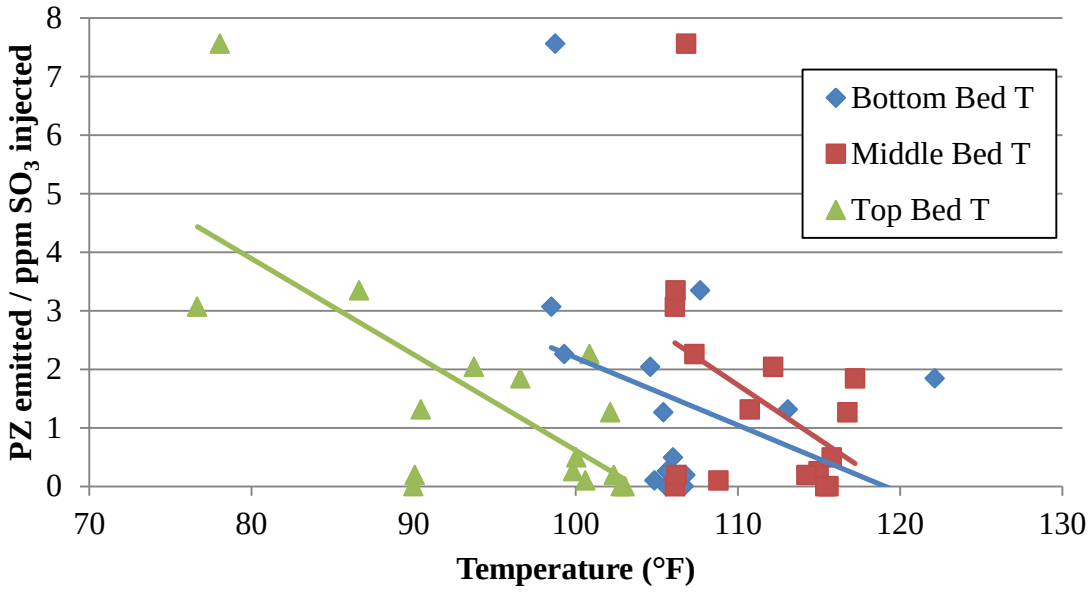


**Figure 5.13: Normalized amine emissions as a function of absorber bed temperatures**

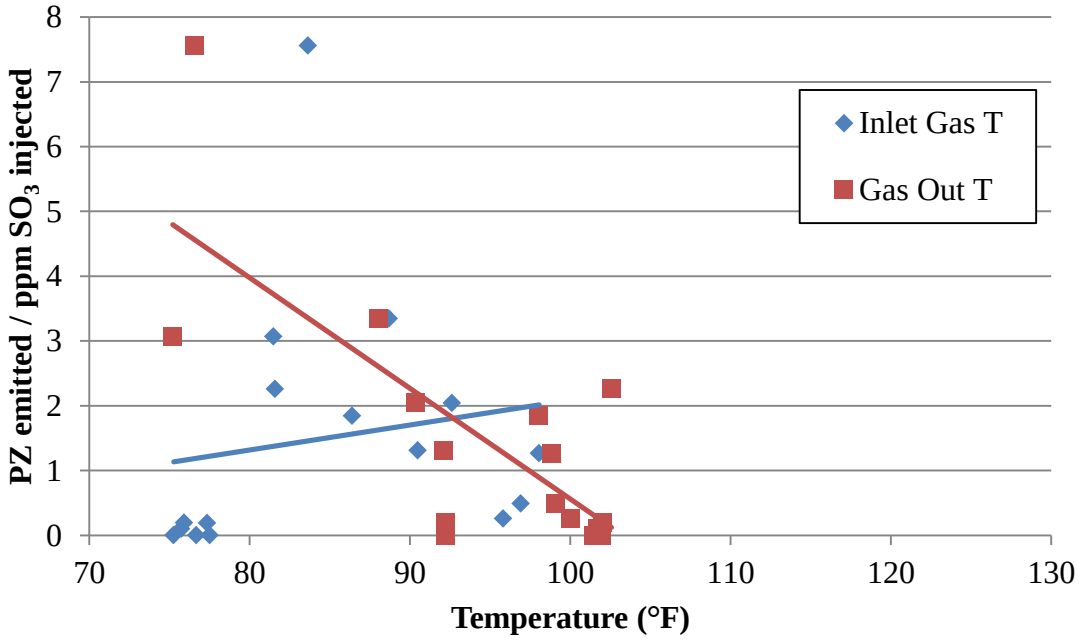

**Figure 5.14: Normalized amine emissions as a function of absorber inlet and outlet gas temperatures**

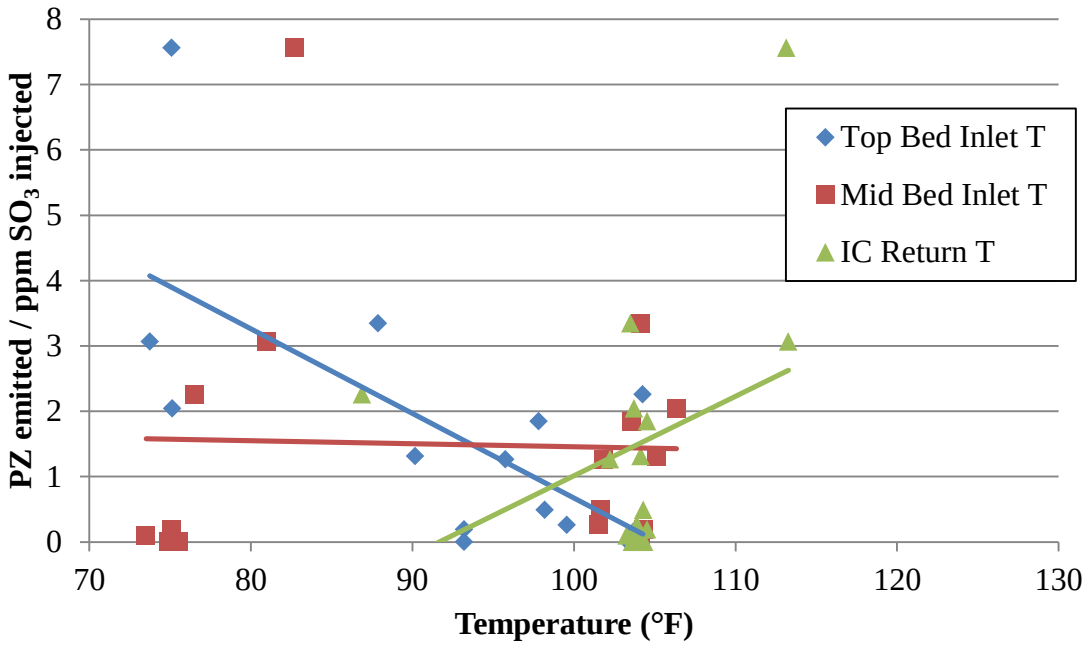


**Figure 5.15: Normalized amine emissions as a function of absorber solvent temperatures**

Table 5.7 gives the slopes and $R^2$ correlations for each of the temperature parameters.

**Table 5.7: Slope and $R^2$ correlations for absorber temperatures with respect to normalized amine emissions**

| Parameter | Slope | $R^2$ | Confidence (%) |
|---|---|---|---|
| **Bottom Bed T** | -0.12 | 0.11 | 31 |
| **Middle Bed T** | -0.19 | 0.17 | 31 |
| **Top Bed T** | -0.16 | 0.51 | 56 |
| **Inlet Gas T** | 0.04 | 0.03 | 19 |
| **Gas Out T** | -0.17 | 0.56 | 60 |
| **Top Bed Inlet T** | -0.13 | 0.49 | 52 |
| **Mid Bed Inlet T** | -0.00 | 0.00 | 20 |

| | | | |
|---|---|---|---|
| **IC Return T** | 0.12 | 0.12 | 33 |

Only the inlet gas temperature and the intercooling return temperature have positive trends, meaning that increasing the temperature generally increases the emissions. For all other temperature parameters, increasing the temperature decreases the amine emissions.

The top bed temperature, gas outlet temperature, and top bed solvent inlet temperature all have the highest $R^2$ correlations. This indicates that these parameters are the most relatable with the amine emissions. Gas temperatures are observed to generally have higher $R^2$ correlations than solvent temperatures, indicating that vapor phase conditions have a greater impact on aerosol emissions than the liquid solvent.

Regression analysis for all eight temperature parameters was performed. Table 5.8 presents the regression analysis results, while Figure 5.16 gives the regression model predicted normalized amine emissions in comparison to the actual normalized amine emissions.

**Table 5.8: Regression analysis results for absorber temperature parameters with respect to normalized amine emissions**

| | Normalized Amine Emissions | Standard Error |
|---|---|---|
| | *ppm* | |
| **$R^2$** | 0.78 | - |
| **Significance F** | 0.08 | - |
| **Standard Error** | 1.36 | - |
| ***Coefficients*** | | |
| **Intercept** | 34.01 | 17.92 |
| **Bottom Bed T** | 0.14 | 0.19 |
| **Middle Bed T** | -0.05 | 0.37 |
| **Top Bed T** | 0.18 | 0.74 |
| **Inlet Gas T** | 0.12 | 0.09 |
| **Gas Out T** | -0.51 | 0.85 |
| **Top Bed Inlet T** | 0.05 | 0.19 |
| **Mid Bed Inlet T** | -0.09 | 0.05 |
| **IC Return T** | -0.17 | 0.13 |

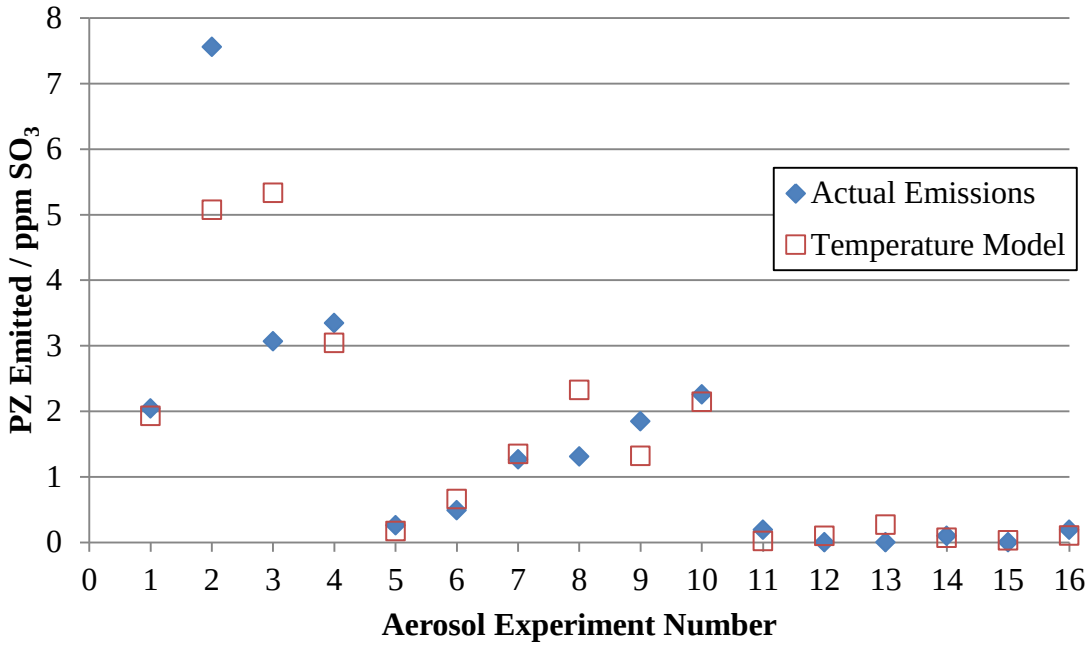


**Figure 5.16: Regression model predicted normalized amine emissions in comparison to the actual normalized amine emissions for absorber temperature parameters.**

The regression model performs best for aerosol tests that occurred later in the campaign; these tests also generally produced lower amine emissions per mole of $SO_3$ injected, and involved lower $SO_3$ generation rates. Overall the model was fairly effective at predicting the normalized amine emissions, with significant outliers in tests 2, 3, and 8. As this is a small sample size of only sixteen data points and 8 adjustable parameters, it is recommended that aerosol tests continue at future pilot plant campaigns to gather more data.

### 5.4.2 Flow Rate Correlations with Amine Emissions

Three different flow rate parameters were correlated to the normalized amine emissions. The average values for these parameters during each aerosol test are

presented in Table 5.9. The intercooling (IC) flow rate is the extraction and return flow rate for the intercooling system. The water wash flow rate is the flow rate for the water wash system when it was used. Finally, L/G is the ratio of the total solvent and gas flow rates through the absorber column.

**Table 5.9: Average flow rates throughout UT-SRP absorber during aerosol tests**

| Run | Date | IC Flow Rate | WW Flow Rate | L/G |
|---|---|---|---|---|
| *#* | | *lb/hr* | *lb/hr* | *mol/mol* |
| **1** | 4/26/17 | 4900 | 800 | 3.08 |
| **2** | 4/27/17 | 1400 | 1800 | 0.82 |
| **3** | 4/27/17 | 1400 | 1700 | 0.81 |
| **4** | 5/1/17 | 9900 | 2600 | 5.66 |
| **5** | 5/2/17 | 2700 | 3600 | 1.22 |
| **6** | 5/2/17 | 2700 | 3400 | 1.22 |
| **7** | 5/2/17 | 2700 | 2900 | 1.22 |
| **8** | 5/3/17 | 7100 | 2300 | 4.33 |
| **9** | 5/4/17 | 5400 | 2700 | 1.98 |
| **10** | 5/4/17 | 10000 | - | 5.90 |
| **11** | 5/9/17 | 8800 | - | 5.96 |
| **12** | 5/9/17 | 8800 | - | 5.89 |
| **13** | 5/9/17 | 8800 | - | 4.83 |
| **14** | 5/9/17 | 8700 | - | 4.83 |
| **15** | 5/10/17 | 10400 | 3600 | 4.82 |
| **16** | 5/10/17 | 10700 | 3500 | 4.79 |

The average flow rates for each aerosol experiment can be plotted with respect to amine emissions per mole of $SO_3$ injected. This is presented in Figure 5.17. L/G is multiplied by 1000 to scale with the intercooling and water wash flows.

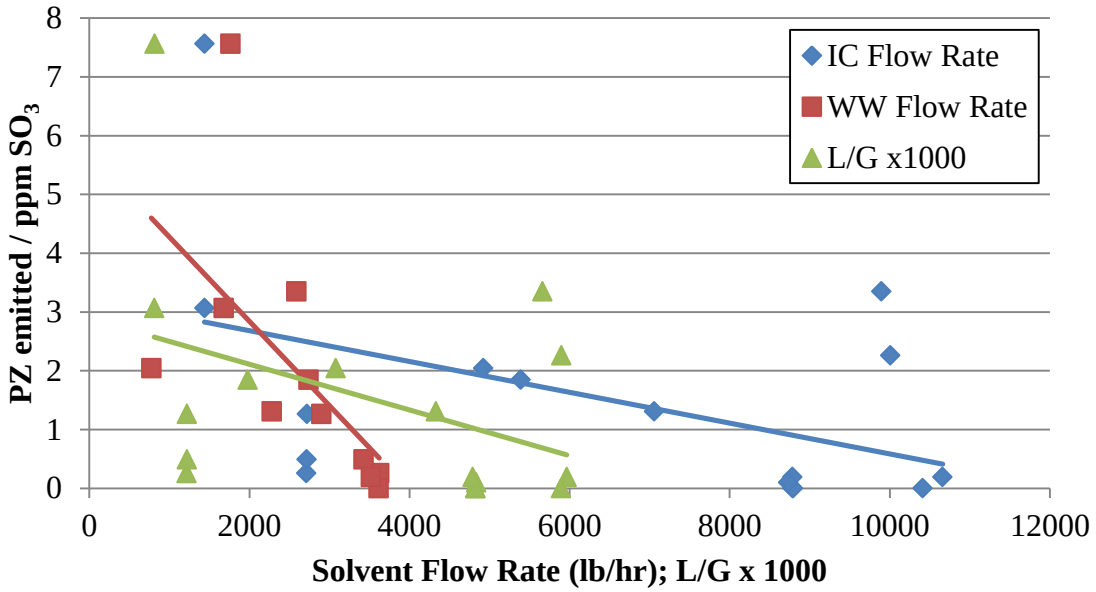


**Figure 5.17: Normalized amine emissions as a function of absorber flow intercooling flow rate, water wash flow rate, and L/G**

Table 5.10 gives the slopes and $R^2$ correlations for each of the flow rate parameters.

**Table 5.10: Slope and $R^2$ correlations for absorber flow rates with respect to normalized amine emissions**

| Parameter | Slope | $R^2$ | Confidence (%) |
|---|---|---|---|
| **IC Flow Rate (lb/hr)** | -0.0003 | 0.21 | 37 |
| **WW Flow Rate (lb/hr)** | -0.0014 | 0.38 | 43 |
| **L/G (m/m)** | -0.0004 | 0.16 | 38 |

All flow parameters have relatively small slopes with negative trends, indicating that increases in amine emissions are a weak negative function of the liquid flow rates. The water wash flow rate has the highest $R^2$ correlation value, indicating that the water

wash flow is the most relatable to the amine emissions. This maintains the trend of process parameters in the top bed having the highest correlations with amine emissions.

Regression analysis for flow rate parameters was performed. Table 5.11 presents the regression analysis results, while Figure 5.18 gives the regression model predicted normalized amine emissions in comparison to the actual normalized amine emissions. The temperature parameter regression model is included in Figure 5.18 as well. Aerosol tests that did not incorporate the water wash were not used in the regression analysis.

**Table 5.11: Regression analysis results for absorber flow rate parameters with respect to normalized amine emissions**

| | **Normalized Amine Emissions** | **Standard Error** |
|---|---|---|
| | *ppm* | |
| **$R^2$** | 0.42 | - |
| **Significance F** | 0.26 | - |
| **Standard Error** | 2.00 | - |
| ***Coefficients*** | | |
| **Intercept** | 6.05 | 2.34 |
| **IC Flow Rate** | -0.00008 | 0.001 |
| **WW Flow Rate** | -0.001 | 0.001 |
| **L/G** | -0.09 | 1.63 |

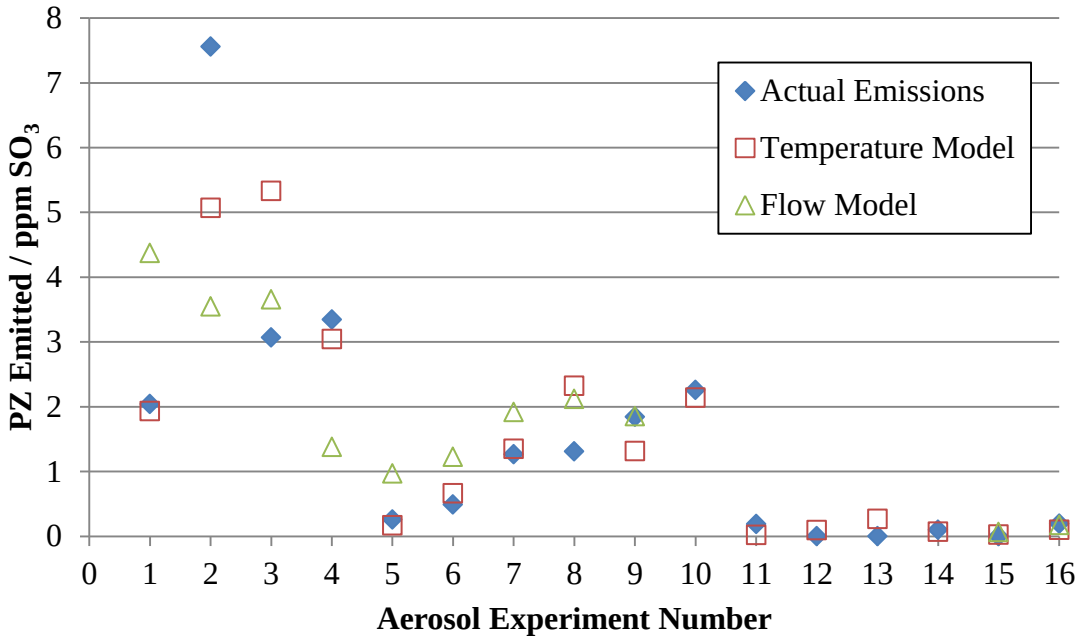


**Figure 5.18: Regression models predicted normalized amine emissions in comparison to the actual normalized amine emissions for absorber flow and temperature parameters.**

The regression model for absorber column flow rates is a poor predictor of amine emissions. The predictive model using absorber temperatures is more accurate, showing that absorber temperatures have a greater significance in amine emissions than the flow rates through the process.

### 5.4.3 Gas Phase Composition Correlations with Amine Emissions

The inlet and outlet gas phase $CO_2$ compositions as measured by FTIR sampling were correlated to the normalized amine emissions. The average values for these parameters during each aerosol test are presented in Table 5.12.

**Table 5.12: Average inlet and outlet $CO_2$ compositions during UT-SRP aerosol tests**

| Run | Date | $CO_2$ In | $CO_2$ Out |
|---|---|---|---|
| # | | *vol %* | *vol %* |
| **1** | 4/26/17 | 12.00 | 1.48 |
| **2** | 4/27/17 | 3.92 | 0.00 |
| **3** | 4/27/17 | 3.61 | 0.00 |
| **4** | 5/1/17 | 19.67 | 0.90 |
| **5** | 5/2/17 | 4.90 | 0.17 |
| **6** | 5/2/17 | 5.12 | 0.17 |
| **7** | 5/2/17 | 5.45 | 0.19 |
| **8** | 5/3/17 | 19.16 | 1.25 |
| **9** | 5/4/17 | 8.05 | 0.33 |
| **10** | 5/4/17 | 14.86 | 0.61 |
| **11** | 5/9/17 | 15.35 | 1.44 |
| **12** | 5/9/17 | 15.71 | 1.48 |
| **13** | 5/9/17 | 15.16 | 1.43 |
| **14** | 5/9/17 | 12.88 | 1.21 |
| **15** | 5/10/17 | 19.55 | 2.38 |
| **16** | 5/10/17 | 19.48 | 2.38 |

The average gas phase $CO_2$ for each aerosol experiment can be plotted with respect to amine emissions per mole of $SO_3$ injected. This is presented in Figure 5.19. The bottom axis is on a logarithmic scale.

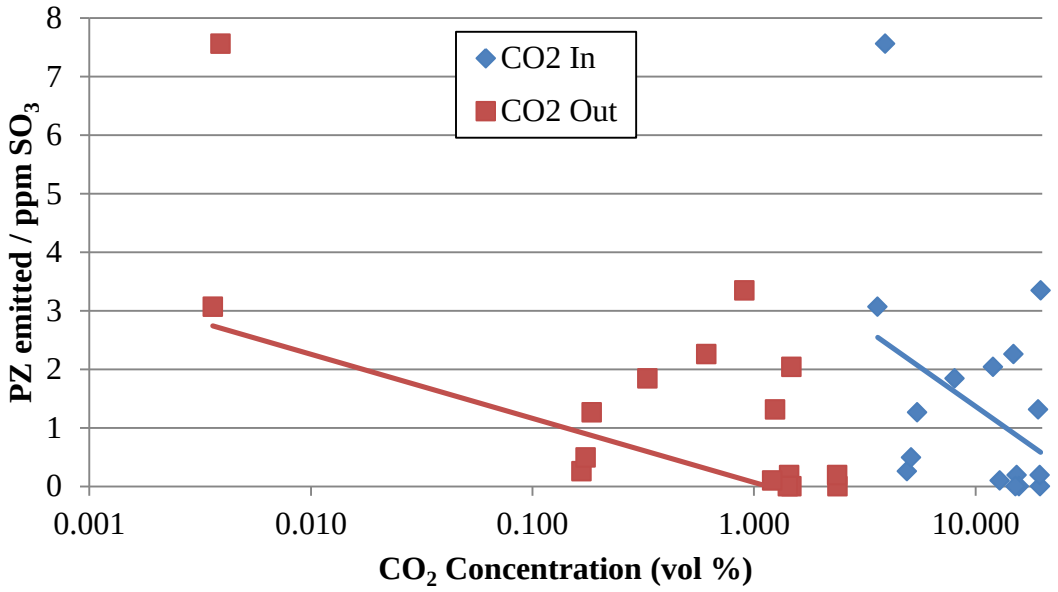


**Figure 5.19: Normalized amine emissions as a function of absorber inlet and outlet $CO_2$**

Table 5.13 gives the slopes and $R^2$ correlations for the inlet and outlet $CO_2$ process parameters.

**Table 5.13: Slope and $R^2$ correlations for absorber gas phase $CO_2$ compositions with respect to normalized amine emissions**

| Parameter | Slope | $R^2$ | Confidence (%) |
|---|---|---|---|
| **Inlet $CO_2$** | -0.12 | 0.14 | 33 |
| **Outlet $CO_2$** | -1.30 | 0.27 | 36 |

Both $CO_2$ compositions have negative slopes, showing that reducing $CO_2$ content throughout the absorber column correlate with increasing amine emissions. The $R^2$ correlations are low for both $CO_2$ compositions, indicating that the amine emissions are only weakly related to the $CO_2$ content.

Regression analysis for inlet and outlet $CO_2$ composition parameters was performed. Table 5.14 presents the regression analysis results, while Figure 5.20 gives the regression model predicted normalized amine emissions in comparison to the actual normalized amine emissions.

**Table 5.14: Regression analysis results for absorber $CO_2$ content with respect to normalized amine emissions**

| | **Normalized Amine Emissions** | **Standard Error** |
|---|---|---|
| | *ppm* | |
| **$R^2$** | 0.28 | - |
| **Significance F** | 0.11 | - |
| **Standard Error** | 1.80 | - |
| ***Coefficients*** | | |
| **Intercept** | 2.31 | 1.11 |
| **$CO_2$ In** | 0.07 | 0.14 |
| **$CO_2$ Out** | -1.80 | 1.12 |

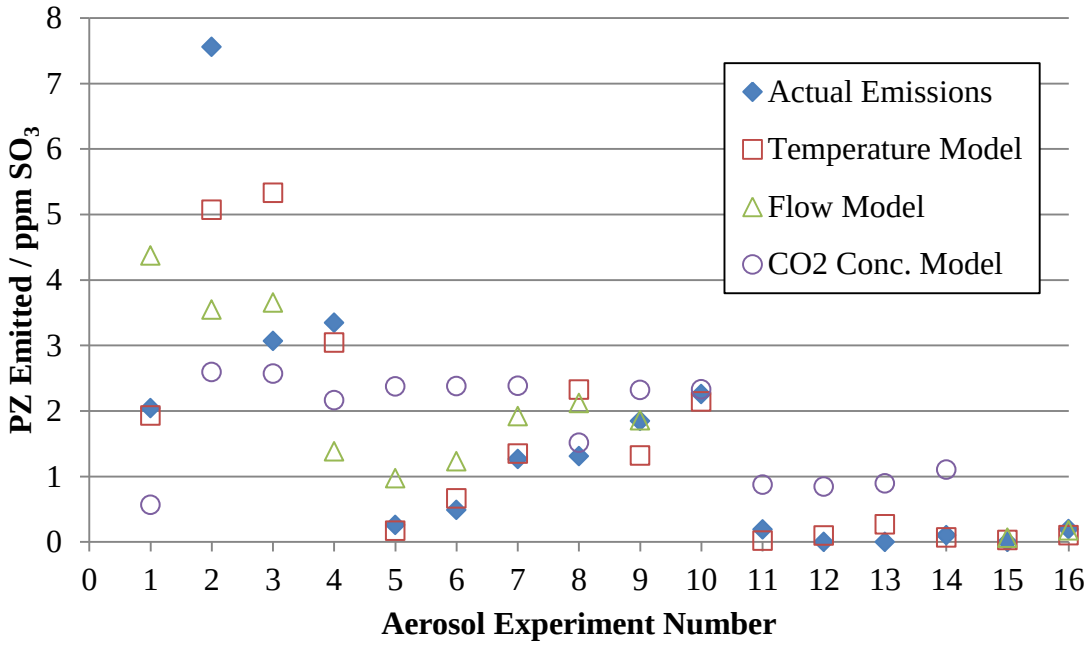


**Figure 5.20: Regression models predicted normalized amine emissions in comparison to the actual normalized amine emissions for absorber flow, temperature, and $CO_2$ composition parameters.**

The regression model for absorber $CO_2$ compositions does not adequately predict amine emissions. This shows that temperature and flow rates are more significant factors in amine emissions than the $CO_2$ composition at the absorber inlet and outlet.

### 5.4.4 Solvent Composition Correlations with Amine Emissions

The lean (inlet) and rich (outlet) solvent $CO_2$ and piperazine compositions were correlated to the normalized amine emissions. The average values for these parameters during each aerosol test are presented in Table 5.15. $CO_2$ and piperazine concentrations were determined through titration methods outlined in Appendix D. $CO_2$ lean and rich loadings are varied based on the pilot plant run conditions. The piperazine content in the

solvent will vary as the $CO_2$ loading changes, and as water condenses and evaporates from the solvent due to temperature changes in the process.

**Table 5.15: Average lean and rich solvent $CO_2$ and piperazine compositions during UT-SRP aerosol tests**

| Run | Date | Lean $CO_2$ | Lean PZ | Rich $CO_2$ | Rich PZ |
|---|---|---|---|---|---|
| # | | *wt %* | *wt %* | *wt %* | *wt %* |
| **1** | 4/26/17 | 6.57 | 29.17 | 9.81 | 28.26 |
| **2** | 4/27/17 | 7.02 | 30.08 | 8.95 | 29.51 |
| **3** | 4/27/17 | 7.02 | 30.08 | 8.95 | 29.51 |
| **4** | 5/1/17 | 6.57 | 28.80 | 9.71 | 27.93 |
| **5** | 5/2/17 | 5.79 | 28.19 | 9.03 | 27.31 |
| **6** | 5/2/17 | 5.79 | 28.19 | 9.03 | 27.31 |
| **7** | 5/2/17 | 5.79 | 28.19 | 9.03 | 27.31 |
| **8** | 5/3/17 | 5.39 | 29.00 | 9.20 | 27.94 |
| **9** | 5/4/17 | 5.01 | 28.82 | 9.21 | 27.65 |
| **10** | 5/4/17 | 5.01 | 28.82 | 9.21 | 27.65 |
| **11** | 5/9/17 | 6.37 | 27.29 | 10.3 | 26.26 |
| **12** | 5/9/17 | 6.37 | 27.29 | 10.3 | 26.26 |
| **13** | 5/9/17 | 6.37 | 27.29 | 10.3 | 26.26 |
| **14** | 5/9/17 | 6.37 | 27.29 | 10.3 | 26.26 |
| **15** | 5/10/17 | 6.52 | 27.48 | 9.30 | 26.74 |
| **16** | 5/10/17 | 6.52 | 27.48 | 9.30 | 26.74 |

The solvent $CO_2$ and piperazine composition for each aerosol experiment can be plotted with respect to amine emissions per mole of $SO_3$ injected. This is presented in Figure 5.21 for $CO_2$ content and Figure 5.22 for amine content.

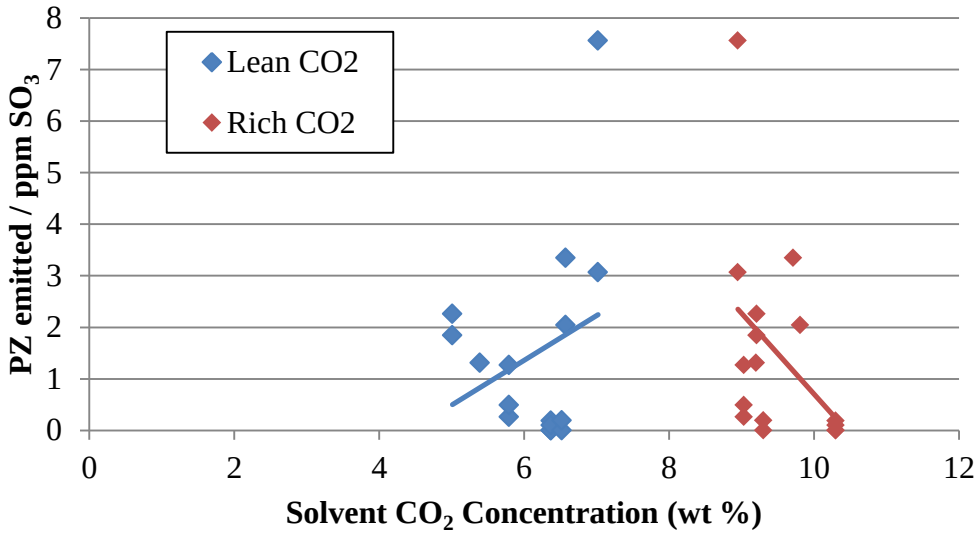


**Figure 5.21: Normalized amine emissions as a function of lean and rich solvent $CO_2$ compositions**

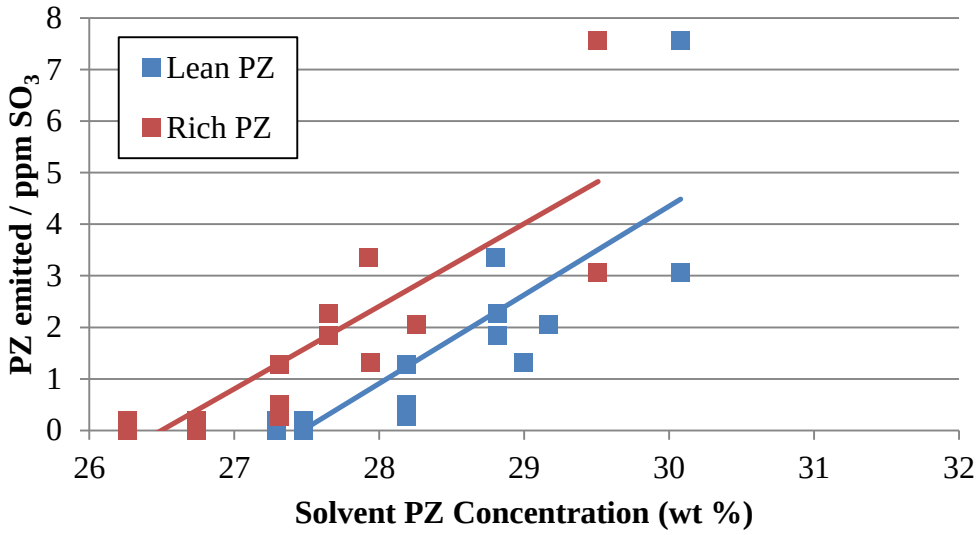


**Figure 5.22: Normalized amine emissions as a function of lean and rich solvent piperazine compositions**

The slopes and $R^2$ correlations for the solvent properties are presented in Table 5.16.

**Table 5.16: Slope and $R^2$ correlations for lean and rich solvent $CO_2$ and piperazine compositions with respect to normalized amine emissions**

| Parameter | Slope | $R^2$ | Confidence (%) |
|---|---|---|---|
| **Lean $CO_2$** | 0.87 | 0.08 | 30 |
| **Lean PZ** | 1.72 | 0.70 | 59 |
| **Rich $CO_2$** | -1.57 | 0.18 | 31 |
| **Rich PZ** | 1.60 | 0.72 | 64 |

The $CO_2$ content in both the lean and rich phases have minimal correlations with the amine emissions. Increasing the lean solvent $CO_2$ content loosely corresponds with increases in amine emissions, while decreasing the rich solvent amine content has a marginally stronger correlation with increasing amine emissions.

Both the rich and lean piperazine content show very strong correlations with the amine emissions. In both cases, small increases in the solvent piperazine content result in significant increases in the normalized amine emissions. As the piperazine content in the solvent increases, the amount of piperazine volatilized into the gas phase will also increase. The gas phase piperazine is free to condense into the aerosol drops, resulting in an increase in the aerosol amine content and the subsequent amine aerosol emissions.

These results indicate that the amine solvent content is one of the most influential factors in amine emissions. The findings agree with the bench scale Aerosol Growth Column experimental results presented in Chapter 4.

Regression analysis on the solvent amine and $CO_2$ content was performed. The results are presented in Table 5.17; Figure 5.23 shows a comparison on the model

predicted amine emissions in comparison to the previous models for other parameters, and the actual amine emissions results.

**Table 5.17: Regression analysis results for solvent $CO_2$ and amine content with respect to normalized amine emissions**

| | Normalized Amine Emissions | Standard Error |
|---|---|---|
| | *ppm* | |
| **$R^2$** | 0.75 | - |
| **Significance F** | 0.002 | - |
| **Standard Error** | 1.144 | - |
| ***Coefficients*** | | |
| **Intercept** | -61.24 | 42.92 |
| **Lean $CO_2$** | -1.69 | 16.11 |
| **Lean PZ** | -6.37 | 56.28 |
| **Rich $CO_2$** | 2.48 | 15.32 |
| **Rich PZ** | 8.39 | 57.90 |

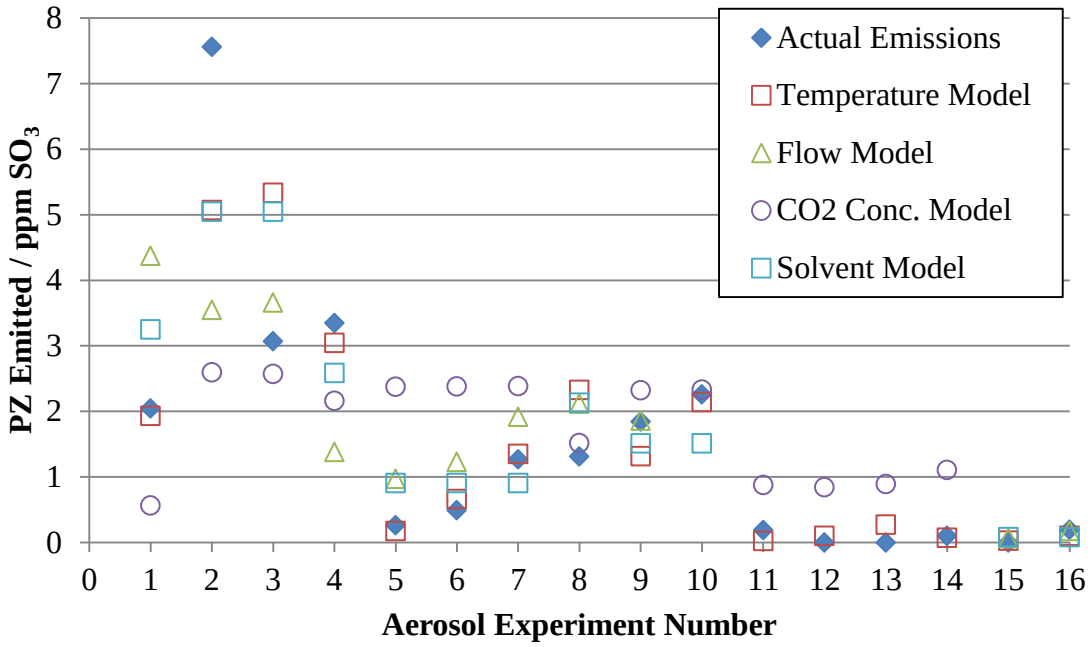


**Figure 5.23: Regression models predicted normalized amine emissions in comparison to the actual normalized amine emissions for absorber flow, temperature, $CO_2$ composition, and solvent composition parameters.**

The regression model utilizing solvent property parameters does an adequate job of matching the actual amine emissions. It performs approximately as well as the temperature model. This supports the hypothesis that the solvent composition plays a significant role in amine emissions.

### 5.4.5 Water Wash Piperazine Content Correlations with Amine Emissions

During the April 2017 UT-SRP pilot plant campaign, it was observed through FTIR measurement that the amine concentration exiting the water wash was higher than the concentration entering. It was initially suspected that amine in the water wash solvent was responsible; the amine could be stripped out of the solvent if sufficiently high

temperature differences existed between the gas and solvent, and if the piperazine content in the water wash solvent was high.

The amine content in the water wash solvent was obtained through titration techniques outlined in Chapter 4. The water wash solvent amine content for each aerosol test that utilized the water wash is presented in Table 5.18.

**Table 5.18: Water wash solvent amine content during UT-SRP aerosol tests**

| Run | Date | WW PZ Content |
|---|---|---|
| # | | *wt %* |
| **1** | 4/26/17 | 2.72 |
| **2** | 4/27/17 | 1.44 |
| **3** | 4/27/17 | 1.44 |
| **4** | 5/1/17 | 1.06 |
| **5** | 5/2/17 | 1.33 |
| **6** | 5/2/17 | 1.33 |
| **7** | 5/2/17 | 1.33 |
| **8** | 5/3/17 | 1.57 |
| **9** | 5/4/17 | 1.75 |
| **10** | 5/4/17 | - |
| **11** | 5/9/17 | - |
| **12** | 5/9/17 | - |
| **13** | 5/9/17 | - |
| **14** | 5/9/17 | - |
| **15** | 5/10/17 | - |
| **16** | 5/10/17 | - |

The water wash solvent piperazine content is plotted with respect to the normalized amine emissions in Figure 5.24.

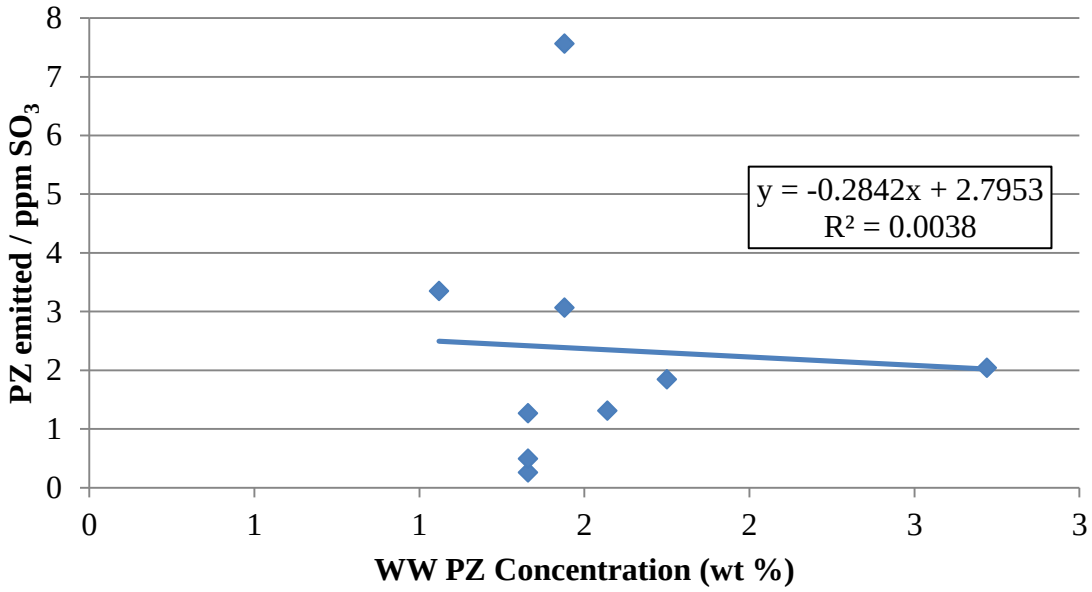


**Figure 5.24: Normalized amine emissions as a function piperazine content in the water wash solvent**

The slope of the resulting trend line is -0.2842, indicating that increasing amine emissions are a weak function of decreasing amine content in the water wash solvent. However, the $R_2$ value is very small at 0.0038; this shows that the amine emissions are not likely to be impacted by the amine content in the water wash solvent.

### 5.4.6 Combined Parameter Regression Model

The previous sections have outlined how temperatures, flow rates, and gas and liquid compositions have correlated with the amine emissions. A regression model was developed to encompass the process parameters with the strongest impact on amine emissions. This model uses the top bed temperature (Table 5.6), top bed inlet solvent temperature (Table 5.6), gas outlet temperature (Table 5.6), and rich piperazine composition (Table 5.15) to predict the amine emissions. Instead of normalizing the

piperazine emissions by the amount of $SO_3$ injected, the inlet $SO_3$ composition was added as an additional parameter (Table 5.1). Table 5.19 gives the regression results, while Figure 5.25 presents the regression model predicted amine emissions increase versus the experimentally determined amine emissions increase (Table 5.4).

**Table 5.19: Regression analysis results most impactful process parameters with respect to amine emissions increase**

| | **Normalized Amine Emissions** | **Standard Error** |
|---|---|---|
| | *ppm* | |
| **$R_2$** | 0.71 | - |
| **Significance F** | 0.02 | - |
| **Standard Error** | 38.31 | - |
| **Coefficients** | | |
| **Intercept** | -1257.87 | 806.32 |
| **Top Bed T (°F)** | -0.26 | 6.61 |
| **Top Bed Inlet T (°F)** | -0.82 | 3.24 |
| **Gas Outlet T (°F)** | 2.27 | 9.24 |
| **Inlet $SO_3$ (ppm)** | 0.69 | 0.37 |
| **Rich PZ Conc. (wt %)** | 42.69 | 21.74 |

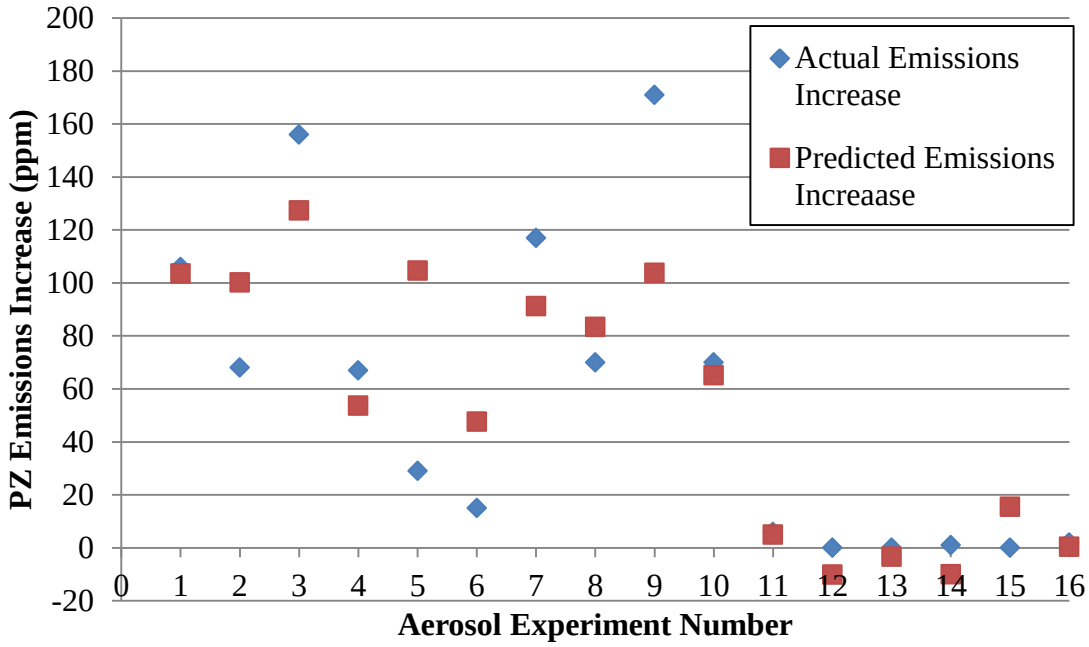


**Figure 5.25: Regression model predicted amine emissions increase in comparison to the actual amine emissions increase.**

The combined parameter regression model was not very accurate in predicting the piperazine emission rate increases for each aerosol test. It occasionally predicted negative emissions, which would be desirable but is very unrealistic.

## 5.5 CONCLUSIONS

Aerosol experiments were performed with the $SO_3$ generator during the April 2017 UT-SRP pilot plant campaign. This campaign was the first UT-SRP campaign to utilize a recently installed water wash process and an expanded FTIR sampling system. A total of 16 different aerosol tests were performed to quantify the impact of process operating conditions on the amine emissions.

### 5.5.1 Piperazine Aerosol Emissions

$SO_3$ aerosol caused amine emissions at the water wash outlet to increase by up to 7.56 ppm of piperazine / ppm of $SO_3$. Piperazine solvent showed resistance to atmospheric emissions through the aerosol phase; 30 ppm of $SO_3$ was often insufficient to produce a measureable amine emission increase. At lower quantities of $SO_3$, the gas phase piperazine is rapidly condenses into the aerosol drops, causing growth to a point that allows for collection within the process. As $SO_3$ increases, an excess of available aerosol nuclei limits the growth rate for the aerosol drops. A higher concentration of aerosol nuclei increases the available surface area for amine condensation, limiting the sizes of aerosol drops. This leads to a higher quantity of smaller aerosol drops that are not captured by impaction due to decreased aerosol diameters.

### 5.5.2 Impact of Temperature on Amine Emissions

Absorber temperatures were found to significantly impact the amine emissions; for every 1 °C increase in the gas outlet temperature, amine emissions were reduced by up to 1.7 ppm per ppm $SO_3$. This is hypothesized to be due to the growth and collection of aerosol by impaction, as higher gas temperatures encourage aerosol growth. The temperatures at the top of the absorber column and water wash were more significant than temperatures at lower levels of the column. Gas temperature showed a higher correlation with the normalized amine emissions than liquid temperature. The gas outlet temperature showed an $R^2$ correlation of 0.56 with the piperazine emissions per ppm $SO_3$. The top bed temperature presented an $R^2$ correlation of 0.51, and the top bed solvent temperature maintained an $R^2$ correlation of 0.49.

### 5.5.3 Effect of Solvent Composition and Flow Rate on Amine Emissions

The solvent amine content was found to strongly correlate with amine emissions; increasing the solvent piperazine content by 1 wt % increased normalized piperazine emissions by 2.3 ppm (per ppm $SO_3$). As the piperazine content in the solvent increased, the amount of piperazine volatilized into the gas phase also increased. The gas phase piperazine was free to condense into the aerosol drops, resulting in an increase in the aerosol amine content and the subsequent amine aerosol emissions. This agrees with the bench scale results in showing that the solvent amine concentration is one of the most important factors in amine emissions.

Solvent flow rates were observed to have less of an impact on the amine emissions as compared to process temperatures. Solvent flow rates closer to the top of the absorber column had higher correlation with amine emissions than solvent flow rates in lower sections of the column. The water wash flow rate showed an $R^2$ correlation value of 0.38 with respect to the piperazine emitted per ppm $SO_3$, while the intercooling flow rate maintained an $R^2$ correlation of 0.21.

The $CO_2$ content in the solvent was shown to have a minimal impact on the amine emissions, with the rich solvent having a slightly greater influence than the lean solvent. Rich loading showed an $R^2$ correlation of 0.18 with the normalized piperazine emissions, while the lean loading had an $R^2$ correlation of 0.08.

### 5.5.4 Water Wash Impact on Amine Emissions

Increasing the water wash flow rate by 225% was found to increase the amine emissions by 10 to 20 ppm. Completely stopping flow through the water wash decreased

amine emissions by 0 to 20 ppm. Decreasing the temperature of the water wash solvent was found to double amine emissions; it is hypothesized that this decreased the sizes of aerosol drops and allowed a greater quantity of aerosol to escape collection by impaction.

The piperazine content in the water wash solvent was found to have very minimal correlation with the water wash amine emissions, with an $R^2$ correlation of 0.004 in relation to the piperazine emitted per ppm $SO_3$.

### 5.5.5 $CO_2$ Effect on Amine Emissions

Reducing the absorber outlet $CO_2$ content was found to weakly correlate ($R^2$ = 0.27) with increasing amine emissions. The gas phase $CO_2$ at the absorber outlet had a greater impact on the amine emissions than the $CO_2$ at the absorber inlet, which showed an $R^2$ correlation of 0.14.

## 5.6 RECOMMENDATIONS

The April 2017 UT-SRP pilot plant campaign was very successful in gathering amine emissions data. However, aerosol size distributions and concentration could not be quantified due to issues encountered with the PDI. Laser alignment on the PDI could not be achieved; the instrument had to be returned to the manufacturer for repairs. It is highly recommended that the PDI be utilized during the next UT-SRP campaign, as this will allow for quantification of aerosol sizes and concentration as process conditions are varied.

Another recommendation is for the procurement and tuning of a mass flow controller for $SO_3$ flow control. The rotameters used in this study were adequate for the

experiments conducted, but a mass flow controller would allow greater precision in $SO_3$ generation rates.

A final recommendation is the pilot scale experiments with different amines and varying solvent compositions. The amine solvent composition was shown to significantly impact the amine emissions; further studies should be performed to expand on this data set. Using different amine solvents could produce insights into the impact of amine structure on aerosol emissions.

## 5.7 ACKNOWLEDGEMENTS

Pilot plant testing requires the cooperation of many different people. The UT-SRP crew was instrumental in making this campaign a success. Special thanks to Henry Bautista, Robert Montgomery, Jarrett Spinhirne, and Frank Seibert for their contributions in setting up and running the pilot plant. Jarrett helped significantly in enabling communications between DeltaV™ and the Gasmet™ CX-4000 FTIR analyzer that were critical for data collection. Thanks to Henry Bautista and Robert Montgomery for being willing to change operating set points on the fly during aerosol tests.

Korede Akinpelumi and Vietnam Nguyen were extremely helpful in setting up the FTIR sampling system and the $SO_3$ generator. Their contributions in helping operate analyzer instruments and the $SO_3$ generator furnace are greatly appreciated.

Eric Chen and his crew were frequently consulted and utilized in preparing for the aerosol tests. Their work in designing and installing the water wash expansion greatly helped this research. Virbin Sapkota, Aramide 'Tolu" Eseyin, Daniel Culpepper, Janelle

Engel, Racheal Reed, Michael Cawthorn, and Hyejin Kim all were vital in preparing and running this campaign.

Yue Zhang contributed her expertise in setting up the DeltaV™ control system are greatly appreciated. Paul Nielson performed the solvent titration analysis that has played a critical role in this research. Kent Fisher was helpful in various pilot plant activities, even if he did attempt to start a fire in the control room one night. Dr. Rochelle contributed in deciding experiment set conditions and in insightful interpretation of data.

Finally, much of the initial setup for FTIR online analysis and aerosol experimental technique have been established by Steven Fulk, a previous graduate student in the Rochelle group. His efforts and insight have helped pilot plant campaigns greatly, even after his graduation.

# CHAPTER 6: FIELD MEASUREMENT OF AMINE AEROSOL BY FTIR AND PDI

This chapter presents results from FTIR and PDI sampling at three different pilot plant facilities: the University of Texas Separations Research Program, the University of Kentucky, Kentucky Utilities, and Louisville Gas & Electric Slipstream Plant, and the National Carbon Capture Center Slipstream Solvent Test Unit. The research in this chapter has been published in *Energy Procedia*[1] (Beaudry, 2017). Steven Fulk contributed in developing and using the algorithm for aerosol amine content, and in quantifying the impact of $SO_2$ and $H_2SO_4$ in amine emissions at the UT-SRP pilot plant. Gary Rochelle provided editing, scientific guidance, and financial assistance. A background on amine emissions is followed by outlines on FTIR and PDI analytical techniques. Overviews of the three amine scrubbing facilities are then presented. The chapter covers the effects of process operating conditions on amine aerosol emission rates by presenting notable examples. Amine emission observations based on the aerosol nuclei source are shown, including the impact of aerosol nuclei removal by upstream baghouse filtration units. The PDI aerosol measurement results are compared to ELPI+™ aerosol measurements that occurred simultaneously. Conclusions on the pilot plant results and recommendations for future tests are provided.

[1] Beaudry M, Fulk S M, Rochelle G T. "Field Measurement of Amine Aerosol by FTIR and Phase Doppler Interferometry." *Energy Procedia*. 2017;114:906-929. Beaudry performed the aerosol sampling, data analysis, writing, and editing for this work.

## 6.1 BACKGROUND

### 6.1.1 Amine Aerosol Losses

Amine solvent losses are a significant issue at amine scrubbing pilot plants. Solvent lost through the absorber overhead represents an environmental and safety hazard, along with having undesirable economic implications. Amine losses can occur in the gas phase as a function of vapor pressure in the absorber column or as a mist composed of aerosol. Aerosol emissions from absorber columns occur when aerosol nuclei are present in the incoming flue gas. Nuclei can be fly ash from the coal combustion process or submicron sulfuric acid drops produced from sulfur in the fuel. The nuclei collect water, amine, and $CO_2$ while traveling through the absorber.

A water wash is used to contact the gas phase with water or a solution unsaturated with amine, resulting in the transfer of the volatile amine from the gas phase to the liquid and mitigating gas phase losses. Washing steps are currently employed to mitigate the emission of amine degradation products, such as ammonia, from $CO_2$ capture facilities. The water wash is ineffective at collecting aerosol smaller than 3 microns because these small drops follow the gas streamline (Mertens, 2013; Mertens, 2014a; Khakharia, 2015).

### 6.1.2 Aerosol at Pilot Plants

Aerosol emissions have been reported at a number of amine scrubbing pilot plants. Mitsubishi Heavy Industries (MHI) found an increase of KS-1 and ethanolamine (MEA) emissions to be proportional to the inlet $SO_3$ to the absorber column (MHI, 2011). MHI used inlet $SO_3$ removal and a series of wash beds and demisters to mitigate amine aerosol emissions.

SINTEF and the Netherlands Organization for Applied Scientific Research collaborated on a $CO_2$ capture pilot plant using 30 wt % MEA as the amine solvent (SINTEF, 2012; da Silva, 2013; Khakharia, 2013; Khakharia, 2014). FTIR measurements of amine emissions at the water wash outlet were found to be significantly higher than predicted by the process model. A Brownian Demister Unit (BDU) was installed downstream of the water wash and reduced emissions to the levels predicted in models. The steps taken show that aerosol, not entrainment or gas-phase losses, was responsible for the majority of amine emissions. Aerosol was found to be dependent on the maximum temperature in the absorber, the quantity of available nuclei for condensation, and the extent of temperature gradients in the absorber and water wash.

A 2012 pilot plant campaign at the National Carbon Capture Center experienced MEA emissions of over 100 ppm; amine vapor emissions were predicted to be less than 3 ppm (Carter, 2012). The increased amine emissions were due to sulfuric acid aerosol with $SO_3$ forming the nuclei source. Amine emissions were found to increase with increasing $SO_3$ levels and with deactivation of the upper absorber bed, and to decrease with reductions in the water wash MEA content and the absorber column solvent temperature.

The $CO_2$ capture test facility at Karlsruhe Institute of Technology measured the loss of MEA through aerosol emissions. A condensation particle counter (CPC) was used to measure particulate concentration, with a soot generator and an $SO_3$ synthesis reactor to produce aerosol nuclei. The soot generator produced an aerosol nuclei concentration between 3E4 and 9E5 $cm^{-3}$, which resulted in MEA emissions of 36 to 72 ppm

(Khakharia, 2013). The addition of $SO_3$ to the absorber column resulted in an aerosol concentration between 1.0E8 and 1.4E8 $cm^{-3}$, depending on the $SO_3$ synthesis reactor production rate. Experiments by Brachert et al. confirmed an aerosol concentration in the range of 1E8 $cm^{-3}$ with sulfuric acid nuclei (Brachert, 2013).

In their Mobile Test Unit, Aker Solutions experienced amine mist formation resulting from 12 ppm $H_2SO_4$ in the flue gas feed from a residual catalytic cracker at Technology Centre Mongstad (Bade, 2014). The resulting amine emissions exceeded 200 ppm during conventional operation. A BDU installed upstream of the absorber column was found to significantly reduce the amount of fine catalyst particles and sulfate anions, resulting in a reduction of amine aerosol emissions.

It is clear that different pilot plants, with different process configurations and amine solvents, experience varying degrees of effect from the presence of aerosol nuclei sources in the flue gas feed. Adaptable and reliable aerosol measurements under a variety of process conditions are needed. Additional research into the interdependency of the process operating conditions and the dynamics of aerosol must be conducted in order to operate processes without growing aerosol, or to condition the aerosol to facilitate collection.

### 6.1.3 Aerosol Growth within the Absorber and Water Wash

Aerosol growth occurs within the absorber column and water wash. Models by Kang et al. predict that PZ aerosol grows from 0.1 μm up to 3.2 μm in diameter in the absorber, and can grow up to 9.6 μm in the subsequent water wash (Kang, 2017). Aerosol growth was found to be controlled by PZ mass transfer in the absorber and water

mass transfer in the water wash. The difference between the gas and solvent temperature, along with the amount of PZ in the gas phase and $CO_2$ loading, were found to heavily influence aerosol growth. Work by Zhang et al. agreed in showing that aerosol will grow faster at higher absorber and water wash operating temperatures due to an increase in the amine mass transfer driving force (Zhang, 2017).

## 6.2 EXPERIMENTAL METHODS

This research focuses on developing and demonstrating methods of measuring aerosol for amine scrubbing, and determining the effect of process conditions on aerosol emissions. In situ measurements are preferred, as extractive measurement techniques can lead to measurement errors from evaporation and condensation, gravitational settling, particle deposition, and flow effects. Results are reported in this paper from a Fourier Transform Infrared Spectrometer and a Phase Doppler Interferometer.

### 6.2.1 Aerosol Measurement Techniques

#### *6.2.1.1 FTIR*

Fourier Transform Infrared Spectrometry (FTIR) utilizes a broadband light source with a configuration of mirrors to measure how a gas sample absorbs infrared light. Only infrared active compounds, such as $CO_2$, $H_2O$, and amines, are detected by the FTIR; nitrogen, oxygen, and other symmetrical compounds with double and triple bonds are inactive. The mirrors in the FTIR are susceptible to damage from liquids, so the FTIR sampling is performed "hot and wet" throughout by maintaining a temperature of 180 °C across the sampling system (Mertens, 2012). This allows for analytical sampling without the need to remove water from the sampled stream, which significantly impacts aerosol

measurement. A consequence of the "hot and wet" approach is a nondiscriminatory analysis of both liquids and vapors; the FTIR cannot differentiate between sampled gases and vaporized liquids. The FTIR analyzers used in this work are Gasmet™ CX-4000 and DX-4000 models; these use identical components, with the only difference in the ruggedized casing for the DX-4000. More details on FTIR analysis can be found in Chapter 2, while FTIR standard operating procedures are available in Appendix A.

#### *6.2.1.2 PDI*

The Phase Doppler Interferometer (PDI) is an optical measurement device that quantifies the particle size distribution and density for aerosol (Artium, 2015). It operates by passing an aerosol drop through a small volume defined by the intersection of two lasers. Photodetectors measure the phase shift of light scattered by aerosol drops. The PDI uses the wavelength of light itself as the measurement scale instead of attempting to quantify light scattering, which reduces interference from window attenuation. The drop diameter is calculated by quantifying the phase shift induced by the beams refracting in the drop. The movement of the particle causes a Doppler shift in the frequency of light scattering, which allows determination of the drop velocity. By combining the velocity of the drops with the quantity detected in a given time span, the aerosol concentration and size distribution in the sampled stream can be determined. The PDI is capable of measuring aerosol between 0.1 and 12.0 μm in diameter, and in a concentration above 1E6 per $cm^3$. Greater detail on PDI measurement theory and operational procedures can be found in Fulk et al. (Fulk, 2017) and in Chapter 2 of this dissertation. Standard operating procedures for PDI operation are produced in Appendix B.

The prototype PDI instrument is built by Artium Technologies, Inc., and consists of a transmitter, receiver, and data processer. The transmitter and receiver are in a combined unit designed to fit around a specially sized spool piece, called the sample cell. The sample cell contains two "windows" for the lasers and a nitrogen purge system to keep the windows free of condensation. The system can be used on any pilot plant with the necessary access ports.

### 6.2.2 Aerosol Measurement Locations

This paper presents measurements at three pilot plants: Separations Research Program (UT-SRP) at the University of Texas, the University of Kentucky, Kentucky Utilities, and Louisville Gas & Electric collaboration (UKy/KU/LG&E), and the National Carbon Capture Center (NCCC) Slipstream Solvent Test Unit (SSTU).

#### *6.2.2.1 UT-SRP*

The UT-SRP Pilot Plant is located at the Pickle Research Campus in Austin, Texas. The research presented in this chapter covers sampling at this facility performed during March 11–27 of 2015. The 16.8" diameter absorber contains 2 packed beds with 10' of RSR-250 structured packing each. The facility is sized to simulate the capture of $CO_2$ from a 0.1–0.2 MW power plant. The flue gas is synthesized from air and $CO_2$, which varies in composition from 3 to 20%. This facility had no water wash at the time, but utilized an air chiller and knockout drum with a 0.3 μm filter to remove condensable components from the treated flue gas. The solvent used was PZ at 5 and 8 molality. The flowsheet of the absorber side of the process is presented in Figure 6.1.

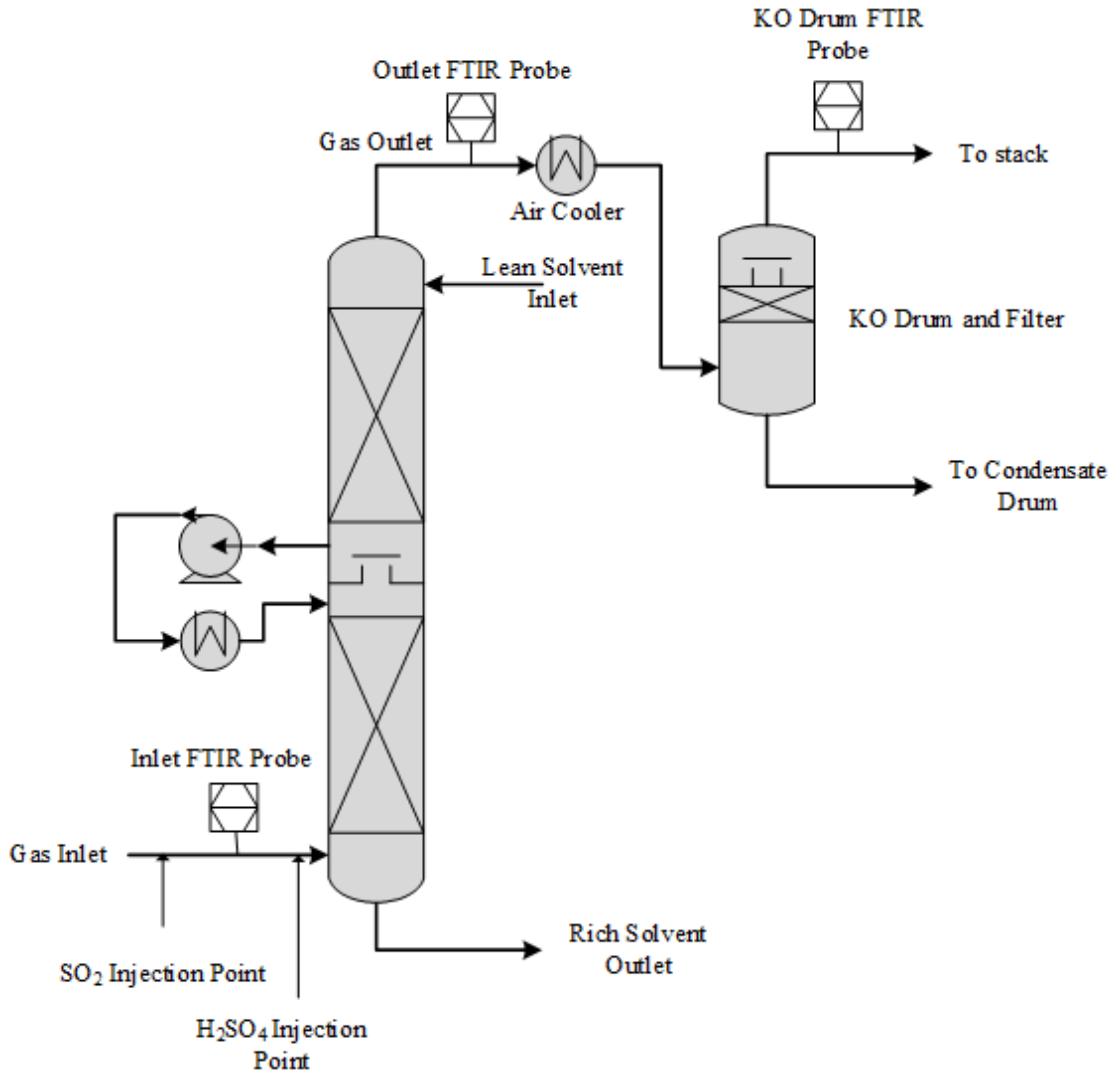


**Figure 6.1: UT-SRP pilot plant absorber side process configuration, with aerosol nuclei injection points and FTIR sample extraction locations.**

The synthetic flue gas contains no aerosol nuclei, so aerosol has been created by direct injection of $SO_2$ gas or vaporized sulfuric acid. Both of these methods have produced aerosol observable through FTIR measurements and visual confirmation (Fulk, 2014).

### *6.2.2.2 UKy/KU/LG&E*

The UKy/KU/LG&E pilot plant is located on a slipstream of the E. W. Brown Generating Station in Harrodsburg, Kentucky. FTIR sampling was performed at this site from August 4–13, 2015. The flue gas from the coal-fired generating station is treated by Flue Gas Desulfurization (FGD) and Selective Catalytic Reductions (SCR) units for $SO_x$ and $NO_x$ control, respectively. The slipstream plant is scaled for capture from a 0.7 MW power plant. The absorber column includes two beds of packing with a simplified water wash. PDI sampling was not performed. A flow diagram of the absorber is presented in Figure 6.2.

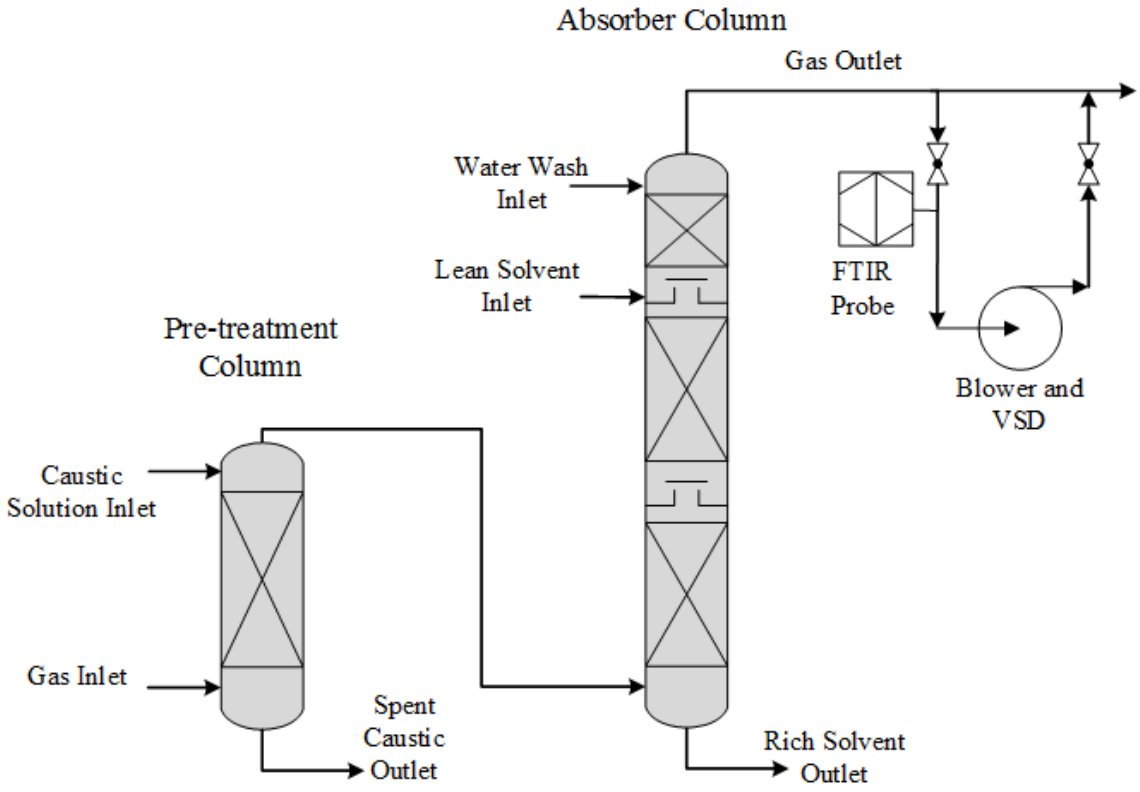


**Figure 6.2: UKy/KU/LG&E Slipstream Plant absorber configuration**

The UKy/KU/LG&E slipstream plant uses a caustic pretreatment column to capture $SO_2$ from the incoming flue gas. The caustic make-up feed to the column can be reduced or stopped to allow $SO_2$ to enter the absorber to determine the effect of $SO_2$ on amine emissions. A once-through water wash is in place at the top of the absorber column. This is not a closed solvent loop; water added in the water wash is allowed to mix with the solvent. This can result in decreased solvent amine content by "watering down" the solvent, so it was seldom employed. The $CO_2$ content in the flue gas can be varied by recycling a portion of the captured $CO_2$ back into the inlet flue gas.

#### *6.2.2.3 NCCC SSTU*

The National Carbon Capture Center (NCCC) is located in Wilsonville, Alabama and run by Southern Company. This facility uses flue gas from the Alabama Power Gaston Station Unit 5, an 880 MW supercritical pulverized coal generation plant. Sampling was performed at this facility from December 1–15, 2015, and from October 4–14, 2016. FTIR and PDI sampling occurred simultaneously at the water wash outlet. Previous research has confirmed the presence of aerosol at this facility (Carter, 2012). Figure 6.3 presents the process flow diagram and sampling configuration for sampling conducted on the NCCC Slipstream Solvent Test Unit.

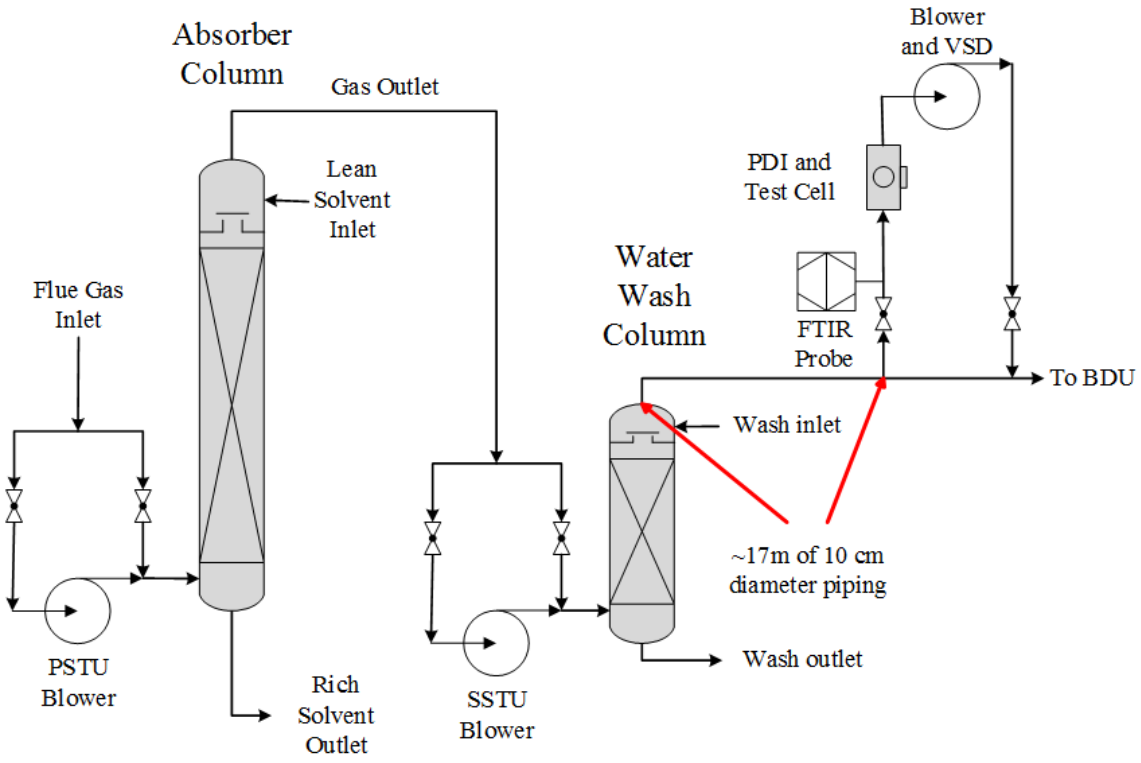


**Figure 6.3: NCCC SSTU absorber configuration and sampling system, with two bypassable blowers**

The SSTU unit at NCCC is capable of using two different process configurations. It can use the upstream PSTU blower to maintain a positive pressure throughout the absorber side of the process, or the SSTU blower can be used between the absorber column and the water wash column. Sampling was performed under both operating conditions. Approximately 50' of 4" OD piping separates the sample location from the wash column. With a superficial gas velocity of approximately 10 ft/s, this gives a residence time of approximately 5 seconds in the piping between the water wash column and the sampling location, which may influence the aerosol sizes and number densities (Fulk, 2017).

## 6.3 RESULTS

Amine emission results are divided into two sections: effects based on process parameter changes, and the varying impacts of aerosol nuclei type and concentration. These results are from all three facilities at which amine emissions sampling was performed; each result is labeled accordingly. Amine emissions based on process operating parameters will examine the impact of blower configurations, outlet $CO_2$ composition, and water wash flow rates and temperatures. The section covering the effects of aerosol nuclei type and concentration shows the varying impacts based on aerosol nuclei type, and the effect of the installation of an upstream baghouse filtration unit on the pilot plant amine solvent emissions.

### 6.3.1 Effect of Process Conditions on Amine Aerosol Emissions

#### *6.3.1.1 Blower Configuration*

On December 7, 2015, the blower configuration at the NCCC SSTU was varied to observe the effect on aerosol emissions. The unit was typically operated with the SSTU blower, the intermediate blower between the absorber and water wash as shown in Figure 3. At approximately 14:00, the SSTU blower was bypassed and the PSTU blower was brought online. The PSTU blower is located upstream of the absorber column. The FTIR analysis of this process change is presented in Figure 6.4.

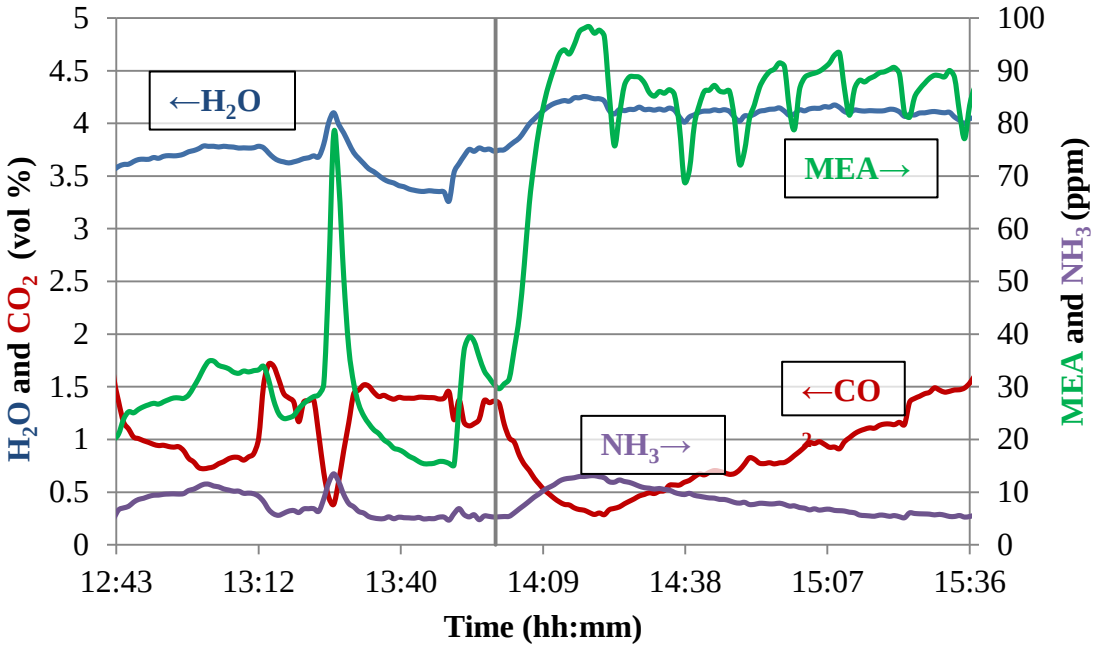


**Figure 6.4: FTIR result of switch from SSTU to PSTU blower on December 7, 2015 at 14:00. Arrows on the FTIR labels correspond to the axes the data are plotted on; water and carbon dioxide on the left axis (vol %), and MEA and $NH_3$ on the right axis (ppm).**

Switching from the intermediate blower to the upstream blower results in a roughly threefold increase in the MEA emissions. PDI analysis was performed over the same time span to observe the effect of the blower configuration on the aerosol size distribution and concentration. The raw aerosol size distribution histogram is presented in Figure 6.5. This is identical to the size distribution generated through the AIMS software used to operate the PDI.

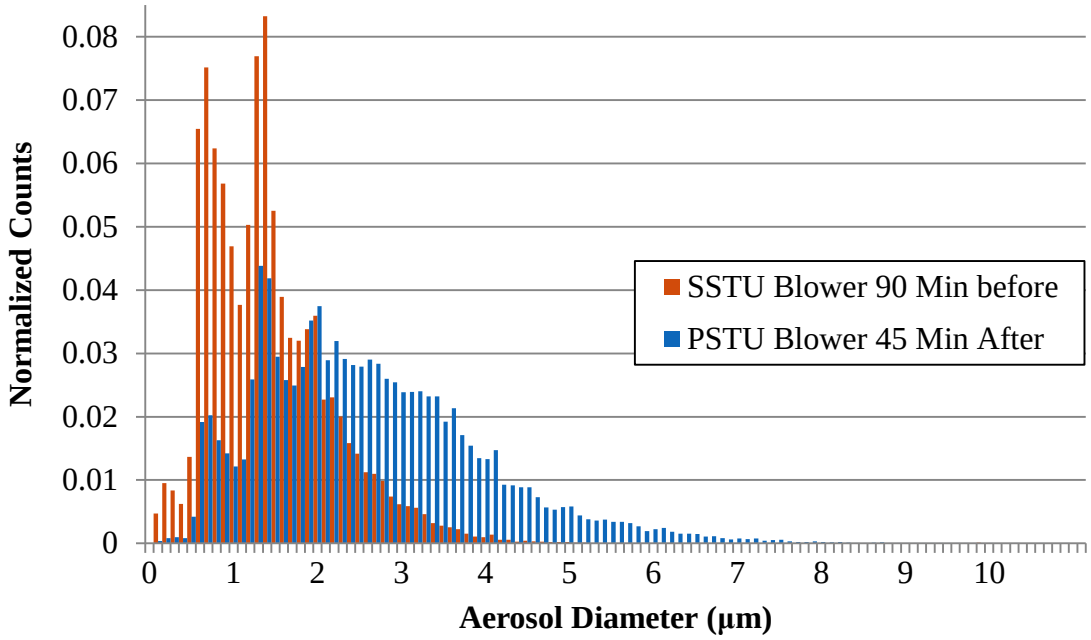


**Figure 6.5: PDI analysis of switch from NCCC SSTU to PSTU blower. The diameter in microns is represented on the bottom axis, and is broken into 0.1 µm bin sizes. The counts in the left axis are normalized by dividing the amount of drops in the bin by the total amount of drops.**

Figure 6.5 presents the particle size distribution of aerosol before and after the blower change. The bottom axis sorts the aerosol by diameter in 0.1 µm bins. The left axis provides counts per bin. Each histogram represents the average of five PDI sampling runs. Figure 6.6 uses the aerosol size distribution to present the cumulative volume fraction.

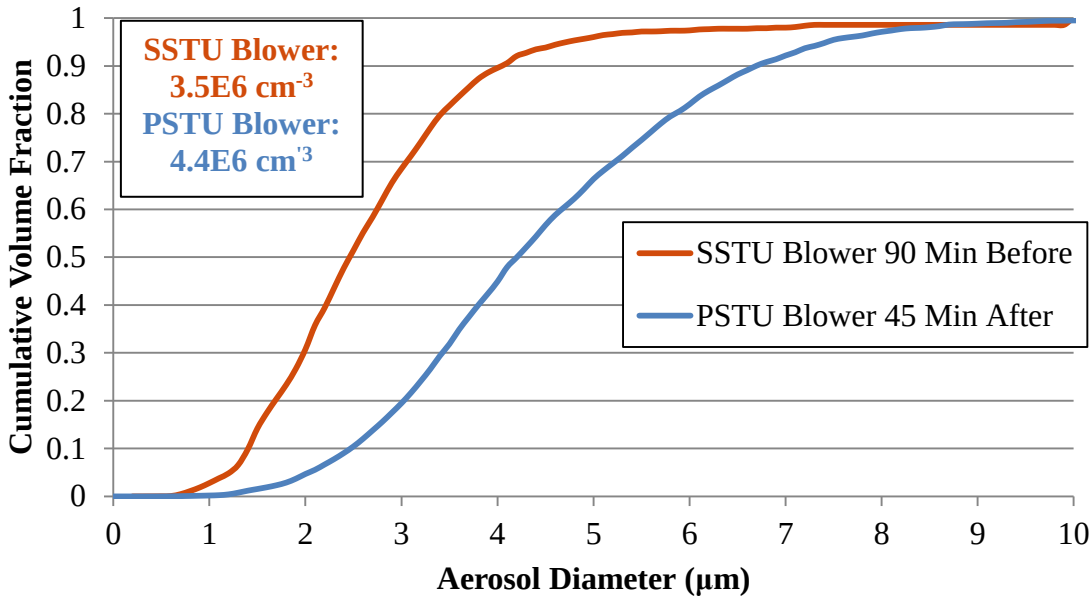


**Figure 6.6: Cumulative volume fraction as a function of aerosol diameter for SSTU to PSTU blower switch. Aerosol diameters are given in µm on the bottom axis. The left axis represents the cumulative volume fraction, or the total volume of aerosol of that diameter and smaller.**

Aerosol sampled after the process change (while operating with the upstream PSTU blower) are significantly larger than aerosol sampled while operating with the intermediate SSTU blower. When operating with the intermediate blower, aerosol smaller than 2.5 µm accounts for 50% of the total emissions volume; with the upstream blower, aerosol smaller than 4.2 µm is responsible for 50% of the emitted volume. This indicates that fewer large aerosol drops are produced when utilizing an intermediate blower. This is theorized to be the result of the centrifugal blower capturing larger aerosol by impaction, or due to evaporation and shrinkage of the aerosol from the enthalpy added to the process by the intermediate blower.

The average aerosol concentration with the SSTU intermediate blower is 3.5E6 $cm^{-3}$, while the PSTU blower results in an average aerosol concentration of 4.4E6 $cm^{-3}$. Aerosol are not only significantly larger while using the upstream blower, but are also present in a higher concentration.

The PDI provides particle size distribution and aerosol concentration for a sampled stream. Using these data, the total volume of liquid collected in the aerosol drops can be calculated. By assuming a constant amine composition in each aerosol drop, the amine emissions due to aerosol alone can be quantified. Thus, the PDI can be used to roughly determine the amine aerosol emission rate. Further clarification on the algorithm used to calculate the amine content in the aerosol phase can be found in work by Fulk et al. (Fulk, 2016). Figure 6.7 presents a comparison of the PDI-calculated MEA emissions to the MEA emissions observed via the FTIR.

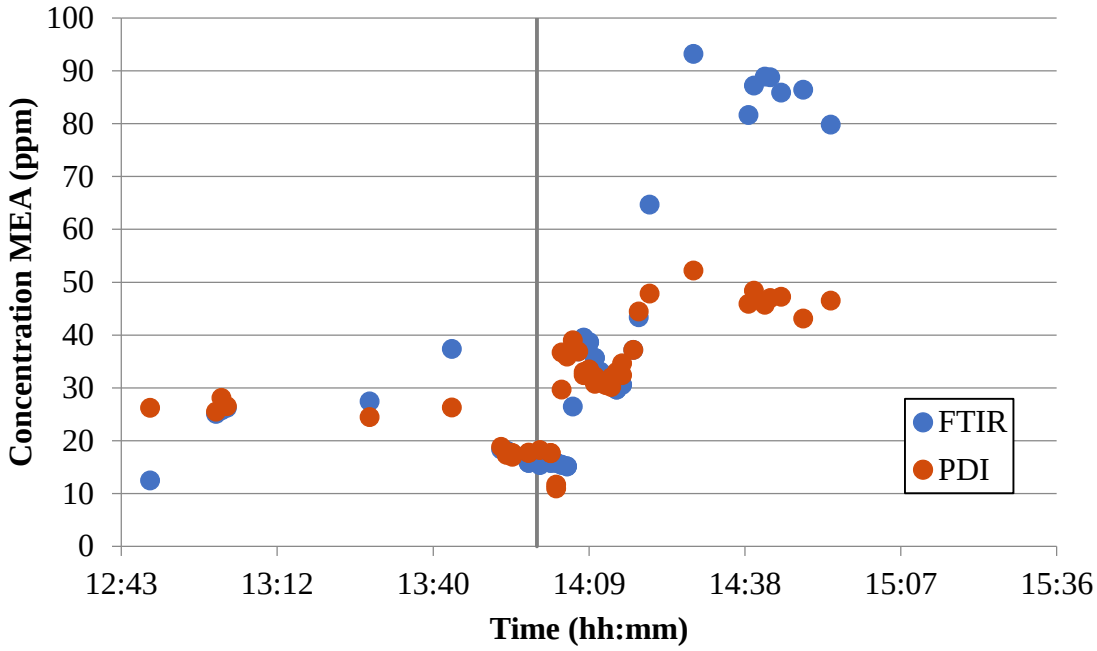


**Figure 6.7: Comparison of PDI-calculated MEA emissions to FTIR-determined MEA emissions for blower change at NCCC SSTU. Amine MEA content was calculated to be 0.023 mol/kg.**

The amine content in the aerosol liquid phase was calculated at 0.023 mol/kg. This analysis was performed for each 24-hour period and the amine content was maintained at a constant value each day. The amine content in the aerosol is not an absolute value, but a useful way to discern the effect of process changes on the amount of amine in the aerosol phase.

Relative agreement was observed between the FTIR-determined and PDI-calculated MEA emissions prior to the blower configuration change at 14:00. Approximately 20 minutes after the process configuration change, the PDI began under-predicting the MEA emissions. This indicates that the process change results in a change

in the amine content in the aerosol phase. In this case, the amount of amine in the aerosol increased; this was observed by the FTIR but not by the PDI due to the use of a daily constant amine composition.

Operation at NCCC with an upstream blower rather than an intermediate one resulted in greater amine aerosol emissions. Aerosol drops are larger, greater in quantity, and have a greater content of amine solvent when the upstream blower is used.

#### *6.3.1.2 Absorber Outlet $CO_2$ Composition*

At the NCCC SSTU, the $CO_2$ capture rate was reduced on December 7, 2015 at 11:20. This was accomplished by reducing the amine solvent flow rate. Over 30 minutes, the $CO_2$ at the water wash outlet increased from ~1% to 2.5%. The FTIR analysis of this change is presented in Figure 6.8.

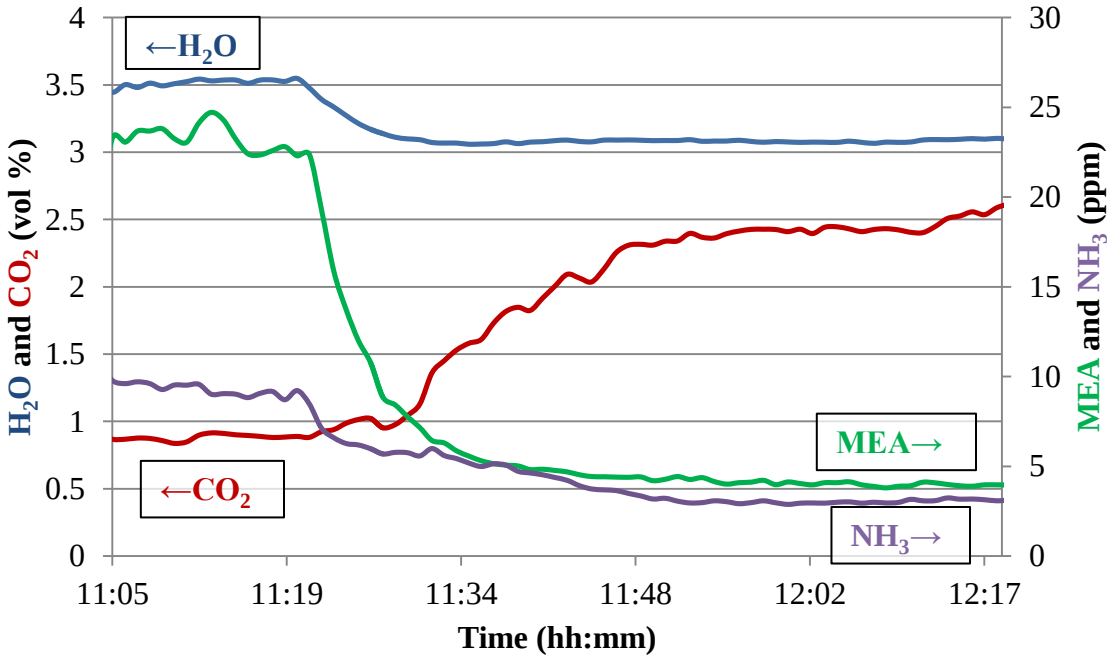


**Figure 6.8: FTIR analysis of reducing $CO_2$ capture rate at NCCC on December 7, 2015 at 11:20. Arrows on the FTIR labels correspond to the axes the data are plotted on; water and carbon dioxide on the left axis (vol %), and MEA and $NH_3$ on the right axis (ppm).**

As the solvent flow rate decreases, the outlet $CO_2$ increases. This coincides with a decrease in the MEA emissions, from ~24 ppm to ~4 ppm. The reduction in the solvent flow rate also plays a role in the MEA emissions and should not be discounted; Chapter 5 of this work elaborates on the role of solvent flow in amine emissions for piperazine solvent.

Figure 6.9 shows the cumulative volume fraction of aerosol as a function of the aerosol diameter for this process change.

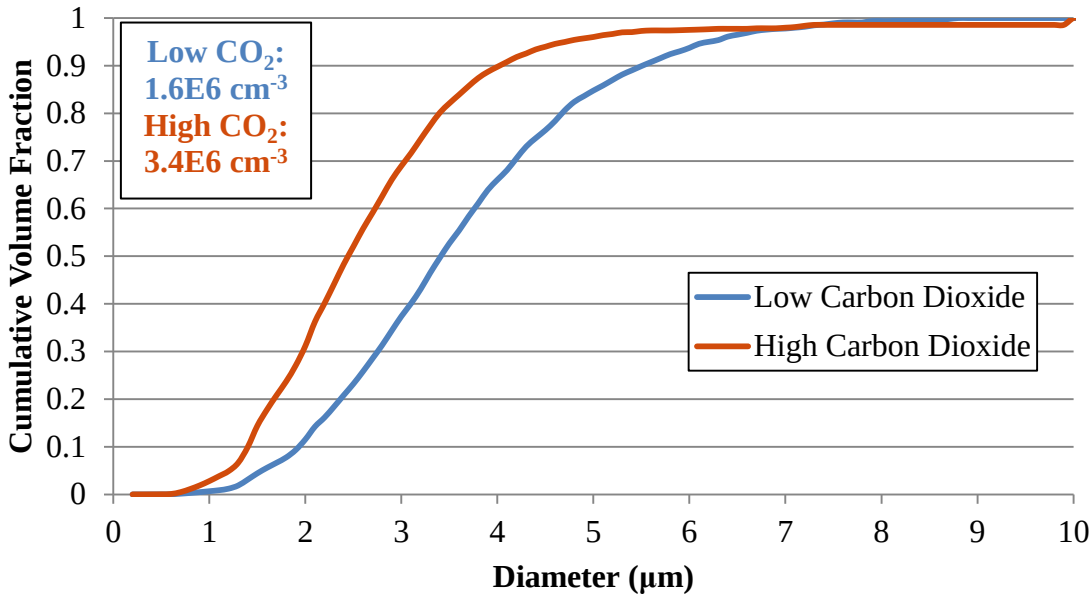


**Figure 6.9: Cumulative volume fraction as a function of aerosol diameter for varying $CO_2$ capture rate. Aerosol diameters are given in µm on the bottom axis. The left axis represents the cumulative volume fraction, or the total volume of aerosol of that diameter and smaller.**

The PDI results show that lower absorber outlet $CO_2$ coincides with larger aerosol diameters. When operating at an increased $CO_2$ capture rate, aerosol smaller than 3.4 µm account for 50% of the total emissions volume. Conversely, with decreased $CO_2$ capture, aerosol smaller than 2.4 µm are responsible for 50% of the emitted volume. The aerosol concentration at the high $CO_2$ capture rate is 1.6E6 $cm^{-3}$, but increases to 3.4E6 $cm^{-3}$ as the $CO_2$ capture rate decreases. Fewer, but larger, aerosol are produced when the $CO_2$ capture rate is high. This results in higher MEA emissions than a larger quantity of smaller aerosol would produce.

Figure 6.10 presents a comparison of the PDI-calculated MEA emissions with the FTIR-analyzed MEA emissions, alongside the $CO_2$. The amine content in the aerosol liquid phase was calculated at 0.023 mol/kg.

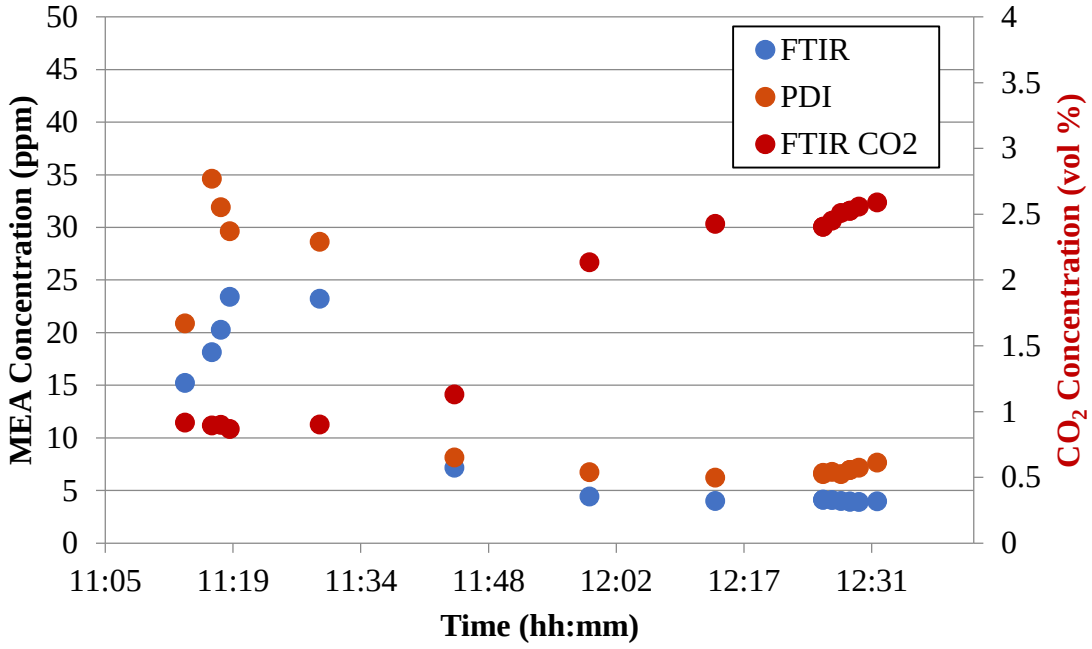


**Figure 6.10: Comparison of PDI-calculated MEA emissions to FTIR-determined MEA emissions at NCCC, along with FTIR-determined $CO_2$. Amine MEA content was calculated to be 0.023 mol/kg.**

Figure 6.10 shows good agreement between the MEA emissions as the $CO_2$ capture rate decreases. This indicates that the calculated amine content in the aerosol phase is not affected by the change in the $CO_2$ capture rate.

A similar test to observe the effect of $CO_2$ on amine aerosol growth was performed at the UKy/KU/LG&E slipstream plant. The $CO_2$ at the absorber inlet was varied by recycling captured $CO_2$. Sampling was performed to observe the effect of $CO_2$

on amine emissions. Figure 6.11 presents the FTIR results from this test. FTIR sampling was performed at the water wash outlet with the water wash deactivated on August 10, 2015 at approximately 16:00.

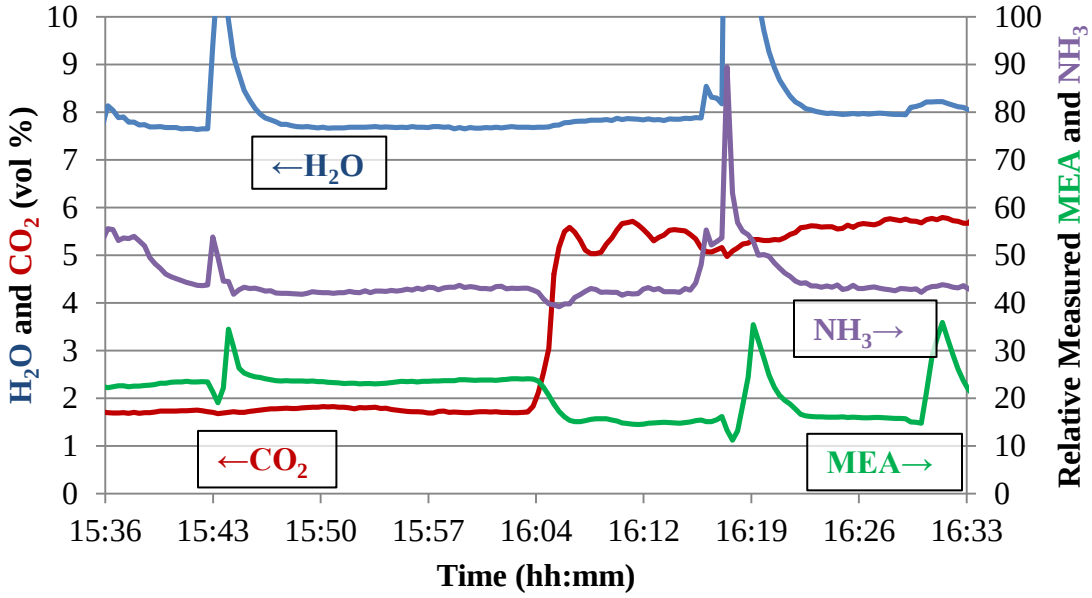


**Figure 6.11: FTIR analysis of inlet $CO_2$ effect on MEA emissions on August 10, 2015 at 16:00. Arrows on the FTIR labels correspond to the axes the data are plotted on; water and carbon dioxide on the left axis (vol %), and MEA and $NH_3$ on the right axis.**

The $CO_2$ at the absorber inlet increased from 12 to 16 wt % at 16:00, resulting in an increase in the $CO_2$ at the absorber outlet of roughly 4 wt %. This resulted in an immediate decrease of MEA emissions by roughly 10%, with all other process conditions remaining constant, including solvent flow rate. This agrees with the results from NCCC in finding that increasing the outlet $CO_2$ reduces the amine aerosol emissions.

In Figure 6.11, the spikes in MEA, $NH_3$, and $H_2O$ every ~22 minutes are due to a process configuration condition at the UKy/KU/LG&E slipstream plant that returns condensate from a downstream process into the water wash section of the absorber column.

Overall, the amine aerosol emissions decrease as the gas phase $CO_2$ increases. Lower absorber outlet $CO_2$ coincide with larger aerosol diameters, despite an increase in the quantity of aerosol produced. $CO_2$ did not have an observable effect on the amine content within the individual aerosol drops.

#### *6.3.1.3 Water Wash Flow Rate*

A simplified water wash was used at the UKy/KU/LG&E slipstream plant. Figure 6.12 presents the FTIR analysis at the water wash outlet before, during, and after water wash operation. The green vertical line indicates the beginning of water wash operation and the red vertical line indicates termination. This test was initiated on August 11, 2015 at 15:40.

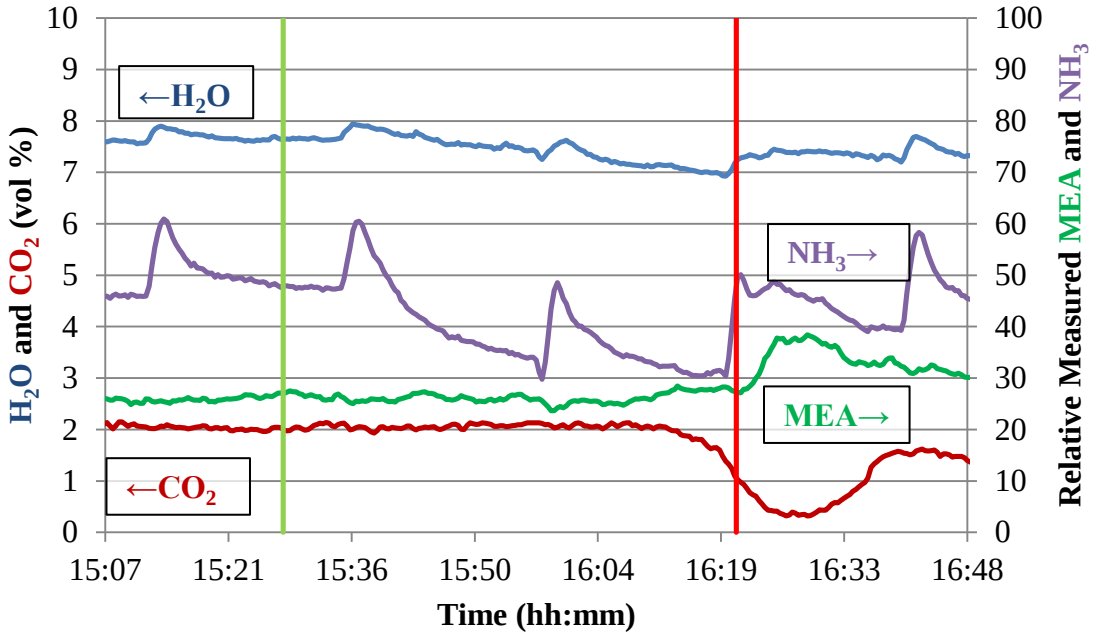


**Figure 6.12: FTIR analysis of a simplified water wash at UKy/KU/LG&E slipstream plant on August 11, 2015 at 15:40. Arrows on the FTIR labels correspond to the axes the data are plotted on; water and carbon dioxide on the left axis (vol %), and MEA and $NH_3$ on the right axis (ppm). The first (green) vertical line indicates the beginning of the test, and the second (red) its completion.**

The simplified water wash was found to be an effective means of reducing ammonia emissions at the absorber outlet. A roughly 40% reduction in ammonia emissions was observed in the short time spent operating the water wash. The MEA emissions were not reduced with the water wash use. This indicates that the majority of MEA emissions at this facility are due to aerosol, as the water wash is ineffective at aerosol mitigation (Mertens, 2013; Mertens, 2014a; Khakharia, 2015).

### *6.3.1.4 Water Wash Temperature*

FTIR and PDI sampling was performed at the NCCC SSTU to determine the effect of the water wash temperature on amine aerosol emissions. On December 12, 2015, the water wash temperature was increased from 20 °C to 23.2 °C over the course of approximately 90 minutes, starting at 09:30. This process change is reflected in the FTIR analysis in Figure 6.13.

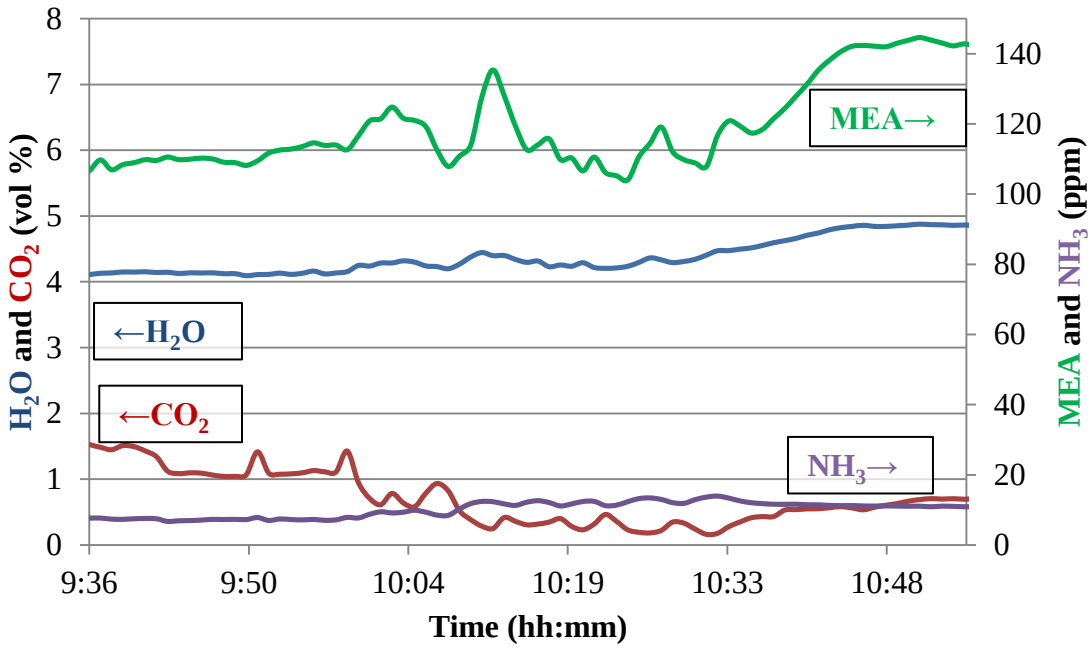


**Figure 6.13: FTIR analysis of effect of increasing water wash temperature from 09:37 to 10:55 at the NCCC SSTU on December 12, 2015. Arrows on the FTIR labels correspond to the axes the data are plotted on; water and carbon dioxide on the left axis (vol %), and MEA and $NH_3$ on the right axis (ppm).**

MEA emissions increased from ~105 ppm to > 140 ppm over the course of 90 minutes. The water vapor increased as well to match the increasing temperature in the wash column.

Figure 6.14 presents the cumulative aerosol volume fraction as a function of the aerosol diameter.

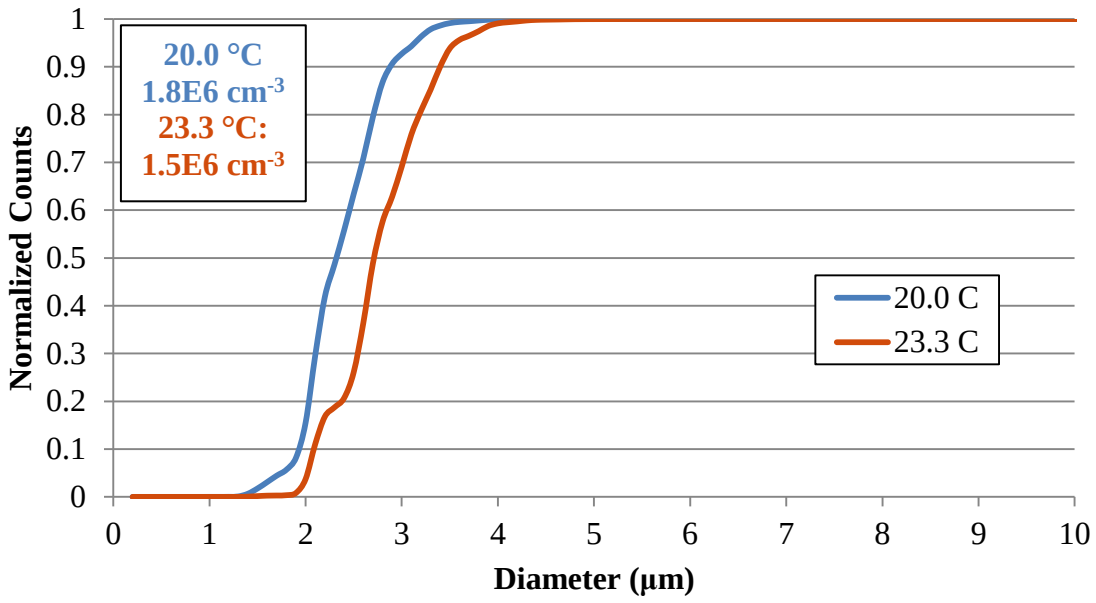


**Figure 6.14: Cumulative volume fraction as a function of aerosol diameter for varying water wash temperature at the NCCC SSTU.**

Water wash at 20 °C results in aerosol smaller than 2.3 µm accounting for 50% of the total emissions volume. At a water wash temperature of 23.3 °C, aerosol smaller than 2.7 µm are responsible for 50% of the emitted volume. The aerosol concentration varied minimally between the two water wash temperatures; 1.5E6 $cm^{-3}$ at the higher temperature and 1.8E6 $cm^{-3}$ at the lower temperature. This indicates that increasing the

water wash temperature increases the amine aerosol emissions mostly by increasing the aerosol sizes while slightly increasing the aerosol concentration.

Figure 6.15 compares the PDI-calculated emissions from amine in the aerosol to the amine emissions quantified by the FTIR.

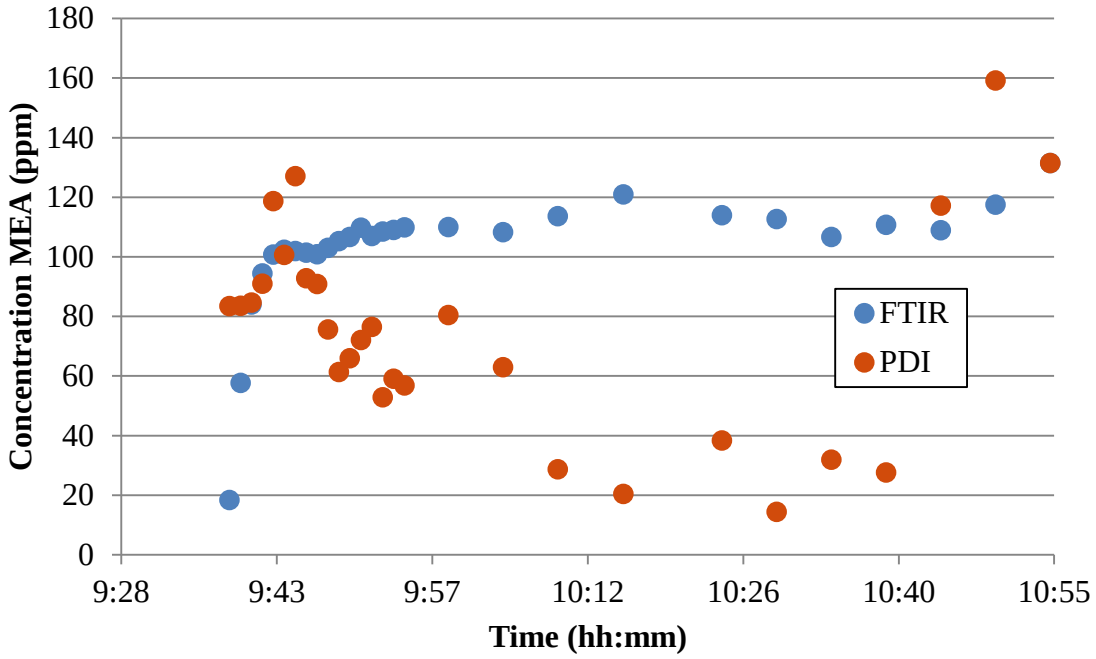


**Figure 6.15: Comparison of PDI-calculated MEA emissions to FTIR-determined MEA emissions for increasing water wash temperature at NCCC SSTU. Amine MEA content was calculated to be 0.12 mol/kg.**

Relatively close agreement is observed between the PDI-calculated and FTIR-determined MEA emissions at the beginning of the selected sampling run. As the water wash temperature increases, the FTIR shows a gradual increase in the amine emissions. This increase is not reflected in the PDI-calculated emissions. This indicates that the amine in the aerosol phase varies as a result of the increasing water wash temperature. In

this case, the PDI is under-predicting the amine content, showing that the increasing water wash temperature increases the amine content in the aerosol phase.

Summarily, an increase in the water wash temperature resulted in an increase in amine emissions at the NCCC SSTU, due to larger diameter aerosol. The aerosol concentration was minimally affected by the water wash temperature. The increased temperature also increases the amount of amine solvent in the aerosol phase.

### 6.3.2 Effect of Aerosol Nuclei on Amine Aerosol Emissions

#### *6.3.2.1 $SO_2$*

The UKy/KU/LG&E slipstream plant uses a caustic pretreatment column to prevent $SO_2$ from entering the absorber column, as shown in Figure 6.2. By stopping the caustic make-up feed to the column, $SO_2$ can be allowed to enter the process. Figure 6.16 presents the effect of $SO_2$ on amine aerosol emissions. This test was performed on August 7, 2015; $SO_2$ breakthrough occurred shortly after 14:00.

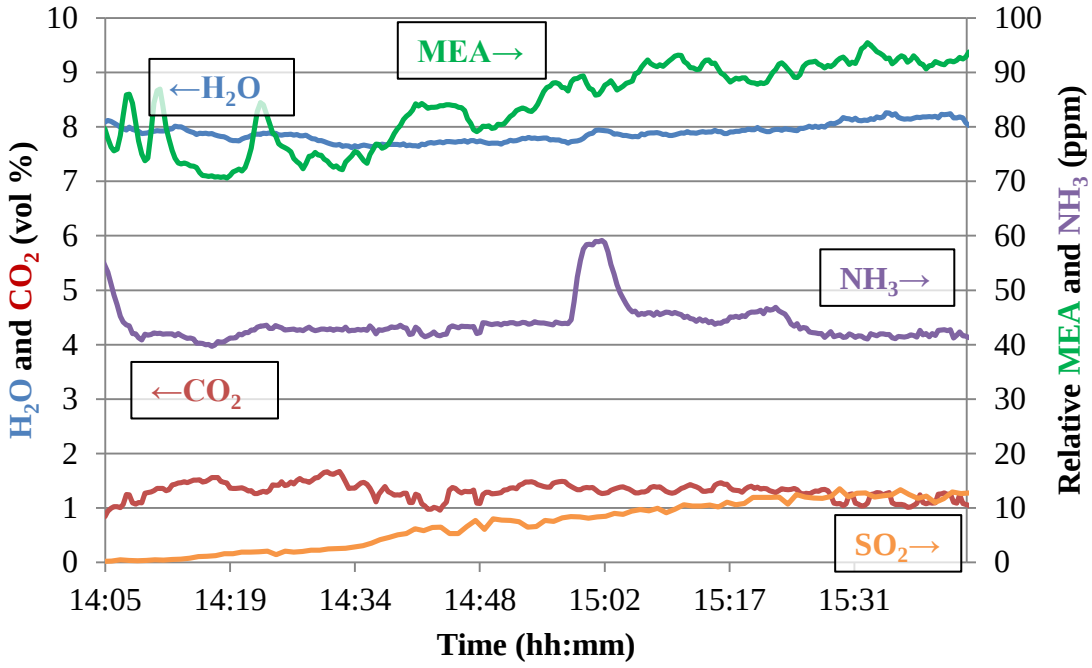


**Figure 6.16: FTIR analysis of $SO_2$ effect on MEA emissions at UKy/KU/LG&E slipstream plant on August 7, 2015 at 14:00. Arrows on the FTIR labels correspond to the axes the data are plotted on; water and carbon dioxide on the left axis (vol %), and $SO_2$, MEA, and $NH_3$ on the right axis (ppm).**

MEA emissions increased at the absorber outlet due to an increase in amine aerosol emissions. Allowing $SO_2$ to enter the absorber column resulted in an increase in MEA emissions of 12 to 93%. MEA emissions rose in proportion to inlet $SO_2$ at a rate of up to 3.9 moles of MEA per mole of inlet $SO_2$.

The UT-SRP pilot plant is equipped to inject sulfur dioxide into the process stream. The injection point is located upstream of the process inlet FTIR analyzer, as indicated in Figure 6.1, and allows for the measurement of the $SO_2$ by FTIR. Piperazine was used as the amine solvent. On March 13, 2015, $SO_2$ was injected into the process

stream at approximately 85 ppm. Figure 6.17 presents the FTIR results; this test was initiated shortly after 10:00 and lasted approximately one hour. Labels at the top of the figure indicate the sampling location, which is also shown in Figure 6.1.

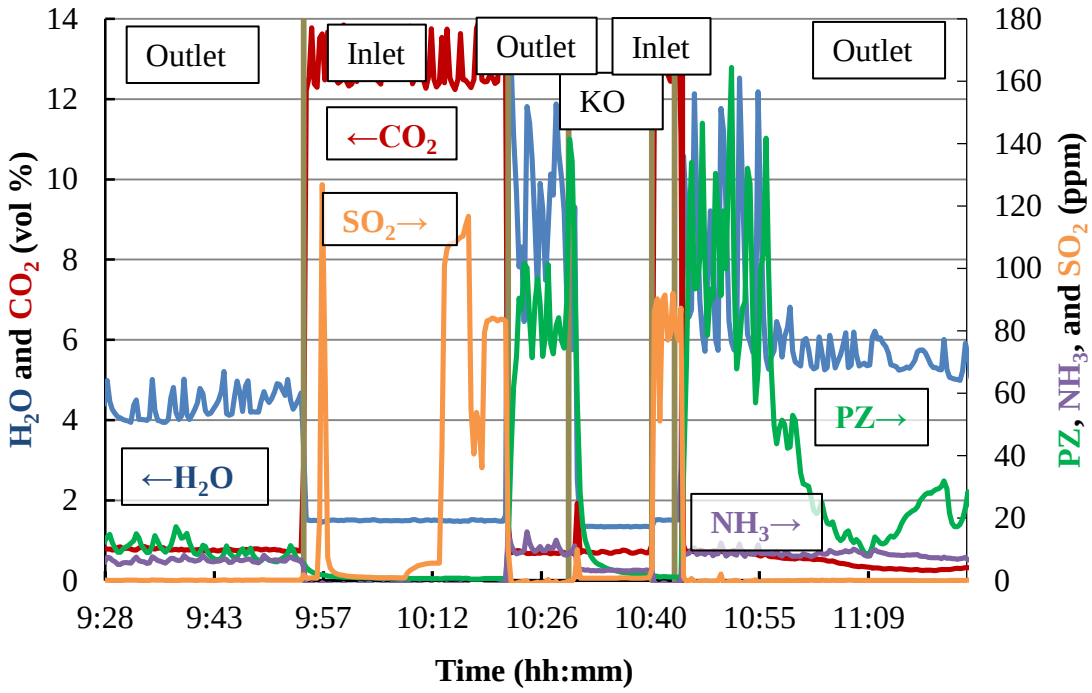


**Figure 6.17: Effect of 85 ppm $SO_2$ injection on piperazine aerosol formation at UT-SRP pilot plant, March 2015. Arrows on the FTIR labels correspond to the axes the data are plotted on; water and carbon dioxide on the left axis (vol %), and piperazine, $SO_2$, and $NH_3$ on the right axis (ppm).**

On stabilization of the $SO_2$ injection rate, PZ emissions increased from ~10 ppm to 80–160 ppm at the absorber outlet. Amine aerosol emissions rapidly decreased once $SO_2$ injection ceased at 11:00. Six different tests were performed with $SO_2$ injection at

the UT-SRP pilot plant, under a slight variation of process conditions. These are summarized in Table 6.1.

**Table 6.1: Test summary of $SO_2$ injection on PZ aerosol formation at UT-SRP, March 2015**

| Test | 1 | 2 | 3 | 4 | 5 | 6 | Average |
|---|---|---|---|---|---|---|---|
| **Date (2015)** | 3/13 | 3/13 | 3/13 | 3/24 | 3/25 | 3/26 | |
| **Baseline PZ (ppm)** | 9.4 | 19.7 | 8.9 | 17.2 | 40.3 | 67.0 | 27.1 |
| **$SO_2$ Injected (ppm)** | 82.5 | 26.4 | 26.0 | 28.0 | 27.7 | 27.0 | 36.3 |
| **PZ Increase (ppm)** | 86.1 | 38.4 | 67.5 | 0.5 | 22.9 | 3.2 | 36.4 |
| **Ratio ($SO_2$:PZ)** | 1.0 | 1.5 | 2.6 | 0.0 | 0.8 | 0.1 | 1.0 |

On average, $SO_2$ was injected to generate a concentration of ~36 ppm. This resulted in an increase of PZ emissions by ~36 ppm, giving a 1:1 ratio of mole inlet $SO_2$ per mole increase in PZ aerosol emissions.

At both the UKy/KU/LG&E slipstream plant and the UT-SRP pilot plant, the presence of $SO_2$ at the absorber inlet was found to increase amine aerosol emissions. MEA emissions increase in proportion to $SO_2$ at 0.3–3.9 mol MEA per mol $SO_2$ at the UKy/KU/LG&E plant, and piperazine emissions at the UT-SRP plant increased an average of 1 mol piperazine per mol $SO_2$.

#### *6.3.2.2 $H_2SO_4$*

Sulfuric acid injection was performed at the UT-SRP pilot plant with a liquid vaporizer and injector (LVI). The design and construction of the LVI is outlined by Fulk (Fulk, 2016).

On March 26, 2015, $H_2SO_4$ was injected into the process at approximately 10 ppm. The FTIR measurement of key components is presented in Figure 6.18.

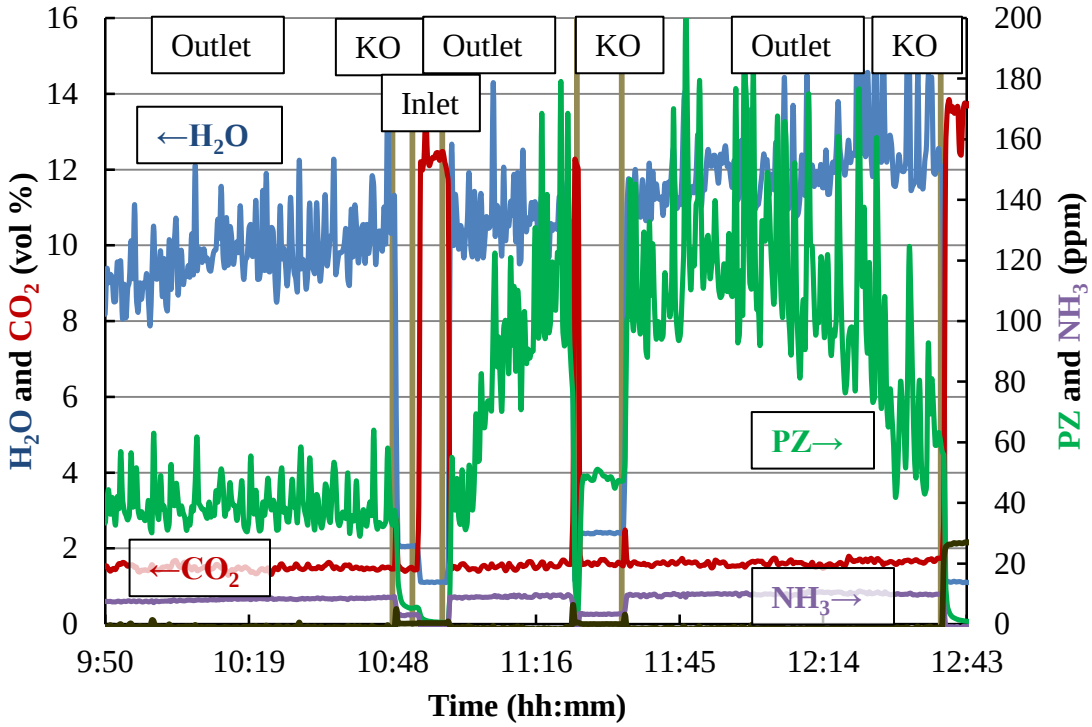


**Figure 6.18: Effect of $H_2SO_4$ injection in piperazine aerosol formation at UT-SRP pilot plant, March 2015. Arrows on the FTIR labels correspond to the axes the data are plotted on; water and carbon dioxide on the left axis (vol %), and piperazine, $SO_2$, and $NH_3$ on the right axis (ppm).**

$H_2SO_4$ injection was initiated shortly after 11:00 and resulted in an increase of piperazine emissions from ~40 ppm to ~110–200 ppm. Four $H_2SO_4$ injection tests were performed and are summarized in Table 6.2.

**Table 6.2: Test summary of $H_2SO_4$ injection on PZ aerosol formation at UT-SRP pilot plant, March 2015**

| Test | 1 | 2 | 3 | 4 | Average |
|---|---|---|---|---|---|
| **Date** | 3/16 | 3/16 | 3/20 | 3/26 | |
| **Baseline PZ (ppm)** | 28.4 | 28.4 | 26.7 | 38.9 | 30.6 |
| **$H_2SO_4$ Injected (ppm)** | 10.0 | 13.7 | 10.0 | 10.0 | 10.9 |
| **PZ Increase (ppm)** | 9.3 | 27.0 | 22.6 | 67.3 | 31.6 |
| **Ratio** | 0.9 | 2.0 | 2.3 | 6.7 | 3.0 |

An average of 10.9 ppm of $H_2SO_4$ was injected during each of the 4 tests; this resulted in an increase of piperazine emissions by an average of 31.6 ppm, giving 3 ppm piperazine per ppm $H_2SO_4$ in the inlet flue gas. These values are comparable to the April 2017 UT-SRP pilot plant aerosol test results, which are presented in Chapter 5 of this work. The 2017 UT-SRP campaign used an $SO_3$ generator to produce aerosol nuclei; an average addition of 55 ppm of $SO_3$ resulted in an average emissions increase of 1.5 ppm piperazine per ppm $SO_3$ injected.

#### *6.3.2.3 Effects of Upstream Baghouse Filtration*

A baghouse filtration unit was constructed and brought online at the National Carbon Capture Center after the 12/2015 sampling campaign. The baghouse was installed to capture mercury, arsenic, and other heavy metals. Activated carbon is injected and dispersed in the flue gas duct upstream of the baghouse. The metals adsorb onto the activated carbon, which is collected on the bag filters in the baghouse. As the baghouse collects particulate on the bag filters, a cake layer forms and allows the collection of smaller particulates, such as fly ash aerosol nuclei. To reduce pressure drop through the baghouse, the filters are cleaned by the use of a pulsed jet, which directs a

counterflow burst of air through the bag filter to drop dust from the filter into a collection hopper (Swanson).

A lagniappe of the baghouse flue gas treatment is the improved removal of $SO_3$. Hydrated lime injection upstream of the baghouse already collects a substantial quantity of $SO_3$; adsorption onto the activated carbon and subsequent removal in the baghouse further reduces the $SO_3$ (Looney, 2014). Figure 6.19 presents an overview of the flue gas treatment steps at NCCC Gaston Unit 5.

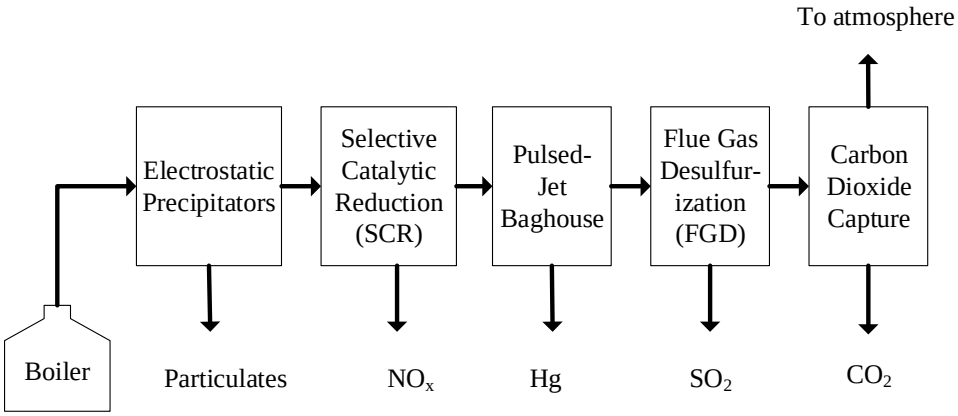


**Figure 6.19: Flue gas treatment steps at NCCC Gaston Unit 5 boiler**

The $SO_3$ content at the SCR outlet has been measured at 13 ppm. Prior to the baghouse installation, $SO_3$ was entering the $CO_2$ capture process between 7 and 9 ppm, even with the hydrated lime addition. After the baghouse was brought online, the $SO_3$ content at the baghouse outlet was measured at 0.5 ppm.

FTIR and PDI sampling was performed at the NCCC SSTU between October 4$^{th}$ and 14$^{th}$, 2016. The purpose of this sampling campaign was to determine the effectiveness of the upstream baghouse filtration system at aerosol nuclei removal.

*6.3.2.3.1 FTIR Amine Emission Results*

FTIR sampling was performed over the entirety of the sampling campaign. The MEA emissions results were compared to the values from the December 2015 sampling campaign to determine the effectiveness of the baghouse at reducing MEA emissions. Figure 6.20 presents a comparison of the MEA emissions over 24 hour periods; one for 12/12/2015, and another for 10/10/2016.

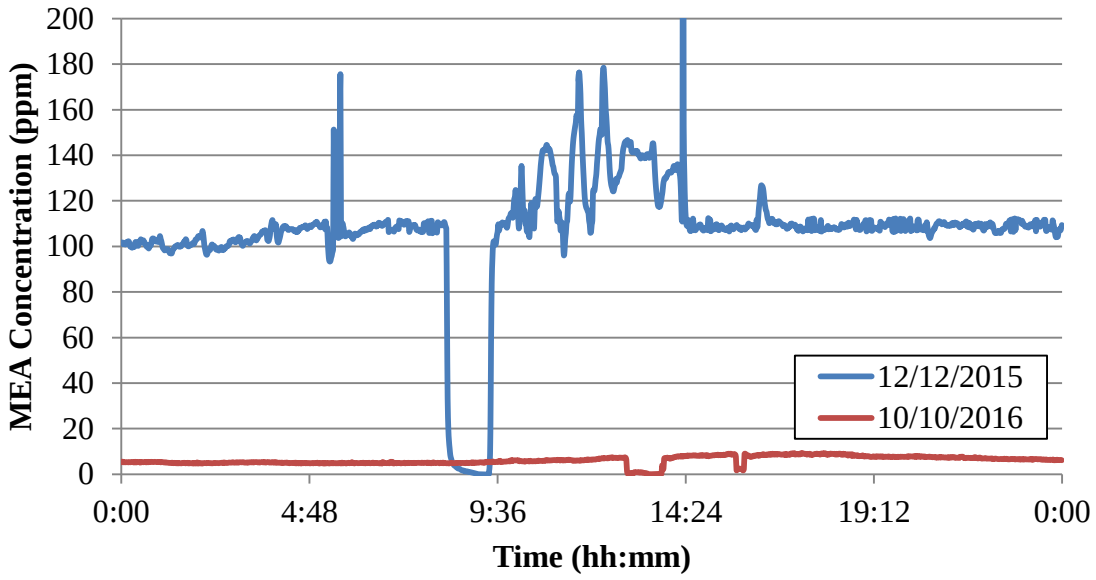


**Figure 6.20: MEA emissions at NCCC SSTU water wash outlet, before (12/12/15) and after (10/10/16) baghouse installation**

MEA emissions from the SSTU were between 100 to 110 ppm prior to the installation of the baghouse. These emissions were reduced to between 5 to 10 ppm after the baghouse startup. Similar operating conditions were maintained in the SSTU during both operating periods, indicating that the baghouse is responsible for a significant reduction in the amine emissions due to removal of aerosol nuclei.

*6.3.2.3.2 PDI Aerosol Results*

The PDI was successfully utilized for aerosol characterization during the December 2015 sampling campaign. Aerosol drops as small as 0.1 μm were detected, with concentrations up to 10E7 $cm^{-3}$.

PDI sampling was repeated on the SSTU during the October 2016 campaign. During this sample run, no aerosol drops were detected. The apparent absence of aerosol was initially believed to be due to PDI instrument malfunction or user error. Diagnostic tests and troubleshooting results determined that the PDI was operating properly and that any aerosol emissions from the process consisted of aerosol smaller than 0.1 μm in diameter.

The low outlet MEA is the primary indicator of a reduced aerosol emissions. If a large concentration (>1.0E6 $cm^{-3}$) of aerosol nuclei are present in the inlet flue gas, MEA emissions will be an order of magnitude or greater than predicted by volatility alone.

As previously noted, the PDI operates by passing aerosol drops through intersecting laser beams. The PDI test cell is equipped with an observational window for manual confirmation of operation. An estimation of the aerosol concentration can be made by observing the intensity of the lasers; bright lasers indicate a high concentration, while faint lasers indicate a low concentration in the sampled stream. Figure 6.21 presents the PDI laser intersection as viewed in December 2015, while Figure 6.22 shows the same beam crossing in October 2016.

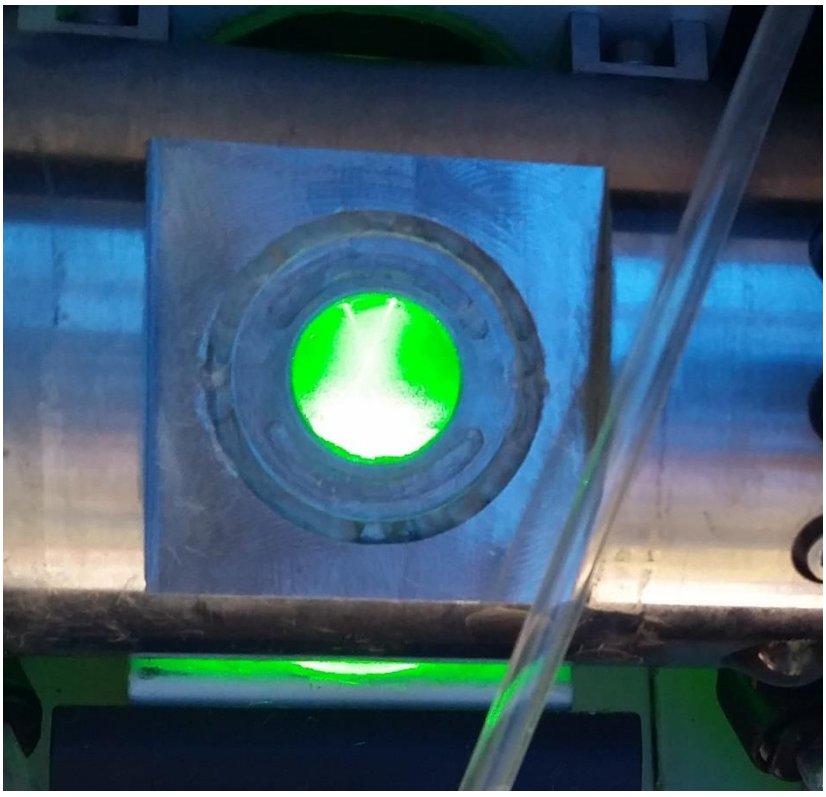

**Figure 6.21: PDI laser intersection from NCCC SSTU sampling, December 2015**

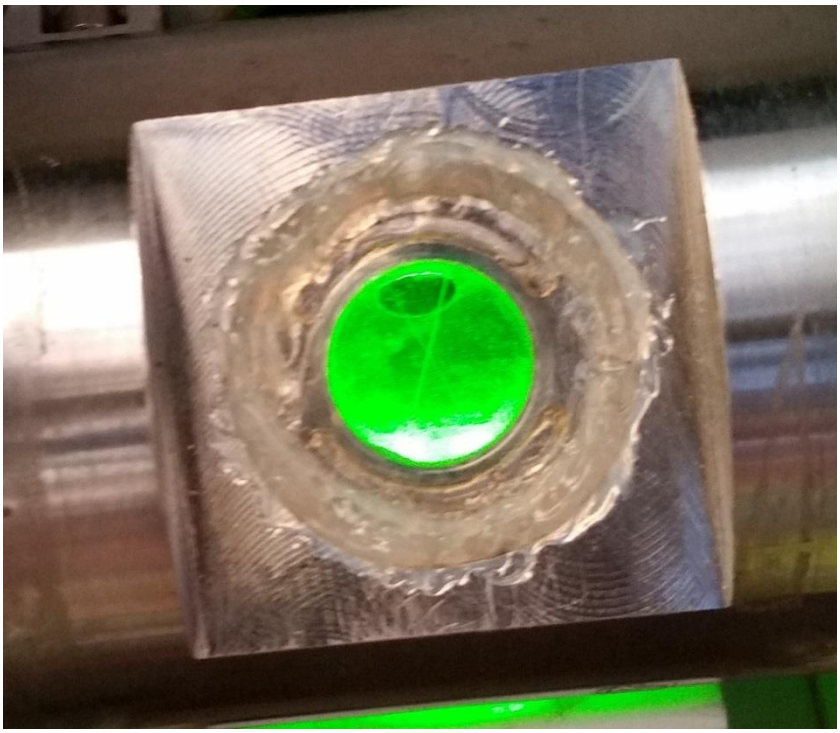

**Figure 6.22: PDI laser intersection from NCCC SSTU sampling, October 2016**

The laser intensity is significantly reduced from December 2015 to October 2016, due to a reduction in aerosol concentration and size. Although the lasers were still visible during the October 2016 tests, the PDI did not detect any aerosol, indicating that aerosol in the sampled stream were smaller than the lower bound of detection of 0.1 μm for the PDI.

The PDI is calibrated with an oscilloscope. The oscilloscope is used to observe the three raw photodetector signals; symmetrical Doppler-burst Gaussian signals indicate the passage of a drop through a beam path. A fourth signal is used as an indicator of a drop passing through the intersecting laser beams. Signal activity observed on the oscilloscope is a clear indication of the presence of measureable aerosol. Figure 6.23

presents an oscilloscope readout from December 5, 2015, while Figure 6.24 presents an oscilloscope display from October 10, 2016.

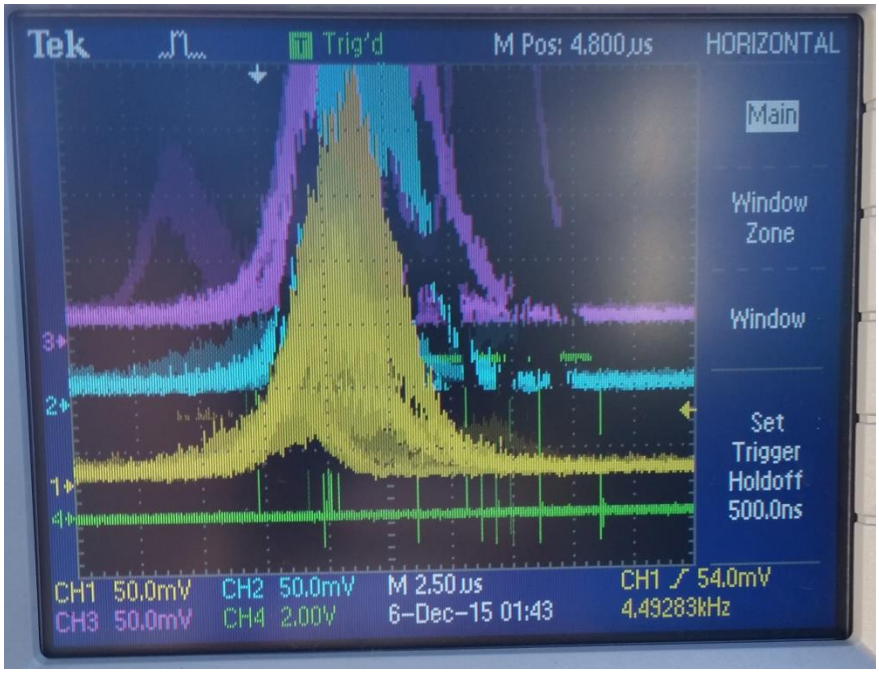


**Figure 6.23: Oscilloscope readout from 12/5/15 sampling at NCCC SSTU**

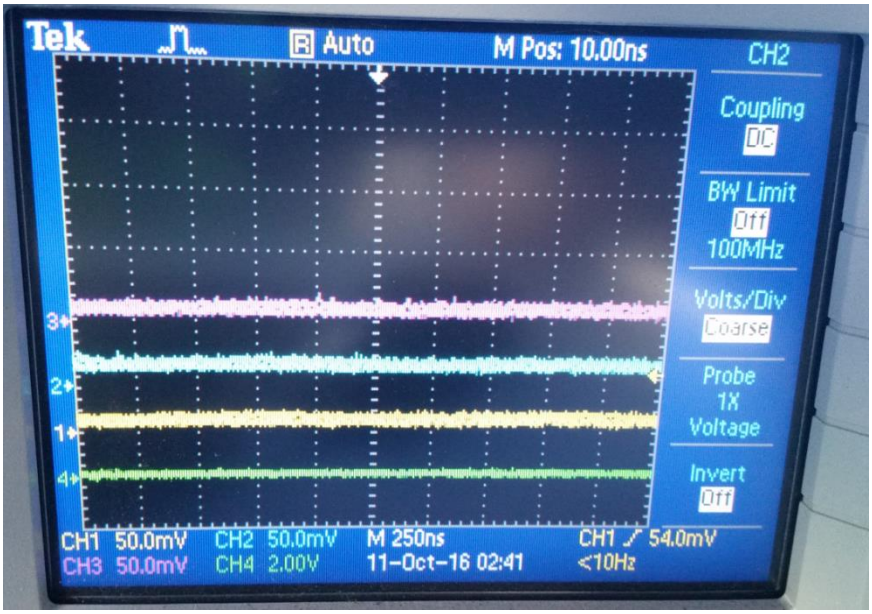


**Figure 6.24: Oscilloscope readout from 10/10/16 sampling at NCCC SSTU**

In Figure 6.23, channels 1-3 display Gaussian Doppler bursts, indicating the presence of aerosol drops. The plateaus in the green gate signal indicate the passage of a drop through the beam intersection. Despite identical voltage and range settings, the oscilloscope readout in Figure 6.24 shows no Doppler bursts from the photodetector signals. This further confirms the absence of aerosol drops at sizes greater than 0.1 μm.

*6.3.2.3.3 FTIR Measured Ammonia Emissions*

Ammonia emissions at the SSTU water wash outlet were measured by FTIR throughout the October 2016 sampling campaign. The presence of $NH_3$ in the outlet stream from an amine scrubbing unit indicates amine oxidation. Figure 6.25 presents the ammonia emissions from the SSTU over a 6-day period.

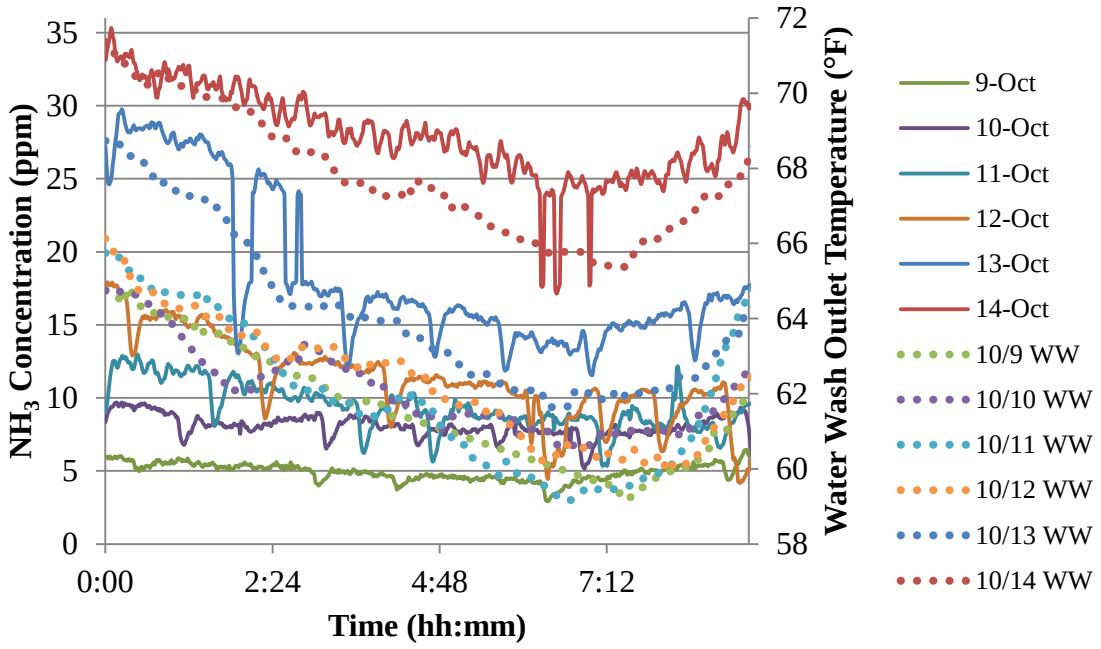


**Figure 6.25: Ammonia emissions from NCCC SSTU, 10/9/2016 to 10/14/2016. Solid lines are ammonia (left axis), while dashed lines are temperature (right axis)**

Midnight until 9:00 AM is the time range for the presented data; minimal operational changes occurred during this time each day. The solid lines represent the ammonia at the water wash outlet, given in ppm and scaled to the left x-axis. The dashed lines represent the temperature of the gas stream exiting the water wash column in °F, and are scaled to the right x-axis.

From 10/9 to 10/12, the water wash outlet temperature remained relatively consistent. The ammonia emissions increase each successive day in this series, indicating that amine oxidation is occurring. Over the last two days of sampling, the water wash outlet temperature increased from the temperature of the previous four days. This resulted in further increases in ammonia emissions in addition to the daily increase in the

ammonia at the water wash outlet. Amine oxidation in the process results in an increase in ammonia each successive day of operation, but operating the water wash at a lower temperature can help mitigate the ammonia emissions.

## 6.4 COMPARISON OF PDI AND ELPI+™ AEROSOL MEASUREMENTS

Work by Saha et al. quantified aerosol size distribution and concentration with an ELPI+™ (Saha, 2017). These measurements were performed on the NCCC SSTU and Pilot Solvent Test Unit (PSTU); in the case of the SSTU measurements, the ELPI+™ sample was extracted from the process immediately downstream of the PDI sampling location during sampling in December of 2015. Figure 6.26 presents a schematic of the ELPI+™ extraction system for NCCC SSTU sampling.

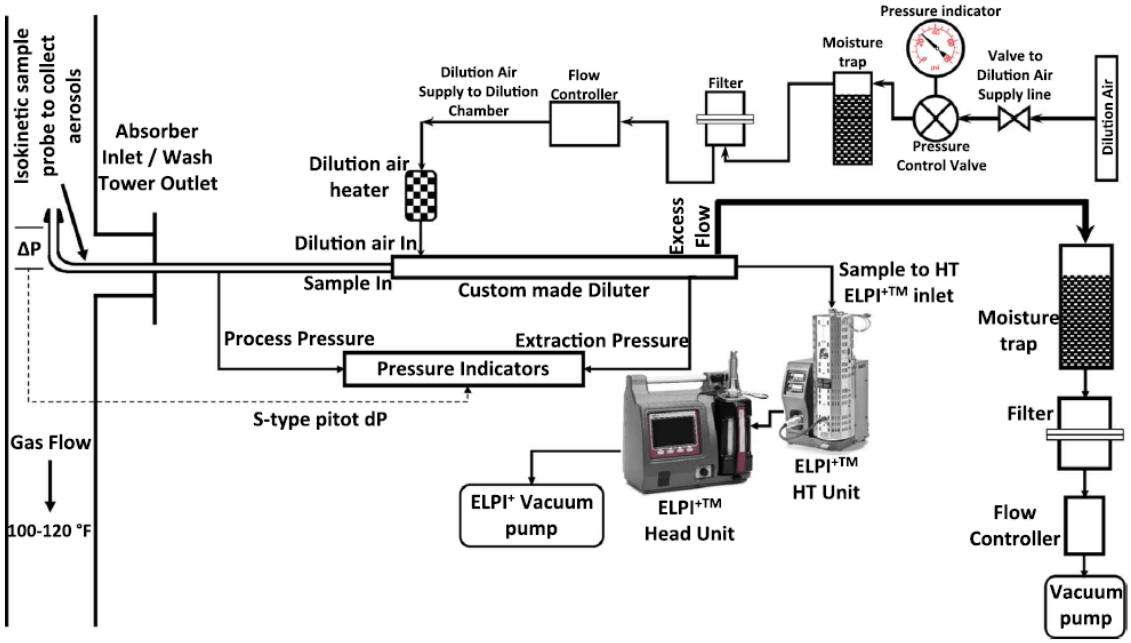


**Figure 6.26: Sample extraction system for ELPI+™ analysis at NCCC SSTU (Saha, 2017)**

Dilution temperature was found to significantly affect the aerosol size distribution; adding the dilution air to the process at 90 °C caused the ELPI+™ to find a median aerosol diameter of 0.1 µm, while adding dilution air at 180 °C produced a median aerosol diameter of 0.01 µm.

Aerosol concentrations were found to be in the range of 10E6 to 10E7 $cm^{-3}$. Roughly 10-12% of very small aerosol (0.01 µm) were observed at the water wash outlet as compared to the absorber inlet, indicating that significant aerosol collection or coagulation was occurring within the absorber and water wash. 50% of the aerosol sampled were at sizes of 0.2 µm or smaller, with virtually 100% of aerosol below 1.0 µm in diameter. The cumulative number count for ELPI+™ testing on the NCCC SSTU is shown in Figure 6.27.

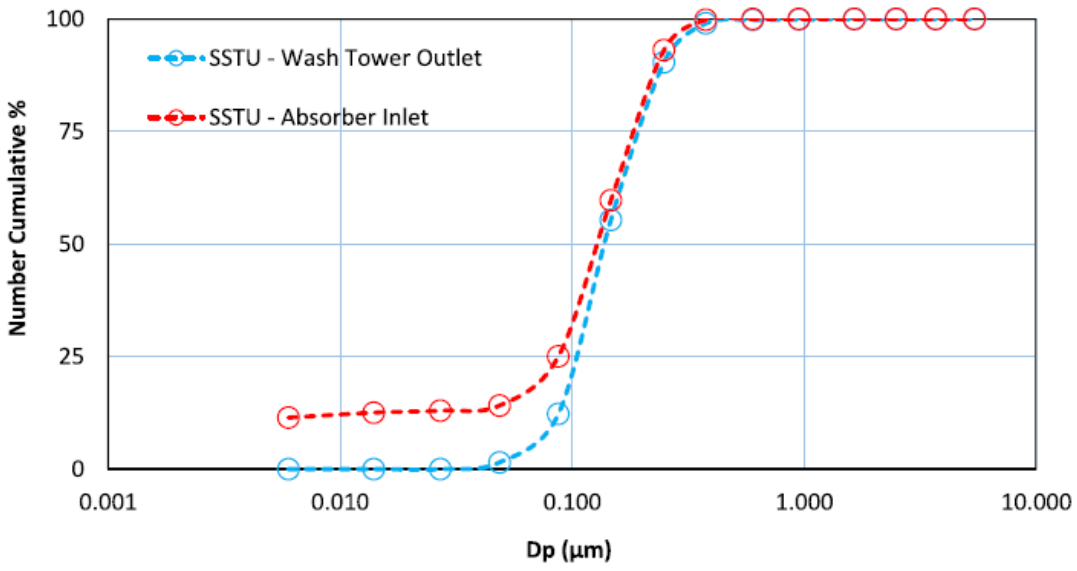


**Figure 6.27: ELPI+™ measured cumulative number count during NCCC SSTU sampling (Saha, 2017)**

The aerosol concentration results are found to be in relative agreement with the PDI analysis results. PDI sampling during this time span found aerosol concentrations between 1.4E5 and 9.4E6 $cm^{-3}$.

However, stark disagreement is found between the ELPI+™ and the PDI. The PDI observed significant quantities of aerosol at sizes above 1.0 µm in diameter. Figure 6.28 presents a PDI-determined cumulative number distribution for sampled aerosol.

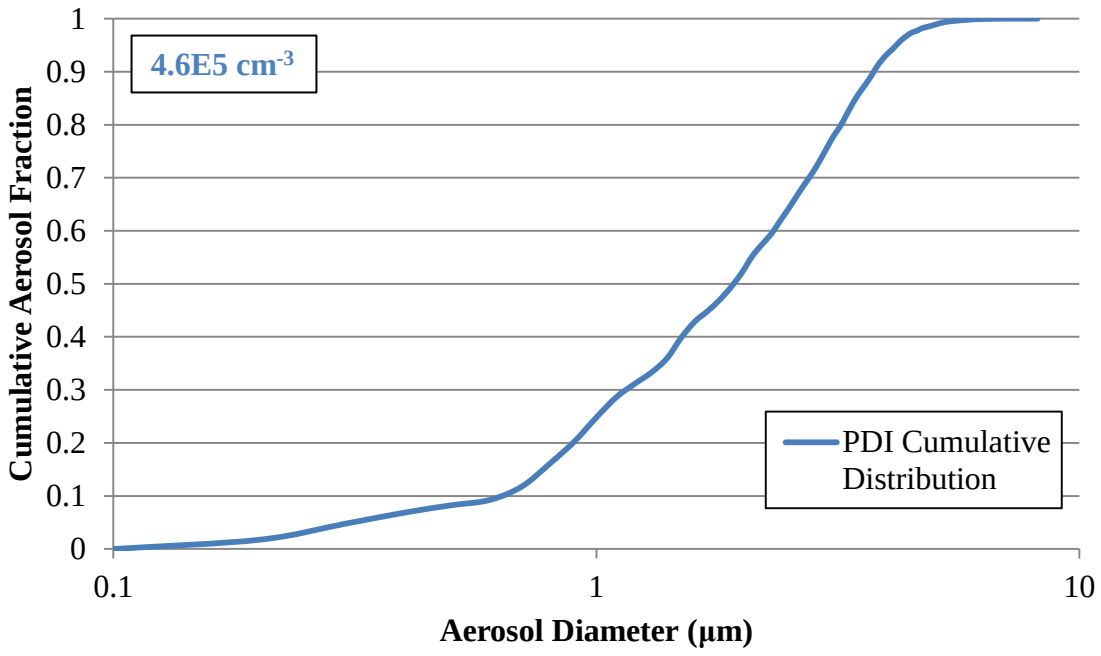


**Figure 6.28: Cumulative aerosol distribution as determined by PDI sampling at NCCC SSTU**

PDI analysis found 50% of the sampled aerosol were at sizes below 2.0 µm in diameter. This is an order of magnitude larger than the sizes determined with the ELPI+™.

It is hypothesized that the ELPI+™ dilution has a significant impact on the aerosol sizes. As evidenced throughout this work, the gas phase temperature plays a substantial role in the aerosol size distribution, growing and shrinking aerosol as the temperature and supersaturation vary. By adding heated and desiccated air to the sampling process, water in the aerosol phase evaporates and results in shrinkage of the aerosol. While this has a minimal impact on the aerosol concentration, this appears to effect the size distribution. Future ELPI+™ results must be considered with this dilution effect in mind.

## 6.5 CONCLUSIONS

Amine emission quantification was performed via FTIR and PDI at three different sites: the National Carbon Capture Center Slipstream Solvent Test Unit (SSTU), the University of Kentucky, Kentucky Utilities, and Louisville Gas and Electric (UKy/KU/LG&E) Slipstream plant, and the University of Texas Separations Research Program (UT-SRP).

### 6.5.1 FTIR and PDI Field Analysis

FTIR and PDI measurements were used to observe the effects of amine scrubbing conditions on amine aerosol growth and emissions. The FTIR was successful at quantifying amine emissions in excess of 1000 ppm, and observing how process conditions caused variations in emissions. PDI sampling was found to be effective at determining aerosol sizes (0.1 to 12 μm) and concentration (up to 9.4E6) at the pilot scale. An algorithm utilizing the aerosol size distribution and concentration was used to

calculate the content of amine within the aerosol, and successfully quantified changes in the aerosol amine content due to changes in the process conditions.

### 6.5.2 Effect of Baghouse Flue Gas Pretreatment

An upstream baghouse flue gas treatment unit at NCCC reduced amine emissions by a factor of 10 to 20 through the collection of fly ash and $SO_3$ aerosol nuclei. Any aerosol present were below detection limits of the PDI (<0.1 μm in diameter). Baghouses can be an effective amine aerosol mitigation strategy through the elimination of aerosol nuclei.

### 6.5.3 $SO_2$ and $H_2SO_4$ Presence in Inlet Flue Gas

The presence of $SO_2$ in the inlet flue gas was found to increase MEA emissions by up to 3.9 mol MEA per mol $SO_2$, and increased piperazine emissions by 1 mol piperazine per mol $SO_2$. The presence of sulfuric acid in the inlet flue gas increased piperazine emissions by 3 mol piperazine per mol $H_2SO_4$.

### 6.5.4 Impact of Blower Configuration on Amine Aerosol Emissions

The configuration of the pilot plant was found to play a significant role in aerosol emissions. Operating with a blower upstream of the absorber, rather than between the absorber and the water wash, was found to approximately triple the amine emissions. The upstream blower increased aerosol sizes by 70 % and increased the aerosol concentration by 9E5 per $cm^3$. The amine content within the aerosol phase also increased. The amine emissions reduction with the intermediate blower is theorized to be due to collection of aerosol through impaction within the blower.

### 6.5.5 Comparison of PDI and ELPI+™ Aerosol Sizing Technologies

A comparison of ELPI+™ and PDI sampling techniques simultaneously operating at the same sampling location showed similar values for aerosol concentration. The aerosol size distributions showed significant variance between the two analyzers, with the PDI reporting a 50% diameter cutoff an order of magnitude larger than the ELPI+™. It is theorized that the desiccation and dilution of the sampled steam prior to entering the ELPI+™ greatly reduces the aerosol sizes due to the evaporation of volatile components from the aerosol phase.

### 6.5.6 Impact of Outlet $CO_2$ on Amine Emissions

Increasing the absorber outlet $CO_2$ reduced amine aerosol emissions to $1/6^{th}$ of the original value at NCCC, and by 40 % at UKy/KU/LG&E. Aerosol at lower $CO_2$ contents were 42 % larger in diameter but reduced in concentration by 47 %. The gas phase $CO_2$ was found to have no discernible effect on the amine content in the aerosol phase.

### 6.5.7 Impact of Water Wash on Amine Aerosol Emissions

Further evidence of the inability of the water wash to curtail aerosol emissions was observed. Increasing the water wash temperature by 3.2 °C was found to increase amine emissions by 33 % at the NCCC SSTU. This was due in part to aerosol diameters increasing by 17 %, and aerosol drops containing a higher concentration of amine solvent. The process configuration at NCCC was incapable of capturing the larger aerosol produced from the increased water wash temperature.

## 6.6 RECOMMENDATIONS

Efforts should be made to produce additional comparisons of the ELPI+™ and PDI aerosol analyzers. Experiments undertaken with a goal of producing a material and mass balance around the ELPI+™, possibly with FTIR analysis, would be instrumental in quantifying the effectiveness of these two analyzer systems.

Variations in the amine solvent molality and amine type would significantly contribute to the understanding of aerosol formation and growth mechanisms. This research only covers piperazine and ethanolamine; the effects of varying the amine structure and functional groups would generate interesting results.

Varying the process configuration, such as the blower arrangement, produced surprising results in amine aerosol emissions. Efforts should be taken to seek out other variations in process conditions to quantify this potential impact on amine emissions, and to determine if this is a viable option for aerosol mitigation.

Future generations of the PDI analyzer should focus on improving the robustness of the equipment. A crack that formed in the window of the transmitter/receiver unit set research back several months due to the difficulty in obtaining the optical crown glass necessary for the window. This window can be easily damaged during assembly of the PDI system, and cracks can block the laser passage, rendering the system inoperable. The PDI laser crossing can become misaligned due to vibrational forces, either in transport or due to proximity to rotating equipment in pilot plants. The laser alignment is not easily performed on the third generation PDI. Future systems may consider a fixed alignment that is more robust in construction.

The sample extraction for FTIR analysis involves the use of heated sampling probes to maintain a temperature of 180 °C across the sampling train. Due to faulty design, the probes are prone to burning through electrical wires and causing short circuits. This has compromised the sampling system and has resulted in analyzer failures in the field. It is highly recommended that these probes be replaced with a more reliable sample extraction technique. If not replaced, the FTIR probes should be positioned in locations not susceptible to liquid accumulation. The probes should also be oriented in an upright position, so the inevitable failure of the probe doesn't result in liquid from the process entering the rest of the FTIR sampling system.

## 6.7 ACKNOWLEDGEMENTS

At the University of Kentucky, Kentucky Utilities, and Louisville Gas and Electric Slipstream plant, Kunlei Liu and Jesse Thompson were invaluable for providing logistics and financial support. Their advice and assistance were instrumental in developing field sampling techniques and data interpretation. David Link and Michael Manahan also proved to be helpful advisors. The operations and engineering crews at the slipstream plant were vital in the success of the sampling campaigns.

Justin Anthony and John Carroll at the National Carbon Capture Center were invaluable in coordinating the sampling campaign logistics and providing equipment and construction as needed. The operations and maintenance crews at the NCCC SSTU were always friendly and helpful. Their banter and sports debates provided appreciated entertainment during unit downtimes.

As always, the University of Texas Separations Research Program was a pleasure to work with. Steve Briggs, Robert Montgomery, and Dr. Frank Seibert were very helpful in preparing for and conducting pilot plant campaigns.

Special thanks to Eric Chen and his crew for their exhaustive efforts in preparing for pilot plant campaigns, and for frequently providing manpower and consulting for the sampling endeavors conducted in this research.

The entirety of the Rochelle research group at UT Austin was extensively involved in the UT-SRP campaign. Steven Fulk planned and conducted the aerosol experiments, and provided incredibly valuable research and input on performing field sampling experiments. Matt Walters configured the DeltaV™ control system during the March 2015 UT-SRP campaign. Conlin Kang not only worked extensively on aerosol growth models, but created with the VBA coding necessary to combine the PDI and FTIR measurements for aerosol amine composition calculations. Finally, special thanks to Dr. Rochelle, for financial and scientific support.

# CHAPTER 7: CONCLUSIONS AND RECOMMENDATIONS

The following chapter presents the major findings and conclusions for this research. Results for aerosol generator development, bench scale experiments, aerosol generation at the pilot scale, and field measurements are shown. Recommendations for future experiments and improvements for apparatuses and analyzers are also given.

## 7.1 CONCLUSIONS

### 7.1.1 $SO_3$ Aerosol Generation

$SO_3$ was reliably and safely provided at 10 to 100 ppm for the bench-scale (100 LPM) and pilot scale (10,000 LPM) test systems with a vanadium pentoxide catalytic reactor using $SO_2$ in air. The computational modeling and construction of the $SO_3$ aerosol generator is a significant achievement from this research. Experiments at the UT-SRP pilot plant and on the bench-scale Aerosol Growth Column require an aerosol source for the synthetic flue gas.

#### *7.1.1.1 Pilot Scale $SO_3$ Generator Experiments*

The generator produced $SO_3$ at rates between 0.23 and 1.68 grams per minute, at $SO_2$ conversion between 81 and 98 %. This resulted in $SO_3$ between 9 and 112 ppm, which was sufficient for amine aerosol generation. The $SO_3$ generator was tested during the April 2017 UT-SRP pilot plant campaign. $SO_3$ generation was performed in 16 test runs with varying process conditions and reactor flow rates. Due to the success of the reactor at higher generation rates, it is possible to produce $SO_3$ at rates that are sufficient for pilot plants larger than the 0.1 MWe UT-SRP unit, including the 0.7 MWe PSTU unit at the National Carbon Capture Center.

#### *7.1.1.2 Bench Scale $SO_3$ Generator Experiments*

$SO_3$ generation experiments on the bench scale Aerosol Growth Column produced 20 to 50 ppm of $SO_3$ in the synthetic flue gas, at conversion in excess of 97 %. Mean aerosol diameters from this process measured between 1.5 and 2.3 μm, with aerosol concentrations in the gas stream between 4E3 and 7E4 per $cm^3$. The $SO_3$ generator is shown to be as equally effective at the bench scale as the pilot scale.

#### *7.1.1.3 $SO_3$ Generator Model*

After pilot scale tests, the Polymath $SO_3$ generator model was updated with more accurate parameters; this included an increase in the activation energy from 42,331 to 42,900 kJ/mol in the Arrhenius equation (Equation 3.16). This allowed the reactor model to more accurately predict the $SO_3$ conversion, increasing the model conversion from 92.1 % to the experimentally determined 93.5 %. The Polymath model was developed to size the reactor and predict optimal $SO_3$ generation rates. These optimal operating conditions were used to establish operational guidelines for the generator.

### 7.1.2 Bench Scale Aerosol Generation and Measurement

A series of bench scale aerosol generation and measurement experiments were performed on the Aerosol Growth Column (AGC). The solvent flow rate and amine composition were varied, along with the inlet flue gas $CO_2$ and $SO_3$. Each variable was found to impact the aerosol sizes and concentration, and the amine emitted through the outlet flue gas. The solvent $CO_2$ loading, flue gas outlet temperature, and absorber column temperature profile were also shown to affect amine emissions and aerosol properties.

#### *7.1.2.1 Piperazine Emissions*

Piperazine emissions were below 0.5 ppm with 3 m piperazine; increasing the amine solvent concentration to 5 m resulted in piperazine emissions from 0.5 to 9.3 ppm. Increasing the solvent flow rate from 0.8 to 2.4 LPM resulted in increased piperazine emissions by up to 6.9 ppm. Lowering the temperature bulge from the middle of the column to the bottom decreased piperazine emissions by a factor of eight; this is due in part to a reduction in the absorber outlet temperature by up to 5 °C.

#### *7.1.2.2 Mean Aerosol Diameter*

Reducing solvent flow increased the observed mean aerosol diameters by up to 0.4 μm. Increased inlet $SO_3$ increased mean aerosol diameters by up to 0.4 μm. With 3 m piperazine, the measured mean aerosol diameter ranged between 1.5 and 2.24 μm. As the solvent piperazine increased, the mean aerosol diameter increased to a range between 1.73 and 2.27 μm.

At reduced solvent piperazine, increasing the inlet $CO_2$ increased the mean aerosol diameter by up to 0.09 μm per 1 vol % $CO_2$. This effect was lessened as the solvent amine content increased. Raising the temperature bulge stage from the bottom to the middle of the absorber increased the mean aerosol size by up to 0.3 μm.

#### *7.1.2.3 Aerosol 50% Volume Cutoff Size*

Higher solvent flow increased the aerosol 50% volume cutoff size by up to 1.3 μm. At reduced amine in the solvent, increasing the inlet $CO_2$ increased the 50% volume cutoff size by up to 0.12 μm per 1 vol % $CO_2$, This effect was lessened with increased

amine in the solvent. The temperature bulge stage location and gas outlet temperature did not present significant correlations with the aerosol 50% volume cutoff size.

#### *7.1.2.4 Aerosol Concentration*

Aerosol at the bench scale were measured in concentrations from 4E3 to 7E4 per $cm^3$. The aerosol concentration was found to increase as the $CO_2$ in the solvent increased; increasing the solvent $CO_2$ by 1 % increased the aerosol concentration by up to 2.5E4 per $cm^3$. Increasing the inlet $SO_3$ also correlated with an increasing aerosol concentration, with an $SO_3$ increase of 30 ppm resulting in aerosol concentration increases up to 6.6E4 per $cm^3$.

### 7.1.3 Pilot Plant FTIR Measurements with $SO_3$ Generation

Aerosol experiments were performed with the $SO_3$ generator during the April 2017 UT-SRP pilot plant campaign. This campaign was the first UT-SRP campaign to utilize a recently installed water wash process and an expanded FTIR sampling system. A total of 16 different aerosol tests were performed to quantify the impact of process operating conditions on the amine emissions rates.

#### *7.1.3.1 Piperazine Aerosol Emissions*

$SO_3$ aerosol caused amine emissions at the water wash outlet to increase by up to 7.56 ppm of piperazine / ppm of $SO_3$. Piperazine solvent showed resistance to atmospheric emissions through the aerosol phase; 30 ppm of $SO_3$ was often insufficient to produce a measureable amine emission increase. At lower quantities of $SO_3$, the gas phase piperazine is rapidly condenses into the aerosol drops, causing growth to a point that allows for collection within the process. As $SO_3$ increases, an excess of available

aerosol nuclei limits the growth rate for the aerosol drops. A higher concentration of aerosol nuclei increases the available surface area for amine condensation, limiting the sizes of aerosol drops. This leads to a higher quantity of smaller aerosol drops that are not captured by impaction due to decreased aerosol diameters.

#### *7.1.3.2 Impact of Temperature on Amine Emissions*

Absorber temperatures were found to significantly impact the amine emissions; for every 1 °C increase in the gas outlet temperature, amine emissions were reduced by up to 1.7 ppm per ppm $SO_3$. This is hypothesized to be due to the growth and collection of aerosol by impaction, as higher gas temperatures encourage aerosol growth. The temperatures at the top of the absorber column and water wash were more significant than temperatures at lower levels of the column. Gas temperature showed a higher correlation with the normalized amine emissions rates than liquid temperature. The gas outlet temperature showed an $R^2$ correlation of 0.56 with the piperazine emissions per ppm $SO_3$. The top bed temperature presented an $R^2$ correlation of 0.51, and the top bed solvent temperature maintained an $R^2$ correlation of 0.49.

#### *7.1.3.3 Effect of Solvent Composition and Flow Rate on Amine Emissions*

The solvent amine content was found to strongly correlate with the amine emissions rate; increasing the solvent piperazine content by 1 wt % increased normalized piperazine emissions by 2.3 ppm (per ppm $SO_3$). As the piperazine content in the solvent increased, the amount of piperazine volatilized into the gas phase also increased. The gas phase piperazine was free to condense into the aerosol drops, resulting in an increase in the aerosol amine content and the subsequent amine aerosol emissions rates. This agrees

with the bench scale results in showing that the solvent amine concentration is one of the most important factors in amine emissions.

Solvent flow rates were observed to have less of an impact on the amine emissions rates as compared to process temperatures. Solvent flow rates closer to the top of the absorber column had higher correlation with amine emissions than solvent flow rates in lower sections of the column. The water wash flow rate showed an $R^2$ correlation value of 0.38 with respect to the piperazine emitted per ppm $SO_3$, while the intercooling flow rate maintained an $R^2$ correlation of 0.21.

The $CO_2$ content in the solvent was shown to have a minimal impact on the amine emissions, with the rich solvent having a slightly greater influence than the lean solvent. Rich loading showed an $R^2$ correlation of 0.18 with the normalized piperazine emissions, while the lean loading had an $R^2$ correlation of 0.08.

#### *7.1.3.4 Water Wash Impact on Amine Emissions*

Increasing the water wash flow rate by 225% was found to increase the amine emissions by 10 to 20 ppm. Completely stopping flow through the water wash decreased amine emissions by 0 to 20 ppm. Decreasing the temperature of the water wash solvent was found to double amine emissions; it is hypothesized that this decreased the sizes of aerosol drops and allowed a greater quantity of aerosol to escape collection by impaction.

The piperazine content in the water wash solvent was found to have very minimal correlation with the water wash amine emissions rates, with an $R^2$ correlation of 0.004 in relation to the piperazine emitted per ppm $SO_3$.

#### *7.1.3.5 $CO_2$ Effect on Amine Emissions*

Reducing the absorber outlet $CO_2$ content was found to weakly correlate ($R^2$ = 0.27) with increasing amine emissions. The gas phase $CO_2$ at the absorber outlet had a greater impact on the amine emissions than the $CO_2$ at the absorber inlet, which showed an $R^2$ correlation of 0.14.

### 7.1.4 Field Measurement of Amine Aerosol by FTIR and PDI

Amine emission quantification was performed via FTIR and PDI at three different sites: the National Carbon Capture Center Slipstream Solvent Test Unit (SSTU), the University of Kentucky, Kentucky Utilities, and Louisville Gas and Electric (UKy/KU/LG&E) Slipstream plant, and the University of Texas Separations Research Program (UT-SRP).

#### *7.1.4.1 Effect of Baghouse Flue Gas Pretreatment*

An upstream baghouse flue gas treatment unit at NCCC reduced amine emissions by a factor of 10 to 20 through the collection of fly ash and $SO_3$ aerosol nuclei. Any aerosol present were below detection limits of the PDI (<0.1 μm in diameter). Baghouses can be an effective amine aerosol mitigation strategy through the elimination of aerosol nuclei.

#### *7.1.4.2 FTIR and PDI Field Analysis*

FTIR analysis was successful at quantifying amine emissions in excess of 1000 ppm, and observing how process conditions caused variations in emissions. PDI sampling was found to be effective at determining aerosol sizes (0.1 to 12 μm) and concentration (up to 9.4E6) at the pilot scale. An algorithm utilizing the aerosol size

distribution and concentration was used to calculate the content of amine within the aerosol, and successfully quantified changes in the aerosol amine content due to changes in the process conditions.

#### *7.1.4.3 $SO_2$ and $H_2SO_4$ Presence in Inlet Flue Gas*

The presence of $SO_2$ in the inlet flue gas was found to increase MEA emissions by up to 3.9 mol MEA per mol $SO_2$, and increased piperazine emissions by 1 mol piperazine per mol $SO_2$. The presence of sulfuric acid in the inlet flue gas increased piperazine emissions by 3 mol piperazine per mol $H_2SO_4$.

#### *7.1.4.4 Impact of Blower Configuration on Amine Aerosol Emissions*

Operating with a blower upstream of the absorber, rather than between the absorber and the water wash, was found to approximately triple the amine emissions. The upstream blower increased aerosol sizes by 70 % and increased the aerosol concentration by 9E5 per $cm^3$. The amine content within the aerosol phase also increased. The amine emissions reduction with the intermediate blower is theorized to be due to collection of aerosol through impaction within the blower.

#### *7.1.4.5 Comparison of PDI and ELPI+™ Aerosol Sizing Technologies*

A comparison of ELPI+™ and PDI sampling techniques simultaneously operating at the same sampling location showed similar values for aerosol concentration. The aerosol size distributions showed significant variance between the two analyzers, with the PDI reporting a 50% diameter cutoff an order of magnitude larger than the ELPI+™. It is theorized that the desiccation and dilution of the sampled steam prior to entering the

ELPI+™ greatly reduces the aerosol sizes due to the evaporation of volatile components from the aerosol phase.

#### *7.1.4.6 Impact of Outlet $CO_2$ on Amine Emissions*

Increasing the absorber outlet $CO_2$ reduced amine aerosol emissions to 17 % of the original value at NCCC, and by 40 % at UKy/KU/LG&E. Aerosol at lower $CO_2$ contents were 42 % larger in diameter but reduced in concentration by 47 %. The gas phase $CO_2$ was found to have no discernible effect on the amine content in the aerosol phase.

#### *7.1.4.7 Impact of Water Wash on Amine Aerosol Emissions*

Further evidence of the inability of the water wash to curtail aerosol emissions was observed. Increasing the water wash temperature by 3.2 °C was found to increase amine emissions by 33 % at the NCCC SSTU. This was due in part to aerosol diameters increasing by 17 %, and aerosol drops containing a higher concentration of amine solvent. The process configuration at NCCC was incapable of capturing the larger aerosol produced from the increased water wash temperature.

## 7.2 RECOMMENDATIONS

### 7.2.1 $SO_3$ Aerosol Generation

The feed gas flow control requires improvement. The $SO_3$ generator currently uses rotameters of varying scales to control the feed rate of the inlet gas. Switching to a mass flow controller would improve the precision of the flow control at lower feed rates. A correctly sized mass flow controller can be used at both the bench and pilot scale and negate the necessity of multiple rotameters.

### 7.2.2 Bench Scale Aerosol Generation and Measurement

There are three main recommendations for future bench scale aerosol experiments: variations in the amine solvent, temperature changes, and reductions in the inlet $SO_3$. Further recommendations involve additions to the Aerosol Growth Column apparatus.

The concentration of piperazine in the solvent was found to significantly impact the aerosol properties and amine emissions. This effect should be studied further. Future experiments should also observe how the amine structure and the presence of functional groups on the amine compound effect the aerosol concentration and size distribution.

As noted previously, inlet temperature conditions were not varied in this work. Due to the effects of the temperature bulge location and outlet gas temperatures on the aerosol properties and amine emissions, it is recommended that future experiments be conducted with variations of inlet solvent and gas temperature.

The inlet $SO_3$ composition was varied between 20 and 50 ppm for the experiments in this research. Future experiments on the AGC should attempt to use lower $SO_3$, in the range of 1 to 10 ppm. This presents a more realistic scenario to compare to full scale amine scrubbing processes. An additional base case test of the AGC without aerosol injection would be helpful in providing baseline data on operations.

The AGC provides an interesting test bed for qualifying the effectiveness of aerosol removal devices. Swirl tubes or other cyclonic separators could easily be tested on the apparatus without significant modifications.

The design and construction of a water wash column for the AGC would provide additional data on aerosol growth within amine scrubbing processes. Due to the extensive work required for this expansion, this is a lower priority recommendation.

The random packing used in the AGC does not provide a large amount of surface area for gas-liquid contact. Replacing the random packing with a structured packing that is designed to allow aerosol passage would improve the solvent flow distribution within the column. Designing and 3D printing structured packing components would be a useful project for an undergraduate researcher.

### 7.2.3 Pilot Plant FTIR Measurements with $SO_3$ Generation

The April 2017 UT-SRP pilot plant campaign was very successful in gathering amine emissions data. However, aerosol size distributions and concentration could not be quantified due to issues encountered with the PDI. Laser alignment on the PDI could not be achieved; the instrument had to be returned to the manufacturer for repairs. It is highly recommended that the PDI be utilized during the next UT-SRP campaign, as this will allow for quantification of aerosol sizes and concentration as process conditions are varied.

An additional recommendation is for pilot scale experiments with different amines and varying solvent concentrations. The amine solvent composition was shown to significantly impact the amine emissions rate; further studies should be performed to expand on this data set. Using different amine solvents could produce insights into the impact of amine structure and functional groups on aerosol emissions rates.

### 7.2.4 Field Measurement of Amine Aerosol by FTIR and PDI

Efforts should be made to produce additional comparisons of the ELPI+™ and PDI aerosol analyzers. Experiments undertaken with a goal of producing a material and mass balance around the ELPI+™, possibly with FTIR analysis, would be instrumental in quantifying the effectiveness of these two analyzer systems.

Baghouse flue gas pretreatment was found to effectively eliminate amine aerosol emissions. Further investigation should be performed at additional sites to provide further insight into this effect.

Varying the process configuration, such as the blower arrangement, produced surprising results in amine aerosol emissions. Other variations in process conditions should be sought out to quantify potential impacts on amine emissions, and to determine if these are viable options for aerosol mitigation.

Future generations of the PDI analyzer should focus on improving the robustness of the equipment. A crack that formed in the window of the transmitter/receiver unit set research back several months due to the difficulty in obtaining the optical crown glass necessary for the window. This window can be easily damaged during assembly of the PDI system, and cracks can block the laser passage, rendering the system inoperable. The PDI laser crossing can become misaligned due to vibrational forces, either in transport or due to proximity to rotating equipment in pilot plants. The laser alignment is not easily performed on the third generation PDI. Future systems may consider a fixed alignment that is more robust in construction.

The sample extraction for FTIR analysis involves the use of heated sampling probes to maintain a temperature of 180 °C across the sampling train. Due to faulty design, the probes are prone to burning through electrical wires and causing short circuits. This has compromised the sampling system and has resulted in analyzer failures in the field. It is highly recommended that these probes be replaced with a more reliable sample extraction technique. If not replaced, the FTIR probes should be positioned in locations not susceptible to liquid accumulation. The probes should also be oriented in an upright position, so the inevitable failure of the probe doesn't result in liquid from the process entering the rest of the FTIR sampling system.

# APPENDIX A: PILOT PLANT FTIR SAMPLING STANDARD OPERATING PROCEDURES

## A.1 BACKGROUND

The following standard operating procedure outlines the preparation and conduction of FTIR sampling at UT-SRP and at field sites. Photos and diagrams are included as necessary to provide visual aid to the reader.

### A.1.1 Safety

Proper PPE must be worn during pilot plant work. Hard hats, safety glasses, and full leg and upper arm coverage are required. Leather or cloth gloves are to be worn when using non-powered hand tools and while loading and unloading equipment. Steel toed boots are required at some facilities and are recommended at all times.

Heated elements used in FTIR sampling can cause burn injuries. Elements must be sufficiently cooled before working with heated components.

Electrical hazards are present with FTIR sampling. The electrically heated sampling system can be damaged during transportation or installation. Wire insulation must be intact and terminal connections secure before powering on heated sampling system components.

## A.2 INSTALLATION

### A.2.1 Heated Probes

Gas samples are extracted using Universal Analyzer, Inc. Model 277S heated probes. Each probe contains a heated ceramic filter to remove entrained liquids and

particulates. Probes are maintained at 180 °C. The probe bodies weigh approximately 20 lbs. and are 9” x 9” x 10”. The probe tips extend 20” from the body with a 10” insertable length, and are 1” in diameter.

#### *A.2.1.1 UT-SRP Installation*

At the UT-SRP pilot plant, the probes are to be installed at 135° relative to the flow direction in the column to minimize sampling sheeting liquid from condensation and large entrained droplets (Figure A.1). The probe is secured to the process by a 1” Swagelok compression fitting. FTIR probe insertion locations at UT-SRP (and all other pilot plant facilities), are 1” NPT fittings; therefore, 1” Swagelok to 1” MNPT bored-through adapter fittings are used for this mating. At UT-SRP, the adapter fittings connect to 1” half-couplings welded to a short section of 1.25” Sch. 10 piping.

The probe tips are designed to be inserted 1.75” into the process stream to avoid pipe wall flow effects. The probe tip depth is set by the Swagelok compression fitting ferrule location. Stainless steel ferrules are used on several of the probes, ensuring a consistent but immovable probe depth. The remaining probes do not have ferrules in place, and use graphite ferrules. Graphite ferrules will not permanently attach to the probe tip, ensuring that the probe insertion depth can be varied and allowing for use at multiple sampling locations.

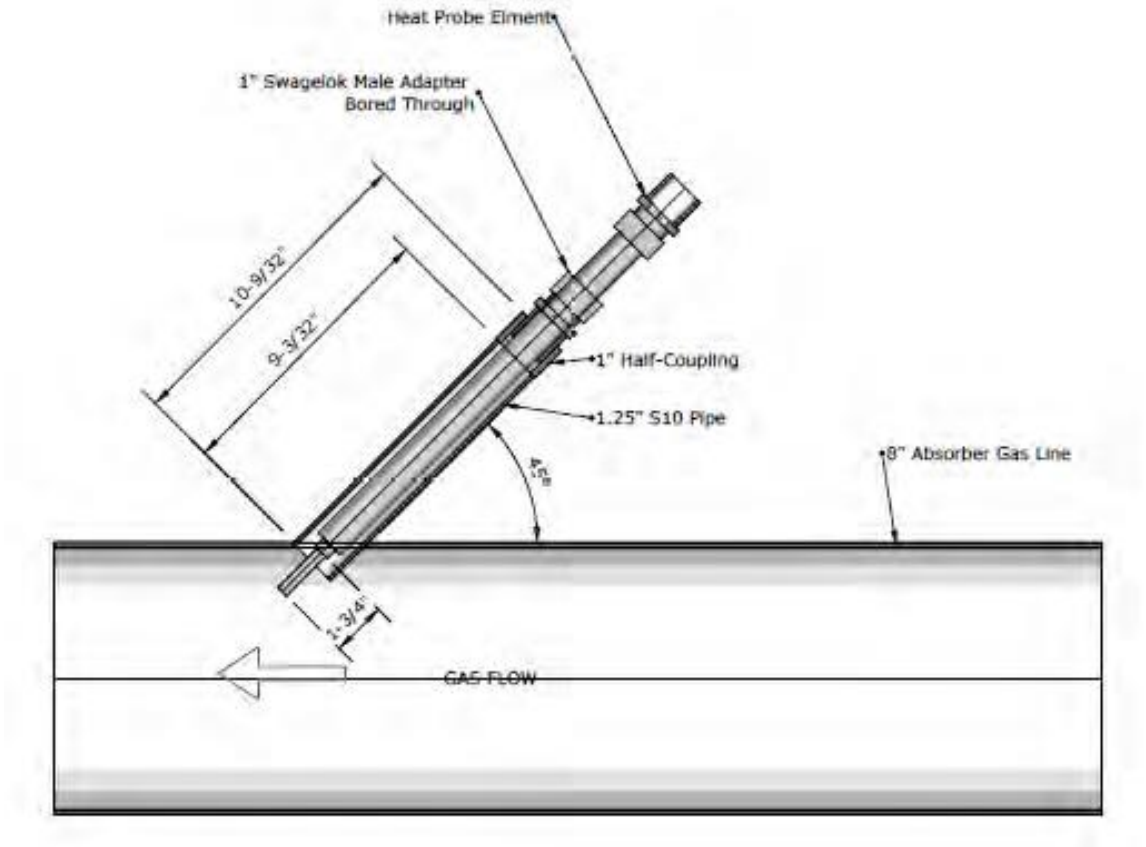


**Figure A.1: UT-SRP Sample Probe Installation**

### *A.2.1.2 Field Installation with Isolation*

Sample ports will be provided at most pilot plants. A standard environmental emission sampling port is 4" 150#, but any port that allows sufficient clearance for the 1" OD probe is useable. Sampling at these locations can be configured for only FTIR sampling, or for combined FTIR and PDI (Phase Doppler Interferometer) sampling.

*2 A.2.1.2.1 Without PDI*

Sampling without the PDI allows for the probes to be inserted directly into the process stream. The sample port must be configured for 1" FNPT, either through

flanging or bushings. The 1” Swagelok compression fitting to 1” MNPT fitting is connected at this point. If sample probes with steel ferrules are desired at this location, the probe can be inserted through the adapter and valve and into the process. Probes with the steel ferrules should not be installed while the process is running, as this will result in the release of process gas. Figure A.2 presents an FTIR-only sampling diagram.

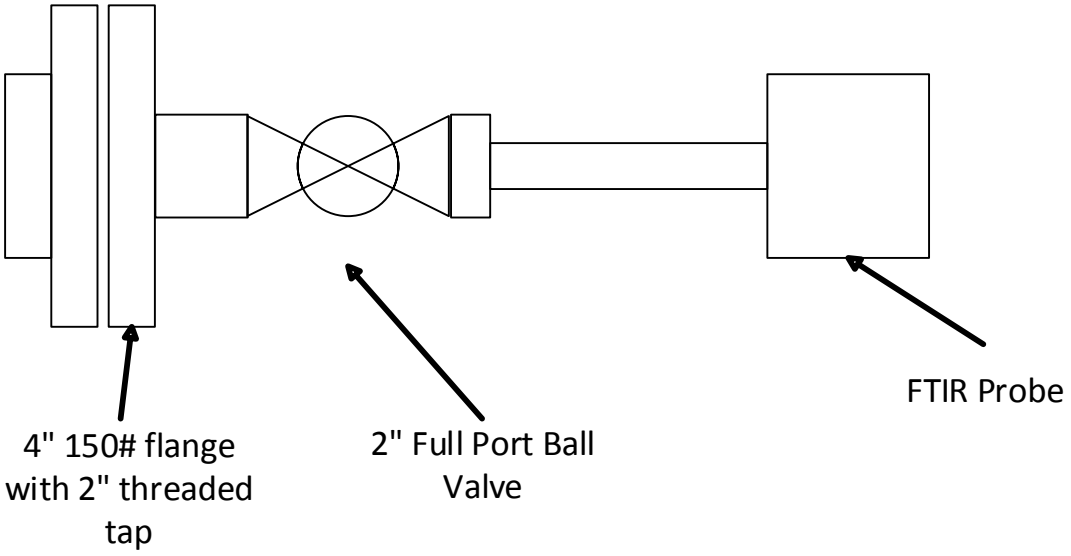


**Figure A.2: FTIR-only sampling configuration**

Sample probes with graphite ferrules can be inserted into sample ports while the process is operating. Install the 1” Swagelok compression fitting to 1” MNPT adapter onto the sample port. Insert the graphite ferrule and 1” Swagelok nut onto the adapter. With the sample port closed, begin sliding the sample probe into the process through the nut-ferrule-fitting assembly. Once the maximum diameter of the probe is through the fitting, the sample isolation valve can be opened and the probe may be fully inserted.

*3 A.2.1.2.2 With PDI*

Extractive sampling must be used when simultaneously sampling with the PDI and FTIR. This method of sampling uses a blower to extract gas out of the process, where it can be analyzed by both instruments. A 1" piping cross is installed immediately downstream of the sample port, with the 90° bends directed up and down rather than horizontally. Install a 6-8" length, 1" pipe nipple, and 1" coupling on the upper bend of the cross. A short 1" diameter nipple and drain valve are installed on the downward leg of the cross. The remaining horizontal outlet from the cross can then be attached to a 1" flange and connected to the PDI sample cell. The blower is connected with flexible 1" tubing to the outlet of the PDI sample cell. This is presented in Figure A.3. The blower outlet can be connected to a return point at the process, or at another location that can accommodate 20–30 lpm of gas flow.

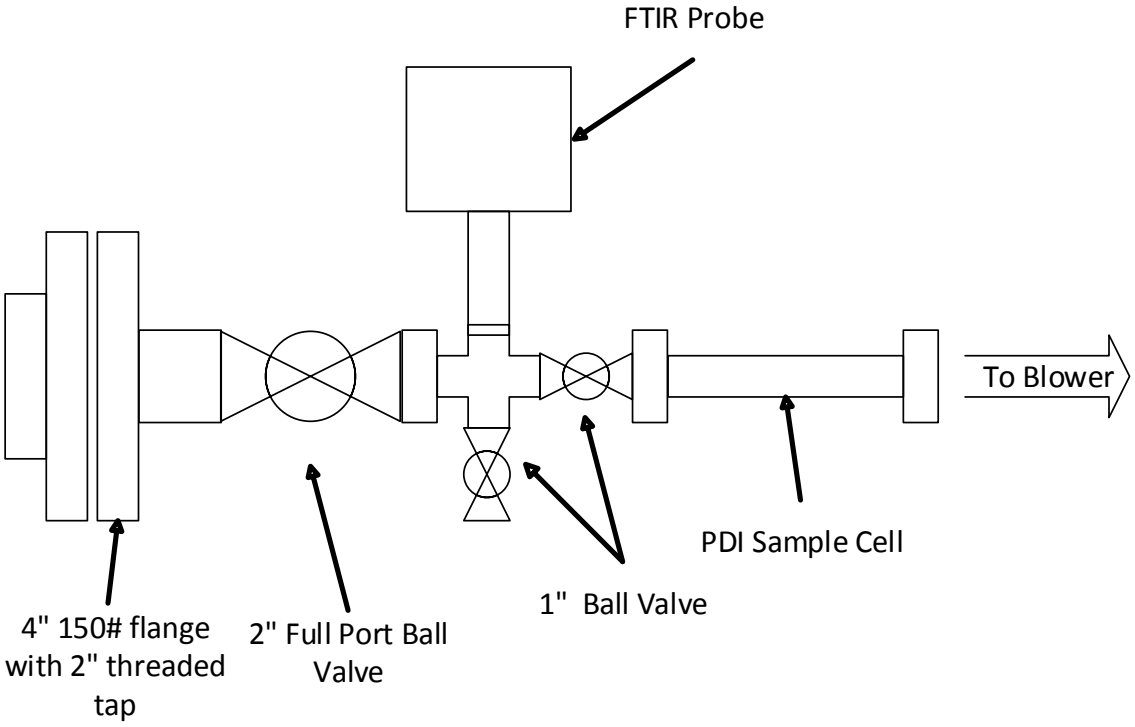


**Figure A.3: Extractive sampling for simultaneous PDI and FTIR sampling**

It is important that sample probes with graphite ferrules are used for extractive sampling, because the probe depth must be manually adjusted. Due to the smaller diameter of the system, the probe tip cannot be inserted 1.75" into the process stream. It is recommended that the probe tip be inserted 0.25" past the wall of the piping cross. Insert the probe to this depth, and tighten the 1" Swagelok nut on the probe to secure the probe depth in place.

The sample probe must be secured to prevent rotation. During field sampling, it is recommended that ratchet straps are used to secure the probe to existing structures or scaffolding in the unit.

#### *A.2.1.3 Direct Column Installation*

The sample probes can be inserted directly into process equipment through existing ports. At UT-SRP, probes are inserted into the absorber column between the 1st and 2nd stages of packing, and between the 2nd and 3rd stages. A port must have sufficient clearance for the 1" probe tip diameter; 1.25" piping or greater is recommended. The probe entry into the structure should be uninhibited by the presence of packing or column structure, as this can affect the flow dynamics around the probe tip.

The port must be adapted with flanges or bushings to a 1" FNPT fitting. The 1" Swagelok compression fitting to 1" MNPT adapter can be mated at this point. Sample probes with steel or graphite ferrules can be used. It is important that probe installation only happens while the process is not running; otherwise gas and solvent release will occur.

#### *A.2.1.4 Power and Thermocouple Connections*

Power is supplied to the probes by the use of 14 AWG wire, and temperature measurement data is transmitted by shielded K-type thermocouple wire. At UT-SRP, these wires are passed through rigid and liquid-tight conduit to the Level 2 CHARMS box, and temperature at the probe is controlled through the DeltaV™ control system. Follow these steps for probe connection at UT-SRP:

1. Determine the length of liquid-tight conduit necessary to reach from the terminal box to the probe in the field. Liquid-tight conduit should not be longer than 6 feet.

2. Run the (3) 14 AWG power wires (live, neutral, and ground) and the shielded K-type thermocouple wire through the conduit.

3. Connect the liquid-tight conduit at the probe end. Run the wires into the probe itself. Connect the power and thermocouple wires to the appropriate terminal blocks inside the probe (Figure 1.4). Thermocouple wires should match their corresponding wire sheathing color. For the power wires, ground connects to block 6, neutral to block 4, and live to block 2.

4. Run the power and thermocouple wires into the terminal box. Connect the liquid-tight conduit to the box. Terminate the wires at the proper terminal blocks. Within each terminal box, the terminal blocks on the left side are for the probe, and on the right side for the heated pads (Section 1.3).

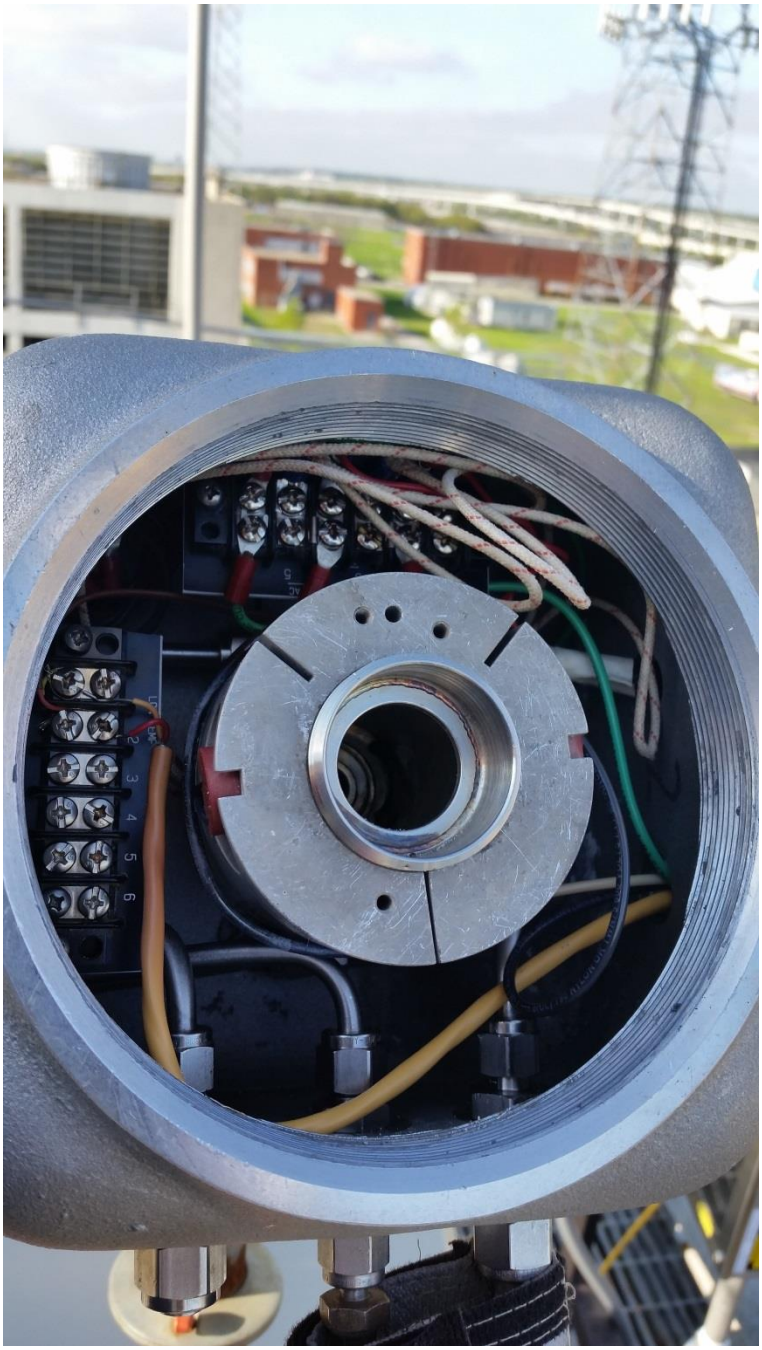

**Figure A.4: Heated probe internal wiring**

### A.2.2 Heated Sample Lines

Heated sample lines are used to maintain 180 °C from the sample probe to the stream switching location. These sample lines are manufactured by Clayborn Labs, and vary in length and diameter from site to site. If new lines are to be procured, it is recommended to order lines with replaceable inner lines, and with 0.375" inner diameters.

The heated sample lines contain an inner heated tubing section and a smaller diameter unheated tube. The unheated tubing is for FTIR calibration. It is recommended that both the heated and unheated tubes be connected to the sample probes. For sample locations that can be isolated from the process, this can be helpful for FTIR calibrations. The sample and calibration Swagelok fittings are labeled on the sample probes; the calibration connection is a ¼" male Swagelok compression fitting, and the sample connection is a 3/8" male Swagelok compression fitting.

Power is provided to the lines from 3x12 AWG wiring. The wires are located at the analyzer end of the sample line. Ampheno[l®] connections are soldered on for lines at UT-SRP and at field sites. K-type thermocouple wires with male connectors are also located here.

#### *A.2.2.1 UT-SRP Heated Lines*

UT-SRP uses 5 heated lines for multipoint FTIR sampling. These have been permanently installed in the unit and are supported with aluminum cable trays, as outlined in Appendix C. Ensure the sample lines are properly connected to the sampling probes prior to process startup.

#### *A.2.2.2 Portable Heated Lines*

Portable heated lines are used at facilities without permanent FTIR sample capabilities. During temporary sampling campaigns, the sample lines are allowed to rest on the grate or ground but must be out of the walking paths of technicians and operators. Lines should be positioned so the analyzer end, with the power and thermocouple leads, is next to the power distribution system.

### A.2.3 Heated Pads

Cleanair® SKU 1223 heated pads are used to maintain the 180 °C temperature across unheated sections of the sampling system, especially the gaps between the heated probe and the sample line. Once the sample lines are connected to the probes, cover the PTFE tubing between the probe and the sample line with the flexible pad. Use the Velcro® on the pad to secure the pad in place. A gap between the pad and the PTFE tubing is acceptable, but it is recommended that the tubing be no longer than the length of the heated pad.

At UT-SRP, the heated pads are temperature controlled through the DeltaV™ CHARMS system. Rigid and liquid-tight conduit is used to protect the power and thermocouple wires. The pads are wired directly to the UT-SRP terminal boxes and through grip-cord connections on the bottom of the terminal boxes. Inside the terminal boxes, the power and thermocouple leads are connected to the terminal blocks on the right side of the box. In the field, the pads are wired with NEMA 15A plugs on the power leads and K-type thermocouple male leads on the thermocouple wires. These can

be plugged in at the power distribution box (See Section 1.6). Power and thermocouple extension cords are used as necessary.

### A.2.4 Sample Switching Units

#### *A.2.4.1 UT-SRP MSSH (Multipoint Heated Stream Switcher)*

As there are 5 sampling locations and only one FTIR, sample location switching is required at UT-SRP. This is accomplished by the use of the MSSH. The MSSH is located on the west side of the CEER building (Figure A.5). Nitrogen is fed to the MSSH for FTIR background purposes, and instrument air is used to power an eductor system. The eductor uses the Venturi effect to generate suction on the sample lines that are not actively being sampled, to reduce the system response time. The MSSH is heated to 180 °C. Stream selection for the MSSH is controlled through the DeltaV™ in the UT-SRP control room.

**Figure A.5: MSSH at UT-SRP**

### *A.2.4.2 Portable Two-Stream Switching Units*

The MSSH is a permanent feature at UT-SRP. If multiple sample points are desired during field operations, portable stream switching boxes are used. These stream switching units use a pair of 3-way valves to redirect flow. An eductor inside each box ensures suction through the non-sampled line; when the valves are correctly aligned, this will reduce lag time when switching sampling locations. The eductor suction rate is controlled by the regulator on the left side of the box while facing. The box temperature is maintained at 180 °C by Briskheat™ temperature controllers; heat tape wraps the

interior tubing, valves, and eductor. Two switching boxes have been built, and have interchangeable parts if field repairs are necessary. Figures A.6 through A.8 present the portable switching boxes at varying stages of construction.

**Figure A.6: Stream switching box interior. Eductor is located at the bottom of the box. Waste stream from the eductor exits at the bottom of the box. Sample exit to the right. The two sample inlets are behind the valves at the top of the box.**

**Figure A.7: Switching boxes with heat tape and wiring. Heat tape and thermocouple wiring enters the rear of the box through grip-cord connections. Sample selection valves are visible at the top of the box (yellow handles).**


**Figure A.8: Switching box in the field. Sampling and bypass instructions are on the top of the box: user places the valve handle over the selected operation.**

### A.2.5 FTIR Analyzer

Two FTIR analyzers are used for compositional analysis of the sampled streams. The Gasmet™ DX-4000 is a rugged portable unit that is best suited for field work. The Gasmet™ CX-4000 is a rack mounted FTIR analyzer that is best suited for indoor use but can be adapted for work on pilot plant skids. Both analyzers have identical internal components and operating software.

#### *A.2.5.1 Portable DX-4000*

The portable DX-4000 is a modular system composed of the FTIR analyzer, sample pump and filter unit, and CPU and user interface. This is presented in Figure A.9.

**Figure A.9: DX-4000 analyzer setup. The FTIR analyzer is yellow box on the left side. CPU and user interface are adjacent on top of the table. The sample pump and filter unit is the metal box below the analyzer.**

1. When setting up the DX-4000, use of a table is recommended to support the equipment. The table legs should end in horizontal bars at the ground level, rather than four independent feet, because most sampling locations are on grated floors (see Figure A.9), and horizontal bar legs will prevent the table legs from slipping through the grating.

2. Place the DX-4000 analyzer on the table in a way that the sample inlet and outlet are close to the edge of the table. This will allow easier access and mobility for the heated jumper line between the analyzer and the pump and filter unit.

3. Place the sample pump and filter unit on the ground below the DX-4000 analyzer. Orient the sample pump outlet fitting in the same direction as the analyzer inlet.

4. Connect the heated jumper to the sample pump outlet, and then to the analyzer inlet. This attaches by a ¼" Swagelok compression fitting. The sample pump fitting is a more difficult connection and should be accomplished first. Power is provided to the heated jumper through the sample pump and filter box. Screw the jumper plug into the provided Hirschmann™ Amphenol® connection.

5. Using PTFE tubing, run a 5- to 6--foot long sample outlet line from the analyzer to a location below the grate level. This does not have to be returned to the process, as flow through the analyzer is only 5 lpm.

6. Connect the heated sample line from the sampling location or stream switching unit to the sample pump inlet.

7. Position the CPU and connect the RS-232 serial cable between the FTIR analyzer and the CPU. The CPU can be positioned on the table or on the ground.

8. Connect the monitor, keyboard, and mouse to the CPU.

9. Power is supplied to each piece of equipment by the use of surge protectors. All electrical equipment (Pump, analyzer, CPU, and monitor) can be on the same surge protector.

10. Connect the $N_2$ purge to the FTIR analyzer. The purge line is the 1/8" PTFE line that connects to a gas flow regulator. Connect the regulator to a N2 line and turn on flow to the regulator. The regulator is set to 7–8 psig.

11. The analyzer status can be checked by selecting “View” in Calcmet™ and clicking “Hardware Status”. The sample cell temperature and pressure are presented, among other status indicators. Verify that the cell temperature is 180 °C (+/- 2 °C) before performing any operations with the FTIR. Ensure that the cell pressure is at or greater than ambient pressure, but less than 1100 mbar.

#### *A.2.5.2 Rack-Mounted CX-4000*

The CX-4000 is designed to mount inside a server rack, and is not weather resistant, although with suitable protection the CX-4000 can be used outdoors temporarily. Figure A.10 presents the CX-4000 in the lab at UT-SRP. At the top of the server rack is the CPU, and the analyzer is placed immediately below. A roll-out keyboard and monitor are prominently visible in the figure. Temperature controllers for the pump, filter, and jumper line are below the keyboard, and the variable frequency drive for pump suction control is the white box close to the bottom of the rack. This server rack configuration is designed for ease of use; therefore, it is only necessary to plug in power, $N_2$, and sample flow prior to system startup.

**Figure A.10: CX-4000 FTIR analyzer and associated components**

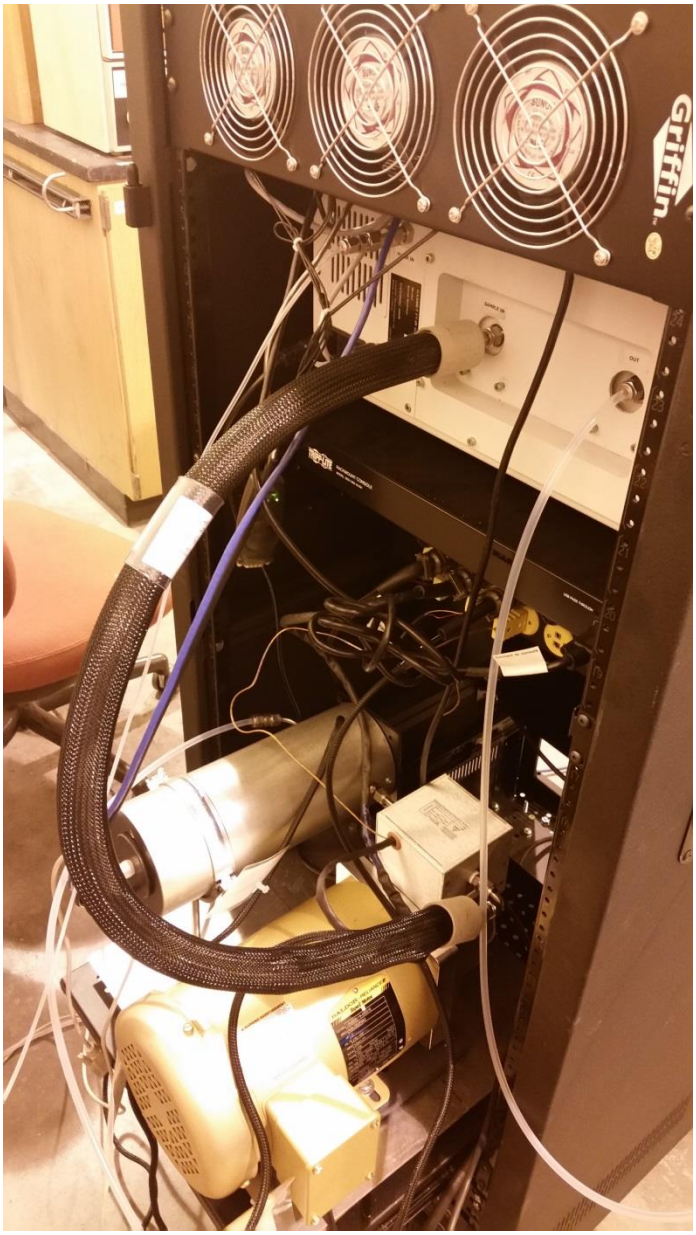


**Figure A.11: Reverse side of CX-4000 analyzer cabinet. Sample inlet is next to the filter (Silver cylinder). From there, the sample is passed through the sample pump (Gold cylinder) and then the heated jumper line to the analyzer inlet. Power and thermocouple connections for heated components are visible as well.**

The CX-4000 can be easily used at UT-SRP, since all FTIR analyzers are indoors. For sample switching using the MSSH, the analyzer can be wheeled into the southwest corner of the CEER analytical lab just west of the control room. An existing heated line passes through the wall and connects the MSSH to the analyzer filter inlet, on the back side of the server rack. This heated jumper connects via Amphenol® connections and K-type thermocouple lines to the temperature controllers of the server rack, located at the back side of the analyzer cabinet.

It is recommended that exhaust from the analyzer be passed through a knockout pot before release. This can be accomplished by the use of plastic Erlenmeyer flasks with double entry stoppers. These are available in the analytical lab at CEER.

The CX-4000 can be used in the server rack configuration at other locations besides UT-SRP. However, extra care must be taken to ensure that the system is made weather resistant. This can be accomplished by covering the server rack with weatherproof plastic tarps and securing the tarps with bungee cords and zip ties. Positioning the server rack is a more difficult undertaking than the portable DX-4000 analyzer system, due to the heavy weight of the combined server rack system. It is recommended that a crane be used to position the analyzer cabinet on the necessary level at the field site.

As noted previously, the sample pump suction rate is controlled by a variable frequency drive for the server rack-mounted analyzer system. Variable frequency drives do not work with ground fault circuit interrupter circuits due to the microvoltage frequency variations in these circuits. Therefore, using a variable frequency drive on a

non-GFCI circuit will trip the breaker when the pump is activated. If the server cabinet-mounted CX-4000 is to be used outdoors, ensure that this pump is connected to a non-GFCI outlet, and that the non-GFCI outlet is properly configured for outdoor use. To turn the pump on, select "On" from the variable frequency drive. When the FTIR analyzer is on, the sample pump should be on as well, regardless of whether $N_2$ or process gas is sampled.

### A.2.6 Power Distribution

#### *A.2.6.1 UT-SRP*

Power distribution and temperature control for the heated pads and probes is routed through the Level 2 CHARMS box and controlled through DeltaV™. Prior to restarting the sampling system, verify that all connections for the pads and probes are in the correct configuration and actively turn on. There are 14 controller slots in the L2 CHARMS box; 1–7 control the 5 probes with 2 spare controller slots, and 8–14 are used for the pads, again with two spares.

For the heated lines and MSSH, temperature control is maintained through the Level 1 CHARMS box, located on the west side of CEER near the MSSH. Power and thermocouple connections have been made already, and should remain so as these lines are permanently installed.

#### *A.2.6.2 Field Sites*

Power is provided to the heated probes, pads, and sample lines by the use of a portable electrical distribution box. This was designed and fabricated at UT-SRP and is presented in Figure A.12. Power is provided to the box by a 3 x 12 AWG wire. The live

and neutral wires are split into terminal blocks and distributed from there. Each heated component actually has two circuits; one for the power to the equipment itself, and another for power to its respective temperature controller. Solid state relays at the top of the box in Figure A.12 control the power to the heated equipment. Circuit breakers are paired off: one controls the power to the heated element, and the other the power to the controller. The first 4 circuit breakers from the left in Figure A.12 control the pads; the next 4 control the probes, and the final 6 control the heated lines (2 sample lines plus a jumper from the switching box to the pump).

Temperatures are maintained by SL4824-VR-D temperature controllers. These are single-loop controllers. Two different types of controllers are used: 24V and 120V. **IT IS IMPORTANT NEVER TO CONNECT THE 24V TO THE 120V, AS THIS WILL DESTROY THE CONTROLLERS.** Power to the 24 V controllers is routed through a transformer (White and blue box in the middle-right of Figure 1.11) to provide the necessary operating voltage. The controllers are in the same order as the circuit breaker pairs; first two controllers for pads, second two for probes, and last three for the heated lines.

The power and thermocouple lines from the heated components can be plugged in at the bottom of the power distribution box. NEMA 15A plugs are provided for the pads and probes, and Amphenol® connectors for the lines. All 7 heated components have K-type thermocouple connections. The order of plugging in components is the same as the circuit breaker pairs and the controllers; first two power and thermocouple plugs for the two pads, second pairs for the probes, and final 3 power and thermocouple pairs for the

heated lines.  Exercise caution to ensure that no lines are crossed while making electrical connections.

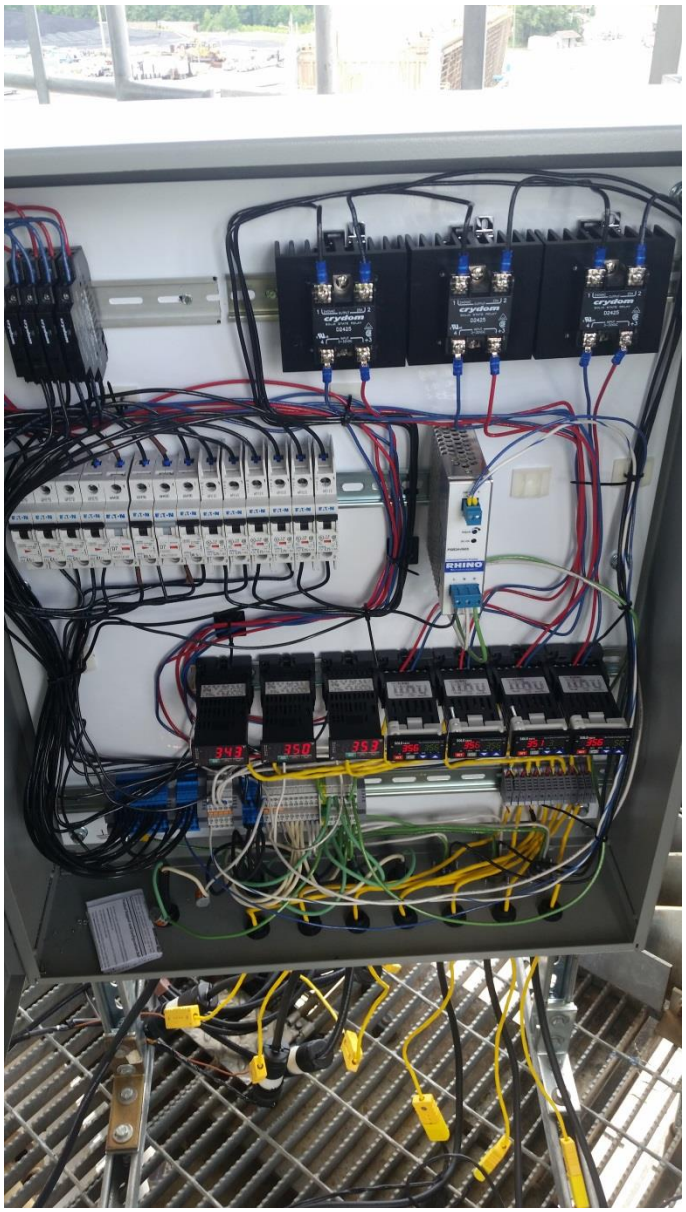


**Figure A.12: Electrical power distribution box**

### A.2.7 $N_2$ and Air Supply

#### *A.2.7.1 UT-SRP*

$N_2$ is needed for background scans for the FTIR analyzers. These scans must be performed every 24 hours and take roughly one hour to complete. At UT-SRP, $N_2$ is fed to the MSSH; this simplifies background scans by allowing the initial steps for background preparation to take place in the control room.

$N_2$ is also needed for the analyzer purge, which must always remain open. This is outlined in Section A.2.5.

Plant or Instrument Air is necessary to power the eductor for the MSSH. Clean, dry air is required for this; any particulates or liquids can potentially clog the small orifice in the eductor, rendering the system inoperable. A filtration and desiccant system is located inside the CEER analytical lab; instrument air comes from the wall behind the lab bench on the south side of the analytical lab. A 3/8" line runs to the filter and desiccant system, which removes oil, water, and particulates from the stream. The clean air is then fed through the wall to the MSSH outside CEER. The filter should be cleaned and the desiccant replaced prior to each campaign.

#### *A.2.7.2 Field Sites*

The FTIR analyzer requires a $N_2$ purge at all times, as outlined in Section A.2.5. $N_2$ is also necessary for background scans. If using a probe at a location with an isolatable sample valve, connect a $N_2$ line and block valve to the calibration line of the sample line. When a background scan needs to be performed, it will only be necessary to close the valve at the sample location and open the isolation valve for $N_2$ flow through

the calibration line to the sample probe. This method is recommended for extractive sampling systems as well, due to the ease of isolating these systems from the process.

If none of the sample locations can be isolated, a $N_2$ inlet must be added to at the outlet of the stream switching box. This is presented in Figure A.13.

1. Add a ¼" Swagelok compression tee at the sample switching outlet. Connect the jumper from the stream switching box to the sample pump/filter unit at one outlet of the tee.

2. Connect a block valve, and then a needle valve, to the other outlet of the tee. The block valve is for isolation, and the needle valve is for flow control.

3. Connect the needle valve to the $N_2$ flow.

It is recommended that the $N_2$ flow for backgrounds be made through the sample probes if possible, in order to reduce the length of unheated sections of the sample system and for ease of operations.


**Figure A.13: Sample switching box with $N_2$ background adaptation.**

## A.3 INITIALIZING OPERATIONS

### A.3.1 FTIR Initial Setup

1. Ensure $N_2$ flow is on to the FTIR analyzer purge and sample inlet.

2. Turn on power to the FTIR analyzer. This will begin heating and purging the cell. Heat and purge with $N_2$ for 24 hours prior to beginning operations.

3. Turn on power to the CPU, monitor, and sample pump/filter. The pump/filter unit has a pair of power switches; one for the pump, and another for the heated elements. Ensure that both have been turned on, and that the green LED readouts for the heated element controls are showing a temperature for 2 of the 3 controllers.

4. Turn on the Briskheat™ controller for the stream switching box. This will begin heating the stream switching box. Make sure both sample switching valves are in the "Bypass" position.

5. Turn on $N_2$ or air flow to the stream switching box. A regulator pressure of 20 psig is sufficient for adequate suction on both sample lines, but can be adjusted if necessary.

6. Begin heating the heated elements. It is recommended that the lines be heated to 180 °C first, and then the sample pads and probes turned on. The heated elements can draw a significant amount of power when first turned on; in cold weather conditions, this can exceed 20 amps and can cause breaker trips due to over-amperage. The heated lines draw more power than the probes or pads; therefore, getting these up to temperature first reduces the risk of tripping a breaker.

7. Wait 24 hours with $N_2$ flow to the sample inlet of the analyzer before performing initial background scan.

### A.3.2 Performing Background Scan

1. If this is the initial background scan, the analyzer system has been under $N_2$ for 24 hours and is ready to go. If the analyzer has been actively sampling, perform the following:

a) Turn the system to $N_2$ flow. At UT-SRP, this involves selecting "$N_2$" at the control room for the FTIR connected to the MSSH. For the inlet FTIR, this involves manually swapping the sample line with an $N_2$ line, and turning on the $N_2$ flow. In the field, if using extractive or isolatable sampling, close the sample port and turn on $N_2$ to the heated sample line calibration line. If using sample probes that cannot be isolated from the process, turn the switching box sample valves so both are bypassing, and turn on the $N_2$ flow, as specified in Section A.2.7 B.

b) Keep $N_2$ flow on the system for 45 minutes. Keep actively sampling during this time. After 45 minutes, there should be very minimal measured components left in the system, ($H_2O$ <0.01 vol %, $CO_2$ <0.01 vol %, Amine & $NH_3$ & $SO_2$ < 1 ppm).

2. Turn off continuous 1-minute sampling.

3. Under "Options", select "Measuring times." Change the measuring time from 1-minute to 5-minute scans.

4. Go under "Options" again and reselect "Measuring times." Confirm that the scan length has been changed from 1 minute to 5 minutes.

5. Under "Measure", select "Background". Background scan is now performing. This will take 12–15 minutes.

6. Once the background scan is complete, view the spectra at the bottom left corner of the Calcmet™ screen. It should look similar to Figure A.14. A pair of peaks around 2400 cm-1 indicate the presence of $CO_2$. $H_2O$ will generate peaks around 1500 and 3500 cm-1. Amine solvent will show up around 3000–3400 cm-1.

7. If the background looks adequate, go to "Options" and select "Measuring times". Change the scan length from 5 minutes to 1 minute. Repeat this step to confirm Calcmet™ acknowledged the scan length change.

8. Resume continuous measurement. This can be accomplished by selecting "Measure" in the menu bar and clicking "Continuous". Another method is to click the circle with the arrow icon on the menu bar.

9. If continuous measurement shows the lack of measured components after 2 or 3 scans, switch back to active sampling of the process. At UT-SRP, return to the control

room and switch off the $N_2$ flow and resume the rotational sampling procedure. At field sites, turn off the $N_2$ to the sample calibration line and open the sample port if using an isolatable sampling system. If using a system that does not allow isolation, turn off the $N_2$ downstream of the stream switching box, as specified in Section A.2.7 B, and select the desired sample location at the stream switching box.

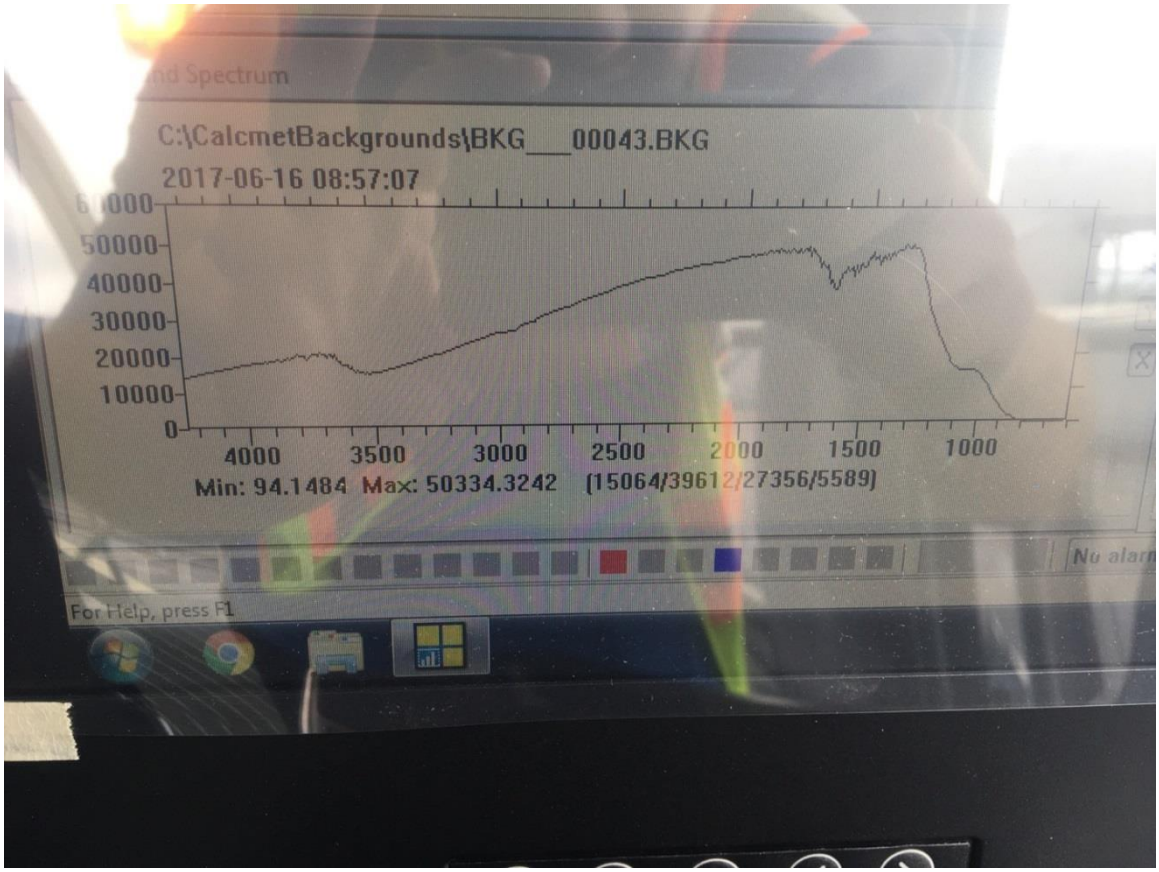


**Figure A.14: Adequate background scan**

## A.4 SAMPLING OPERATIONS

### A.4.1 Heated Elements Controls

At UT-SRP, all components can be turned on simultaneously from the control room while feeding $N_2$ through the MSSH. In the field, power is occasionally limited

and must be managed to prevent tripping breakers with over-amperage. To turn on the heated pads, probes, and lines:

1) Turn on the stream switching box Briskheat™ controller. Turn on air or $N_2$ flow to the eductor regulator. Select "Bypass" for both sample valves.

2) Plug in the power distribution box.

3) Turn on the circuit breaker pairs in the power distribution box. Fully power and heat the sample lines first, as these draw more power than other components. Once the lines are up to temperature, turn on the power to the sample probes and pads.

4) Ensure that gas is actively flowing through the sample system while heating up components

5) Once all components are up to temperature, the system is ready to sample (provided that the FTIR has been heating and purging for at least 24 continuous hours prior to sampling).

### A.4.2 Sample Switching

For sample point switching at UT-SRP, the DeltaV™ interface allows for manual selection of sample locations, or can automatically switch between sampling locations every 10 minutes.

Refer to Figures A.8 and A.13 for stream switching in the field using the stream switching boxes. When selecting a sample point, turn its corresponding valve handle to point right, in the direction of the "Sample" arrow. Turn the other valve so its handle is pointed towards the user, in the direction of "Bypass". When switching sample points,

alternate the valve handle positions so the selected stream valve handle points to "Sample" and the non-sampled stream valve handle points to "Bypass".

## A.5 SYSTEM SHUTDOWN

### A.5.1 $N_2$ Purging

Before fully shutting down the FTIR sampling system, purge the FTIR analyzer, pump, filter, and heated jumper with N. This is outlined in the beginning of Section A.3.2. This will ensure that residual water and amine solvent do not condense in the analyzer.

### A.5.2 Shutting Down Heated Equipment

1) Isolate sample probes if possible.

2) Turn off power to heated elements at the power distribution box.

3) Turn off power to stream switching box. Turn off $N_2$ or air flow through eductor.

4) Turn off FTIR pump, filter, and heated jumper.

5) Shut down analyzer computer.

6) Turn off power to analyzer. $N_2$ flow can be stopped at this point. $N_2$ purge can also be terminated.

## A.6 FTIR FIELD SAMPLING CHECKLIST

The following is a list of equipment, spare parts, and tools for FTIR field sampling. It is not an exhaustive list, but can serve as a guide for field sampling campaigns.

### A.6.1 FTIR Components

Heated Probe(s)

Probe adaptors (NPT to Compression fitting)

Teflon Tape (1”)

Graphite Ferrules + spares

Heated Sampling Line(s)

Heated Pad(s)

Control Box(es)

Heated switching unit(s)

Extension Cord

FTIR Analyzer

Surge Protector

FTIR Monitor

FTIR Keyboard

FTIR Mouse

FTIR CPU

FTIR Sample Pump

FTIR Heated Sample Pump Line

$N_2$ Tubing and manifold w/ valves & tee’s.

FTIR Exhaust Tubing

Flanges for sample port connections (Ensure correct sizes)

Nuts and bolts for sample port connections (Verify sizes)

Gaskets for sample port connections

### A.6.2 PDI Components

PDI Transmitter/receiver

Oscilloscope

Sample Cell

PDI Monitor

PDI transmitter/receiver box

PDI Power and Advanced Signal Analyzer box

PDI purge box

Blower

Tubing and ring clamps for blower

1” NPT to barbed tube adapters for blower tubing

### A.6.3 Tools

Wire strippers/cutters

Electrical Tape

Multi-bit screwdriver

Sharpie x 2

Mini flat screwdriver

Linemen’s pliers (crimping pliers)

Tape Measure

Needle Nose Pliers

Pipe Wrench

Adjustable Hex Wrench

Zip Ties

Flashlight

Duct Tape

Ear Plugs

Crescent Wrench x 2

Notebook

Pens

Metric and Standard Hex Wrenches

Tarps

Rope

Swagelok parts boxes

Teflon® tape pick

Tube Cutter (metal)

Tube bender

Soldering kit

Voltmeter

### A.6.4 Spare Parts

Temperature controllers

12 AWG wire

3x12 AWG wire

Thermocouple wire

14 AWG wire

Spare FTIR purge regulator

Spare NPT piping pieces

Thermocouple plugs, M and F

Spare 120V plugs

Spare wire terminals/connectors

### A.6.5 Other

Hard Hat

Safety glasses

Gloves x 2

Steel Toed Boots

Safety Glasses x 2

Sunscreen

Wasp Spray

Bug Spray

5 Gallon (20 L) buckets

Folding Chair

Bungie Cords

Towels

Rain gear

Ratchet straps

Site-specific paperwork (drug tests, security clearance, etc.)

# APPENDIX B: PHASE DOPPLER INTERFEROMETER STANDARD OPERATING PROCEDURES

## B.1 BACKGROUND

The following standard operating procedure outlines the preparation and conduction of PDI sampling for the Aerosol Growth Column and at pilot plants. Photos and diagrams are included as necessary to provide visual aid to the reader. Further details are provided in Chapter 2 of this work for technical specifications, and in the PDI instruction manual (Artium, 2015).

### B.1.1 Safety

Proper PPE must be worn during pilot plant work. Hard hats, safety glasses, and full leg and upper arm coverage are required. Leather or cloth gloves are to be worn when using non-powered hand tools and while loading and unloading equipment. Steel toed boots are required at some facilities and are recommended at all times.

The PDI lasers must only be activated when the transmitter/receiver unit is mated with the test cell. Polarized safety glasses are to be worn when there is a risk of contact with the lasers.

Respirators should be available when operating the $SO_3$ generator for aerosol production at the bench scale. The respirators must be worn when entering the walk-in fume hood when $SO_2$ flow is active.

### B.1.2 PDI Theory of Operation

Phase Doppler Interferometry is a laser based nondestructive aerosol measurement technique. The PDI instrument measures the particle size distribution, total particulate concentration, and velocity of an aerosol cloud. The analyzer presented here is designed to measure aerosol drops between 0.1 and 12.0 μm in diameter, at aerosol concentrations greater than $10^6$ $cm^{-3}$.

The PDI measurement technique uses the phase shift of light for particle sizing, as opposed to the intensity of light. The use of the phase of light as opposed to intensity reduces the attenuation errors caused by optical window fouling and multiple scattering from the same particle. Proper aerosol sizing requires the measured signal amplitude to be greater than the background scattering noise, and that particles pass in the correct flow path, (no back flow). Optical window attenuation (fogging) can reduce the signal amplitude to a point below detection limits, but this is an issue prevalent in all photodetector-based analysis systems.

### B.1.3 PDI Hardware

#### *B.1.3.1 Power Supply*

The power supply provides power and instructions to the transmitter and receiver unit. The PDI used in this work uses a single multi-pin cable that mates with a keyed connection at the transmitter/receiver end. The cable breaks out to power leads for the receiver and transmitter, photomultiplier BNC-type signal connectors, an Ethernet communications connection, and a USB type B cable. The USB cable is used to transmit

information on the photomultiplier tube (PMT) gain, aperture settings, laser settings, and the phase calibration source information.

The power supply box is presented in Figure B.1. The box is stored in a weather-resistant box called the electronics enclosure, along with the other electronic components for the PDI analyzer. Electricity is supplied to the power supply and other components by the use of a power strip at the bottom of the enclosure.


**Figure B.1: PDI electronic enclosure**

### *B.1.3.2 Advanced Signal Analyzer (ASA)*

The ASA performs amplification, filtering, analog to digital conversion, and burst signal detection on the raw signals from the receiving optics. The three BNC cables (Labeled Raw A, Raw B, and Raw C), from the transmitter/receiver cable are connected to the input signals connections at the back of the ASA box, not the raw signals BNC

connectors. An Ethernet cable from the computer connects to the ASA box as well; this is used to send digitalized information to the computer for software processing.

### *B.1.3.3 Transmitter/Receiver Unit*

The transmitter in the combined receiver/transmitter unit contains the laser source, Bragg cell, and reflectors to generate beam spacing and the crossing angle for the sample volume. The laser is activated by the use of a keyed switch at the back side of the receiver/transmitter unit, next to the keyed power cable connection. The laser should not be activated unless the transmitter/receiver unit is properly affixed to the test cell, to prevent hazardous optical conditions. Figure B.2 gives a photo of the PDI transmitter/receiver unit.

**Figure B.2: PDI Receiver/transmitter unit**

A laser alignment port is installed on this prototype PDI, as shown at the bottom of the unit in Figure B.2. This is used to adjust the position of one of the laser beams; moving this beam path up or down impacts the size of the sample volume generated from

the beam crossing. This port is capped by a small chained knurled fitting on the side of the receiver/transmitter unit.

The receiver contained within the combined transmitter/receiver unit includes the photodetectors, aperture, and focusing lenses. The prototype PDI used in this research uses a fixed optical configuration. This eliminates the possibility of using different lenses or apertures, but requires significantly less alignment than previous prototypes.

#### *B.1.3.4 Test Cell*

The custom prototype PDI used in this research uses a custom test cell for process gas and laser containment. This test cell is a modified 150# flanged Schedule 10 304SS pipe spool piece. Three crown glass windows are provided for the transmitter, receiver, and for user visual confirmation. Aluminum guides and dowel pins are used to properly align the test cell with the transmitter/receiver unit. The test cell is locked in place by the use of swivel arms with wing nuts. A photo of the test cell is presented in Figure B.3, and of the optical end of the transmitter/receiver unit in Figure B.4.

**Figure B.3: PDI test cell at the bench scale**

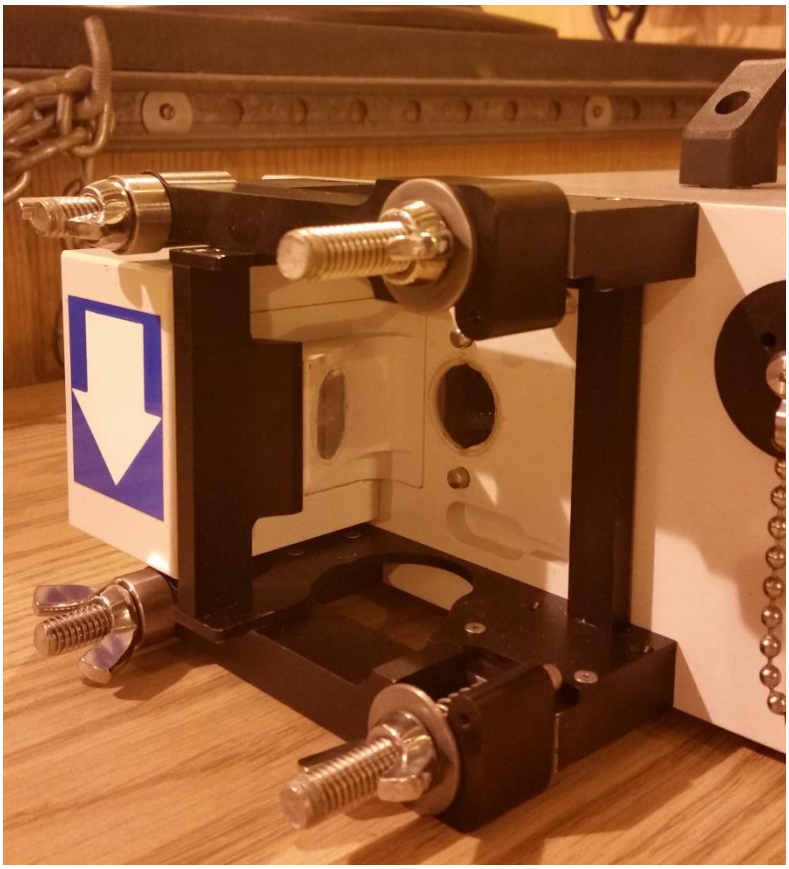

**Figure B.4: PDI transmitter/receiver optical end, which aligns and secures the test cell.**

Flow direction arrows are indicated on both the transmitter/receiver and the test cell to ensure correct orientation.

### *B.1.3.5 Oscilloscope and User Interface*

An oscilloscope, (Tektronix® TDS2014C, 100 MHz, 4-channel, 2G.s), is used for calibration and troubleshooting. Figure B.5 presents the PDI sampling setup on the AGC. The electronics enclosure is below the table; the keyboard and mouse are stored in this

enclosure during transport. A monitor for the CPU is stored in the weatherproof enclosure for the PDI transmitter/receiver unit, test cell, and oscilloscope.


**Figure B.5: PDI electronics enclosure, monitor, keyboard, and oscilloscope**

## B.2 INSTALLATION

The following sections outline the installation of the PDI analyzer on the Aerosol Growth Column, and at pilot plant locations. Sampling at pilot plants can be conducted with or without FTIR sample extraction at the same sample point. The electrical and communications connections are outlined, and the window purge system setup is described.

### B.2.1 Aerosol Growth Column

The Aerosol Growth Column (AGC) is used for bench scale amine scrubbing aerosol tests. This apparatus is located at the Pickle Research Center CEER building. Further description on the AGC is available in Appendix D.

The PDI is used for in-situ sampling at the bench scale. No sample extraction is necessary; the full flow from the AGC passes through the test cell. Figure B.6 presents the PDI transmitter/receiver unit and test cell in place on the AGC.

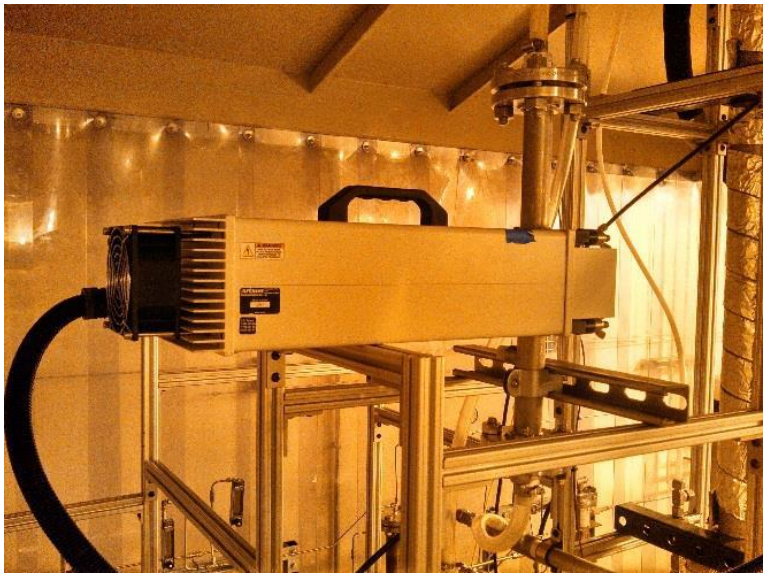

**Figure B.6: PDI transmitter/receiver and test cell on the AGC**

The PDI transmitter/receiver unit must be mated to the test cell prior to installation, at both the bench and pilot scale. This is due to the difficulty in aligning the test cell within the guidance tracks of the transmitter/receiver unit.

1. The transmitter/receiver unit is placed on its side on a flat, secure surface. When facing the optical end of the unit, the arrow side should be down. Loosen the locking wingnuts and allow the swinging latch arms to drop.
2. Insert the four 1/8" purge inlet and outlet tubing into the push to connect ports on the test cell. It is recommended that the purge tubing be aligned to point outward from the test cell window. Only the Y fittings for the purge need to be installed at this time; the ¼" connections to the rest of the purge system can be connected once the transmitter/receiver and test cell are in place.

3. Carefully slide the test cell onto the tracks of the PDI transmitter/receiver unit. Perform this operation slowly, and do not push excessively if resistance is met. The push to connect pieces are extremely easy to damage and misalign. If twisted or pushed excessively, the silicon sealant will break and the system will leak and prove inoperable. Avoid contact between the push to connect pieces and the transmitter/receiver unit guides.

4. Lock the test cell in place on the transmitter/receiver unit. This is accomplished by swinging the latch arms back in place and evenly tightening the wingnuts. Ensure that there is no looseness in the mating between the test cell and the transmitter/receiver unit.

The test cell can be locked in place on the AGC via a strut with pipe clams, as shown in Figure D.6. The transmitter/receiver unit sits on another support. The outlet tubing from the AGC adapts to a 1" 150# flange, which is bolted to the inlet of the test cell. Another 1" 150# flange connects to the test cell outlet, and feeds the gas from the test cell to the AGC condenser. Finally, the power and communications cable from the electronics enclosure can be connected with the port at the back of the transmitter/receiver unit. Align the cable connections, carefully press the cable in place, and twist the knurled lock to lock the cable in place.

### B.2.2 Pilot Plant Sampling Without FTIR

PDI sampling at pilot plants can be performed independently of FTIR sampling. This is the case at UT-SRP, which uses a permanent FTIR sampling system. Ex-situ

sampling is used for pilot plant PDI sampling; this involves extracting a sample from the process gas stream by the use of a VSD-controlled blower, and returning the sampled gas to the process downstream of the sample extraction point.

The PDI test cell is mated with the transmitter/receiver unit, as outlined in Section B.2.1. An isolation valve should be placed at the outlet of the process sample port. The port should be flanged down to 1" 150# for connecting with the test cell. An additional piping tee and isolation valve can be placed upstream of the test cell for calibration and test cell purging. A schematic of this is shown in Figure B.7.

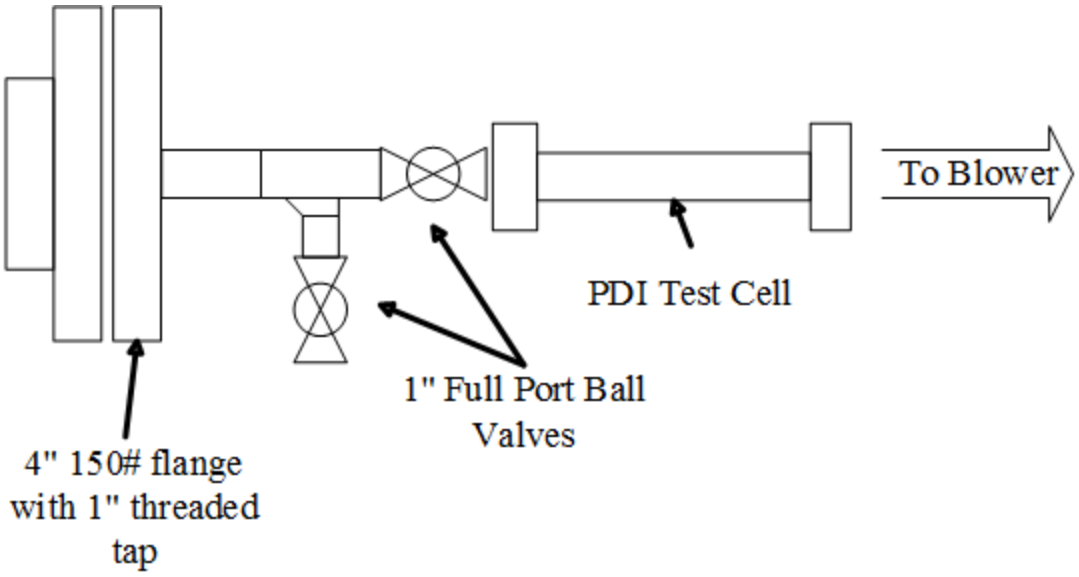


**Figure B.7: PDI-only sampling configuration**

The PDI transmitter/receiver and test cell is best installed by two people. However, this is not always possible during field work. If no help is available, ratchet straps attached to equipment in the pilot plant can be used to secure the PDI transmitter/receiver unit and test cell at the right height to allow for connecting to the

sample extraction point. An example of this is shown in Figure B.8; the ratchet strap runs through the receiver/transmitter handle and wraps around the outlet piping from the water wash outlet at the UT-SRP plant. The transmitter/receiver unit should be upright; this will help prevent condensation from accumulating on the transmitter and receiver windows of the test cell.

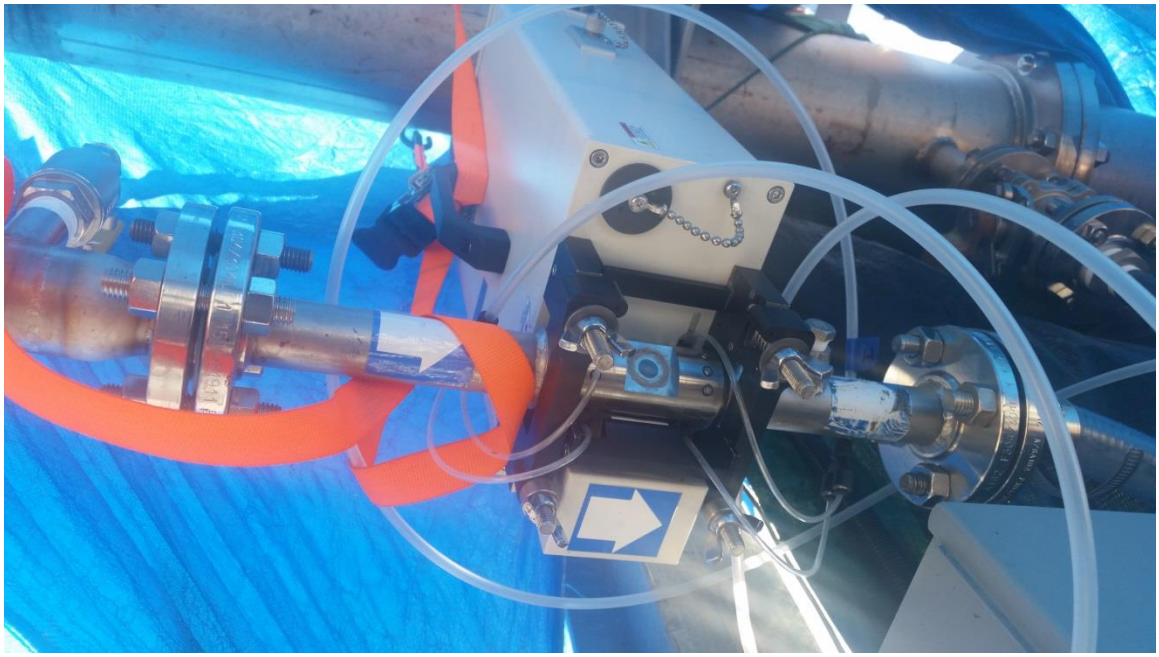

**Figure B.8: PDI transmitter/receiver and test cell supported at the UT-SRP pilot plant**

The outlet of from the test cell connects to the VSD-controlled blower. An Ametek® Rotron® EN303AG58L Regenerative Blower is used for PDI extractive sampling. The blower's flow rate is controlled via a variable speed drive; velocity through the extractive sampling loop is determined by the PDI, and should be set to match the process gas velocity.

A 1” 150# flange with a barbed tube fitting adaptor connects the test cell to the blower inlet tubing. 1-1/4” ID suction and delivery hose (US Plastics, #54252) is used on the extractive sampling system. Hoses are secured to the barbed fittings with ring clamps. The hose from the test cell outlet connects to the blower inlet, and another length of hose connects from the blower outlet to the process sample return port. The blower can be run in forward or reverse as needed.

A final step involves insulating the piping upstream of the test cell. For 1” piping, aluminum-clad foam pipe insulation can be used. This is the same material used as insulation on the Aerosol Growth Column absorber. Fiberglass water heater insulation can also be used, but care should be taken to not breathe in fibers from this material.

### B.2.3 Field Sampling With FTIR

The National Carbon Capture Center (NCCC) and University of Kentucky, Kentucky Utilities, and Louisville Gas and Electric (UKy/KU/LG&E) pilot plants do not have permanent FTIR sampling systems. Portable FTIR systems must be employed at these sites to perform sampling. This can be accomplished in conjunction with PDI sampling. Figure B.9 presents a schematic of combined FTIR and PDI sampling.

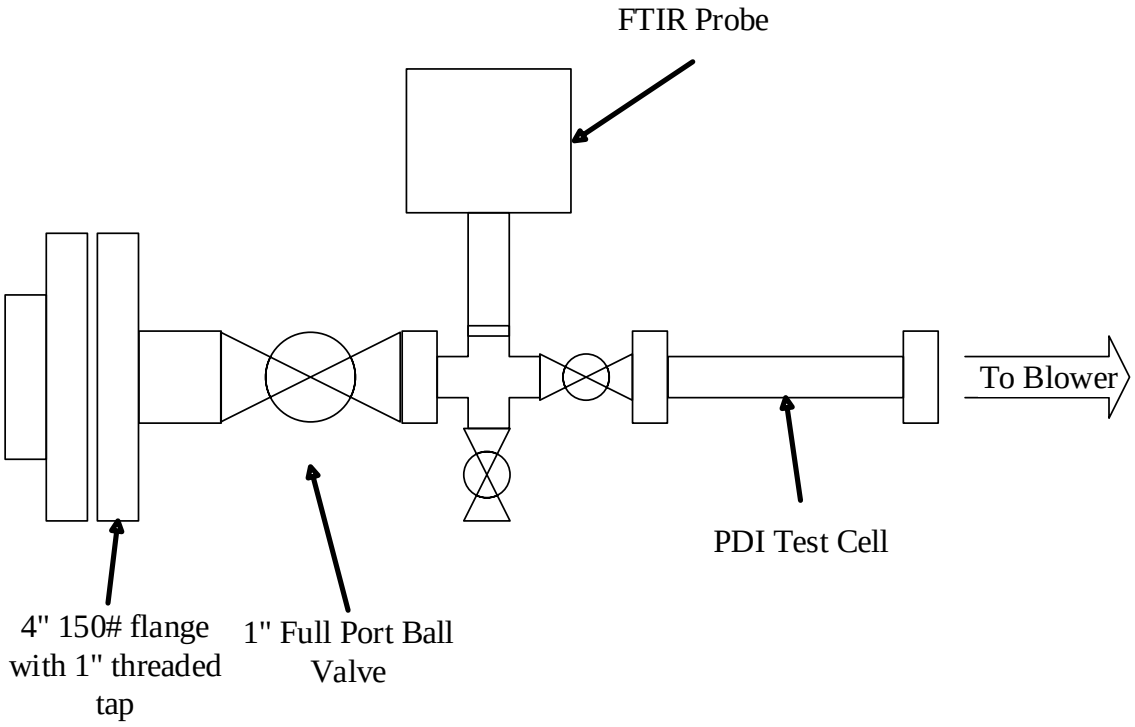


**Figure B.9: Extractive sampling for simultaneous PDI and FTIR sampling**

A piping cross is installed directly downstream of the sample port isolation valve. The upward opening of the cross is used as the FTIR sample extraction point, while the downward opening is connected to a quarter-turn valve. The valve can be used as a drain for accumulated liquids, or as an inlet port for calibrating or purging the PDI test cell. Another isolation valve is placed between the piping cross and the PDI test cell. This allows the PDI test cell to be isolated from the FTIR system, allowing FTIR sampling to occur when the PDI is offline. The outlet from the PDI test cell is passed to the blower as explained in B.2.2. A visual representation of this system in place at NCCC is presented in Figure B.10.

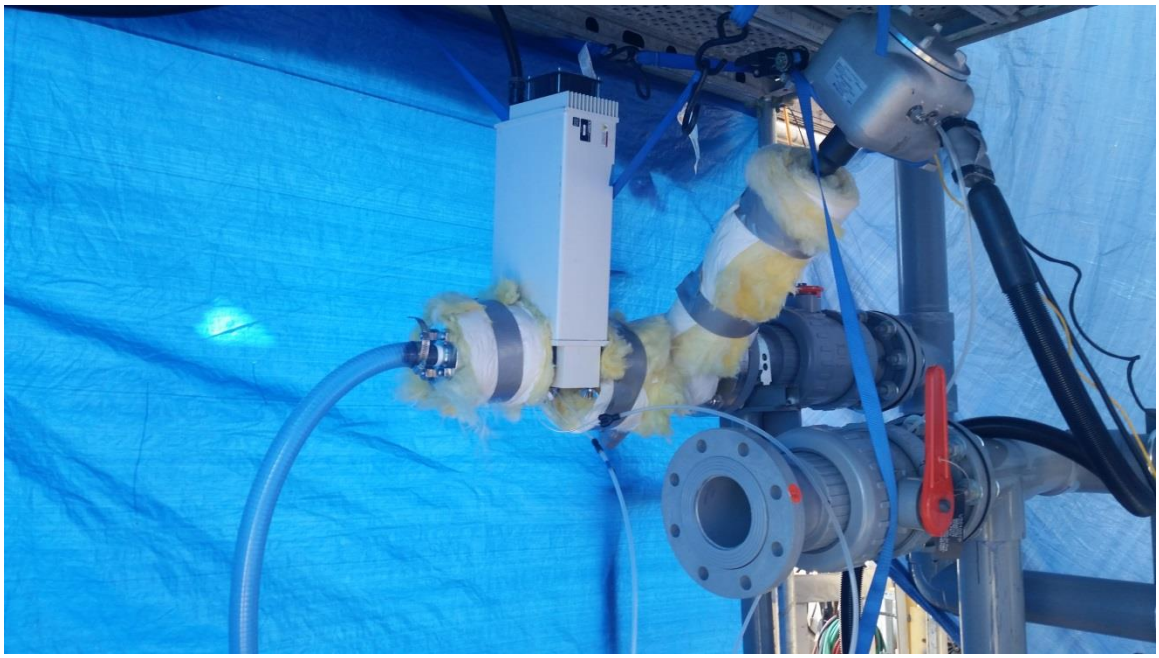

**Figure B.10: Combined PDI and FTIR sampling at NCCC. Fiberglass water heater insulation is used to minimize temperature changes of the sampled stream.**

The heated FTIR probe will need to be secured to ensure it does not rotate. This can be accomplished by the use of ratchet straps, as shown in Figure B.10. Bungee cords are not recommended for this use due to the temperature of the FTIR probe.

### B.2.4 Electrical and Communications Connections

Electrical and communications connections are already configured for the PDI system. It is recommended that no changes be made to the existing configuration; due to the extensive quantity of wires and connection ports, it is easy to make mistakes in rewiring the system. The electronics enclosure can securely hold all the electrical and communications wiring during transit. The only wires that will need to be connected during sampling operations will be the power and communications cable to the PDI transmitter/receiver, and the power cord to the electronics enclosure power bar.

Figure B.11 shows the wiring configuration at the back of the electronics enclosure. The green box 'Monitor Signals' encompasses BNC connections between the ASA box and the oscilloscope. The blue boxes indicate the Ethernet connection between the ASA box and the CPU. The yellow boxes show the USB connection between the power box and the CPU. The connections encompassed in the red box are from the PDI transmitter/receiver unit power and communications cable. A 6$^{th}$ connection from the power and communications cable connects to the power adaptor box, a standalone unit contained inside the electronics enclosure.

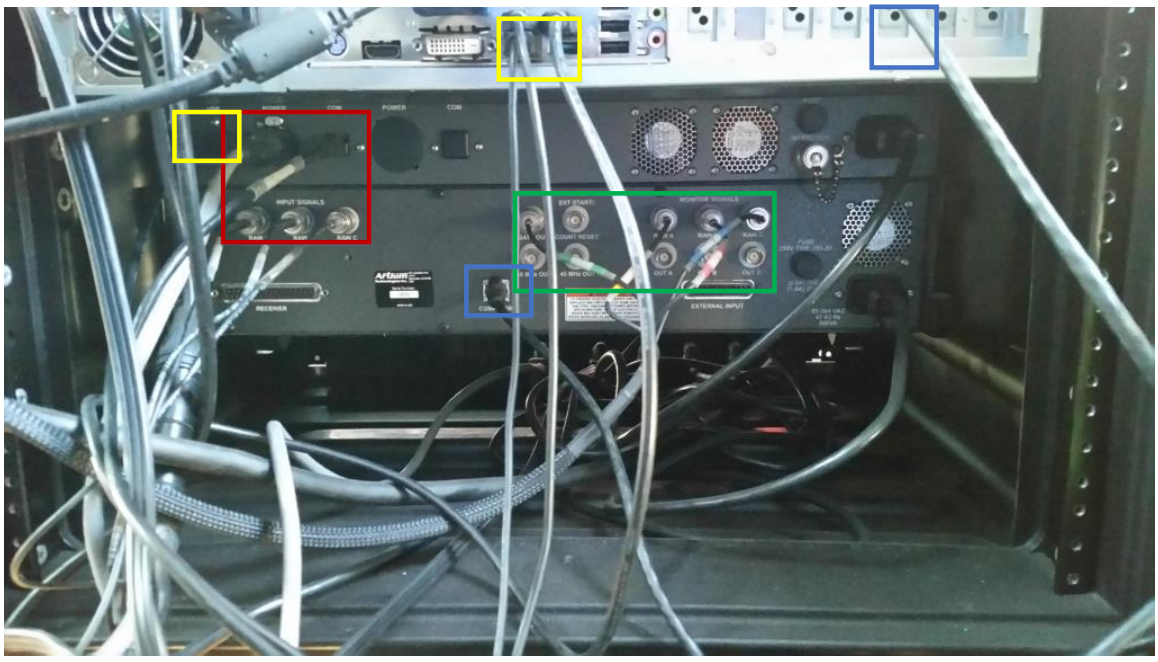

**Figure B.11: Wiring inside PDI electronics enclosure**

BNC connections to the oscilloscope are labeled Channels 1-4. The four channels used are Raw A, Raw B, Raw C, and Gate Out; these display the unfiltered Doppler bursts from each photodetector. The Gate signal indicates the presence of a burst signal,

and rises to 5V when a Doppler burst is detected. This is a key signal to look for on the oscilloscope, as the presence of a Gate signal indicates the passage of a measureable aerosol drop through the sample volume. The signals from Raw A, Raw B, and Raw C on the oscilloscope correspond with the three photodetectors; peaks with these signals are used for laser alignment, phase calibration, and real-time assessment of signal quality.

### B.2.5 Test Cell Window Purge System

Within the test cell, protective cones are in place to keep aerosol from contacting the transmitter and receiver optical windows, in order to reduce fogging and attenuation issues. These are machined in a manner to reduce obstructions to the flow path. The windows are also fitted with microchannels for purge and vacuum flow. The purge is designed to sweep the windows to prevent liquid sheeting or fogging on the optical windows. Connections for the purge are made with 1/8" push-to-connect fittings embedded in o-rings in the test cell body. The push to connect fitting seals are supplemented with silicone sealant to further improve the seal. These push-to-connect fittings are visible as the black fittings above and below the test cell windows in Figure B.3. If damaged, these fittings will become loose and will leak. When this occurs, remove the push to connect fittings and reseat the fittings with fresh silicone sealant. The sealant takes 24 hours to fully cure, so the test cell should not be reconnected with the PDI transmitter/receiver box or allowed to contact moisture until this time span is complete.

A purge flow control box is used to regulate the purge gas fed into and out of the PDI test cell. The box is an 8” x 6” x 6” SS enclosure, with four ¼” Swagelok bulkhead fittings on the underside. This is shown in Figure B.12.

**Figure B.12: PDI purge flow control box**

Purge gas is supplied to the purge flow control box via the leftmost bulkhead. This supplies the inlet gas, and gas to an eductor. The second bulkhead from the left is the gas outlet, and should be vented through a length of tubing to a suitable location.

The bulkhead on the far right is for the purge gas suction, and the bulkhead next to it is for the purge gas inlet. The gas flow into the purge should match the gas flow exiting; this can impact the aerosol concentrations and sizes by dilution if not controlled.

The extraction flow rate should be set as high as possible by the use of the rightmost rotameter, with the leftmost rotameter supplying an inlet flow that matches the outlet flow rate. A small knockout put should be used upstream of the inlet to the purge extraction. This is due to the tendency of liquids to accumulate in that line and plug the eductor, rendering the system inoperable. A knockout pot can be assembled with a plastic Erlenmeyer flask and a double entry stopper. ¼" tubing is suitable for all purge gas connections.

The purge flow control system is susceptible to leaking and loosening connections if not handled with care. It can be easily disassembled and reassembled if necessary. Care should be taken to not overtighten the connections to the rotameters, as these can be easily damaged. If the system is inoperable, a needle valve can be used to regulate flow to the test cell purge inlet, with the test cell purge outlet plugged. The purge flow in this scenario should be at an absolute minimum to not dilute the sampled gas.

## B.3 INITIALIZING OPERATIONS

The PDI and AIMS operating software must be prepared prior to beginning sampling. These steps are outlined in the following section.

### B.3.1 Starting the PDI System

The components in the electronics enclosure must be started in the correct order. Turn on the switches to each component in the following order:

1. Power strip (bottom of enclosure)
2. Power box
3. CPU

4. ASA box
5. Oscilloscope

Wait 5-10 seconds between powering on the CPU and the ASA box.

It is recommended that the PDI CPU clock is synced with the FTIR computer clock, if both are sampling simultaneously. This will aid future data analysis significantly. Both computer clocks should be synced with the pilot plant control system clock, or the LabVIEW™ computer if operating at the bench scale.

### B.3.2 AIMS Initialization

Log onto the computer and start the AIMS software. This should take a few seconds to load. If the AIMS software initializes with the error message 'No ASA detected', shut down the components in the electronics enclosure and repeat startup, taking more time between starting the computer and the ASA box.

Ensure that the 4 signals (3 photodetectors and gate signal) have appeared on the oscilloscope. If not, ensure that the BNC connectors are in the correct locations and securely attached.

### B.3.3 Device Controls

The following sections outline the values for various parameters under the 'Device Controls' left-hand tab in AIMS. Each section is titled by the topside tab name. These values may not correspond with the best possible values for each sampling scenario. Instead, these are recorded as a base case and can be adjusted as necessary.

### *B.3.3.1 Acquisition*

Data collection can be automatically stopped through three different means: a set sampling time, a set number of samples, or free run that stops at the user's input. These are selected in AIMS under the Acquisition tab in the Device Controls left-hand tab. Typical sampling criteria invoked a counts threshold of 10,000, or a sampling time of 5 minutes.

### *B.3.3.2 Validation*

AIMS uses several criteria to validate accurate particulate measurements. These criteria discard samples that might lead to size ambiguity or miscounting. Table B.1 outlines the parameter values. Definitions on each of these values are available in Chapter 2 of this work.

**Table B.1: AIMS Validation tab settings**

| | |
|---|---|
| **Channel 1 Velocity Outlier Filter** | |
| **Enabled:** | **Off** |
| **Learning Rate** | 0.999 |
| **Max Distance from Mean (σ)** | 3 |
| **Channel 1 Diameter Filter** | |
| **Enabled:** | Off |
| **Minimum (µm)** | 0 |
| **Maximum (µm)** | 75 |
| **Diameter Outlier Filter** | |
| **Enabled:** | No |
| **Maximum** | 0 |
| **Channel 1 Diameter Processing** | |
| **Max Fixed Diameter Difference (µm)** | 10 |
| **Max Percent Diameter Difference (%)** | 15 |
| **Lower Intensity Cutoff (%)** | 20 |
| **Number Density Calculation** | |
| **Type:** | Transit Time |

| | |
|---|---|
| **Channel 1 Resettable Clock Filter** | |
| **Enabled:** | Off |
| **Minimum (ms)** | 0 |
| **Maximum (ms)** | 5 |
| **Syncronize Settings:** | Yes |

### *B.3.3.3 Processors*

Table B.2 gives the base case values for parameters under the 'Processors' tab.

**Table B.2: AIMS Processors tab settings**

| | |
|---|---|
| **Channel 1 ASA Processor (PDI)** | |
| **# FFT Bins** | **1024** |
| **SW Burst Detector Enabled:** | On |
| **Analog Filter (MHz)** | 20 |
| **Mixer (MHz)** | Variable |
| **Variable Mixer (MHz)** | 42 |
| **Sampling Rate (MHz)** | 80 |
| **BD Decimation** | 2 |
| **External Input** | Off |
| **Analog Threshold (mV)** | 100 |
| **Channel 1 Data Acquisition** | On |
| **Measureable Velocity** | |
| **Minimum Velocity (m/s)** | -14.5 |
| **Maximum Velocity (m/s)** | 17.8 |
| **Channel 1 DC Offset** | |
| **Peak DC Offset (mV)** | -500 |
| **Elapsed Time Correction** | |
| **Enabled:** | Yes |

### *B.3.3.4 Auto Setup*

Table B.3 presents the values for parameters under the 'Auto Setup' tab.

**Table B.3: AIMS Auto Setup tab settings**

| | |
|---|---|
| **Num. Auto Setup Signals** | **500** |
| **Stop Acquisition on Auto Setup Failure** | **No** |
| **Auto Setup Method** | Sample |
| **Auto Setup** | |
| **Acquisition Mode** | PDI |
| **Auto Setup Mode** | Normal |
| **Processor Auto-Setup Enabled** | No |
| **Gain Auto Setup Enabled** | No |
| **Static Velocity Min (m/s)** | 0 |
| **Static Velocity Max (m/s)** | 30 |
| **Auto Setup Timeout (s)** | 10 |

### *B.3.3.5 Phase Calibration*

Table B.4 presents the values for parameters under the 'Phase Calibration' tab. The 'AB Phase Cal', 'AC Phase Cal', and 'BC Phase Cal' values are subject to change, but should be in this approximate range, provided the GAIN in the 'Optics' tab is not significantly altered

**Table B.4: AIMS Phase Calibration tab settings**

| | |
|---|---|
| **Enabled:** | **Off** |
| **Frequency (MHz)** | **41** |
| **Amplitude (V)** | 0.9 |
| **Visibility (V)** | 1 |
| **Channel 1 Phase Calibration** | |
| **AB Phase Cal (°)** | -3.83 |
| **AC Phase Cal (°)** | -6 |

| | |
|---|---|
| **BC Phase Cal (°)** | -2.17 |
| **Channel 1 Calibration Type** | |
| **Phase Calibration Type:** | Multi-Point |

#### *B.3.3.6 Optics*

Table B.5 gives the values for parameters listed under the 'Optics' tab.

**Table B.5: AIMS Optics tab settings**

| | |
|---|---|
| **Channel 1 Photodetector Gain** | |
| **Gain (V)** | **600** |
| **Channel 1 Transmitter** | |
| **Wavelength (nm)** | 532 |
| **Focal Length (mm)** | 25 |
| **Beam Separation (mm)** | 17.46 |
| **Beam Diameter (mm)** | 0.95 |
| **Expander Factor** | 1 |
| **Frequency Shift (MHz)** | 40 |
| **Fringe Spacing (µm)** | 0.8 |
| **Beam Waist (µm)** | 17.8 |
| **Channel 1 Receiver** | |
| **Front Focal Length (mm)** | 35 |
| **Slit Aperture (µm)** | 10 |
| **Collection Angle (°)** | 65 |
| **Index of Refraction** | 1.33 |
| **Scattering Mode** | Refraction |
| **Static Range (µm)** | 0.1-11.5 |

### B.3.4 Performing Phase Calibration

Phase calibration is to be performed prior to beginning sampling each day. Phase delays must be accounted for due to the sensitivity of particle sizes to the phase and due to the high frequencies occurring within the analyzer's processors, signal cabling, and photodetectors. Phase delay is calibrated by using a calibration diode that produces

synthetic Doppler signals at the expected frequency of the process to be measured. The Doppler frequency is proportional to the "real" particle velocity, requiring a guess of the flow conditions to be made. The signal frequency can be determined by the use of Equation B.1; the calculated expected signal frequency is inputted into the "Frequency" selection under the Phase Calibration tab in AIMS.

$$f_r = f_D + f_S = \frac{v}{\delta} + f_S \tag{B.1}$$

where:

$f_r$ = Expected signal frequency (MHz)

$f_D$ = Doppler frequency (MHz)

$f_S$ = Bragg cell shift frequency, 40 MHz

$v$ = Expected mean velocity of the process sample (meters/s)

$\delta$ = Fringe spacing, 0.8 μm (m)

Phase calibration is performed prior to turning the lasers on. Selecting "Quick Phase Calibration" determines the phase offset of each photodetector pair, and automatically adjusts this value in the software. The phase offset should only vary by a few degrees; this procedure should be repeated until there is little to no change in each offset value. The photodetector signals on the oscilloscope should reach approximately 200 mV; if not, the "Amplitude" value can be adjusted. A typical amplitude value is 0.9, and is a function of the PMT gain. It is sometimes useful to sample the aerosol stream with the uncalibrated PDI to determine approximate PMT gain settings prior to phase calibration.

### B.3.5 Turning On Lasers

Once the initial settings have been configured in AIMS and phase calibration has been performed, the transmitter/receiver lasers can be activated. This is performed by turning the key at the back of the transmitter/receiver unit. The small red light at the back of the transmitter/receiver unit will alight, and visual confirmation of the lasers can be confirmed by the presence of green light at the test cell optical window. Lasers are never to be turned on when the transmitter/receiver is not connected to the test cell, due to the optical hazard presented by the Class 3B lasers.

### B.3.6 Laser Alignment

A laser alignment port is installed on this prototype PDI, as shown at the bottom of the unit in Figure B.2. This is used to adjust the position of one of the laser beams; moving this beam path up or down impacts the size of the sample volume generated from the beam crossing. This port is capped by a small chained knurled fitting on the side of the receiver/transmitter unit. Opening the knurled knob and inserting a long #2 hex driver allows access to the alignment port. The hex driver will not fully inset immediately; the hex driver will require some jiggling and rotating to fully insert into the alignment port. Only minor adjustments are necessary for PDI laser alignment; typically, less than half a turn in either direction is necessary to properly realign the lasers.

This operation may need to be performed upon relocation and reinstallation of the PDI system at field sampling sites. Proper laser alignment will result in an increase in the magnitude and frequency of peaks for signals 1-3 on the oscilloscope, and an increase in the frequency of the Gate signal as well. A visual representation of proper laser

alignment as seen through the oscilloscope is presented in Figure B.13. The produced Doppler signal should have a well-defined high and low frequency, with a Gaussian pedestal component and a high frequency and amplitude burst signal. Multimodal peaks indicate a misaligned laser, or the presence of multiple aerosol drops in the sample volume. An aerosol source must be present when aligning the laser. A Pari Trek S Compact Nebulizer (Catalog number J-P47F45LCS-CN) provides a steady aerosol stream with water, and is stored with the PDI analyzer system. The sampled process stream can also be used as an aerosol source if necessary.

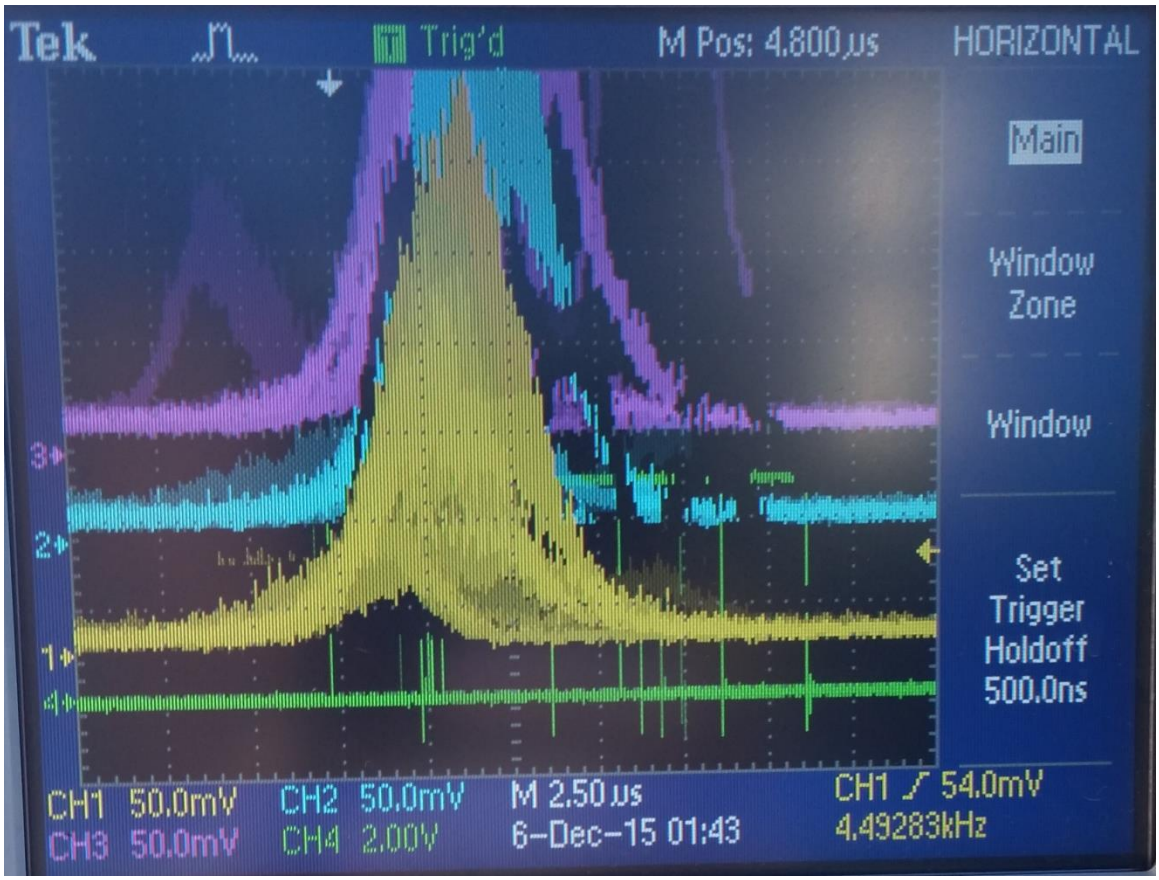

**Figure B.13: Oscilloscope readout of proper PDI laser alignment. Photodetector signals (Channels 1, 2, and 3) show Doppler bursts, Gate signal (Channel 4) shown with high frequency.**

## B.4 SAMPLING OPERATIONS

AIMS file naming protocol should be established prior to beginning bench or pilot scale sampling. Under the left hand tab listing in AIMS, go to the 'Data Library' tab. The file directory is listed, along with a space for the run name. Each successive sampling run by the PDI will add to the run name; for example, if the run is named 'Test', the first sampling run in AIMS will produce a run titled 'Test0000', the second run titled 'Test0001', and so forth.

### B.4.1 Sampling

AIMS will begin collecting data from the transmitter/receiver unit once the user clicks the green 'Start' button at the top left of the AIMS application. The PDI run will complete when 5 minutes have passed or 10,000 samples have been quantified, whichever occurs first.

Live results from the run can be viewed by selecting the 'Results' tab from the left hand tabs listing. Figure B.14 presents an example readout from this screen. A diameter histogram is presented at the top, and gives the diameter of aerosol measured on the x-axis versus the counts on the y-axis. A velocity histogram on the bottom gives the aerosol drop velocities on the bottom axis and counts on the y-axis. The right side of the screen gives pertinent data collection information, including sizing data on the sampled

aerosol, the total counts, and the data collection rate. The histogram bin width should be set to 0.1 μm for maximum resolution.

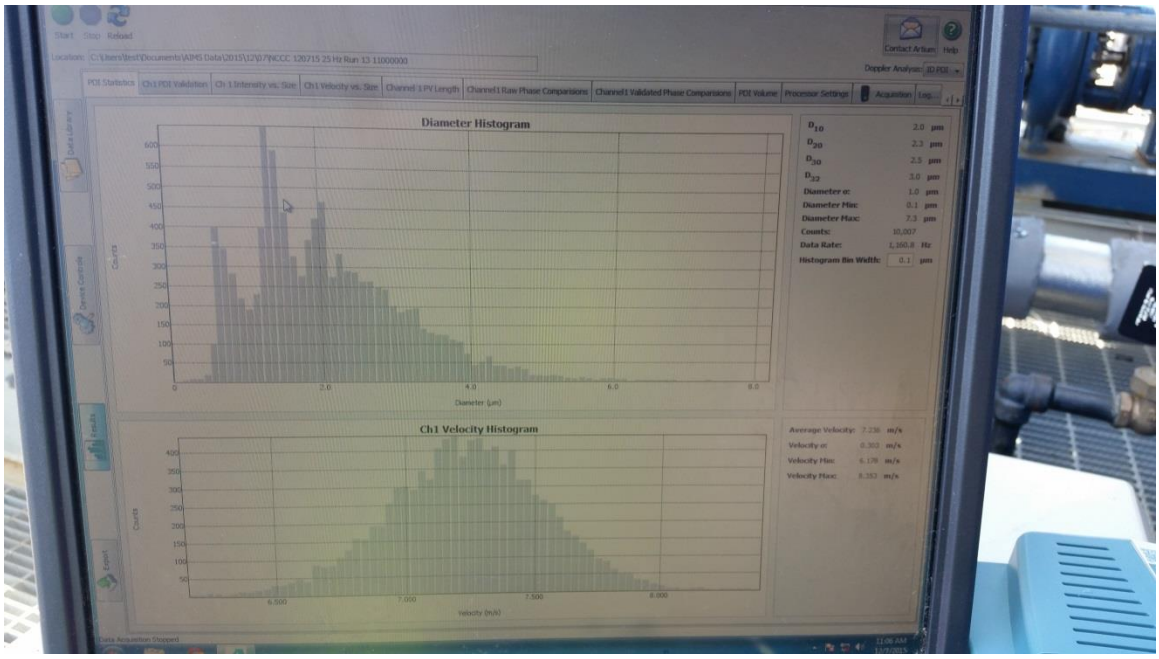


**Figure B.14: Example AIMS PDI data readout from 'Results' tab**

The validation percentages can be observed under the 'Channel 1 PDI Validation' tab in the 'Results' tab. The 'Ch 1 SNR/Frequency Validation' values are the most important. Passing percentages in the range of 60 to 80 % are suitable; higher is obviously more ideal, and shows better performance by the PDI. Varying the validation criteria from Section B.3.3.2 and B.3.3.3 can raise and lower the passing percentages.

### B.4.2 Gain Adjustment

A final adjustment can be made to maximize the measured aerosol. The Gain value presented in Section B.3.3.6 can be raised or lowered if necessary. The photodetector signals are amplified several orders of magnitude by the photomultiplier tubes, in order to produce electrical signals. The "Gain" value adjusts the PMT voltage

to a point where the scattered light refracted from the aerosol is detectable. The intensity of light scattered from refraction is proportional to the square of the aerosol diameter, so smaller particles need higher gain to be detected. However, increasing the gain increases the signal noise. A tradeoff exists between minimum detectable size and acceptable signal to noise ratio. The PMT gain is configured in Auto-setup, but can be manually adjusted by viewing the signal intensity versus diameter plots; the gain is set so the largest particles reach the detector saturation. Figure B.15 presents an example Gain result from the 'Ch 1 Intensity vs. Size' tab under the 'Results' left hand tab.

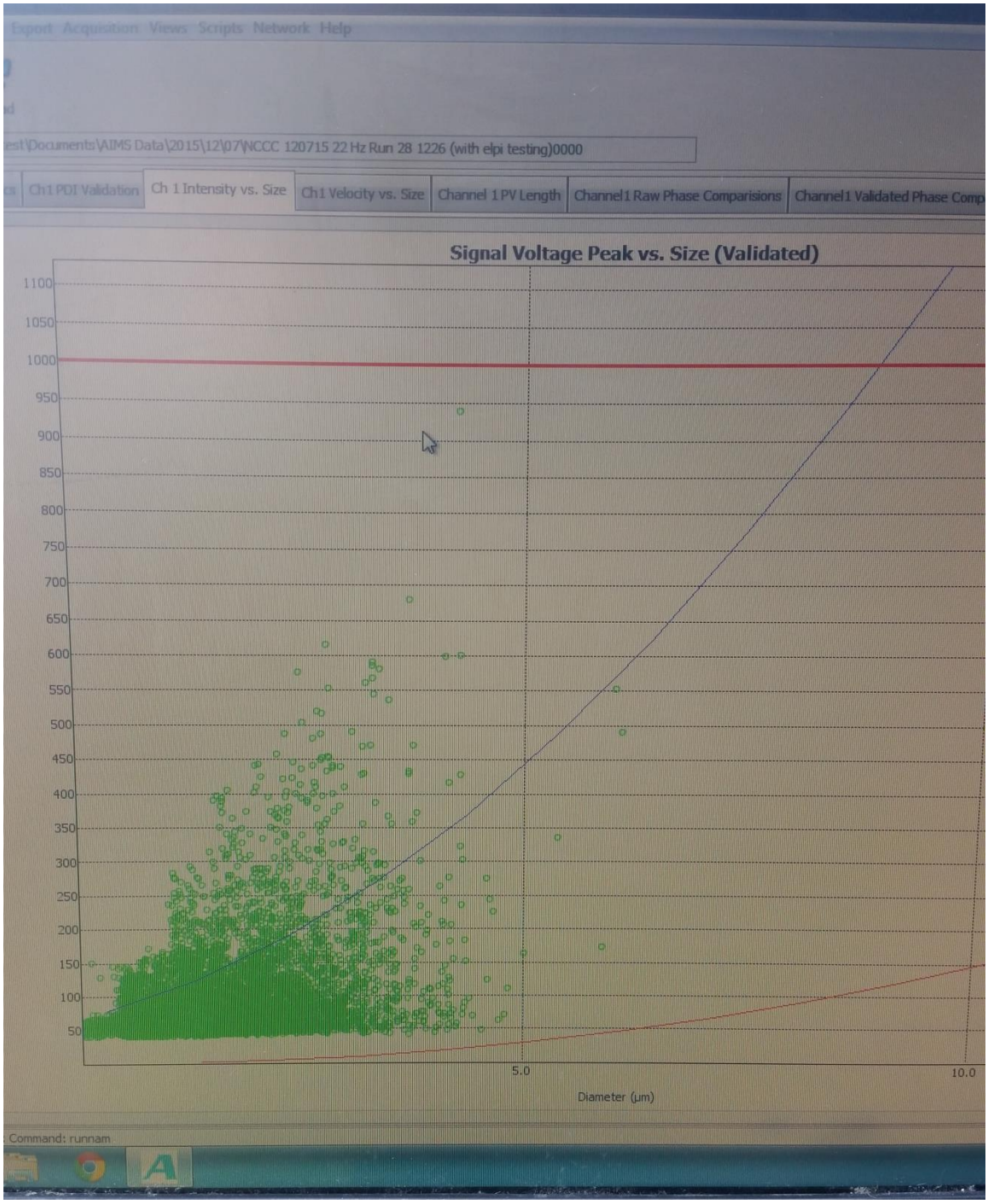


**Figure B.15: Example GAIN results**

In Figure B.15, the Gain can be increased if necessary to include more of the observed aerosol in the data set. The phase calibration should be performed again if the Gain is adjusted.

## B.5 SYSTEM SHUTDOWN

### B.5.1 Data Retrieval

Every PDI sampling run produced 29 different Excel files, each containing a certain category of data. The experiments in this work utilize the Excel files labeled "Count_Diameter", "Diameter Counts Total", "Number Density", "SNR_Frequency_Pass", and "Start_Time". The "Count_Diameter" gives the particle size distribution of the measured aerosol. "Diameter Counts Total" provides the total number of aerosol quantified. This is useful for normalizing the aerosol count diameter. "Number_Density" gives the measured aerosol concentration per $cm^3$. "SNR_Frequency_Pass" gives the rate at which measured aerosol exceed the signal-to-noise ratio; above 60% is adequate for aerosol measurement. "Start_Time" gives the start time of the PDI sample run, and is used to link the PDI data to other process data. The directory paths to these files can be found by opening AIMS and selecting "Data Library" on the left-hand menu.

### B.5.2 PDI Shutdown

The following steps should be followed when shutting down PDI sampling:

1. Turn off the PDI transmitter/receiver lasers by the use of the key at the rear of the unit.

2. Close out the AIMS software and shut down the PDI computer. The other components in the electronics enclosure can be powered off as well.

3. At the bench scale, the purge flow to and from the PDI test cell can be stopped. For pilot scale experiments, it is recommended that the test cell be isolated from the sampled process gas stream and flow maintained if PDI testing is to be resumed. Condensation accumulates easily in the test cell and can fog the windows, inhibiting PDI measurements. By isolating and purging the test cell, the PDI will be ready to resume measurements when necessary.

### B.5.3 Equipment Disassembly

#### *B.5.3.1 Bench Scale*

PDI equipment can be disassembled from the AGC in reverse of how it was assembled. Disconnect the power and communications cord from the back of the transmitter/receiver unit. The inlet and outlet 1" 150# flanges from the AGC can be disconnected from the PDI test cell. Unclamp the PDI test cell from the strut support, and carefully remove the combined system from the process. The test cell can be carefully separated from the transmitter/receiver unit, and both hardware pieces can be stored in the weatherproof storage box.

#### *B.5.3.2 Pilot Scale*

This is best performed by two people. Begin by isolating the sampling system from the process, and disconnecting the PDI test cell from the blower. Loosen the ring clamp and pull off the 1-1/4" suction hose, and then remove the flange with the barbed tube fitting. The PDI test cell can be disconnected from the rest of the sample train. The

test cell should still be locked in place with the PDI transmitter/receiver unit, and still supported by the ratchet straps. The combined transmitter/receiver and test cell can be carefully released from the ratchet strap while supported by the second person, and placed on a secure surface. The test cell can be removed from the transmitter/receiver unit and both pieces of hardware secured in the weatherproof storage box.

If the PDI sampling was performed in conjunction with FTIR sampling, the FTIR sampling part of the apparatus can be disassembled piecewise. Ensure that the heating to the FTIR system is off and the components have sufficiently cooled.

# APPENDIX C: UT-SRP FTIR SAMPLING SYSTEM

## C.1 BACKGROUND

This appendix covers the details of designing and installing the permanent FTIR sampling system at UT-SRP. The Gasmet™ CX-4000 FTIR and accessories are presented. Sampling probes and pads, and the installed supports for the heated sample lines, are also covered. Finally, instructions for enabling communications between the analyzer Calcmet™ software and the UT-SRP DeltaV™ control system are provided.

### C.1.1 Safety

The UT-SRP pilot plant underwent significant modifications in the winter of 2017. The existing FTIR sampling system was extensively overhauled to be permanently positioned in the pilot plant structure. This involved supporting the FTIR sample lines with lightweight aluminum cable trays.

The UT-SRP pilot plant is located on the south side of the Center for Energy and Environmental Resources (CEER) building, exposing it to strong southern winds gusts of unpredictable intensity and direction. This can be hazardous for personnel. Installation of the aluminum cable trays was challenging, as the lightweight trays were easily caught in the wind. Care must be taken during these conditions to ensure the safety of everyone in the unit. Two or more people should work together when installing trays, and should ensure that the trays are well secured to their fittings in the unit. Work should be postponed during especially windy conditions.

## C.2 FTIR ANALYZER

### C.2.1 FTIR Analysis

Fourier Transform Infrared Spectrometry (FTIR) utilizes a broadband light source cast through a configuration of mirrors to measure how a sample absorbs infrared radiation. Only infrared active compounds (polyatomic and hetero-nuclear diatomic molecules), such as $CO_2$, $H_2O$, and amines, will be detected by the FTIR. The mirrors in the FTIR are susceptible to damage from liquids, so the FTIR sampling is performed "hot and wet' by maintaining a temperature of 180 °C across the sampling system from the extraction point to the analyzer.

Table C.1 shows the wavenumber (reciprocal wavelength) ranges used to quantify total emissions (Fulk, 2016). These are the measurement ranges used for each sampled component.

**Table C.1: Analysis regions used for FTIR spectra**

| Component | Concentration | Range 1 [$cm^{-1}$] | Range 2 [$cm^{-1}$] | Range 3 [$cm^{-1}$] | # of References |
|---|---|---|---|---|---|
| $H_2O$ | vol % | 2475–2600 | 3000–3375 | -- | 8 |
| $CO_2$ | vol % | 926–1150 | 2065–2245 | 2550–2700 | 10 |
| PZ | ppmv | 2500–3100 | -- | -- | 11 |
| $NH_3$ | ppmv | 895–1300 | 2475–2600 | -- | 7 |
| $SO_2$ | ppmv | 1050–1450 | 2500–2600 | -- | 7 |

### C.2.2 FTIR Analyzer

The FTIR analyzer used at UT-SRP is a Gasmet™ CX-4000. Table C.2 presents the technical specifications for this analyzer.

**Table C.2: Gasmet™ CX-4000 Technical Specifications**

| Parameter | Value/Description |
|---|---|
| *Model* | |
| Model # | CX-4000 |
| Mounting Position | Horizontal |
| Line Voltage | 120 VAC |
| Fittings | ¼" Imperial, Compression |
| Gaskets | Kalrez[c] |
| Software | Calcmet™ V11.118, Windows 7 (64-bit) |
| *Interferometer* | |
| Interferometer Type | Temet Carousel Interferometer (GICCOR) |
| Beamsplitter/Window Material | ZnSe |
| Wavenumber Range | 900-4200 $cm^{-1}$ |
| *Sample Cell* | |
| Temperature | 180 °C |
| Path Length | 5.0 m |
| Sample Cell Volume | 0.4 L |
| Gasket Material | Kalrez® |
| Coating | Ni + Rh + CVD Au |
| Mirrors | Fixed, protected Au coating |
| Protective Coating | $MgF_2$ |
| Window Material | $BaF_2$ |
| Sample Cell Pressure Measurement | Yes |
| Detector Type | Mercury, Cadmium, Tellurium, Pelletier Cooled (MCPT) |
| IR Source | SiC, 1550K |
| *DSP/Power Board Settings* | |
| Speed Setting | 5 Hz |
| Resolution | 8 $cm^{-1}$ |
| Scan Frequency | 10 spectra/s |
| Comport Speed | 57600 bps |
| EPROM Type | Standard |
| Digital Interface | 9-pole D-connector RS232 protocol serial |
| *Measuring Parameters* | |

| | |
|---|---|
| Zero point calibration | |
| Zero point drift | Every 24 hours with $N_2$ |
| | <2% of measuring range per zero point calibration interval |
| Accuracy | |
| Temperature drift | 2% of measuring range |
| Pressure influence | <2% of measuring range per 10K change |
| | 1% of measuring range per 1% sample pressure change |

The analyzer is housed in a server rack cabinet, along with the CPU and user interface keyboard-monitor unit. This is presented in Figure C.1.

**Figure C.1: Gasmet™ CX-4000 FTIR in server rack**

Immediately below the user interface is a heated element control box. This supplies power to the heated sample line, filtration unit, suction pump, and jumper line to the FTIR. Fuji Electric PXR3 Temperature Controllers are used to provide PID temperature control to maintain a temperature of 180 °C. K-type thermocouples provide thermal measurements of the filtration and pumping components. Amphenol™ wiring ports are used for power distribution to each of the heated elements.

### C.2.3 FTIR Filter

The sampled gas is first passed through the heated filter. An Atmoseal ® FPD-4-7/1-B02 filter was selected for this application. This filter uses a bayonet-type T-handle filter with a 1" ID by 7" length element for removal of 0.1 μm or larger particles. Table C.3 presents the technical specifications of the filter.

**Table C.3: Atmoseal ® Filter Technical Specifications**

| Parameter | Value/Description |
|---|---|
| Part number | FPD-4-7/1-B02 |
| Voltage | 120 VAC (60 Hz) |
| Full load amps | 2.0 A |
| Enclosure | 316 SS |
| Thermocouple Type | K |
| Filter Type | Bayonet |
| Maximum Temperature | 400 °F |
| Port Size and Type | ¼" NPT |
| Element Length and ID | 7" x 1" |

### C.2.4 FTIR Pump

Suction through the FTIR system is maintained by an Air Dimensions, Inc.® Dia-Vac-R201 heated sample pump, model number R201-FP-IE3-M. A Baldor® Super-E motor powers the pump. Technical specifications on this motor are presented in Table

C.4, and on the pump head in Table C.5. The pump and head for this sampling system are designed to draw 5 Lpm of gas through 5/16" ID tubing over a length of 200', as necessary to sample from the 8th floor to the ground level at the NCCC PSTU.

**Table C.4: Baldor ® Super-E ® FTIR Sample Pump Motor Technical Specifications**

| Parameter | Value/Description |
|---|---|
| Catalog number | 1202035119-000010 |
| Specification number | M35J302P862 |
| Serial number | X1702M23881 |
| Horsepower | 0.5 |
| Voltage | 230/460 VAC (60 Hz) |
| Phase(s) | 3 |
| Full load amps | 1.54/0.77 A |
| RPM | 1735 |
| NEMA nominal efficiency | 82.5% |
| Power factor | 74% |
| Service factor | 1.25 |
| Frame | 56C |
| Enclosure | TEFC |
| Insulation class | F |
| KVA code | K |
| Design code | B |

**Table C.5: Baldor ® Super-E ® FTIR Sample Pump Technical Specifications**

| Parameter | Value/Description |
|---|---|
| Model number | R201-FP-IE3-M |
| Heater power | 150 W (2x 75 W) |
| Voltage | 115 VAC (60 Hz) |
| Current Draw | 1.3 A |
| Head material | 316SS |
| Diaphragm material | Teflon® |
| Temperature range | 30–400 ºF |
| Max. ambient temperature | 140 ºF |
| Enclosure | Explosion proof |
| Port connectors | 1/4" NPT |

The heated pump flow rate is controlled with a variable frequency drive (VFD). The VFD is used to control the pump motor speed by adjusting the input frequency. The

VFD used in this application is a Baldor® Electric ABB Microdrive, model # ACS-250-01U-02A3-1. It can be seen in Figure C.1 mounted on the front lower half of the FTIR server rack. Figure C.2 presents the rear view of the FTIR cabinet; the sample pump and filter are visible.

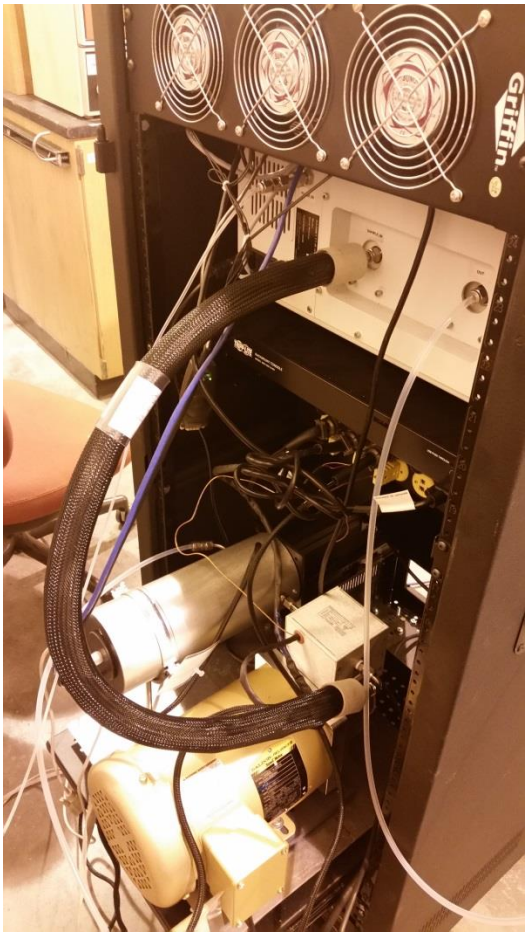

**Figure C.2: FTIR in server rack from rear. The heated filter is the silver cylinder in the back. This connects to the heated pump head, the silver box. The heated sample line is the black hose from the pump head to the FTIR.**

### C.2.5 FTIR $CO_2$ Calibration

On completion of construction, the inlet FTIR was configured to sample calibration gases. This was performed to verify a successful build of the FTIR system, and to collect sample spectra calibration purposes. Calibration gases of 3.0, 6.0, 15.0, and 25.0 vol % $CO_2$ were used. The UT-SRP pilot plant has an existing calibration gas tubing system in place for testing the Vaisala® NDIR sensors that is adaptable for use with FTIR analysis. Table C.6 presents the calibration results for both the Southern FTIR and UT-SRP FTIR.

**Table C.6: Inlet and outlet UT-SRP FTIR calibration results**

| **Inlet (Southern)** | | | | |
|---|---|---|---|---|
| **Cal Gas** | Spectra | FTIR Value | Error | Error |
| ***Vol %*** | *#* | *Vol %* | *Abs* | *%* |
| **3.0** | #01660 | 2.908 | 0.092 | 3.07 |
| **6.0** | #01685 | 6.602 | -0.602 | 10.03 |
| **15.0** | #01716 | 15.66 | -0.66 | 4.40 |
| **25.0** | #01770 | 26.806 | -1.806 | 7.22 |
| **Outlet (UT-SRP)** | | | | |
| **Cal Gas** | Spectra | FTIR Value | Error | Error |
| ***Vol %*** | *#* | *Vol %* | *Abs* | *%* |
| **3.0** | #32930 | 2.88 | 0.12 | 4.00 |
| **6.0** | #32956 | 6.213 | -0.213 | 3.55 |
| **15.0** | #32970 | 15.585 | -0.585 | 3.90 |
| **25.0** | #33000 | 26.022 | -1.022 | 4.09 |

The inlet FTIR performed adequately, with a maximum error of 10%. This error is due to the use of the UT-SRP calibration reference files, which are transferable. The calibration references were updated for both FTIRs upon the completion of this test.

## C.3 FTIR SAMPLING SYSTEM

The existing FTIR sampling system was overhauled in preparation for the April 2017 campaign. Adding an extra bed of packing in the absorber column required a lowering of the existing column sump and the addition of a column spool piece at the top. This shifted the existing inlet FTIR sample location down several feet, and raised the outlet sampling location up approximately 10 feet. Two additional FTIR sampling locations were added for absorber performance characterization and to aid in aerosol tests. These sample locations are between the first and second stage of the absorber, and between the second and third stage. The fifth and final FTIR sampling location at the knockout drum outlet remained unchanged from the March 2015 campaign.

### C.3.1 Sample Probes

The FTIR sample is extracted using Universal Analyzer, Inc. Model 277S heated probes. Each probe contains a heated filter to knock out entrained liquids and particulates. Table C.7 presents the technical specifications of these probes.

**Table C.7: Universal Analyzers, Inc. Model 277S Heated Probe Technical Specifics**

| Parameter | Value/Description |
|---|---|
| *Operating Specifications* | |
| Sample flow rate | 0–20 L/min. (0.7 CFM) |
| Calibration gas requirement | Sample flow rate plus 10% |
| Operating pressure drop at 10 L/min. | 12” water column (3.0 kPa) |
| Maximum stack gas temperature | 700 ºF (371 ºC) |
| Oven and vaporizer temperature | 350 ºF (176 ºC) |
| Dimensions | 9” x 9” x 10” (230 mm x 230 mm x 250 mm) |
| Weight | 20 lb. (9.1 kg) |
| Input power requirement | 350 W (Custom) |
| Input voltage requirement | 115 VAC, 50/60 Hz |

| | |
|---|---|
| *Material Specifications* | |
| Filter chamber heater type | Rod heaters in aluminum tube, PID controlled |
| Filter chamber material | 316SS |
| Filter element type | Ceramic 2µm (Standard Option) |
| Chamber material | 316SS |

Figures C.3 through C.7 show the FTIR probes installed at the sampling locations.


**Figure C.3: FTIR Sample probe at absorber inlet**

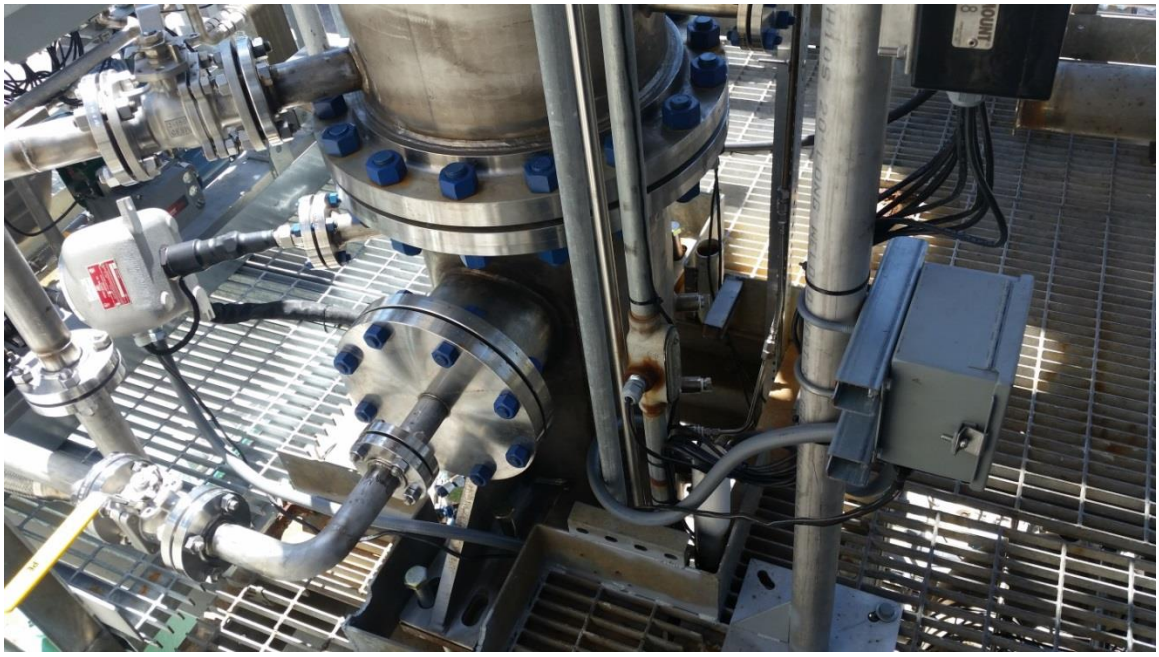

**Figure C.4: FTIR sample probe between first and second stages of absorber. The box on the right contains terminal junctions for the FTIR probe and heated pad**

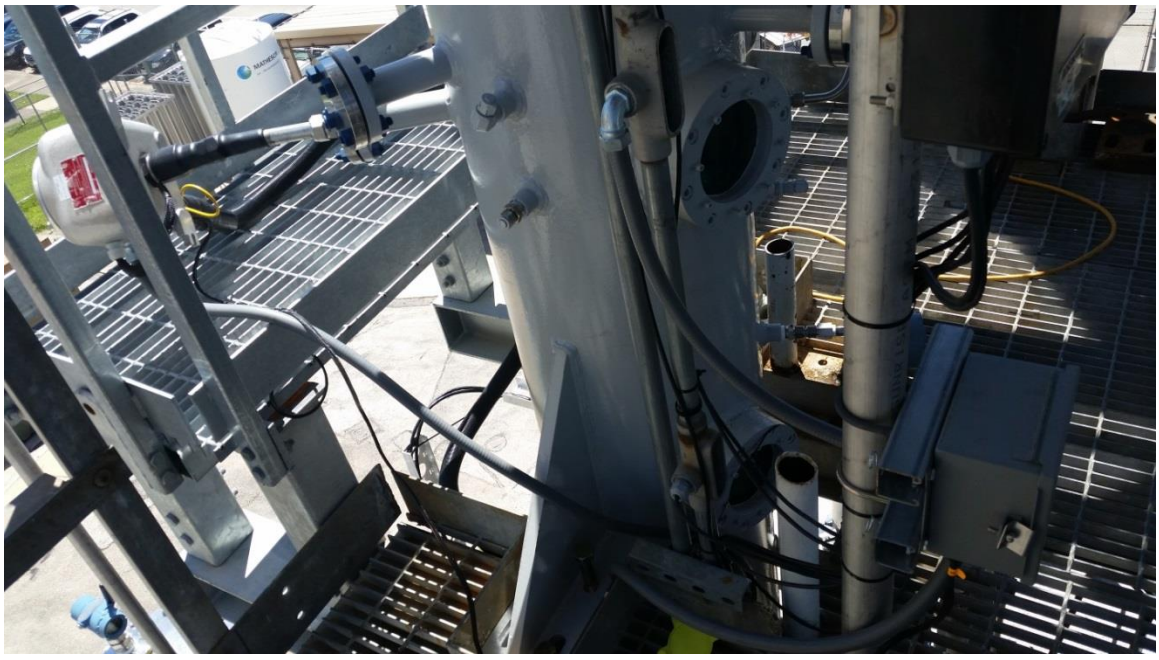

**Figure C.5: FTIR sample probe between second and third stages of absorber. The box on the right contains terminal junctions for the FTIR probe and heated pad**

**Figure C.6: FTIR sample probe at the absorber outlet. The box at the bottom of the picture contains terminal junctions for the FTIR probe and heated pad**

**Figure C.7: FTIR sample probe at the knockout drum outlet**

### C.3.2 Heated Pads

Heated pads are used to maintain the 180 °C temperature across the connection between the FTIR probe and the sample line. Cleanair® SKU 1233 heated pads are used at this plant. Table C.8 presents the specifications for the heated pads.

**Table C.8: CleanAir ® SKU Heated Blanket Technical Specifics**

| Parameter | Value/Description |
|---|---|
| Max. Operating Temperature | 400 ºF |
| Ambient Temperature | 0 ºF |
| Heat Output | 42.7 W |
| Operating Voltage | 120 VAC |
| Measured Resistance | 337.1 Ω |
| Latch Mechanism | Velcro® Release |
| Dimensions (Open) | 4" x 3" x 1" (L x W x H) |
| Dimensions (Closed) | 4" x 6" x 1/2" (L x W x H) |

The electrical wires from the heated probes and heated pads are wired to breakout terminal boxes by the use of Liquidtight weatherproof conduit. Shielded thermocouple wiring is also distributed through these boxes. The breakout boxes connect to the existing conduit system at the plant. This conduit was used to run power and thermocouple lines to the Level 2 CHARMS box, which connects to the pilot plant's DeltaV™ control system for PID control of the pad and probe temperatures. The wiring in the Level 2 CHARMS box is presented in Figure C.8.

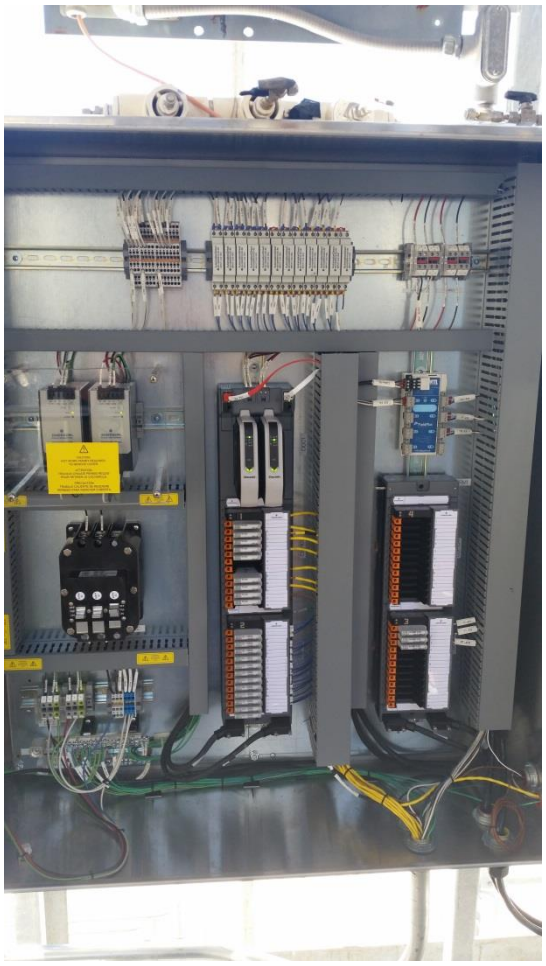

**Figure C.8: Level 2 CHARMS box for heated pad and probe temperature control. Thermocouple and power wires enter through the conduit at the bottom.**

### C.3.3 Heated Sample Line Supports

Once extracted by the probe, the sampled process gas is passed to the heated sample lines. The sample lines were affixed to existing structures in the pilot plant during the March 2015 campaign. For the April 2017 campaign, lightweight aluminum cable trays were procured to support the sample lines in both vertical and horizontal runs.

Figures C.9 through 13 show the cable tray sample line support system at various locations in the unit.

**Figure C.9: Heated FTIR sample lines and supporting cable tray for absorber knockout drum and second/third stage sample locations**

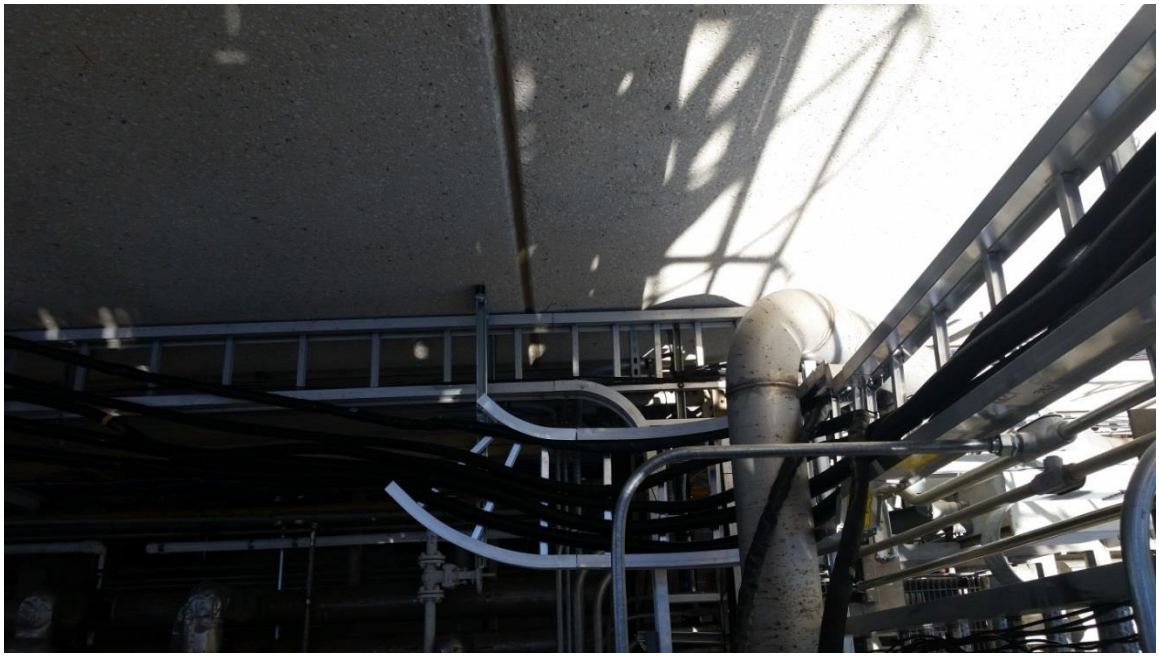

**Figure C.10: Beginning of vertical run for cable tray. The two lines heading to the bottom of the picture are for the absorber inlet and first/second stage sample points**

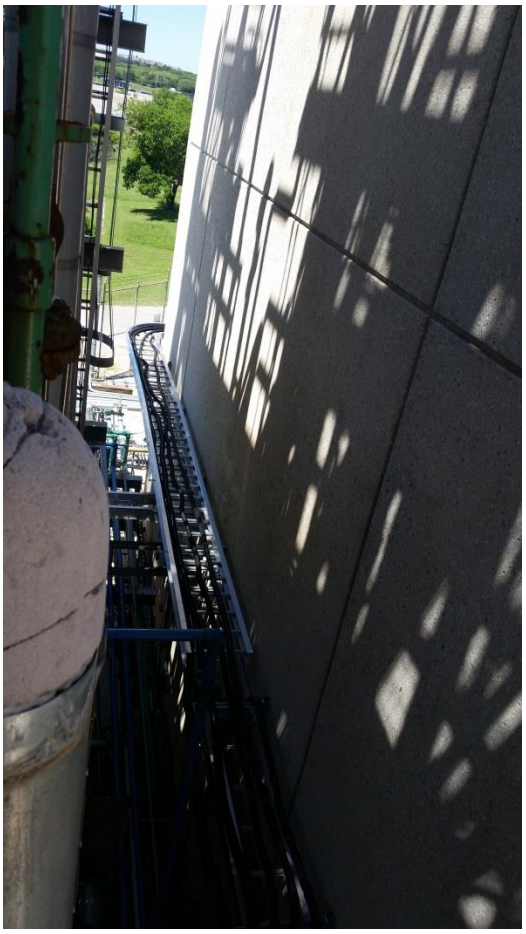

**Figure C.11: Horizontal cable tray support for heated FTIR sample lines along south wall of CEER building**

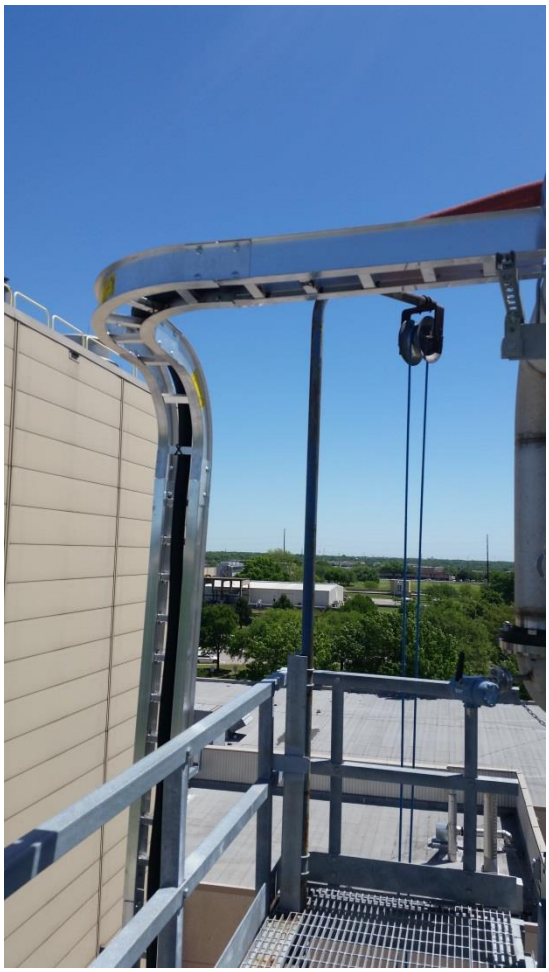

**Figure C.12: Cable tray support and heated FTIR sample line for absorber outlet**

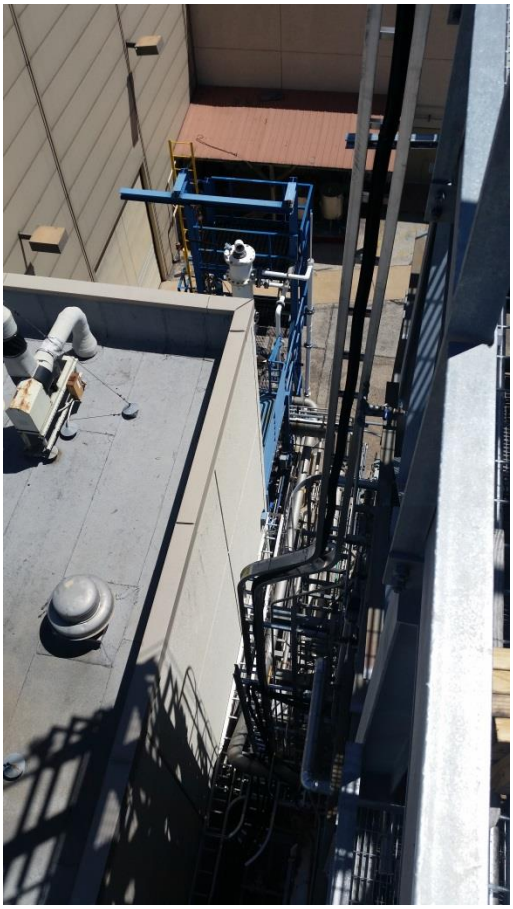

**Figure C.13: Cable tray support for heated FTIR sample line from absorber outlet.**

Four of the heated sample lines terminate at the MSSH, (multi-point heated sample switching system): the absorber first/second stage, absorber second/third stage, absorber outlet, and knockout drum outlet. The configuration and operation of the MSSH has been outlined in Chapter 2 of this work. An eductor in the MSSH ensures that flow is maintained across all sample lines, regardless of which line is sent to the FTIR for sampling. The MSSH temperature and stream selection is specified from the control room via the DeltaV™ control scheme. Figure C.14 shows the cable tray support for the sample lines, and the lines terminating at the MSSH.

**Figure C.14: Cable tray support and heated lines at termination at the MSSH**

A single sample line from the MSSH is fed through the wall to the FTIR sampling system. Suction on this line is maintained by the FTIR system pump.

## C.4 FTIR-DeltaV™ Communications

The most significant issue faced with this FTIR system upgrade concerned the communications between the DeltaV™ control system and the FTIR instrumentation. These communications were necessary for multiple reasons. First, it was vital for data consolidation to integrate the FTIR readings into the DeltaV™ data log. This ensures that all the collected process data is processed in a single spreadsheet and reduces

potential transcription errors. The Delta V™ – FTIR communications link was important due to the use of the Inlet FTIR for controlling the inlet $CO_2$ concentration. The UT-SRP pilot plant previously used Vaisala CARBOCAP® Carbon Dioxide Transmitter Series GMT220 silicon-based NDIR sensors to measure the $CO_2$ concentrations at the absorber inlet and knockout drum outlet. These have an upper detection limit of 20 vol % $CO_2$; during the April 2017 UT-SRP campaign, the inlet $CO_2$ concentration was varied to up to 25 vol %. Thus, FTIR integration with the DeltaV™ control system was necessary for pilot plant operations.

The goal of this section is to outline the steps that are necessary to enable communications between the FTIR system and DeltaV™. This is an expansion of the work by Fulk (2016).

### C.4.1 FTIR to CPU Communications

The Gasmet™ CX-4000 FTIR Analyzer communicates with the controlling CPU via a RS-232 serial cable. A USB to Serial adapter was procured to aid in this connection. It is important to note that not all USB to Serial adapters have the same pin configuration; the adapter that worked was purchased from Staples.

Once the physical connection is made, the analytical software must be configured. Open the Gasmet™ software, and open the "Configuration' option under 'Tools' in the menu bar. The analyzer-to-CPU communications are configured under the 'Analyzer' tab. Calcmet™ uses a Baud rate of 57600 and a 24-bit Data Format. The Serial port can be found through trial and error; select a port, save the configuration settings, restart

Calcmet™, and then select ‘Hardware Status’ under the “View” menu bar icon. A passing ‘Hardware Status’ window is presented in Figure C.16.

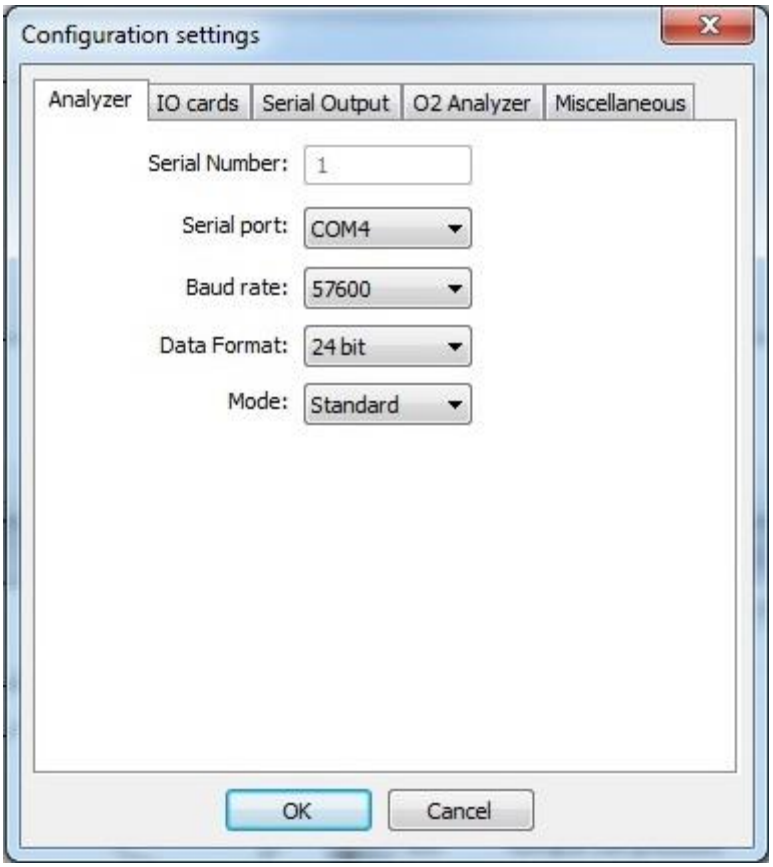


**Figure C.15: Configuration for CX-4000 to CPU Communications**

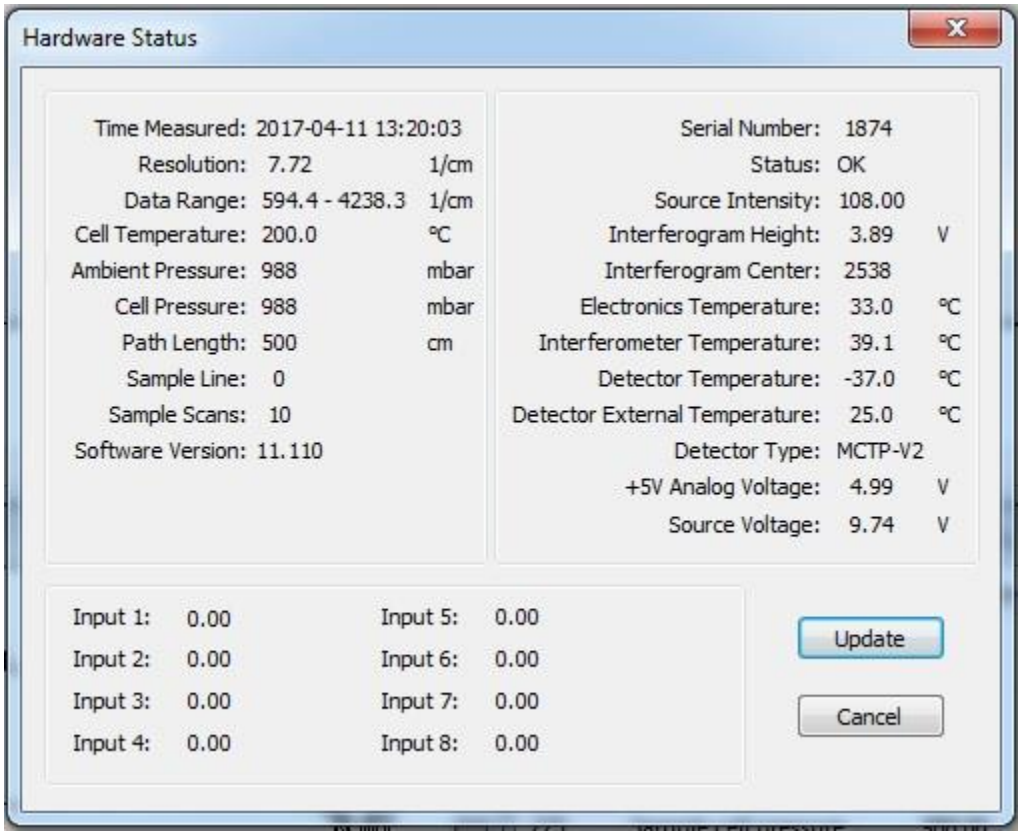


**Figure C.16: Hardware Status window for Calcmet™. If this appears after inputting the configuration settings, communications are effectively enabled between the CX-4000 and Calcmet™.**

### C.4.2 FTIR-DeltaV™ Serial Cable Connection

A 9-pin serial cable is used to physically connect the FTIR to DeltaV™. This is an RS-232 cable, and uses the Modbus serial communications protocol. A male DB9 connector is used on the FTIR end, and stripped and ferruled wires at the DeltaV™ terminal. Figure C.17 presents the serial cable wire crossover configuration, while Figure C.18 shows the wiring configuration at the DeltaV™ terminal.

| FTIR RS-232 DB-9 Cable | | | DeltaV™ S-Series Terminal Block | |
|---|---|---|---|---|
| **Circuit** | **Pin #** | | **Pin #** | **Circuit** |
| Shield | 1 | | 1 | Ground (GND) |
| Receive Data (RXD) | 2 | | 2 | -- |
| Transmit Data (TXD) | 3 | | 3 | Transmit Data (TXD) |
| Data Terminal Ready (DTR) | 4 | | 4 | -- |
| Ground (GND) | 5 | | 5 | Receive Data (RXD) |
| Data Set Ready (DSR) | 6 | | 6 | -- |
| Request to Send (RTS) | 7 | | 7 | Data Terminal Ready (DTR) |
| Clear to Send (CTS) | 8 | | 8 | Data Set Ready (DSR) |

**Figure C.17: RS-232 Terminal Block Crossover Configuration for FTIR to DeltaV™ Serial Communications Cable (Fulk, 2016)**

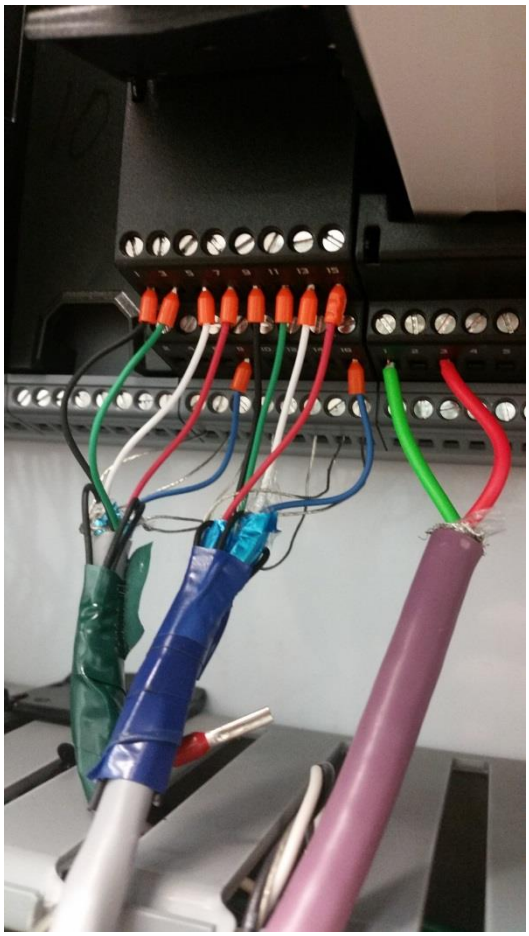

**Figure C.18: RS-232 Terminal Block Pin Connections for FTIR to DeltaV™ Serial Communications Cable, at the DeltaV™ Terminal. The wire with the green tape is for the outlet FTIR, while the blue-taped wire is for the inlet.**

### C.4.3 Configuring Calcmet™

The FTIR output settings must be properly configured to enable communications with DeltaV™. Modbus operates by storing data in registries that are assigned contents by the user; for the FTIR controller card, data registry starts at 30001. This must be assigned through Calcmet™; while in the Calcmet™ interface, access the 'Analysis

Settings' under the 'Edit' menu bar. Figure C.19 presents the Modbus tab under the 'Analysis Settings' window.

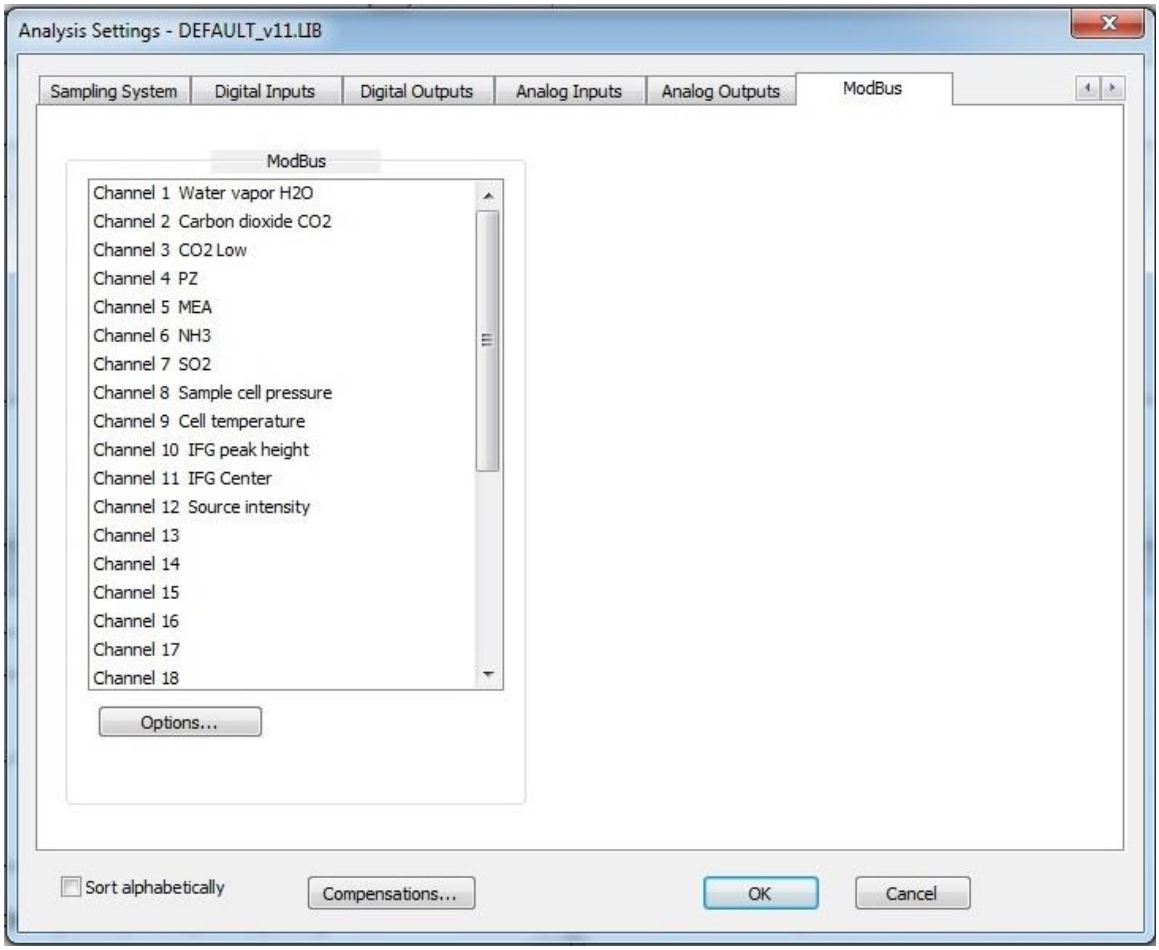


**Figure C.19: Modbus configuration under Calcmet ™ Analysis Settings. To select a component or parameter to link to a channel, highlight the Modbus channel and click 'Options'**

Next, the serial output must be configured. This can be performed by opening the 'Tools' menu bar icon and selecting 'Configuration.' This time, select the 'Serial Output' tab. The proper configuration settings are presented in Figure C.20.

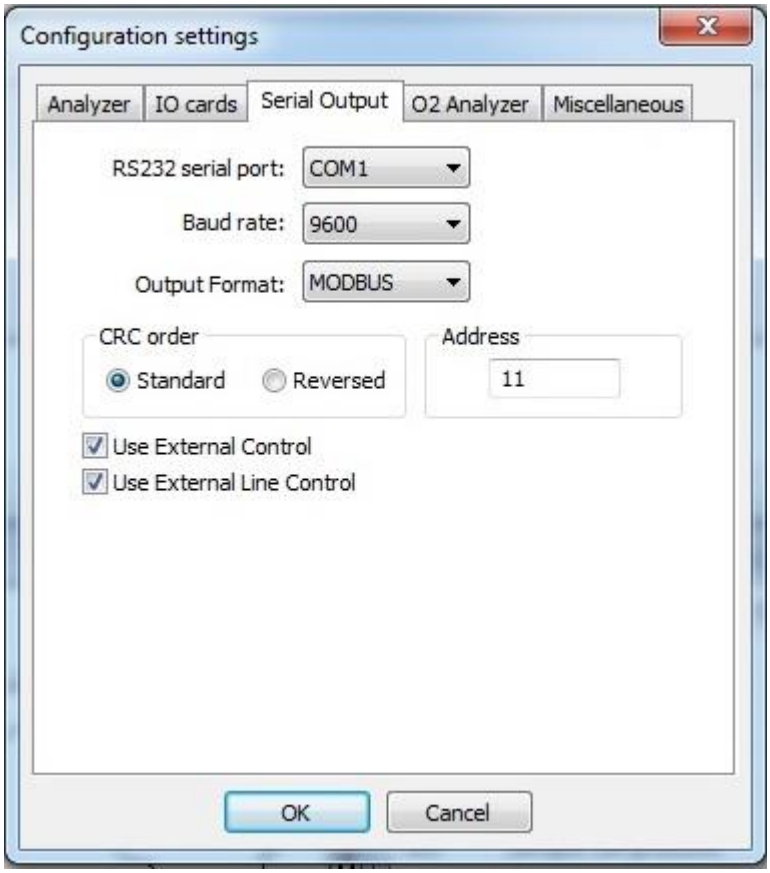


**Figure C.20: Configuration for Gasmet™ to DeltaV™ Serial Communications**

COM1 must be selected for the RS-232 serial port because legacy COM1 is used, which utilizes IRQ4 and address 03F8. Under Windows Device Manager, all other communications devices (USB and Serial) must be configured to not use COM1, IRQ4, or address 03F8. These settings can be found for each communication port by right-clicking a port in Device Manager and selecting 'Properties'. From there, the communications port number can be changed through the 'Port Settings' tab and the IRQ and address changed through the "Resources' tab, as presented in Figure C.21.

For the Calcmet™ to DeltaV™ communications, the Baud rate is set at 9600, with an Output format of Modbus. CRC order is standard and DeltaV™ is configured to

recognize the address as 11. Ensure that 'Use External Control' and 'Use External Line Control' are also selected.

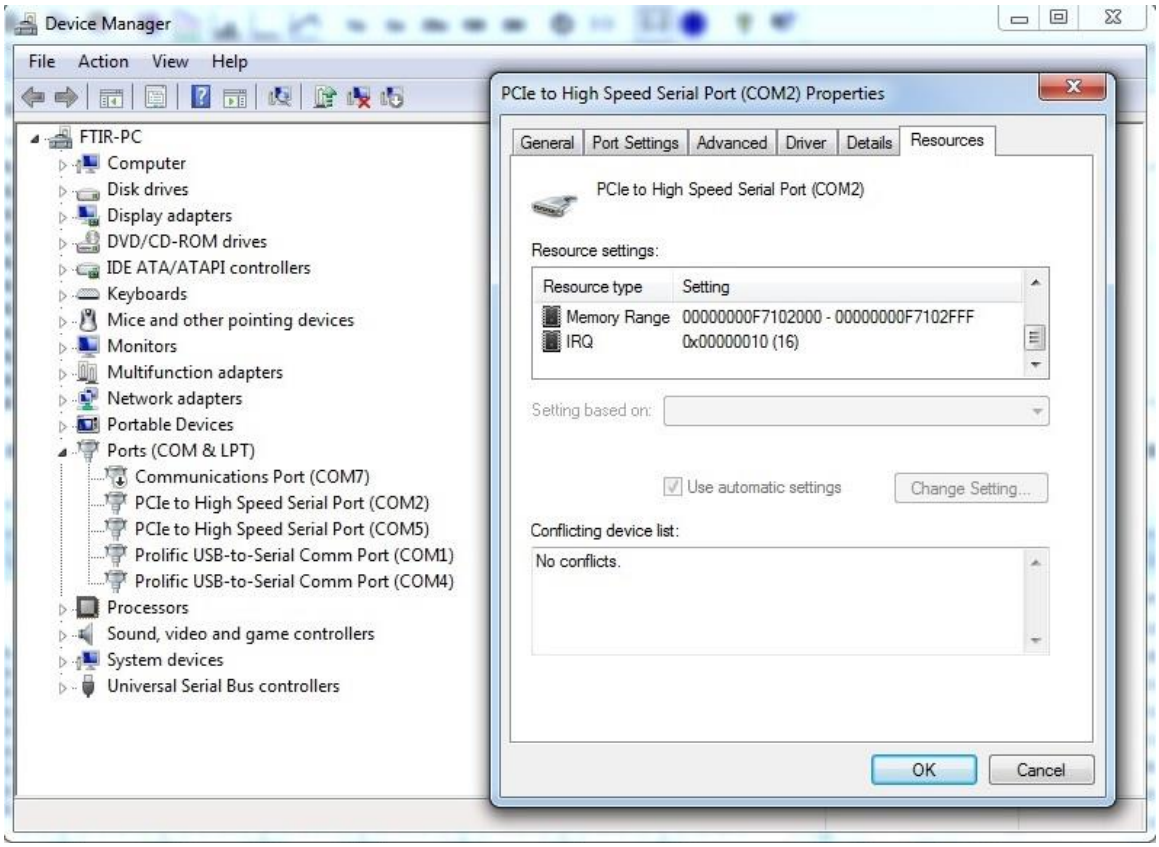


**Figure C.21: Device manager configuration for communications ports**

The COM1 port should be configured next. This can be accessed through Windows Device Manager and right clicking on 'COM1' under 'Ports'. Select properties, and then open the 'Port Settings' tab. The 'Bits per second' (Or Baud rate) is 9600, 'Data bits' is 8, 'Parity' is None, 'Stop bits' is 1, and None is selected under 'Flow Control'. This window is presented in Figure C.22.

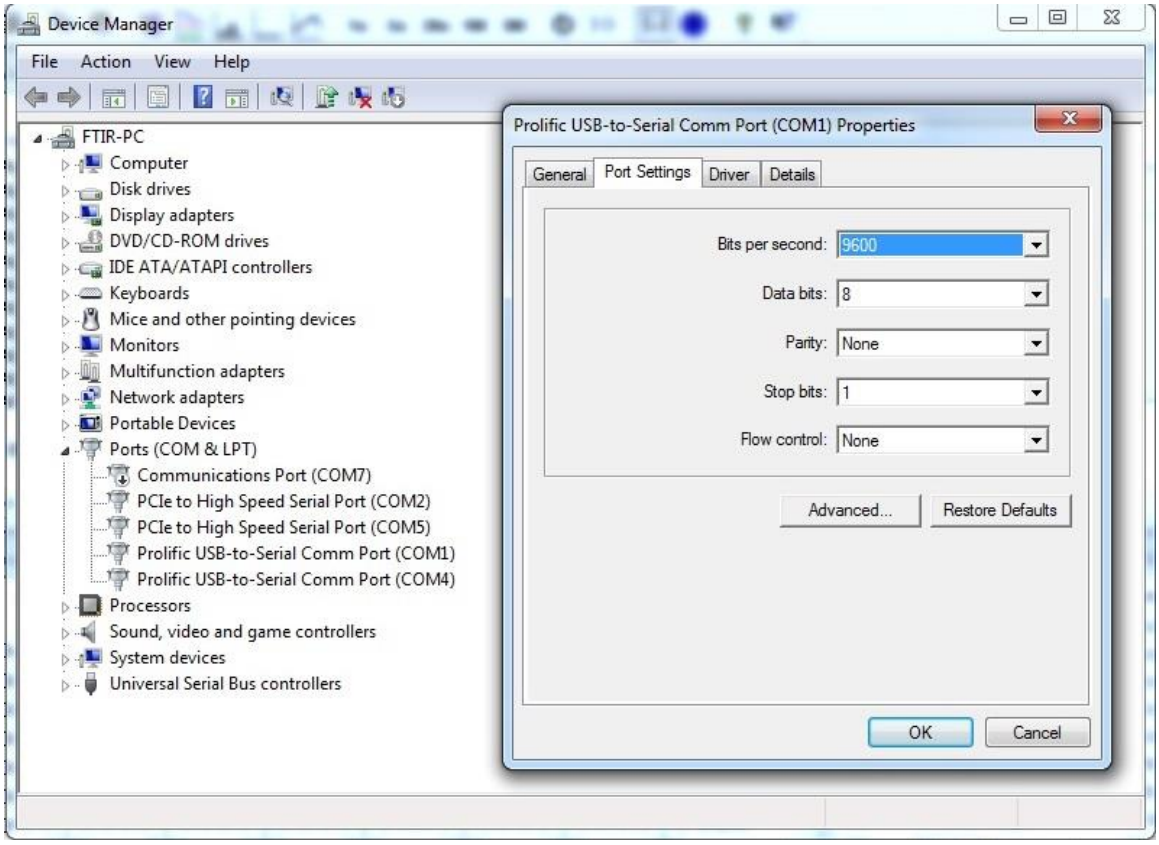


**Figure C.22: Configuration for COM1 port**

Finally, the result output from Calcmet™ can be configured. In the Calcmet™ software, select 'Options' in the menu bar. Click on 'Results Output' to open up the configuration window, as presented in Figure C.23.

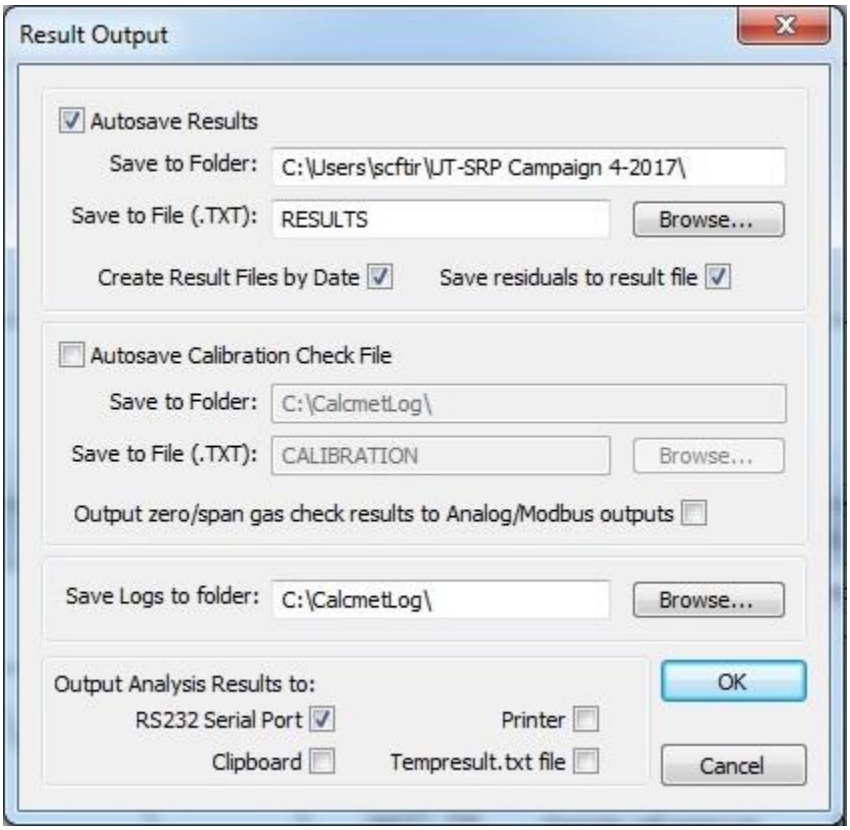


**Figure C.23: Gasmet™ Result Output Configuration Window**

Specify a folder to autosave results files to; it is best to create a new folder for each sampling campaign. Calibration check files do not need to be autosaved. On the bottom of the window, ensure that 'RS232 Serial Port' is selected for 'Output Analysis Results to:'.

### C.4.4 Configuring DeltaV™ for FTIR Communications

DeltaV™ must be properly configured before communications with the FTIR analyzer. The configuration settings can be accessed through the 'FTIR Modbus Calculation Block' in DeltaV™, as presented in Figure C.24.

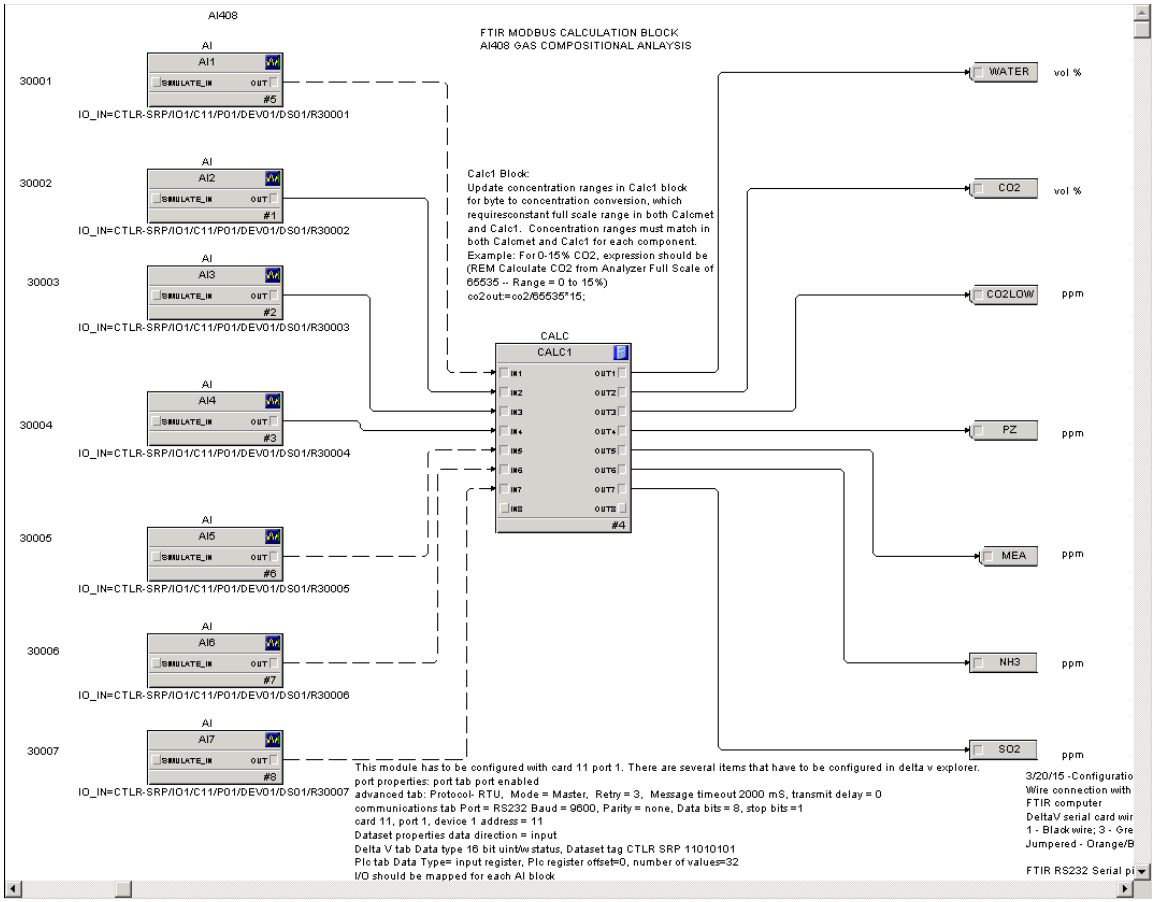


**Figure C.24: FTIR Modbus Calculation Block I/O Diagram in DeltaV™ (Fulk, 2016).**

This module is configured to Card 11, Port 1; as mentioned previously, FTIR output registries begin at address 30001, corresponding to the Modbus output channel in Calcmet™. The values received from the FTIR analyzer are converted to concentration numbers in the CALC1 block in the center of Figure C.24.

The digital output from the FTIR is a two-byte output from the FTIR registry. This limits the significant figures that can be read by DeltaV™. A way around this limitation is to transmit the data as a percentage of the maximum of the specified

measurement range of the FTIR. The measurement range is set by double clicking the 'Ranges' bar for a component in the 'Analysis Results' window in Calcmet™. It is important to note that the ranges for each component must match in Calcmet™ and DeltaV™.

The following tabulation is the code for the CALC1 block in DeltaV™ (Fulk, 2016):

```
CALC1
REM INPUT
water:=in1;
co2:=in2;
co2low:=in3;
pz:=in4;
mea:=in5;
nh3:=in6;
so2:=in7;
REM CALCULATIONS
REM Calculate Water from Analyzer Full Scale of 65535 -- Range = 0 to 30%
waterout:=water/65535*30;
REM Calculate CO2 from Analyzer Full Scale of 65535 -- Range = 0 to 15%
co2out:=co2/65535*15;
REM Calculate CO2low from Analyzer Full Scale of 65535 -- Range 0 to 500ppm
co2lowout:=co2low/65535*500;
```

REM Calculate PZ from Analyzer Full Scale of 65535 -- Range = 0 to 100ppm

pzout:=pz/65535*100;

REM Calculate MEA from Analyzer Full Scale of 65535 -- Range = 0 to 100ppm

meaout:=mea/65535*100;

REM Calculate NH3 from Analyzer Full Scale of 65535 -- Range = 0 to 20ppm

nh3out:=nh3/65535*20;

REM Calculate SO2 from Analyzer Full Scale of 65535 -- Range 0 to 50 ppm

so2out:=so2/65535*50;

REM OUTPUT

out1:=waterout; out2:=co2out;

out3:=co2lowout;

out4:=pzout; out5:=meaout; out6:=nh3out; out7:=so2out;

# APPENDIX D: AEROSOL GROWTH COLUMN STANDARD OPERATING PROCEDURES

This appendix gives an in-depth description of the Aerosol Growth Column and the components used in construction. Further details are provided in the dissertation by Fulk (2016). A standard operating procedure for aerosol tests is subsequently presented. Instructions for changing the solvent inventory and determining solvent composition are then provided.

## D.1 BACKGROUND

### D.1.1 AGC Construction

The AGC is designed as a batch process in order to simplify operations and the control scheme. A stripping section is not involved in the process; while this allows for ease of operation, the solvent in the system cannot be regenerated and eventually becomes saturated with $CO_2$. This requires the changing of the amine solvent for each day's experiment.

Figure 4.1 presents a process flow diagram of the AGC. Synthetic flue gas is fed to a presaturator, which humidifies and heats the gas to a set temperature. The humid gas is fed to the bottom of the absorber column, where the amine solvent countercurrently contacts the gas and absorbs the $CO_2$. Outlet flue gas passes through a shell and tube condenser to knock out condensable components, and is then vented to the fume hood.

Figure D.1 gives a flow diagram of the AGC apparatus.

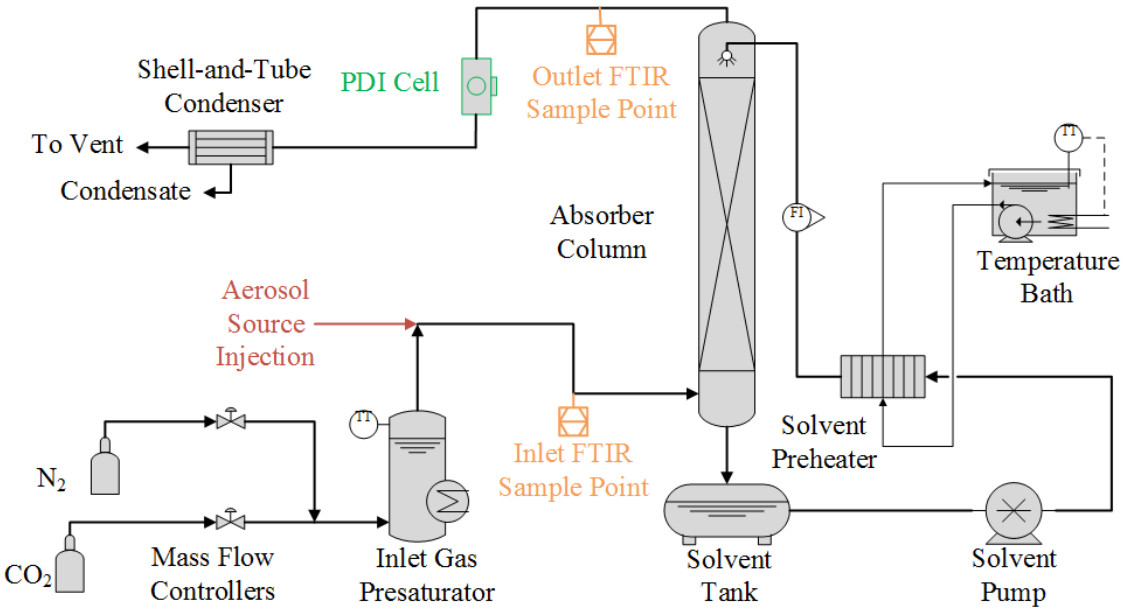


**Figure D.1: Aerosol Growth Column flow diagram**

The synthetic flue gas is bubbled through a presaturator to humidify and heat the gas. The presaturator is constructed from 6" 304SS Schedule 10 pipe with 150# flanges. The water temperature is controlled with a screw-plug immersion heater and a temperature controller. Head space temperature is recorded in LabVIEW™ with a K-type thermocouple. Gas sparging inside the presaturator occurs through a 3/8" straight tube with several small holes. Upon exiting the presaturator, the humid flue gas is mixed with the aerosol nuclei and then introduced at a flanged tee at the bottom of the absorber column. Water depth in the presaturator is maintained at 12-15".

The absorber column is built from a 1-1/2" 304SS Schedule 10 pipe with #150 flanged end connections. Random packing was selected for the absorber column. Small scale laboratory packing have a high density that would result in unwanted aerosol capture and not provide representative bench scale results. Therefore, a smaller surface-

area packing (RSR0.3) was selected. Packing support is provided by removable Swagelok tube fitting lugs and a mesh screen. 6 feet of packing is used in the column; this scales well with full sized $CO_2$ absorber columns to give a representative approximate $CO_2$ removal performance, and this provides equivalent residence time for aerosol growth.

The temperature profile in the absorber column is measured by six K-type thermocouples inserted equidistant across the packing height. Anther K-type thermocouple measures the gas temperature at the absorber outlet. Temperatures are logged in LabVIEW™. The column is insulated with R6.3 aluminum-clad, elastomeric insulation. Pressure drop across the packing is measured by a manometer connected to the gas inlet and outlet lines.

A countercurrent shell and tube condenser is used to control the condensation of the saturated gas leaving the absorber. The condenser is constructed from ½" SS tubing and 1" piping. Swagelok fittings with graphite ferrules enable disassembly of the condenser if necessary. Chilled water from the CEER building at 10 °C is fed through the tube side of the exchanger.

### D.1.2 Gas Flows

Nitrogen for the AGC is taken from an outdoor dewar. A manifold at the AGC fume hood splits $N_2$ supply into four streams: absorber gas supply, the FTIR purge and background supply, the $SO_3$ generator purge, and the PDI window purge. Flow to the absorber is controlled by an analog 100 SLPM Brooks 5851 I-Series mass flow controller

(MFC). Inlet pressure to the MFC is regulated to 40 psig. The MFC is controllable through the LabVIEW™ software.

$CO_2$ for the AGC can be obtained from two sources: gas cylinders or the UT-SRP $CO_2$ storage tank. An overhead line supplies $CO_2$ from the storage tank into the AGC fume hood. A leg off this line in an adjacent lab can be connected to a regulator on a $CO_2$ gas cylinder. Pressure off the cylinder is regulated to 50 psig with a Y11-N245D320, CGA320 regulator. Care must be taken when conducting experiments while using bone dry $CO_2$ through this regulator, as it is subject to freezing closed and stopping flow. A heat gun can be used to unthaw the regulator; however, it is easier to use $CO_2$ from the UT-SRP storage tank if available. The gas flow rate to the AGC is regulated by a 15 SLPM Brooks 5850 I-Series MFC, and can be controlled through LabVIEW™.

### D.1.3 Solvent Flows

The solvent inventory is stored in a 16 gallon SS tight-head drum (The Cary Company 26B6SS). Solvent is drawn from the pump by a Micropump® A-mount suction pump head controlled by a Cole Parmer Console Drive. The solvent flow rate is measured by a rotameter (Omega FL46302). The pump discharge uses a pressure relief valve, set at 50 psig, to protect against failure by clogged flow.

A cross exchanger with recirculated water is used to control the solvent temperature. The cross exchanger is a Thermal Transfer Systems AN14-20H plate and frame exchanger. Solvent from the exchanger is fed to the column packing by hollow cone spray nozzles (Kyser and Associates 1/4A-316SS2 and 1/4A-316SS-5). Solvent

temperature is measured prior to this point with a K-type thermocouple and recorded in LabVIEW™.

### D.1.4 Control System

The AGC is controlled by an application developed in LabVIEW™. The front panel of the application has controls for the $N_2$ and $CO_2$ flow set points. The temperatures at each point in the process are also displayed here. Data is exported to an Excel spreadsheet; the sheet file name is specified by the user upon starting the application. Further explanation of the control scheme and associated wiring diagram can be found in the dissertation by Fulk (2016).

### D.1.5 Solvent Sampling

Two solvent sample ports are available; one on the suction side of the solvent pump, and another immediately downstream of the solvent loop rotameter. Both are identical and are constructed from a 3/8" Swagelok® tee with a 12.7 mm OD RESTEK® BTO Septa. Liquid samples are drawn with 3 mL syringes and transferred to amber vials for analysis. Section D.3.2 of this appendix provides details on the instrumentation and analytical techniques used for determining the solvent composition.

## D.2 ACG Standard Operating Procedure

The following section outlines the steps to follow for AGC experiments. The AGC LabVIEW™ laptop, FTIR analyzer computer, and PDI system computer should be synced to the same time, down to the second if possible. This will prove beneficial during data analysis at the completion of an experiment.

### D.2.1 Safety

There are a number of safety concerns while operating the AGC system. Proper PPE, including safety glasses, closed-toe shoes, and nitrile gloves should be worn at all times. During solvent sample extraction and amine solvent inventory changes, lab coats should be worn. When switching the FTIR sampling locations via the heated stream switching box, leather welding gloves should be worn for thermal protection. If $CO_2$ from the UT-SRP tank is being used in the experiment, hard hats should be worn outside when opening and closing valves to that part of the system.

The $SO_3$ generator poses a burn risk at multiple locations. Caution should be maintained when working and moving around the generator. There is a risk of gas leakage from the $SO_3$ generator system as the system thermally expands. Due to this risk, the supplied face shield and respirator unit (Advantage™ 3000 Respirator, ZORO G3258857) must be worn when entering the fume hood. The exhaust vent to the $SO_2$/Air gas cabinet should be on at all times.

The PDI lasers must only be activated when the transmitter/receiver unit is mated with the sample cell. Polarized safety glasses are to be worn when there is a risk of contact with the lasers.

### D.2.2 FTIR Preparation

If frequent experiments are occurring, the FTIR analyzer cabinet can remain on with $N_2$ flowing through the sample cell. In the event that the FTIR analyzer was turned off, ensure that the $N_2$ purge has established flow with a pressure at 7-8 psig. If this is not the case, the FTIR will need to be allowed to purge for 24 hours prior to operation.

The FTIR outlet line should be connected to the fume hood with the supplied line. Ensure all connections in the FTIR sample system are wrapped in insulation. The FTIR heated elements can be turned on by flicking the switches to the controllers in the ammo box units. The controllers are set to 180 °C, and control the temperatures in the two heated sample lines and the heated stream switching box. Keep the sample valves closed, with $N_2$ flow to the FTIR. The system takes approximately one hour to fully heat. Figure D.2 presents the interior of the sample switching box. The valve handles are located at the top of the box.

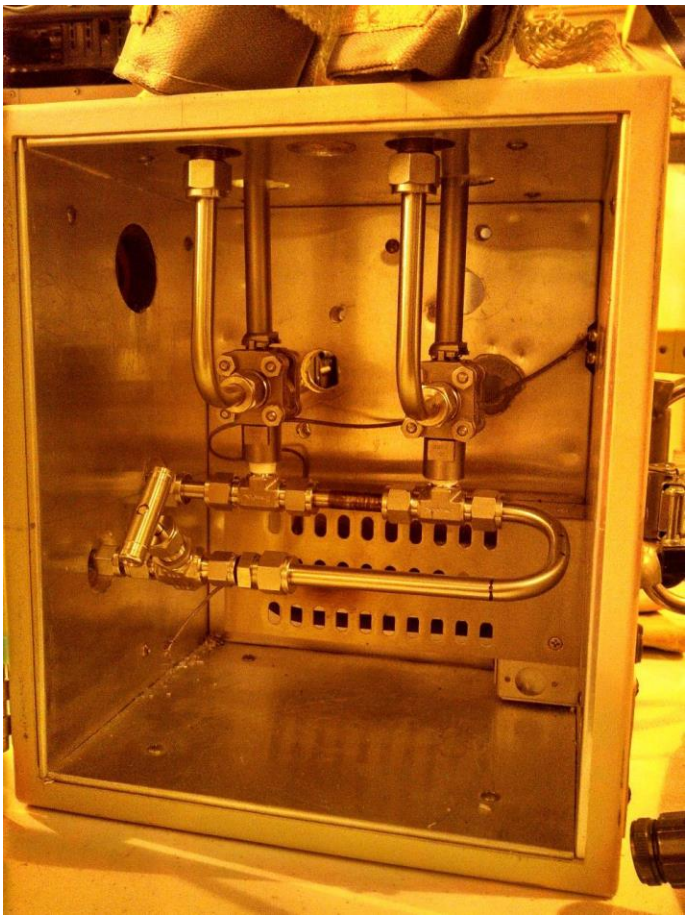

**Figure D.2: Heated sample switching box. Heated sample lines connect at the top of the box. Flow is selected through the 3-way valves and fed to the FTIR pump.**

Once the FTIR analyzer and cabinet components are sufficiently heated to 180 °C, the FTIR status can be checked. This is performed in Calcmet™ by going to the menu bar, selecting "View" and "Hardware Status". Ensure that the sample cell is at 180 ° C (+/- 2° C), and that the sample cell pressure is less than 1100 mbar but greater than the ambient pressure. If the FTIR sample cell is sufficiently heated and has been under $N_2$ flow, a background scan can be performed. Take a few samples and observe the residual until it stops changing. Under "Options" select "Measuring times", and change the sample run time to "5 minutes". Click ok, then repeat this step; a bug in Calcmet™ occasionally ignores this change. Under "Measure", select "Background"; the background scan is now running and will take 12-15 minutes to complete. Once the background scan is complete, view the spectra at the bottom left corner of the Calcmet™ screen. It should be a slope with a relatively unperturbed line between 1800 to 3000 $cm^{-1}$. A pair of peaks around 2400 $cm^{-1}$ indicate the presence of $CO_2$. $H_2O$ will generate peaks around 1500 and 3500 $cm^{-1}$. Amine solvent will show up around 3000-3400 $cm^{-1}$.

If the background looks adequate, go to "Options" and select "Measuring times". Change the scan length from 5 minutes to 20 seconds. Repeat this step to confirm Calcmet™ acknowledged the scan length change. Begin continuous measurement. This can be accomplished by selecting "Measure" in the menu bar and clicking "Continuous". Another method is to click the circle with the arrow icon on the menu bar.

### D.2.3 Electrical Connections

Connect the USB cable from the AGC control enclosure to the LabVIEW™ laptop outside the fume hood. Ensure that the temperature bath and immersion heater are plugged in to the 30A 240V receptacles on the south wall. Turn on power to the AGC control enclosure and put the presaturator heater in standby. This is accomplished by hitting the return key (far right) twice, until the temperature controller reads "stby" in green. Never turn on heaters without flow established.

Open the LabVIEW™ interface on the laptop, and select "AGC PFD V2". The LabVIEW™ application will open. Do not remove the SD USB storage stick from the laptop; it unlocks the encryption on the laptop hard drive.

### D.2.4 AGC Gas Preparations

Verify that the $N_2$ and $CO_2$ sources are open to the system. Open the plug valves at the outlet of the $N_2$ and $CO_2$ MFCs.

### D.2.5 Establishing Flows

On the LabVIEW™ application, under the "Operate" menu bar option, select "Run". LabVIEW™ will prompt you to name the save file. Once completed, LabVIEW™ will commence controlling and recording values in the unit. Set the $N_2$ flow rate through the MFC to 20 LPM. The presaturator heater can now be taken out of park; its default set point is 42 °C and can be varied as needed.

### D.2.6 $SO_3$ Generator Preparation

Turn on $N_2$ flow through the $SO_3$ generator catalyst bed; 100-200 mL/min is sufficient. Begin heating of the catalyst bed by switching on the tube furnace controller

with the top switch, and then the heating elements with the second switch. The system will heat up to 520 °C; this takes approximately 100 minutes.

### D.2.7 Condenser Flow

Open the bypass valve between the cooling water supply and return valves, located on the east wall at the north end of the room. Open the 4" cooling water return and supply valves. Slowly open the 1" return valve and then the 1" supply valve. Close the bypass valve. Cooling water flow can be confirmed by touching the lines or the accumulation of condensation on the condenser on the AGC.

### D.2.8 FTIR Sampling

Open the FTIR heated sample switching box inlet sample valve and turn off $N_2$ flow to the box. The FTIR should already be continuously sampling on 20 second scans. The FTIR will now begin measuring the AGC inlet, with $N_2$ flow from the LabVIEW™ and from the purge for the $SO_3$ generator heating up. Water will show up on the FTIR spectra as well, due to the presaturator. As the $SO_3$ generator heats up, $SO_2$ may begin to appear in FTIR spectra.

### D.2.9 Solvent Flow

Turn on the solvent flow pump and establish flow through the system. Flow can be adjusted by turning the speed dial. A flow rate of 0.8 lpm (0.2 gpm) is a sufficient starting point. Turn on the solvent temperature bath and begin heating the solvent. The heater defaults to 40 °C but the temperature can be varied via the bath control panel.

### D.2.10 PDI Preparation

Establish flow through the purge of the PDI sample cell. Turn on the PDI analyzer in the following order: Power bar, power box, computer, ASA box, and oscilloscope. The computer monitor should turn on automatically. Open AIMS on the computer and ensure there are no errors on startup. If the AIMS error "No ASA detected" occurs, shut down the system and repeat startup, taking more time in between starting the computer and the ASA box. Ensure that the 4 signals (3 photodetectors and gate signal) appear on the oscilloscope.

Perform a phase calibration by selecting the "Device controls" left hand menu option and the "Phase Calibration" selection on the top menu. Observe the signals on the oscilloscope to ensure the presence of Doppler bursts and gate signals. Repeat the phase calibration and ensure that there are minimal changes in the phase differences. Turn on the PDI lasers with the key at the back of the transmitter/receiver unit.

### D.2.11 $CO_2$ Flow

Turn the $N_2$ flow rate up to the desired quantity through the LabVIEW™ application. Establish the desired $CO_2$ flow rate through the process as well. The AGC should now be operating with solvent and gas flows and heating, and FTIR sample analysis at the absorber inlet.

### D.2.12 $SO_3$ Generator Activation

Once the $SO_3$ generator furnace has reached 520 °C, $SO_2$/Air flow through the $SO_3$ generator can be activated. Open the valve at the $SO_2$/Air cylinder and the regulator outlet. The regulator is set to an outlet pressure of 10 psig. Turn the 3-way valve at the

back of the gas cylinder cabinet to $SO_2$/Air flow (Towards the gas cabinet). Set the $SO_2$/Air flow to the desired rate with the rotameter. 15 and 37.5 mL/min correspond to 20 and 50 ppm of $SO_3$, respectively, with 100 LPM of gas flowing through the AGC.

**D.2.13 PDI Measurements**

PDI measurements can now be collected at this time. Establish the run naming protocol under the "Data Library" tab in AIMS. Clicking the "Start" icon on the top left corner of AIMS will initiate a PDI sample run. The run will complete when 5 minutes have passed or 10,000 samples have been quantified, whichever occurs first.

**D.2.14 Changing Set Points**

The gas flow rates and compositions, solvent flow rate, gas and solvent temperatures, and $SO_3$ injection rate can all be changed. Allow 5-10 minutes for each set point to reach steady state. Changing temperatures can take up to 30 minutes to establish steady state. Ensure that steady FTIR inlet and outlet measurements, and PDI aerosol measurements, have been taken for each set point before changing to the next condition. Use the inlet FTIR measurements to confirm the $CO_2$ concentrations are relatively close to the flow set for the $CO_2$ MFC in LabVIEW™.

Solvent samples can be taken at each set run condition. The solvent can be extracted from either sample location. 3-6 mL is sufficient for each desired sample, and can be stored in labeled amber vials for future analysis.

**D.2.15 Shutting Down AGC**

Turn the $CO_2$ flow rate to 0 SLPM. Close the $SO_2$/Air cylinder and allow the pressure in the line to bleed to through the catalyst bed into the process. Close the

regulator valve and switch flow through the catalyst bed to $N_2$ at 100 mL/min. Turn off the heating and controller switches for the $SO_3$ generator furnace.

Turn off the solvent bath heater and the solvent flow rate. Put the presaturator heater back into "Park" by pressing the return key twice. Turn down $N_2$ flow through the AGC to 20 LPM with the LabVIEW™ application. Turn off the PDI lasers and shut down the PDI system. The $SO_3$ generator will take 1.5-2 hours to cool down. Once the temperature is below 200 °C, flow through the catalyst bed can be stopped and the LabVIEW™ application can stop $N_2$ flow. The AGC control enclosure in the fume hood can be switched off, and the LabVIEW™ computer can be shut down.

Turn off flow through the condenser by opening the bypass line, closing the 1" chilled water supply and return valves, and closing the 4" supply and return valves.

#### D.2.16 FTIR Flushing and Shutdown

Close both the inlet and outlet sample valves on the heated stream switching box, and open the $N_2$ needle valve to the box. Turn off power to the heated line and box controllers. Keep the FTIR analyzer sampling and ensure that the system is reading $N_2$ (minimal FTIR active components on spectrum). Turn off continuous sampling, and shut down FTIR system if necessary.

## D.3 Solvent Inventory and Composition Determination

### D.3.1 Changing Solvent Inventory

The Aerosol Growth Column was designed with the flexibility to use a variety of amine solvents. In this work, piperazine was used at varying concentrations. Future experiments are recommended to be performed with a variety of amine solvents.

The existing inventory in the AGC must be drained prior to adding new solvent. This is performed by disconnecting the 3/8" tubing from the pump outlet at the solvent heat exchanger inlet. This line is long enough to extend into a 5 gallon car boy container. Ensure that the red handled isolation valve from the inventory tank is open. The other red handled isolation valve for the open ended black 3/8" line must be closed.

Insert the 3/8" tubing from the pump outlet into the car boy, turn the pump on, and raise the flow rate. The inventory in the tank will begin flowing into the car boy. A total of 10 gallons of amine solvent is stored in the tank for each experiment; this will require the filling of two 5 gallon car boys. Watch the pump as it unloads the inventory tank to ensure that it doesn't run dry.

After draining the existing solvent inventory, the new amine solvent can be added to the tank. Reattach the outlet tubing between the solvent pump and the heat exchanger. Switch the positions of the two red handled valves; the valve at the outlet of the inventory tank should be closed, and the valve to the open ended black 3/8" line should be open. Insert the end of the black 3/8" line to the container holding the amine solvent to be added to the AGC. Turn on the solvent pump, and turn up the flow rate. This will pass the new solvent through the heat exchanger, the rotameter, and the column before entering the solvent tank. Ensure that the rotameter is reading a flow rate.

10 gallons of solvent should be added to the AGC. This provides enough solvent to give adequate time (3-4 hours, depending on amine and $CO_2$ concentration) to conduct aerosol experiments.

### D.3.2 Determination of Solvent Composition

Solvent analysis is performed in the adjacent lab. The solvent amine concentration and $CO_2$ loading are determined through titrations. A Thermo Scientific Orion Star 211 benchtop pH meter with a Thermo Scientific Orion 8172BNWP ROSS Sure-Flow Combination pH electrode is used for each titration. The analytical techniques given are designed for piperazine solvent; the use of other solvents will require a change in the steps undertaken and equations used.

#### *D.3.2.1 Solvent Amine Content*

For amine concentration, 50 mL of water is poured into a beaker and placed with a stir-bar on a stir-plate. The pH probe is inserted, and 0.5 mL of the amine solvent is pipetted into the beaker. Disposable plastic pipettes are used for this application; the pipette is tared by itself on a scale (Sartorius Digital Lab Scale Balance, R200D 0.1 mg Delta, Range 200g), then the before and after masses of the amine are recorded. 0.5 M HCl is mixed dropwise with the stirring solution by the use of a Brinkmann Buret 50 (Model #05M07421). HCl addition is stopped upon reaching a pH of 3.9. Equation D.1 gives the calculated amine solvent concentration.

$$PZ_{conc.} = \frac{2.154\, V_{HCl}}{m_{solvent}} \tag{D.1}$$

where:

$PZ_{conc.}$ = Solvent Piperazine concentration (Mass %)

$V_{HCl}$ = Volume of HCl added (mL)

$m_{solvent}$ = Mass of solvent added (g)

### *D.3.2.2 Solvent $CO_2$ Content*

For $CO_2$ loading, 50 mL of methanol is poured into a beaker and placed with a stir-bar on a stir-plate. The pH probe electrode is inserted, and 0.5 M KOH solution is added to the beaker to bring the pH up to 11.1 – 11.3. This typically takes 2-3 drops from the Titrette 50 mL burette (Model #16E73318). 1.0 mL of amine solvent is pipetted into the beaker; the pipette is tared by itself on the scale, then the before and after masses of the amine are recorded. The burette is reset, and the 0.5 M KOH solution is added dropwise to the stirring solution until the pH reaches the value obtained with the initial 2-3 drops of KOH. Equation D.2 gives the calculated amine solvent $CO_2$ concentration.

$$CO2_{conc.} = \frac{2.2\, V_{KOH}}{m_{solvent}} \tag{D.2}$$

where:

$CO2_{conc.}$= Solvent $CO_2$ concentration (Mass %)

$V_{KOH}$ = Volume of HCl added (mL)

$m_{solvent}$ = Mass of solvent added (g)

For piperazine solvent, the AGC will lose effectiveness at $CO_2$ capture at $CO_2$ solvent concentrations of roughly 7.5 wt. %.

# REFERENCES


Albrecht, H.E., Damaschke, N., Borys, M., Tropea, C. (2003). *Laser Doppler and Phase Doppler Measurement Techniques*. New York, NY: Springer - Verlag Berlin Heidelberg.

Almeida J., Schobesberger S., Kirkby J. "Molecular understanding of the sulphuric acid-amine particle nucleation in the atmosphere." *Nature Letter*. 2013;502:359-363.

Anderlohr C, Brachert L, Mertens J, Schaber K. "Collection and Generation of Sulfuric Acid Aerosols in a Wet Electrostatic Precipitator" *Aerosol Science and Technology*. 2015;49:144-151.

Artium Technologies. "PDI-100 MD User Manual" Artium Technologies, Inc., Sunnyvale, California, United States. 2015.

Bachalo, W.D. (1980). "Method for Measuring the Size and Velocity of Spheres by Dual-Beam Light-Scattering Interferometry." *Applied Optics*. 19(3):363–370.

Bade O M, Knudsen J N, Gorset O, Askestad I. "Controlling Amine Mist Formation in $CO_2$ Capture from Residual Catalytic Cracker (RCC) Flue Gas" *Energy Procedia*. 2014;63:884-892.

Bai, H., Biswas, P., Keener, T.C. (1994). "$SO_2$ Removal by $NH_3$ Gas Injection: Effects of Temperature and Moisture Content." *Ind. Eng. Chem. Res.* 33:1231–1236.

Beaudry M, Fulk S, Rochelle G T. "Field Measurement of Amine Aerosol by FTIR and Phase Doppler Interferometry." *Energy Procedia*. 2017;114:939-951.

Benzinger W., Wenka A., Dittmeyer R. "Kinetic modeling of the SO2-oxidation with Pt in a microstructed reactor." *Applied Catalysis A: General*. 2011;397:209-217.

von Benzon, H-H, Buchhave P. (1993). "The Phase-Doppler Method Applied to Very Small Particles." *Part. Part. Syst. Charact*. 1994(11):55–62.

Bottoms, R. R. (1930). Patent No. 1783901. United States of America.

Brachert L, Kochenburger T, Schaber K. "Facing the Sulfuric Acid Aerosol Problem in Flue Gas Cleaning: Pilot Plant Experiments and Simulation" *Aerosol Sci. and Tech*. 2013;47:1083-1091.

Brachert L, Mertens J, Khakharia P, Schaber K. "The challenge of measuring sulfuric acid aerosols: Number concentration and size evaluation using a condensation particle counter (CPC) and an electrical low pressure impactor (ELPI+)" *J. of Aerosol Sci*. 2014;67:21-27.

Calvert, S., Englund, H. (1984). *Handbook of Air Pollution Technology*. New York, NY: John Wiley & Sons, Inc.

Cao Y, Zhou H, Jiang W, Chen C, Pan W. "Studies of the Fate of Sulfur Trioxide in Coal-Fired Utility Boilers Based on Modified Selected Condensation Methods" *Environ. Sci. Technol*. 2010;44:3429-3434.

Carter, T. (2012). "National Carbon Capture Center: Post-Combustion." In *2012 NETL CO2 Capture Technology Meeting*.

Chen E., Fulk S., Sache D., Lin Y-J., Rochelle G. T. "Pilot Plant Activities with Concentrated Piperazine" *Energy Procedia*. 2014;63:1376-1391.

Closmann, FB. (2011). "Oxidation and Thermal Degradation of Methyldiethanolamine/Piperazine in CO2 Capture." The University of Texas at Austin. Ph.D. Dissertation.

Colburn AP, Edison AG. "Prevention of Fog in Cooler-Condensers" *Industrial and Engineering Chemistry.* 1941:457-458.

"Control of Mercury Emissions from Coal-Fired Electric Utility Boilers" Air Pollution Prevention and Control Division, National Risk Management Research Laboratory, Office of Research and Development, US Environmental Protection Agency, Research Triangle Park, NC. (2003).

Damle A. S., Ensor D. S., Ranade M. B. "Coal Combustion Aerosol Formation Mechanisms; A Review." *Aerosol Science and Technology*. 1981;1:119-133.

da Silva E F, Kolderup H, Goetheer E, Hjarbo K W, Huizinga A, Khakharia P, Tuinman I, Mejdell T, Zahlsen K, Vernstad K, Kyldbakk A, Holten T, Kvamsdal H M, van Os P, Einbu A. "Emission studies from a $CO_2$ capture pilot plant" *Energy Procedia*. 2013;37:778-783.

Davis, J.D. (2009). "Thermal Degradation of Aqueous Amines Used for Carbon Dioxide Capture." The University of Texas at Austin. Ph.D. Dissertation.

Du L, Lukefahr E, Naranjo A. "Texas Department of Transportation Fly Ash Database and the Development of Chemical Composition-Based Fly Ash Alkali-Silica Reaction Durability Index" *J. Materials in Civil Eng*. 2013;25:70-77.

Ehrig R., Ofenloch O., Schaber K., Deuflhard P. "Modelling and simulation of aerosol formation by heterogeneous nucleation in gas-liquid contact devices" *Chemical Engineerin Science*. 2002;57:1151-1163.

Fisher K., Daga A., Hatchell D., Rochelle G. T. MEA and piperazine corrosion of carbon steel and stainless steel" *Energy Procedia*. 2017;114:1751-1764.

Fogler, H S. "Elements of Chemical Reaction Engineering." 4th ed., Pearson Education, Inc., Westford, MA (2006).

Freeman, S.A. (2011). "Thermal Degradation and Oxidation of Aqueous Piperazine for Carbon Dioxide Capture." The University of Texas at Austin. Ph.D. Dissertation

Fulk S M, Rochell G T. "Modeling Aerosols in Amine-based $CO_2$ Capture." *Energy Procedia*. 2013;37:1706-1719.

Fulk S M, Rochell G T. “Quantification of Gas and Aerosol-phase Piperazine Emissions by FTIR Under Variable Bench-scale Absorber Conditions.” *Energy Procedia*. 2014;63:871-883.

Fulk, S M. “Measuring and Modeling Aerosols in Carbon Dioxide Capture by Aqueous Amines.” The University of Texas at Austin, http://rochelle.che.utexas.edu/files/2015/02/Fulk_Dissertation-red.pdf, (2016).

Fulk S M, Beaudry M, Rochelle G T. “Amine Aerosol Characterization by Phase Doppler Interferometry.” *Energy Procedia*. 2017;114:939-951.

Funk PA, Baker, K D. “Dust Cyclone Technology- A Literature Review.” *J. Cotton Sci*. 2013;17:40–51.

Gasmet Technologies Oy. (2009). “Calcmet for Windows: User’s Guide and Reference Manual. Analysis and Controlling Software Version 11.08.”

GASMET-USA, A.Q.A. d/b/a. (2014). “MSSH-7 Stream Switching System User Manual: Revision 0.”

Goff, G.S. (2005). “Oxidative Degradation of Aqueous Methanolamine in $CO_2$ Capture Processes: Iron and Copper Catalysis, Inhibition, and $O_2$ Mass Transfer.” The University of Texas at Austin. Ph.D. Dissertation.

Gretscher H., Schaber K. “Aerosol formation by heterogeneous nucleation in wet scrubbing processes” *Chemical Engineering and Processing: Process Intensification*. 1999;38:541-548.

Heidenreich S., Vogt U., Buttner H., Ebert F. “A novel process to separate submicron particles from gases- a cascade of packed columns.” *Chemical Engineering Science*. 2000;55:2895-2905.

Himes R. “Continuous measurement of SO3 in a Coal-Fired Power Plant.” EPRI, Palo Alto, CA, 2006.

Hoffmann A C, L E Stein., “Gas Cyclones and Swirl Tubes”. Berlin, Germany, Springer-Verlag Berlin Heidelberg New York, 2002.

IPCC, 2005. “IPCC Special Report on Carbon Dioxide Capture and Storage; Prepared by Working Group III of the Intergovernmental Panel on Climate Change.” Cambridge, UK and New York, NY, USA: Cambridge University Press

IPCC, 2007. “Technical Summary. In: Climate Change 2007: Mitigation. Contribution of Working Group III to the Fourth Assessment Report of the Intergovernmental Panel on Climate Change.” Cambridge, UK and New York, NY, USA: Cambridge University Press

Jacobson M. Z., Turco R. P. “Modeling Coagulation Among Particles of different Composition and Size” *Atmospheric Environment*. 1993;28:1327-1338.

Johannessen, T., Christensen, J.A., Simonsen, O., Livbjerg, H. (1997). "The Dynamics of Aerosols in Condensational Scrubbers." *Chemical Engineering Science*. 52(15):2541–2556.

Kamijo T., Kajiya Y., Endo T., Nagayasu H., Tanaka H., Hirata T., Yonekawa T., Tsujiuchi T. "SO3 Impact on Amine Emission and Emission Reduction Technology" *Energy Procedia*. 2013;37:1793-1796.

Kang J-L., Zhang Y., Fulk S., Rochelle G. T. "Modeling Amine Aerosol Growth in the Absorber and Water Wash." *Energy Procedia*. 2017;114:959-976.

Kaufmann S., Loretz Y., Hilfiker K. "Prevention of fog in a condenser by simultaneous heating and cooling" *Heat and Mass Transfer*. 1997;32:403-410.

Khakharia P, Brachert L, Mertens J, Huizinga A, Schallert B, Schaber K, Vlugt T J H, Goetheer E. "Investigation of aerosol based emission of MEA due to sulfuric acid aerosol and soot in a Post Combustion $CO_2$ Capture process" *Int. J. Greenhouse Gas Control*. 2013;19: 138–144.

Khakharia P, Kvamsdal H M, da Silva E F, Vlugt T J H, Goetheer E. "Field study of a Brownian Demister Unit to reduce aerosol based emission from a Post Combustion $CO_2$ Capture process" *Int. J. Greenhouse Gas Control*. 2014;28: 57–64.

Khakharia P. "Aerosol-based Emission, Solvent Degradation, and Corrosion in Post Combustion $CO_2$ Capture." Technische Universiteit Deft, the Netherlands and Geboren te Mumbai, India, http://repository.tudelft.nl/, (2015).

Knudsen J., Jensen J. N., Vilhelmsen P-J., Biede O. "Experience with $CO_2$ capture from coal flue gas in pilot-scale: Testing of different amine solvents." *Energy Procedia*. 2009;1:783-790.

Knudsen, J. N., Bade, O. M., Anheden M., Bjorklund R., Gorset O., Woodhouse S. "Novel concept for emission control in post combustion capture" *Energy Procedia*. 2013;37:1804-1813.

Knudsen, J. N., Bade, O. M., Askestad I., Gorset O., Mejdell T. "Pilot Plant Demonstration of CO2 Capture from Cement Plant with Advanced Amine Technology" *Energy Procedia*. 2014;63:6464-6475.

Kolderup, H., Hjarbo, K.W., Huizinga, A., Tuinman, I., Zahlsen, K., Vernstad, K., Hyldbakk, A., et al. (2012). "WP 1 and 3 in the Project: CCM TQP Amine 6 - Emission Quantification and Reduction."

Lin Y-J., Chen E., Rochelle G. T.. "Pilot plant test of the advanced flash stripper for CO2 capture" *Faraday Discussions*. 2016;192:000-000.

Looney B., Irvin N., Acharya C., Wong J., Glesmann S. "The Role of Activated Carbon in a Comprehensive MATS Strategy". (2014). < http://www.powermag.com/the-role-of-activated-carbon-in-a-comprehensive-mats-strategy/>

Marier P., Dibbs H. P. “The catalytic conversion of SO2 to SO3 by fly ash and the capture of SO3 and SO3 by CaO and MgO” *Thermochimica Acta*. 1974;8:155-165.

Marjamaki M., Keskinen J., Chen D. R., Pui D. Y. H. “Performance Evaluation of the Electrical Low Pressure Impactor (ELPI).” *Journal of Aerosol Science*. 2000;31:249-261.

Mertens J, Knudsen J, Thielens M L, Anderson J. “On-line monitoring and controlling emissions in amine post combustion carbon capture: A field test” *Int. J. Greenhouse Gas Control*. 2012;6:2-11.

Mertens J, Lepaumier H, Desagher D, Theilens M L. “Understanding ethanolamine (MEA) and ammonia emissions from amine based post combustion carbon capture: Lessons learned from field tests” *Int. J. Greenhouse Gas Control*. 2013;13:72–77.

Mertens J, Brachert L, Desagher D, Theilens M L, Khakharia P, Goetheer E, Schaber K. “ELPI$^{+}$ measurements of aerosol growth in an amine absorption column” *Int. J Greenhouse Gas Control*. 2014(a);23:44–50.

Mertens J, Anderlohr C, Rogiers P, Brachert L, Khakharia P, Goetheer E, Schaber K. “A wet electrostatic precipitator (WESP) as countermeasure to mist formation in amine based carbon capture” *Int. J Greenhouse Gas Control*. 2014(b);31:175-181.

Mertens J, Brachert L., Desagher D., Schallert B., Khakharia P., Goetheer E. “Predicting Amine Mist Formation Based on Aerosol Number Concentration and Size Measurements in Flue Gas” *Energy Procedia*. 2014(c);63:893-901.

Mitsubishi Heavy Industries (MHI). (2011, August 16). Amine Emission Control Technology of KM CDR Process TM. *Presented at the Amine Workshop. Palo Alto, California.*

Morton F., Laird R., Northington J. “The National Carbon Capture Center: Cost-effective test bed for carbon capture R&D” *Energy Procedia*. 2013;37:525-539.

Nair P. V. N., Vohra K. G. “Growth of aqueous sulphuric acid droplets as a function of relative humidity” *J. of Aerosol Sci*. 1975;6:265-271.

Nguyen B-T N. “Amine Volatility in $CO_2$ Capture.” The University of Texas at Austin, https://repositories.lib.utexas.edu/handle/2152/21988, (2013).

Pfeifer P, Zscherpe T, Haas-Santo K, Dittmeyer R. “Investigations on a Pt/TiO2 catalyst coating for oxidation of $SO_2$ in a microstructured reactor for operation with forced decreasing temperature profile” *Applied Catalysis A: General*. 2011;391:289-296.

Radziemski, L.J., Solarz, R.W., Paisner, J.A. (1987). *Laser Spectroscopy and Its Applications*. Optical En. New York, NY: Marcel Dekker, Inc.

Rao A. B., Rubin E. S. “A Technical, Economic, and Environmental Assessment of Amine-Based $CO_2$ Capture Technology for Power Plant Greenhouse Gas Control” *Environ. Sci. Technol*. 2002;36:4467-4475.

Saha C., Irvin J. H. “Real-time aerosol measurements in pilot scale coal fired post-combustion CO2 Capture.” *Journal of Aerosol Science.* 2017;104:43-57

Schaber K.. “Aerosol formation in absorption processes” *Chemical Engineering Science*. 1995;50:1347-1360.

Schaber K., Korber J., Ofenloch O., Ehrig R., Deuflhard P. “Aerosol formation in gas-liquid contact devices- nucleation, growth and particle dynamics” *Chemical Engineering Science*. 2002;57:4345-4356.

Sexton, A.J. (2008). “Amine Oxidation in CO2 Capture Processes.” The University of Texas at Austin. Ph.D. Dissertation

Sexton A., Dombrowski K., Nielsen P., Rochelle G. T., Fisher K., Youngerman J., Chen E., Singh P., Davidson J. “Evaluation of Reclaimer Sludge Disposal from Post-combustion CO2 Capture” *Energy Procedia*. 2014;63:926-939.

Shale, C.C. (1973). “Ammonia Injection: A Route to Clean Stacks.” In *Pollution Control and Energy Needs*., 195–205. Washington DC.

Sinanis S., Wix A., Ana L., Schaber K. “Characterization of sulphuric acid and ammonium sulphate aerosols in wet flue gas cleaning processes” *Chemical Engineering and Processing: Process Intensification*. 2008;47:22–30.

SINTEF. (2012, January 25). Emission Study at the Maasvlakte $CO_2$ Capture Pilot Plant. *University of Texas Conference on Carbon Capture and Storage.* Austin, Texas.

Sipperley, C.M., Bachalo, W.D. (2014). “Triple Interval Phase Doppler Interferometry : Improved Dense Sprays Measurements and Enhanced Phase Discrimination.” In *17th International Symposium on Applications of Laser Techniques to Measure Fluid Mechanics*. Lisbon, Portugal.

Srivastava R K, Miller C A. “Emissions of Sulfur Trioxide from Coal-Fired Power Plants” *J. Air & Waste Manage. Assoc.*. 2004;54:750-762.

Swanson, M. “Technical Paper T-139: Baghouse Applications”. < http://www.astecinc.com/images/file/literature/Astec-T-139-Baghouse-Applications-EN.pdf>

Uyanga I. J., Idem R. O. “Studies of SO2 and O2 Induced Degradation of Aqueous MEA during CO2 Capture from Power Plant Flue Gas Streams.” *Ind. Eng. Chem. Res*. 2007;46:2558-2566.

van der Gjip, S., Huizinga, A., Kester, L., Khakharia, P., Tuinman, I., van Os, P. (2012). “Emission Reducing Technologies: Aerosols.” In *The University of Texas Conference on Carbon Capture*. Austin, TX.

Voice, A.K. (2013). “Amine Oxidation in Carbon Dioxide by Aqueous Scrubbing.” The University of Texas at Austin. Ph.D. Dissertation

Warren D. R., Seinfeld J. H. “Simulation of Aerosol Size Distribution Evolution in Systems with Simultaneous Nucleation, Condensation, and Coagulation.” *Aerosol Science and Technology,* 1985;4:31-43

Wix A, Brachert L, Sinanis S, Schaber K. “A simulation tool for aerosol formation during sulphuric acid absorption in a gas cleaning process” *J. Aerosol Sci*. 2010;41:1066–1079.

Yue G. K., Hamill P. “The homogeneous nucleation rates of $H_2SO_4$-$H_2O$ aerosol particles in air” *Journal of Aerosol Science*. 1979(a);10:609-614.

Yue G. K. “A quick method for estimating the equilibrium size and composition of aqueous sulfuric acid droplets” *Journal of Aerosol Science*. 1979(b)201;10:75-86.

Zhang Y., Rochelle G. T. “Absorber Performance with High CO2.” *Energy Procedia*. 2014;63:1329-1338.

Zhang Y., Kang J-L., Fulk S., Rochelle G. T. “Modeling Amine Aerosol Growth at Realistic Pilot Plant Conditions.” *Energy Procedia*. 2017;114:1045-1060.

# VITA

Matthew Robert Beaudry attended Lamar University from 2006 to 2011. During his time at Lamar, Matthew worked as an organic chemistry lab assistant under Marsha Williams. He also undertook a pair of co-op semesters with LyondellBasell Industries, and spent a summer researching biofuels production in the NSF REU program under Dr. Anthony Dean at Colorado School of Mines. Matthew graduated from Lamar in May 2011 and entered the Ph. D. program at the University of Texas at Austin the following August. After spending the first 2+ years on ill-fated battery research, he joined the Rochelle Research Group. Upon graduation, Matthew will begin employment with Integrated Consulting and Qualification, Corp.

Permanent email: mattbeaudry@utexas.edu

This dissertation was typed by the author.